Complexification d'un système LCu(I) pour la coordination et l'activation du dioxygène : étude par spectrométrie de masse et DFT

Matthieu Regnacq

DOCTORAT MATIERE BRETAGNE MOLECULES LOIRE ET MATERIAUX

UBO
Université de Bretagne Occidentale

THÈSE DE DOCTORAT DE

L'UNIVERSITÉ
DE BRETAGNE OCCIDENTALE

ÉCOLE DOCTORALE N° 596
Matière Molécules et Matériaux
Spécialité : Chimie Physique, Chimie Théorique

Par

Matthieu REGNACQ

Growing complexity of $LCu^{(I)}$ to elucidate O_2 coordination and activation: a mass spectrometric and DFT study

Thèse présentée et soutenue à Brest, le 19 mai 2022
Unité de recherche : UMR 6521 CNRS-Université de Bretagne Occidentale, CEMCA
UFR des Sciences et Techniques
6, avenue Victor le Gorgeu, CS 93837
29238 BREST CEDEX 3, FRANCE

Rapporteurs avant soutenance :

Hélène JAMET
Maîtresse de conférences, HDR, DCM,
Université Grenoble Alpes

Yves GIMBERT
Directeur de recherche CNRS, IPCM,
Sorbonne Université

Composition du Jury :

Hélène JAMET	Maîtresse de conférences, DCM, Université Grenoble Alpes
Président du jury Yves GIMBERT	Directeur de Recherche CNRS, IPCM, Sorbonne Université
György LENDVAY	Professeur, Institute of Materials and Environmental Chemistry, TTK, Budapest, HONGRIE
Directeur de thèse Antony MEMBOEUF	Maître de conférences, HDR, Université de Bretagne Occidentale
Co-directeur de thèse Frédéric GLOAGUEN	Directeur de recherche CNRS, Université de Bretagne Occidentale
Invité Nicolas LE POUL	Chargé de recherche CNRS, HDR, Université de Bretagne Occidentale

À ma femme, à mes enfants

À mes parents

Remerciements - Acknowledgments

Mes premiers remerciements vont à vous, mes directeurs de thèse, Antony MEMBOEUF et Frédéric GLOAGUEN, pour la confiance que vous m'avez accordé au moment de lancer ce projet de thèse, pour vos conseils avisés et votre aide tout au long de celle-ci. Je remercie également la Région Bretagne et l'Université de Bretagne Occidentale, pour leur participation égale dans le financement de cette thèse.

En particulier, je souhaite saluer ton investissement, Antony, dans les démarches administratives et sur les aspects de spectrométrie de masse, surtout auprès de Mamie, notre triple-quadripôle à l'âge canonique. Malgré les différentes pannes, elle nous a finalement permis de collecter les données nécessaires… Merci d'avoir passé tant de temps à mes côtés pour me partager tes connaissances et répondre à mes questions, de m'avoir offert une prolongation de contrat pour finir ce travail de thèse et pour ton trait d'humour.

Rapporter un manuscrit de thèse est un travail qui demande un certain investissement. Aussi, je vous remercie chaleureusement, Madame Hélène JAMET et Monsieur Yves GIMBERT, d'avoir accepté cette tâche de lecture, de correction et d'évaluation de mon travail. J'espère que vous aurez autant de plaisir à le lire que j'en ai eu à l'écrire.

Ce travail a été mené au sein de l'UMR 6521 - CEMCA, que je remercie vivement. Je suis particulièrement reconnaissant envers chacun des enseignants, pour leurs cours auxquels j'ai eu le loisir d'assister pendant toutes ses années de formation et envers ses personnels, en particulier Isabelle et Maryline au secrétariat. Je remercie également l'Université de Bretagne Occidentale, l'École Doctorale 3M et Michèle KERLEROUX pour son aide, ainsi que la Direction Europe et International pour la bourse de mobilité de deux mois à Budapest (Hongrie) obtenue pendant cette thèse. Merci également à Matthieu WAELES d'avoir accepté de faire partie de mon comité de suivi individuel de thèse.

I would like to thank you, Pr. György LENDVAY, for welcoming me in Budapest for two months. I am very grateful for all technical and scientific advices you gave me. Thank you also for agreeing to consider this work and for all the administrative tasks you have maid for my accomodation in Budapest, our long discussions and for the boat. Ezerszer köszönöm ! Nagyon hálás vagyok önnek ezért ! Thank you also to you, dear Madam Gabriella LENDVAYNÉ, for your kind attention. A Zserbo tortád emlékezetes volt.

Je voudrais saluer et remercier spécialement Nicolas et Alexandre, pour toutes les discussions autour de ce projet, vos éclairages, propositions et autres conseils. Votre aide autour de la chimie du cuivre-oxygène et des divers indicateurs de chimie quantique m'a été très précieuse. Je remercie aussi mes autres collègues et connaissances de travail, encore présents au laboratoire ou partis vers d'autres contrées, Alicia B., Alicia M., Amélie, Austin, Bénédicte, Carlos, Christophe, David, Ewen, Karunamay, Laurianne, Mahdi, Noémie, Nolwenn, Pablo, Thomas et les doctorants des autres équipes de l'UMR. Merci pour les discussions plus ou moins scientifiques, parfois autour de gâteaux (plus ou moins réussis). J'aurai plaisir à avoir de vos nouvelles de temps en temps. Austin, I am particularly thankful to you for the synthesis you had tried for me. Merci à Hélène C. pour les Cordées de la Réussite auxquelles j'ai eu la chance de participer une année. Dany, enfin, merci de m'avoir accueilli au laboratoire, de m'avoir appris les petits "trucs et astuces" pour avoir un bon signal sur mes spectres de masse. Merci pour les après-midis de sport et les soirées Ligue des Champions.

Étienne, Clara, Madeleine, Baudouin, Marjorie, Pierre-Louis et tous mes autres amis, merci pour les moments passés en votre compagnie et pour l'amitié que vous me témoignez. Grâce à vous, j'ai pu souffler quand j'en avais besoin, et mener des conversations sur des sujets autres que le cuivre…

Spéciale dédicace à ma famille, et en particulier à mes parents, pour leur soutien indéfectible pendant ces longues études. À mes frères et sœurs, qui ont souvent plaisanté à propos du chimiste de synthèse que je ne suis pas. Je vous mets au défi de lire quelques pages et de poser quelques questions, je serai heureux de vous répondre !

Une pensée aussi pour ma belle-famille, pour l'intérêt porté à mon travail, malgré la jeunesse des uns et les orientations plus littéraires ou financières des autres.

Surtout, je voudrais te remercier, Claire, pour l'amour que tu me portes et ton soutien dans les moments difficiles. Nous formons une belle équipe, et j'espère qu'elle restera solide pendant toute notre vie.

Abbreviations[1]

a: Direct Current (DC) stability parameter from Mathieu's equation

a_0, a_x, a_c: Parameters of a hybrid exchange-correlation functional

ABNO: 9-azabicyclo[3.3.1]nonane-N-oxyl

ACT: 4-acetamido-TEMPO

AO: Atomic Orbital

AO: Amine Oxidase

AZADO: 2-azaadamantane-N-oxyl

BDE: Bond Dissociation Energy

BIRD: Black-body Infrared Radiative Dissociation

BPBA: bis(2-pyridylmethyl)tert-butylamine

BPGA: bis(6-pivalamide-2-pyridylmethyl)-(2-acetylmethyl)amine

BPPA: bis(6-pivalamide-2-pyridylmethyl)-(2-pyridylmethyl)amine

bpy: bipyridine

C_j: Concentration of a dissolved species j ($mol.L^{-1}$)

CAR: Collision Activated Reaction

CASSCF: Complete Active Space Self-Consistent Field

CD: Corona Discharge

CEM: Chain Ejection Model

CI: Configuration Interaction

CID: Collision Induced Dissociation

cPCET: see PCET

CPU: Central Processing Unit

CRM: Charge Residue Model

CSI-MS: Cryoelectrospray Mass Ppectrometry

Cys: cysteine (amino-acid, or residue)

d: Capillary diameter (m)

d: Distance (between two atoms, Å)

Da: Dalton (equivalent of unified atomic mass unit : 1 Da = 1,660 539 066.10^{-27} kg)

DβH: Dopamine β-Hydroxylase (or DBH)

DβM: Dopamine β-Monooxygenase (or DBM)

DFT: Density Functional Theory

DHA: dihydroanthracene

1 The units specified here are by default. Abbreviations in italics refer to equations.

DPQ: 4,5-dihydroxy-phenylalanine quinone

E: Exact energy of the system

E_0: Electric field applied in the ESI source ($V.m^{-1}$)

ECD: Electron-Capture Dissociation

E_{correl}: Correlation energy

E^{HF}: Hartree-Fock energy

$E_{pairing}$: Spin-pairing energy

EPR: Electron Paramagnetic Resonance (or also ESR: Electron Spin Resonance)

ETD: Electron-Transfer Dissociation

F: Faraday constant (96 485, 332 123 $C.mol^{-1}$)

f: Fock operator

f_{RF}: Frequency of alternating voltage (radiofrequency ≈ 1 MHz) applied in a quadrupole

G: Free enthalpy (or Gibbs energy)

GAO: Galactose Oxydase

GC: Gas Chromatography

GLO: Glyoxal Oxidase

Glu: glutamine/glutamate (amino-acid, or residue)

H: Hendricks coefficient (depends on dielectric constant ε and on the surface tension γ)

H: Enthalpy

HF: Hartree-Fock

His: histidine (amino-acid, or residue)

HOMO: Highest Occupied Molecular Orbital

HPLC: High-Performance LC

HSAB: Hard and Soft Acid and Base (theory of Pearson)

IEM: Ion Evaporation Model

i_{ES}: Electrospray source current

^{i}Pr: Isopropyl group

IBO: Intrinsic Bond Orbitals

ICP: Inductively Coupled Plasma (ionization torch)

IR: InfraRed

IRC: Intrinsic Reaction Coordinate

IRMPD : InfraRed MultiPhoton Dissociation

$\hat{J}$: Coulomb operator included in v^{HF}

$\hat{K}$: Exchange operator included in v^{HF}

L: Length of the flow tube of the TOF analyzer

L: Ligand

LC: Liquid Chromatography

LMCT: Ligand-to-Metal Charge Transfer

LPMO: Lytic Polysaccharide MonoOxygenase

LUMO: Lowest Unoccupied Molecular Orbital

K_{asso}: Associative equilibrium constant

m: Mass of an ion (kg)

m/z: mass over charge ratio (uma or Da)

Me_1Tren: methyltriethyleneamine

Me_3Tren: tris[2-(methylamino)ethyl]amine

Me_6Tren: tris[2-(dimethylamino)ethyl]amine

MCD: Magnetic Circular Dichroism

Me: methyl group

Met: methionine (amino-acid, or residue)

MO: Molecular Orbital

MOXD1: Monooxygenase X

MRM: Multiple Reaction Monitoring

MS: Mass Spectrometry (MS/MS: Tandem Mass Spectrometry)

MS-RASPT2: Multi-State - 2nd order Perturbation Theory Restricted Active Space

n_j: Number of electrons implied in a redox reaction j

NMR: Nuclear Magnetic Resonnance

OD: Oxidation Degree

OTf: triflate anion ($CF_3SO_3^-$)

PAM: Peptidyl α-Amidating Monooxygenase

PCET: Proton Coupled Electron Transfer (sometimes preceded by c, that stands for concerted)

PES: Potential Energy Surface

Ph: phenyl group

PhIO: iodosobenzene (or iodosylbenzene)

phen: phenantroline

PHM: Peptidyl α-Hydroxylating Monooxygenase

pMMO: Particulate Methane MonoOxygenase

PT: Proton Transfer

Py: pyridine

q: Alternating Current (AC) stability parameter from Mathieu's equation

QHQ: Quadrupole Hexapole Quadrupole

QIT: Quadrupole Ion Trap

QM/MM: Quantum Mechanics/Molecular Mechanics

q_{Ry}: Limit charge of Rayleigh (C)

R_2bpy: 4,4'-disubstituted bipyridyl ligands

RMN: see NMR

R_{Ry}: Limit radius de Rayleigh (m)

r_0: Geometrical parameter of a quadrupole / QIT (distance center – electrode / annular electrode)

r_c: External radius of the metallic capillary of the ESI source (m)

S: Entropy

salen: Tetradentate ligand synthesized from salicylaldehyde (sal) and ethylenediamine (en)

SCF: Self-Confident Field

SID: Surface Induced Dissociation

SIFT: Selected-Ion Flow Tube

SIR: Selected Ion Recording

SOMO: Single Occupied Molecular Orbital

SQUID: Superconducting QUantum Interference Device

t: Time of flight in the TOF analyzer

$\hat{T}$: Kinetic energy operator

^{t}Bu: tertiobutyl group

TACN: 1,4,7-triazacyclononane

TD-DFT: Time-Dependent Density Functional Theory

TEMPO: (2,2,6,6-tetramethylpiperidin-1-yl)oxyl

TIC: Total Ion Current

TMG_3Tren: 1,1,1-tris[2-[N(2)-(1,1,3,3-tetramethylguanidino)]ethyl]amine

TMPA: tris(2-pyridylmethyl)amine (or also TPA)

TMQA: tris(2-quinolylmethyl)amine

TPQ: 2,4,5-trihydroxy-phenylalanine quinone

Tren: tris(2-aminoethyl)amine

tQ: Triple Quadrupole

TOF: Time-Of-Flight (analyzer)

TON: Turn Over Number

TPQ: 2,4,5-trihydroxy-phenylalanine quinone

Tyr: tyrosine (amino-acid, or residue)

TβH: Tyramine β-Hydrogenase (or Monooxygenase)

U: DC voltage applied on the electrodes of a quadrupole or a QIT (V)

UHR: Ultra-High Resolution

UV-Vis: Ultraviolet-visible spectroscopy

V: Voltage applied upstream of the TOF analyzer (acceleration voltage)

$\hat{V}$: Potential energy operator

V_0: Voltage applied between capillary and counter-electrode in the ESI source (V)

V_0: Alternating current (AC) amplitude applied on the electrodes of a quadrupole or a QIT (V)

XAS: X-Ray Absorption Spectrosopy

ZPE: Zero-Point Energy

z: Ion charge

z_0: Geometrical parameter of a QIT (center of the trap – cap electrode distance)

γ: Surface tension ($N.m^{-1}$)

ε_0: Vacuum permittivity ($8{,}854\ 187.10^{-12}\ F.m^{-1}$)

σ: Spin of an electron (± ½)

σ_S: Conductivity ($S.m^{-1}$)

v: Frequency

v_f: Flow rate ($L.s^{-1}$)

v^{HF}: Mean interaction potential sustained by an electron in the HF theory frame

χ: Spin-orbital (= ψω)

Ψ: Wave function

ψ: Space orbital

ω: Temporal frequency

ω_n: Spin function (± 1/2 for an electron)

∇^2 : Laplacian operator (also noted as Δ)

Table of contents

Chapter 2

A Model Reaction for the Understanding of Enzymatic Mechanisms – The Oxidation of Toluene by CuO_2^+

Chapter 3

O_2 Coordination on Cu-bipyridyl Complexes in the Gas Phase – Influence of Functionalization

Chapter 4

Use of Tripodal Ligands for Dioxygen Coordination in the Gas Phase

Conclusions

Appendix – Instrumentation and Molecular Modeling

Annexes – Instrumentation et Modélisation Moléculaire

Résumé en français

Principaux Résultats des Travaux de Thèse

Foreword

The issues related to global warming, the deterioration of ecosystems, or even growing pollution cannot be ignored. In the fight for a more sustainable world, the scientific community is mobilizing to tap into the innumerable riches of nature, drawing inspiration from mineral or biological systems. Nature is so vast that it is not difficult to find a micro-organism, an enzyme, a macro-system capable of degrading such plastic, activating such a molecule, up-cycling such waste.

It is believed that about 40 % of enzymes found in nature contain one or more alkali, alkaline earth or transition metal ions. These metalloproteins have an essential role in cell life. A mono-, di- or polynuclear active site has either a structural role or the capacity to carry out numerous steps of biosynthesis (coordination of small ligands and substrates; transfer of electrons, protons, hydrogen and oxygen atoms; catalysis of reactions). A first issue appears here: large-scale use of enzymes is limited. The bio-systems mentioned above work efficiently, with high specificity, but often have specific constraints (temperature, pressure, pH, etc.), are expensive and have low yields over time. So, the biomimetic approach, that consists in the observation of living systems, their transfer to models and their application, as defined by the ISO/TC266 18458 standard (2015) is a promising way. For example, hydrocarbons oxidation or carbonates valuation, H_2 production (proton reduction), water oxidation are at the center of concerns. To answer that problem, nature uses Cu (a widely available, cheap and low-toxic metal) and O_2 (the most widespread oxidant on Earth). Regarding the activation of O_2, its reduction to water and the range of possible oxidation reactions, although there are fewer copper enzymes – iron enzymes being the most widespread as in plant kingdom as in animal kingdom - they are generally able to perform the same functions (O_2 capture and transport, electron transfer, oxidation). Copper is also involved in the formation of hemoglobin in the immune system, useful against the oxidative stress. The search for efficient and specific systems based on widely accessible compounds is therefore very attractive.

Two major problems then arise. On the one hand, the precise understanding of the operation of living systems and natural phenomena is someway difficult to obtain. On the other hand, the efficiency of new biomimetic systems is sometimes unsatisfactory, due to low selectivity, use of noble metal or rare-earth element or expensive co-substrate, heavy synthetic routes… Thus, a large number of biomimetic systems have been developed for nearly forty years, with the aim of generating industrial feedstocks and fuels. The catalysis of elementary reactions, such as oxygenation of CH bonds has been widely studied, with convincing results. If most of the oxidation mechanisms are now rather well defined, there are still some interrogations.

The role of the environment, in both enzymes and biomimetic models, is of prime importance in the oxidation pathways. The metallic center, the first coordination sphere (*i.e.* the amino-acids, the ligands or the solvent molecules that binds the metallic center), the second coordination sphere (solvent molecules) and the nature of the substrate influence the reaction mechanisms in a nested manner. In this thesis, the main approach is the decomposition of these diverse contributions, to evaluate their influence on catalytic cycles.

First of all, **Chapter I** is a bibliographic survey that treats of the oxidation mechanisms in some mononuclear cuproenzymes (galactose oxidase, lytic polysaccharide monooxygenase, amine oxidase) or non coupled binuclear enzymes (dopamine-β-monooxygenase). Some biomimetic models relative to these enzymes are reported. A comparison between natural and biomimetic oxidation pathways is made, focusing on the identified intermediates. The role of the ligand on the activation of O_2 and the oxidation of substrates is explored in depth. Finally, the reactivity of copper complexes towards O_2 in the gas phase (that allows to overcome the solvent influence) is evoked.

In **Chapter II** is presented the oxidation mechanism of toluene by O_2, mediated by bare Cu^+ ion, as a model for the understanding of the influence of ligands in mechanisms of cuproenzymes. A three-step mechanism is postulated on the basis of DFT calculations, taking the spin state into account. This non-trivial, but somewhat familiar mechanism, is supported by considerations on geometries and molecular orbitals, Bond Critical Point analysis and Bader charges calculations. Geometric and energetic comparisons are made between different DFT functionals, while the nature of intermediates is investigated. The role of the copper center on the reaction is also brought out.

Only a few examples in the literature treat O_2 coordination on Cu complexes in the gas phase. In **Chapter III** are exposed the results of mass spectrometry experiments concerning the coordination of O_2 in the gas phase on mononuclear copper complexes. The nature of these CuO_2 adducts is characterized with the help of DFT calculations. A simple mathematical model allows to consider the influence of the functional groups on the coordination of O_2 in the gas phase.

The presence of water as solvent leads to the formation of copper-hydroxo species, that are able to lose water in the electrospray source of the mass spectrometer. The **Chapter IV** discusses the surprising reactivity of these deprotonated $Cu^{(II)}$ complexes towards O_2 in the gas phase. Indeed, they show exacerbated reactivity towards O_2. Mechanistic investigations were led on deprotonation and O_2 coordination pathways. Depending on the rigidity of the ligand, different results were obtained.

Chapter 1

Insights in Mononuclear Copper Enzymes – Dioxygen Activation and Reactivity

This chapter presents the oxidation mechanisms of substrates by molecular O_2, activated by an ionic copper center. First, general aspects of cuproenzymes will be exposed, from the activation of O_2 to the unveiling of mechanisms that happen in some mononuclear enzymes. Then, the biomimetic approach is exposed, for the elaboration of efficient models. The tight tuning of models is presented through some chosen examples. A main trend of mechanism breaks away, and intermediates are discussed one by one. Finally, in order to decompose the influence of environment on the mechanisms, the intermediates are taken in the gas phase to discard the solvent influence.

1. General aspects of Cu enzymes

1.1. Copper-containing enzymes for O_2 activation

There are a few copper-based enzymes in nature; the identification of which began in 1955, with the demonstration of the insertion of an oxygen atom (from O_2) on a substrate using a fungal tyrosinase[1]. The most known of them are presented in Figure 1[1]. The name of each protein refers to its ability to activate O_2. The oxygenase ability stands for the introduction of one (monooxygenase) or two (dioxygenase) oxygen atoms into a substrate. As for oxidase ability, it corresponds to the catalysis of an oxidation-reduction reaction, which involves dioxygen as the electron acceptor. Both abilities can be observed with the same enzyme (monooxygenases release water, for example). Reaction mechanisms set up by nature has to bypass three major issues: the breaking of the strong bond of O_2, the spin-forbidden reaction of O_2 (in the triplet state) with a substrate (singlet state) and the thermodynamic driving force depending on the strength of the CH bond of the substrate.

1 Other interesting mononuclear copper enzymes are plastocyanins, azurins (they both accomplish electron transfer), LPMOs (breakdown of polysaccharides) and GH61, a family of fungal cellulose degrading polysaccharide monooxygenases.

protein (abbreviation)	no. Cu ions involved in O_2 activation	reaction performed
amine oxidase (AO)	1	aldehydes and H_2O_2 from primary amines
galactose oxidase (GAO)	1	aldehydes and H_2O_2 from alcohols
glyoxal oxidase (GLO)	1	carboxylic acids and H_2O_2 from aldehydes
dopamine β-monooxygenase (DβM)	2 (uncoupled)[a]	hydroxylation of dopamine to yield epinephrine
peptidylglycine α-amidating monooxygenase (PHM)	2 (uncoupled)[a]	hydroxylation at α-position of glycine
quercetin 2,3-dioxygenase (QDO)	1	oxidative ring opening of quercetin
hemocyanin (Hc)	2	reversible binding of O_2
tyrosinase (Tyr)	2	hydroxylation of aromatic ring
catechol oxidase (CO)	2	oxidation of catechol to *o*-quinone
methane monoxygenase (MMO)	*b*	hydroxylation of methane to methanol
ammonia monoxygenase (AMO)	*b*	oxidation of ammonia to hydroxylamine
multicopper oxidases[c]	3	
laccase (Lc)	3	oxidative coupling of catechols
ascorbate oxidase (AO)	3	oxidation of ascorbate
ceruloplasmin (Cp)	3	oxidation of Fe(II) to Fe(III)
Fet3	3	oxidation of Fe(II) to Fe(III)
phenoxazinone synthase (POS)	3	oxidative coupling of aminophenols
cytochrome *c* oxidase	1 (+ Fe))	establishment of membrane proton gradient

Figure 1: Activation or binding of O_2 by Cu proteins. [a] The two Cu ions are separated by ~ 11 Å. Now, it is clear that one Cu center activates O_2, the other is used to do electron transfer. [b] Unclear. [c] Selected examples. Reproduced with permission from [122].

1.2. O_2 activation

Activation is a process during which something is made reactive. In biology, for an enzyme, the activation corresponds to the gain of the ability of their biological function. Few atoms or molecules, such as O_2, needs activation to be reactive. The key to the oxygenation of substrates is the activation of molecular oxygen. Indeed, O_2 is known to be a rather strong oxidant ($E°_{O_2(g)\,/\,H_2O}$ = 1.229 V vs SHE[2]), i.e. an electron acceptor, but with low kinetic rates of reaction. It is due to its ground triplet spin state $^3\Sigma_g^-$ (Figure 2), which forbids the reaction with substrates in singlet spin state. In order to overcome that issue, the activation of dioxygen allows either the crossing to singlet state or the decrease of the triplet-singlet gap. Light- or electronic excitation allows spin inversion $\alpha_{(+1/2)} \rightarrow \beta_{(-1/2)}$ from one mono-occupied π* orbital to the other[3] ($^3\Sigma_g^- \rightarrow {}^1\Delta_g$) or on the same orbital[4] ($^3\Sigma_g^- \rightarrow {}^1\Sigma_g^+$). An electron transfer can take place between dioxygen and a reductant (electron donor), filling the π* orbitals. This reductant can be an electron-rich metal (*i.e.* with a low oxidation degree), that coordinates O_2. One of the best example of such activation is hemoglobin and hemocyanin, and other O_2 carriers: one or two Cu or Fe ions in low oxidation degree transfer electrons to O_2, giving it a $O_2^{\bullet-}$ or even a O_2^{2-} character. The oxidation state of Cu, although it is formal, has a great importance in the global reactivity of a system. Adding one or more electrons on

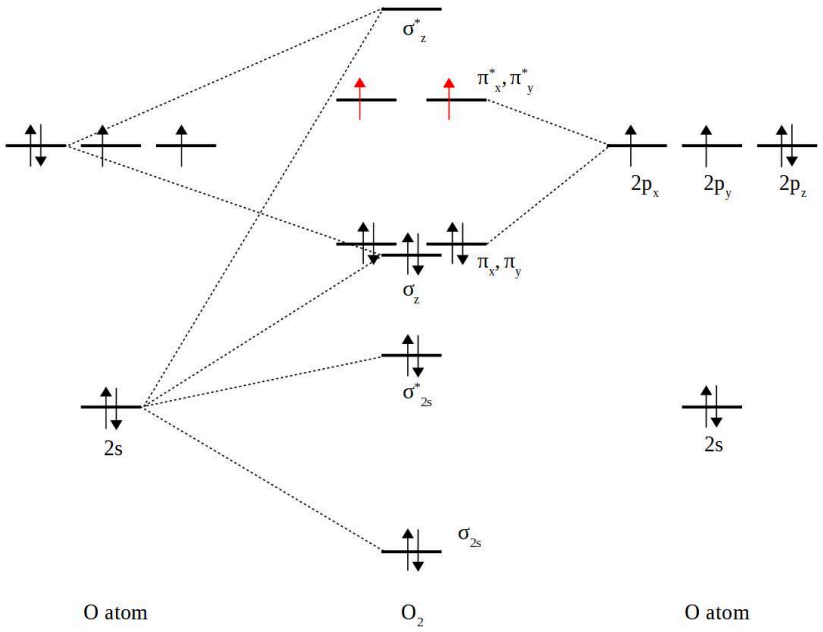

Figure 2: Correlated Molecular Orbital diagram of O_2, in its $^3\Sigma_g^-$ triplet ground state. Single electrons are indicated in red.

π* orbitals weakens the triplet character of O_2, by total or partial delocalization of the spin density on the metal center, or even on the coordinating ligands. The spin state of the dioxygen adduct is a persistent concern in many ligand designs[5]. In some cases, the singlet spin state is even favored by orbital and electronic reorganization[6,7], allowing the oxidation of substrates.

1.3. Mechanistic insights of mononuclear Cu enzymes

Nature prefers Cu to other transition metals to activate O_2, because it favors faster electron transfer (since, it has a higher redox potential, all other things being equal) and possesses the maximum number of d electrons for the activation of O_2[8]. The more O_2 is activated, the more powerful the species are to oxidize strong CH bonds. In general, mononuclear enzymes have oxygenase activity. In spite of their low oxidative power, structures and postulated mechanisms of galactose oxidase (GAO)/glyoxal oxidase (GLO), lytic polysaccharide monooxygenase (LPMO), dopamine β-monooxygenase (DβM)/peptidyl α-hydroxylating monooxygenase (PHM) and amine oxidase (AO) will be deepened here, because of their ability to oxidize substrates with only one active Cu center, *via* highly efficient and sometimes highly selective oxidative pathways. The enzyme family of PHM has, in fact, two uncoupled Cu centers, but can be modeled by mononuclear

complex, with the contribution of an external chemical or electrochemical reductant. Relevant pathways will be detailed here, based on experimental and theoretical works. The crystal structures of native and mutant enzymes (determined by X-ray crystallography) are helpful to determine the environment of active sites. Diverse spectroscopies (UV-Visible, IR, Raman, EPR, XAS, MCD), SQUID measurement (magnetometry used to measure very low magnetic fields), electrochemistry, kinetic experiments and modelization tools (DFT and especially QM/MM calculations) gave reliable indications on the reaction intermediates. Although studied for many years, and often with success, the enzymatic mechanisms are still much debated. In particular, obtaining precise energy barriers is challenging, due to the difficulty of modeling the influence of the enzyme pocket.

1.3.1. Structure and mechanism of galactose oxidase (GAO) and glyoxal oxidase (GLO)

GAO2 and GLO3 are monomeric enzymes that are able to catalyze the regio-selective two-electron oxidation of D-galactose (and primary alcohols) into aldehydes and the two-electron oxidation of aldehydes into carboxylic acids, respectively. As a counter-part, dioxygen undergoes a two-electron reduction into hydrogen peroxide[13]. It is worth noting that their physiological role is the production of H_2O_2, as an anti-bacterial agent or fuel for lignin peroxidase[14]. The active site of GAO is located on the surface of the protein structure (Figure 3.a), allowing the approach of larger substrates. In its active form (Figure 3.b), Cu is surrounded by two histidine (His496 and His581) and two tyrosine (Tyr495, in axial position and Tyr272 residue, in equatorial position) amino-acids. With additional water or acetate ion as ligand, which is replaced by the primary alcohol substrate, the active site adopts a distorted square-based pyramidal geometry.

On the basis of kinetic hydrogen-deuterium exchange studies[15], a ping-pong like mechanism was proposed (Figure 3.c). The T-shaped intermediate 1 affords a Cu^{I} complex that reacts with O_2. From intermediate 1 ($Cu^{(I)}$-tyrosine reduced form) to intermediate 4 or 5 ($Cu^{(II)}$-tyrosyl radical active form), the two-electron reduction of O_2 takes place. After its coordination, O_2 takes one electron on the Cu center (superoxo-adduct, intermediate 2), one hydrogen atom on the equatorial tyrosine residue (hydroperoxo-adduct, intermediate 3) and then, a proton from the axial tyrosine (intermediates 4 and 5). From the totally reduced form, the mechanism goes through semi-oxidized intermediate (intermediate 2), before the obtaining of a fully oxidized form (the active form). H_2O_2 is then released. So, an organic radical is generated on the tyrosine residue, allowing

the metal-driven electron transfers. Then, from intermediate 5 to intermediate 7, the reduction of primary alcohol on the metal-radical complex leads to the corresponding aldehyde, by the reverse way (protonation of Tyr495, followed by electron and H atom transfer from alcoholate to axial Tyr272 radical). From the fully oxidized form (intermediates 4 and 5), the mechanism reaches a semi-oxidized form (intermediate 6) and the GAO is deactivated in its reduced form. The hydrogen atom abstraction is the rate-determining step of the reaction[16]. No crystal structure of the active form with D-galactose coordinated on $Cu^{(II)}$ was published (intermediate 5), but only with H_2O (intermediate 4). H_2O is a labile group, that can be easily replaced by D-galactose. Therefore, the key of the mechanism lies in the stabilization of $Cu^{(II)}$-tyrosyl radical intermediate. This radical is stabilized by a planar partial double-bond with sulfur atom of Cys228 residue, which extends the aromatic system[9]. Tyrosyl radical intermediate is not an exception[17]. It is important to note that O_2 is not the primary oxidant of the alcohol, but regenerates the active form of the catalyst.

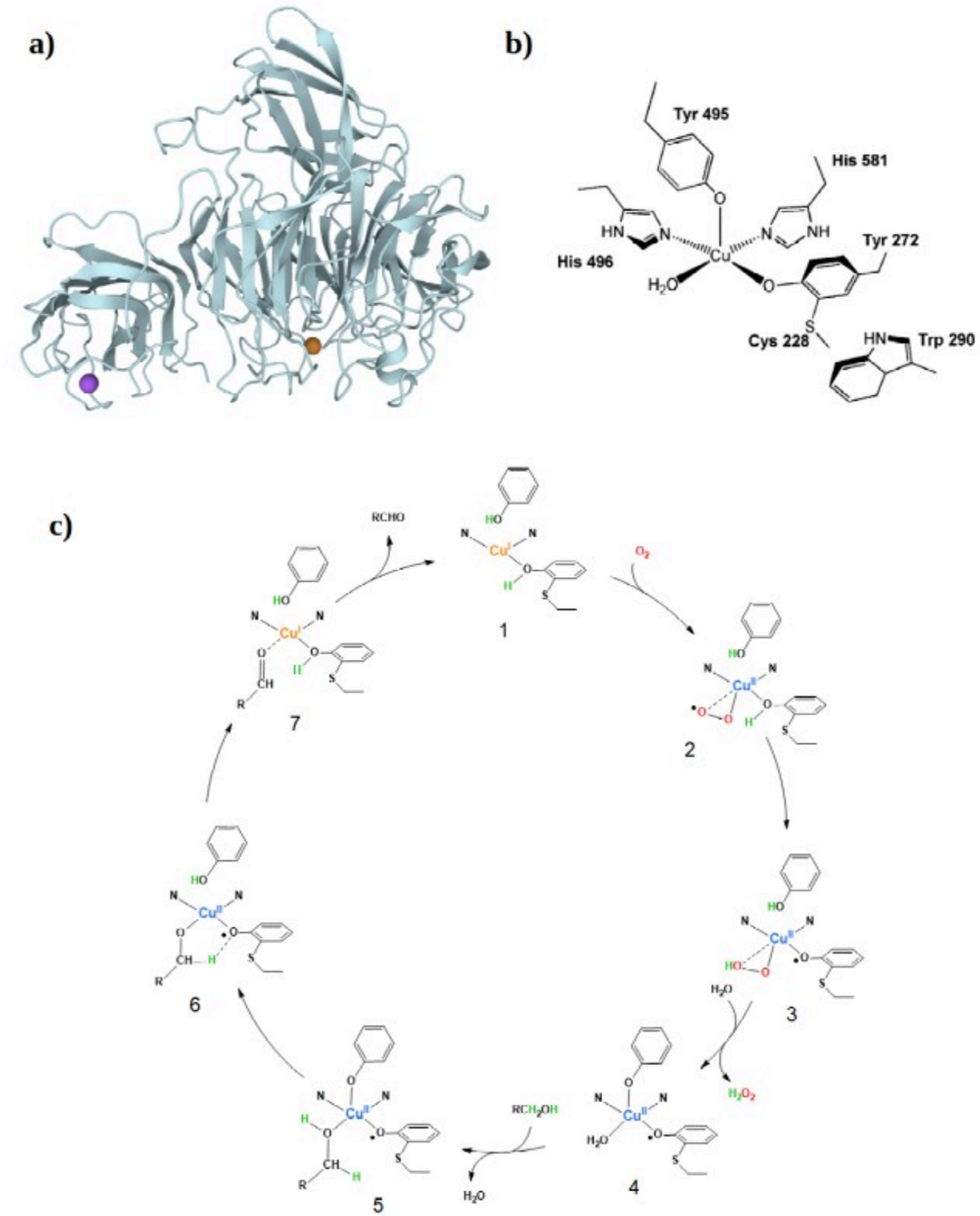

Figure 3: a) Crystallographic structure of galactose oxidase from Hypomyces rosellus[9] *(PDB ID: 1GOG), screenshot from rcsb.org[131]. Cu (orange) and Na (violet) were artificially magnified. b) Active site of GAO/GLO. Figure taken with permission from [130]. One can note the cross-bridged Cys228, placing the sulphur atom in the same plane than Tyr cycle. c) Proposed catalytic cycle of galactose oxidase for the oxidation of alcohols to aldehydes. Figure inspired by [16,122].*

1.3.2. Structure and mechanism of lytic polysaccharide monooxygenase (LPMO)

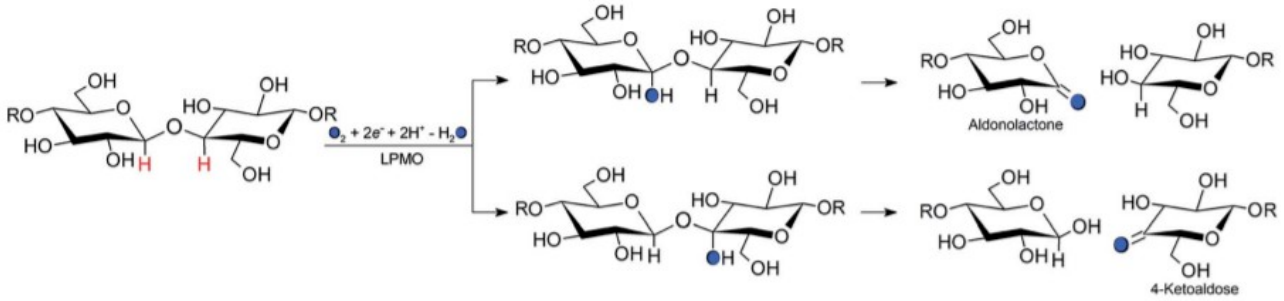

Figure 4: Catalysed oxidation of the glycoside bond. Blue circles represent oxygen atoms from O_2 or H_2O_2. Reproduced from [126].

LPMOs are mononuclear enzymes that are able to oxidize the glycoside bond of polysaccharides (Figure 5.a). The hydroxylation of the glycoside bond leads to the fragmentation of the carbohydrate (Figure 4). The active sites of such enzymes is composed by three nitrogen donor atoms (of which two come from the same histidine; one being aliphatic amine, the other being aromatic) and one oxygen-donor atom (from tyrosine residue) (Figure 5.b). The two histidine coordination pattern is known as the “histidine brace”. The coordination sphere is completed by one (when Cu has a +1 charge) or two (+2 charge) oxygen atoms. The switch from $Cu^{(II)}$ to $Cu^{(I)}$ can be done by ascorbate as reductant. Both O_2 and H_2O_2 can be used to activate the resting state of LPMO. Crystallographic studies revealed a pre-catalytic complex containing pre-bound dioxygen close to the active site[18], as in the PHM family. Such hydrophobic cavities, able to store dioxygen, are sometimes put in evidence by crystallization under xenon atmosphere.

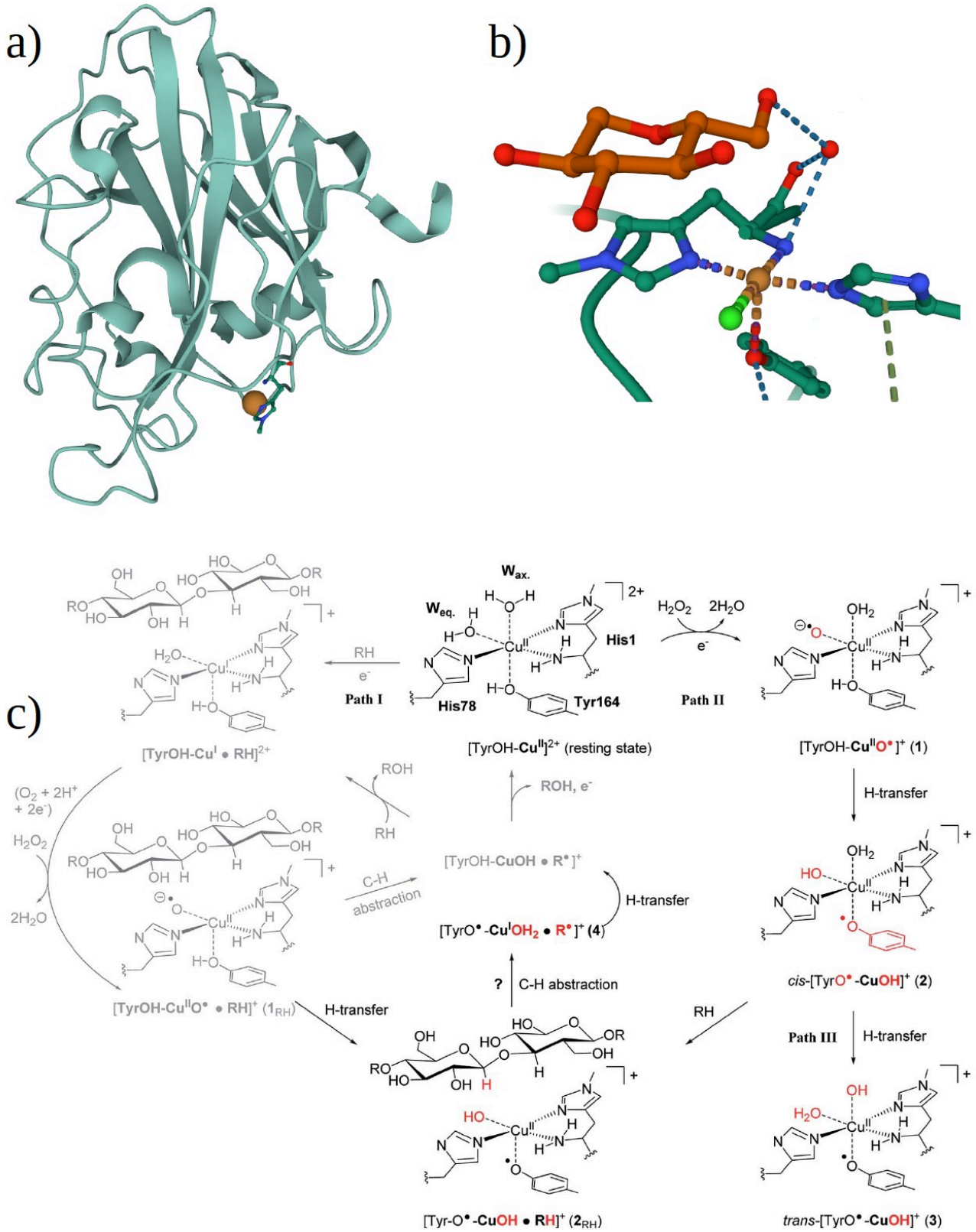

Figure 5: a) Crystal structure of monomeric LPMO from Panus similis *(PDB ID 5ACF)[124]. Cu (orange) was artificially magnified. b) Active site of LPMO with a part of polysaccharide (orange). Screenshots from rcsb.org[131]. C: orange (substrate) and dark green, Cu: dark yellow, O: red, N: blue, Cl: pale green, H are omitted for clarity. c) Proposed mechanisms of LPMO class of enzymes. Reproduced from[126].*

Path I in Figure 5.c was the first mechanism to be postulated, in which the tyrosine amino-acid has no particular role. This path I is also consistent with LPMO types that contains a phenylalanine residue in place of tyrosine[19]. O_2 binds $Cu^{(I)}$ in the equatorial position (end-on coordination) and is reduced at the $Cu^{(I)}$ center leading to a $Cu^{(II)}$-$O_2^{\bullet-}$ (Cu-superoxo) species. However, in that case, CuO_2^+ core is expected to be not strong enough to abstract a hydrogen atom on the substrate, because of the high bond dissociation energy (BDE) of the considered CH bond[20]. The superoxo evolves towards a $Cu^{(II)}$-oxyl species, which is much more reactive, and is able to abstract an H atom either directly on the substrate (Path I) or on the tyrosine residue (Path II). Path I proposes then a remigration of the OH radical on the dehydrogenated carbon atom[20]. Path II was calculated to have lower barrier energies, and the existence of Cu-tyrosyl species was experimentally proven by UV-Visible spectroscopy in some cases[21]. Path II, like in the GAO/GLO case, favors the formation of a tyrosyl residue, as a stabilizer of intermediates and protective from oxidation. In that case, the oxidative species is $Cu^{(II)}$-OH (+III oxidation state was never proven to exist in enzymes). Path III prevents the deactivation of the active site, in the absence of glycoside substrate.

1.3.3. Structure and mechanism of dopamine-β-monooxygenase (DβM) and peptidyl α-hydroxylating monooxygenase (PHM)

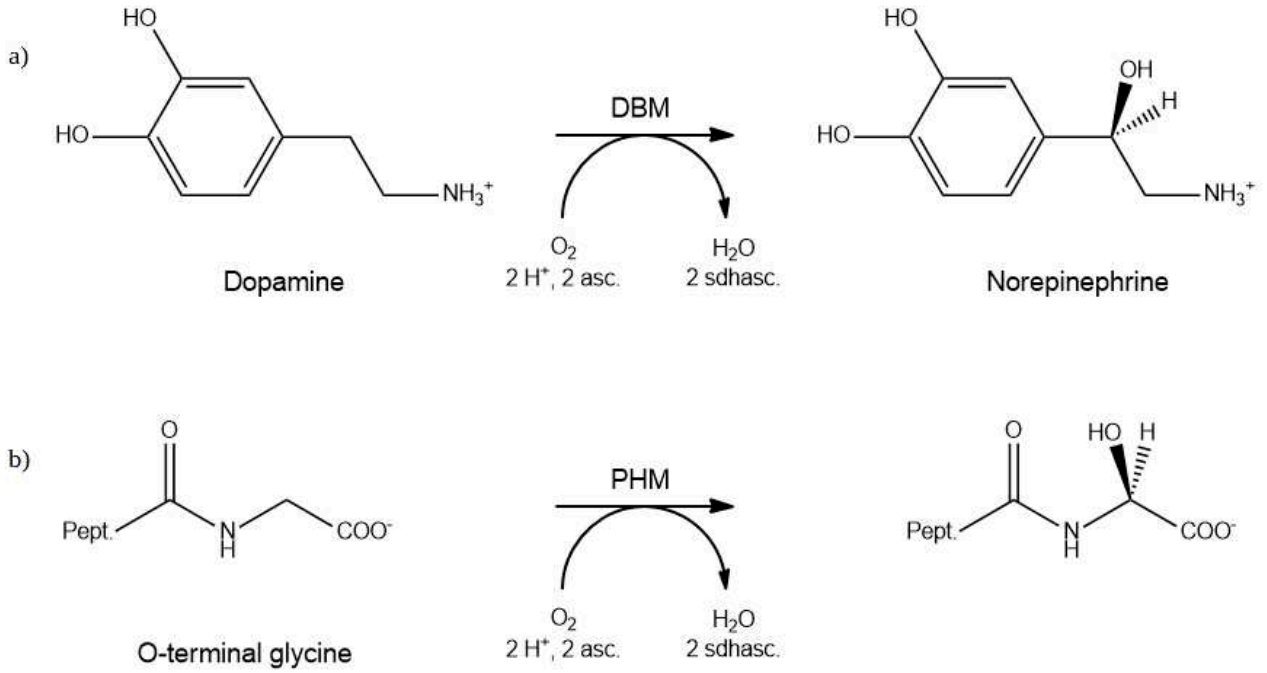

Figure 6: Oxidative reactions catalyzed by DβM (a) and PHM (b). asc stands for ascorbate, sdhasc for semidehydroascorbate.

Dopamine β-monooxygenase or dopamine β-hydroxylase[2] (DβM or DβH) is a copper enzyme that catalyzes the hydroxylation of dopamine into norepinephrine. Its role is the regulation of the rates and ratio of dopamine and norepinephrine, which are implicated in a lot of physiological, neurological and behavioral processes. Ascorbate is used as sacrificial reductant, in order to perform the selective oxidation of subtrates (Figure 6).

2 Peptidyl α-amidating/α-hydroxylating monooxygenase (PAM/PHM), monooxygenase X (MOXD1) and tyramine β-monooxygenase (TβH, the equivalent of DβH for insects) are the other members of eukariotic copper-containing hydroxylases.

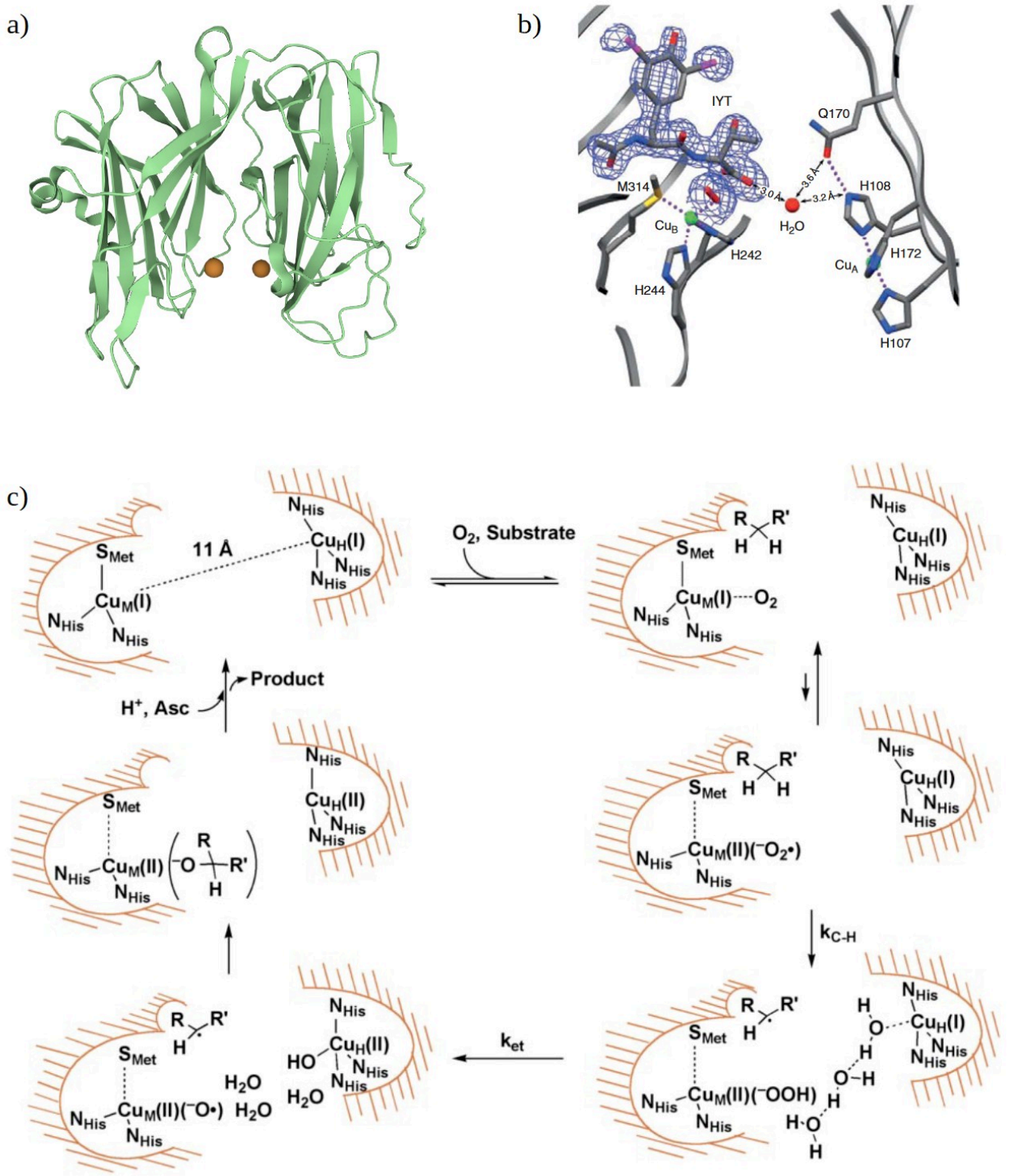

Figure 7: a) Crystal structure of monomeric PHM from Rattus norvegicus *(PDB ID 1YIP)[23]. Cu (orange) were artificially magnified. Screenshot from rcsb.org[131]. b) Active site of PHM with a massive substrate IYT and O_2 bound to Cu_M. Reproduced with permission from [135]. c) Postulated mechanism of DβM class of enzymes. Reproduced from [132].*

DβH is a tetrameric glycoprotein[22]: each monomer (Figure 7.a) has one active site, which binds two copper atoms, named Cu_H and Cu_M, separated by a distance of 11.47 Å. In its oxidized form (+II as oxidation degree), Cu_H exhibits a slightly distorted square planar geometry, with three histidine amino-acids (His107, His108 and His172) and water molecules as ligands. Oxidized Cu_M has a square pyramidal geometry: it is surrounded by one methionine (Met314 in axial position), two histidine (His 242 and His244) amino-acids, completed by H_2O or OH^- in equatorial positions[23].

The mechanism of DβM and PHM has been the subject of extensive research. Some hypothesis were proposed, including the implication of a tyrosyl radical or an acidic residue and were finally discarded[24,25], showing the intense scientific debate around the biochemical mechanisms of Cu enzymes. Finally, a plausible mechanism was determined in 2003 by J.P. Klinman and co-workers on the basis of kinetic measurements and structural considerations (Figure 7.c)[26].

In 2004, the crystallographic structure of PHM containing O_2 was obtained for the first time[27]. The OO distance was refined to 1.23 Å, validating the first step of the mechanism: Cu_M weakly coordinate O_2, before it forms superoxo species ($Cu^{(II)}$-$O_2^{\bullet-}$), for which the coordination mode is still discussed[28]. Notwithstanding, the crystal structure seems to indicate an end-on coordination. However, the substrate binds first to the cavity (by hydrogen-bonding network, with Glu268, Glu239 and Tyr494 amino-acids), before O_2 incoming[29]. Conformational changes consecutive to the electron transfer from Cu_M to O_2 (elongation of the Cu-Met ligation) leads to a favorable orientation for the abstraction of a hydrogen atom on the substrate. Once $Cu^{(II)}$-superoxo is formed (at very low level, because of an unfavorable equilibrium), it was found to react directly with the substrate (and not with the proteic environment, nor with water). So, the abstraction of the H atom on the substrate was theoretically found to be done by the $Cu^{(II)}$-superoxo intermediate in the singlet state, and not by a consecutive $Cu^{(II)}$-hydroperoxo intermediate[30].

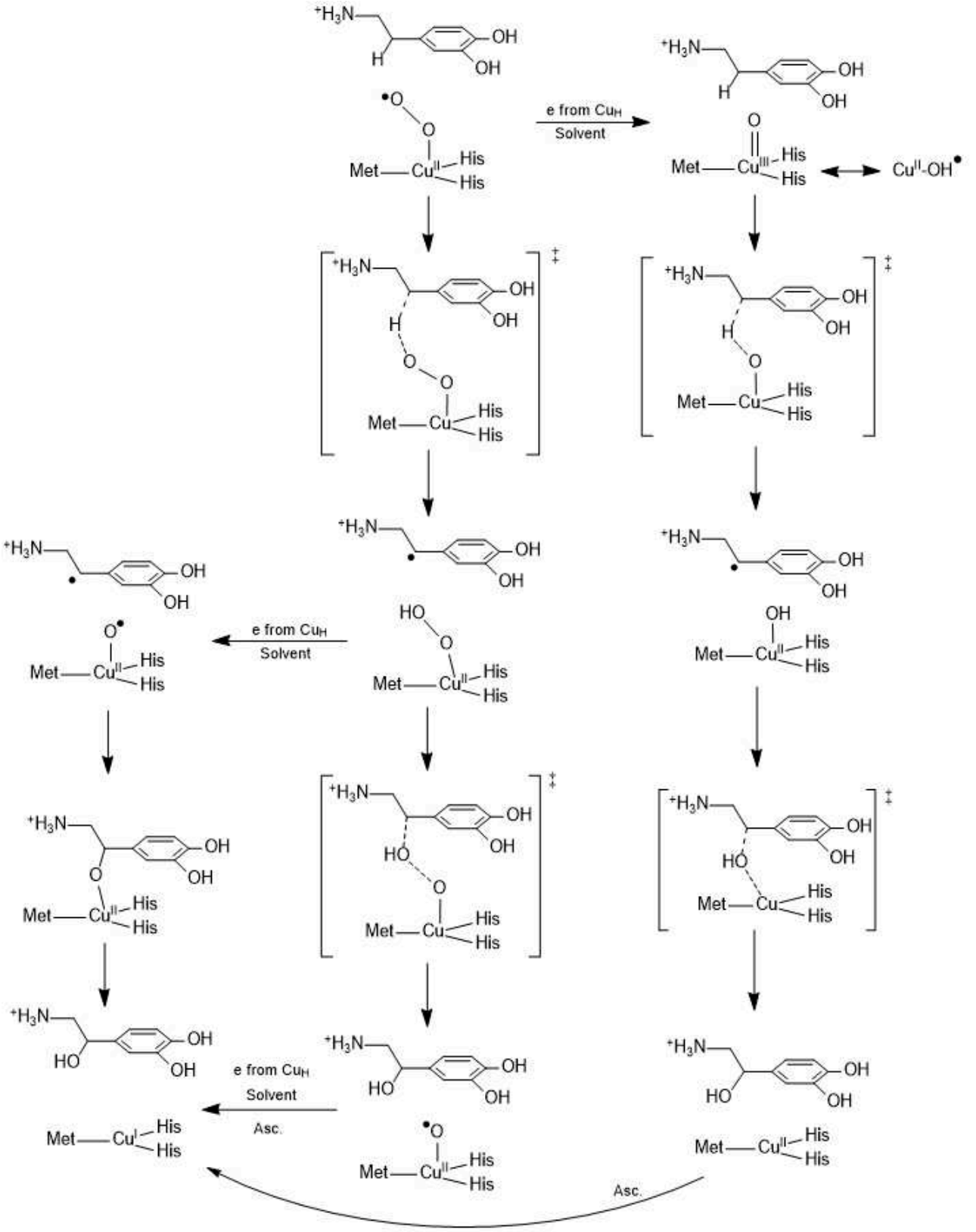

Figure 8: Three different proposals of mechanism for mediated hydroxylation of dopamine. Asc. stands for ascorbate. Left part: Klinman's proposal[26], Middle: Solomon's proposal[30], Right part: Yoshizawa's proposal[125].

In the early 2000's, the nature of the hydroxylating species has been much discussed. Three notable hypothesis on the nature of the hydroxylating species deserve to be looked into (Figure 8). Solomon's proposal lays on a $Cu^{(II)}$-hydroperoxo as the hydroxylating species, and showed by DFT calculations that this pathway is thermodynamically favorable. The remaining $Cu^{(II)}$-$O^{\cdot}$ is then easily reduced to $Cu^{(II)}$-OH. Yoshizawa and co-workers, on the basis of QM/MM (Quantum Mechanics/Molecular Mechanics) calculations, proposed that an even more favorable pathway can be achieved through a $Cu^{(III)}$-oxo/$Cu^{(II)}$-$O^{\cdot}$ hydroxylating species. Although proposed earlier, the mechanism of Klinman and co-workers (through $Cu^{(II)}$-$O^{\bullet -}$ species, deriving from a $Cu^{(II)}$-hydroperoxo species) is based on experimental observations: the rate constant is higher when the substrate contains electron-withdrawing substituents[31] and the mechanism should proceeds through a concerted inner-sphere process. More recently, the authors of an other computational study emitted the hypothesis that the species responsible of the abstraction of $H^{\cdot}$ on the substrate is Cu-OOH^{2+}[32] (i.e. the first step after superoxo formation is the protonation of $CuOO^{+}$), due to a lower energetic barrier. The experimental kinetic values[29] were assessed with this new mechanistic proposal. The fact that Cu_M and Cu_H are separated from approximately 11 Å requires a long-range electron transfer, to achieve the four-electron reduction of O_2 in water (two electrons are provided by the substrate and two others more, one from each Cu). There is no evident skeleton bridge between both Cu sites. So, the actual consideration consists in an electron transfer through water molecules[33]. The last step of the mechanism is the regeneration of the active site, with the help of a proton, that protonates the alcoholate, and of two ascorbate that reduce both $Cu^{(II)}$ to $Cu^{(I)}$. The reduction leads to the decoordination of water molecules, since water is a poor ligand for Cu^{+}.

1.3.4. The case of amine oxidase (AO)

The case of amine oxidase, which is one of the most characterized class of enzymes, gets close to the case of galactose oxidase (GAO)/glyoxal oxidase (GLO). However, several interesting differences deserve to be discussed. All crystallographically resolved amine oxidases are dimers with masses ranging between 140 and 240 kDa (Figure 9.a). Each monomer contains one active site, each having only one Cu ion, surrounded by three histidine and one tyrosine amino-acids (Figure 9.b), the latter being oxidized in 2,4,5-trihydroxy-phenylalanine quinone (TPQ) *via* a 6-electron oxidation (Figure 9.c). The catalytic system uses TPQ as a cofactor to oxidize the amine substrates. Concerning the mechanism of TPQ generation, a pre-catalytic form (B) is formed (from

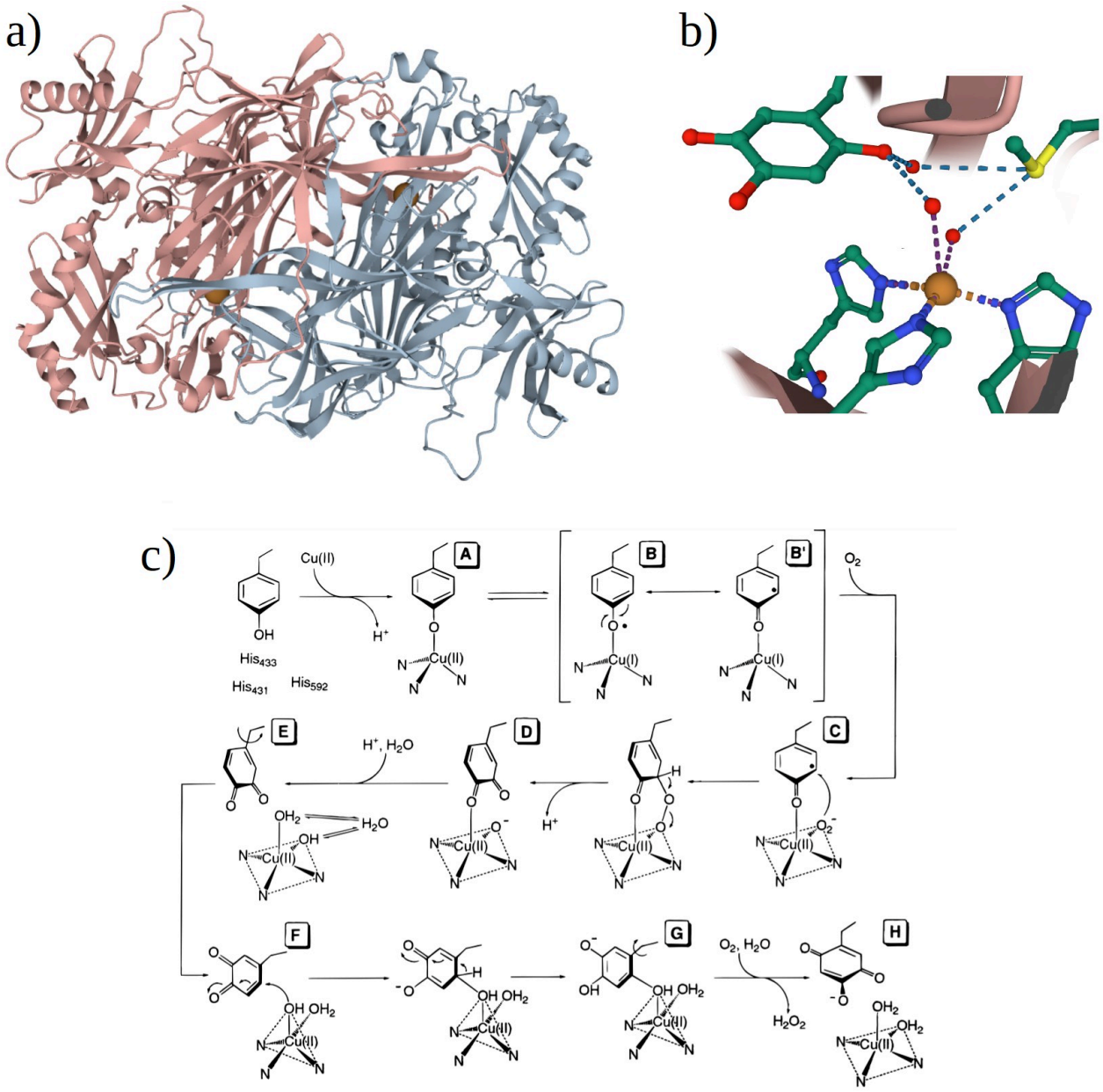

Figure 9: a) Crystal structure of dimeric AO from Arthrobacter globiformis *(PDB ID 1IVX)[128]. Cu (orange) were artificially magnified. b) Active site of AO in its fully oxidized activated form. Screenshots from rcsb.org[131]. c) Postulated mechanism the oxidation of tyrosine in AO class of enzymes. Reproduced with permission from [120].*

an *apo* form, noted A), containing the tyrosinate/tyrosyl radical moiety (also proposed in the mechanism of GAO), put in evidence by its spectral features ($\lambda_{max}(Cu^{(II)}$-tyrosinate = 350 nm). The formation of the pre-catalytic form is the rate-limiting step of the overall mechanism. One can note that, as in the LPMO and PHM cases, O_2 is firstly included in the environment of Cu and binds in a second time to the metal ion[34]. Then, O_2 is able to attack the tyrosyl residue by radical coupling, forming a somewhat bridged structure, that decomposes quickly in dopaquinone and OH (D).

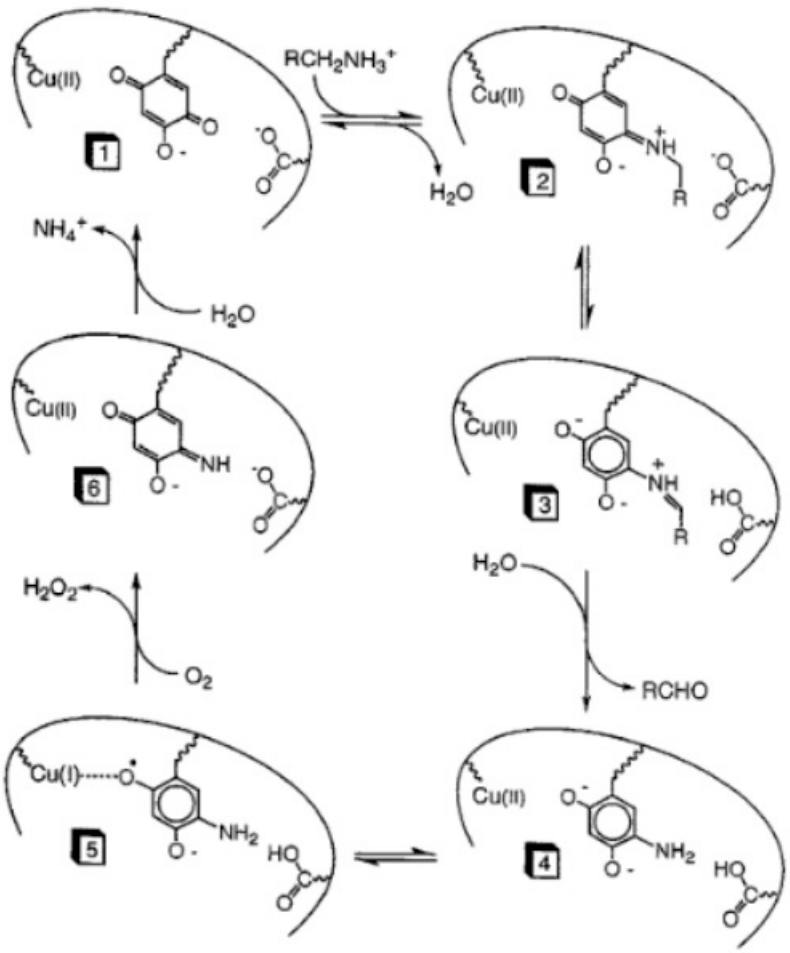

Figure 10: Proposed mechanism for amine oxidation by amine oxidase. Reproduced from [127], Copyright 1996, with permission from Elsevier.

Crystallographic studies have shown that the tyrosine/DPQ/TPQ residue can adopt different conformations[3]. Rotation of DPQ leads to F form, and the exposed carbon atom readily undergoes a nucleophilic reaction, leading to the inactive "on-copper" G form (isolated and characterized by crystallography). G form is then oxidized into H, the active "off-copper" site (Figure 9.b). This mature TPQ is obtained with a k_{obs} equals to 1.5 min^{-1}, when the *apo* form is exposed to O_2[35].

TPQ is then partially reduced (two-electron) into DPQ by amine substrate (which is oxidized into the corresponding aldehyde) before being re-oxidized by O_2 (reduced into H_2O_2). A ping-pong mechanism was proposed (Figure 10), made up of a reductive half-reaction (from intermediate 1 to 4), and an oxidative half-reaction (from intermediate 4 to 1). Cu ion is not implied in the oxidation of the amine substrate. TPQ_{OX} is reduced by the amine into TPQ_{AMO}, forming a

3 PDB IDs 1IVV to 1IVX

substrate Schiff base, converted in a product Schiff base. A basic residue, identified as asparagine, facilitates the abstraction of a proton on the carbon atom bearing the amine group and influences the way the substrate interacts with TPQ[34]. Experimental data showed that the recovery of the "off-copper" TPQ_{OX} form is done *via* an inner-sphere mechanism: a $Cu^{(I)}$-semiquinone was put in evidence, binds O_2 (leading to a $Cu^{(II)}$-superoxo species) and releases H_2O_2[36]. The kinetics of the amine oxidation strongly depends on the nature of the enzyme.

For several considered mononuclear enzymes, structures of the active sites were detailed. The oxidation mechanisms of catalytic pathways exhibit similar behaviors, through O_2 activation, superoxo and hydroperoxo formation (by H atom transfer). Then, depending on the nature of the enzyme (and on the structure of the active site), either the loss of H_2O_2 (and the activation of a cofactor) or the formation of the $Cu^{(II)}$-oxyl (or maybe $Cu^{(III)}$-oxo/$Cu^{(III)}$-OH) core is favored. In some enzymes, the active form is stabilized by a tyrosyl residue. This little review of mononuclear enzymes, active sites and redox mechanisms helps to establish an index of essential structure intermediates, which are at the heart of copper-oxygen chemistry.

2. Models

The use of enzymes, although it is a selective and very efficient “green processes”, is limited by scaling. Changing the tertiary structure of the enzyme by a simple but robust, cheap ligand, with sufficient catalytic properties is challenging and still sought for many years. The rigorous approach of the biomimetic process requires the reproduction of the active site, or of its activity as closely as possible. As we have seen, the active sites of the considered mononuclear enzymes are comprised of a Cu center, which is in the oxidation state +I or +II (and maybe +III). In the considered enzymes, copper is surrounded by at least two nitrogen atoms from histidine amino-acids, and the coordination sphere is completed by oxygen atoms from tyrosine or water molecules, or by one sulfur atom in the case of PHM.

2.1. Models of GAO and GLO

Active sites of GAO and GLO, despite their intimate resemblance, have very different behaviours. Although GLO is a better oxidant than galactose oxidase (by 240 mV, experimentally), it only oxidizes substrates with weaker CH bonds (acetals and carboxylic acids from aldehydes). Active form of GAO, which has a longer lifespan than GLO ($t_{1/2}$ = 7.2 days against 4 days) and despite slower activation, is able to oxidize stronger CH bonds (aldehydes from alcohols). This ability relies on large changes of the enzyme pocket but minimal variation in the structure of the active site[37]. Therefore, a rigorous biomimetic approach is needed. For this purpose, tyrosyl radical needs to be a special point of attention. The Cu^{I}-ligand system have to support a two-electron oxidation, both metal and ligand-centered. Special efforts around aminophenol ligands (Figure 11.a) were deployed. A wide class of salen ligands (Figure 11.b) was derived from these aminophenols[38], giving a somewhat distorted planar conformation to the metallic center. Cu^{II} salts were used to form Cu^{II}-phenolate complexes, in the presence of a base. Then, the one-electron oxidation (by chemical or electro-chemical means) of this metal-phenolate complex can lead, in the limiting cases, to the formation of either a metal ligand radical $M^{n}L^{\bullet}$ complex, or a $M^{n+1}L^{-}$ complex (here, a Cu^{III} might be expected, but is very unlikely). The Cu^{II}-radical character must be marked enough: if the radical character is shared too much with the metal, the Cu^{II} character is weakened and the oxidation reaction of the substrate cannot take place.

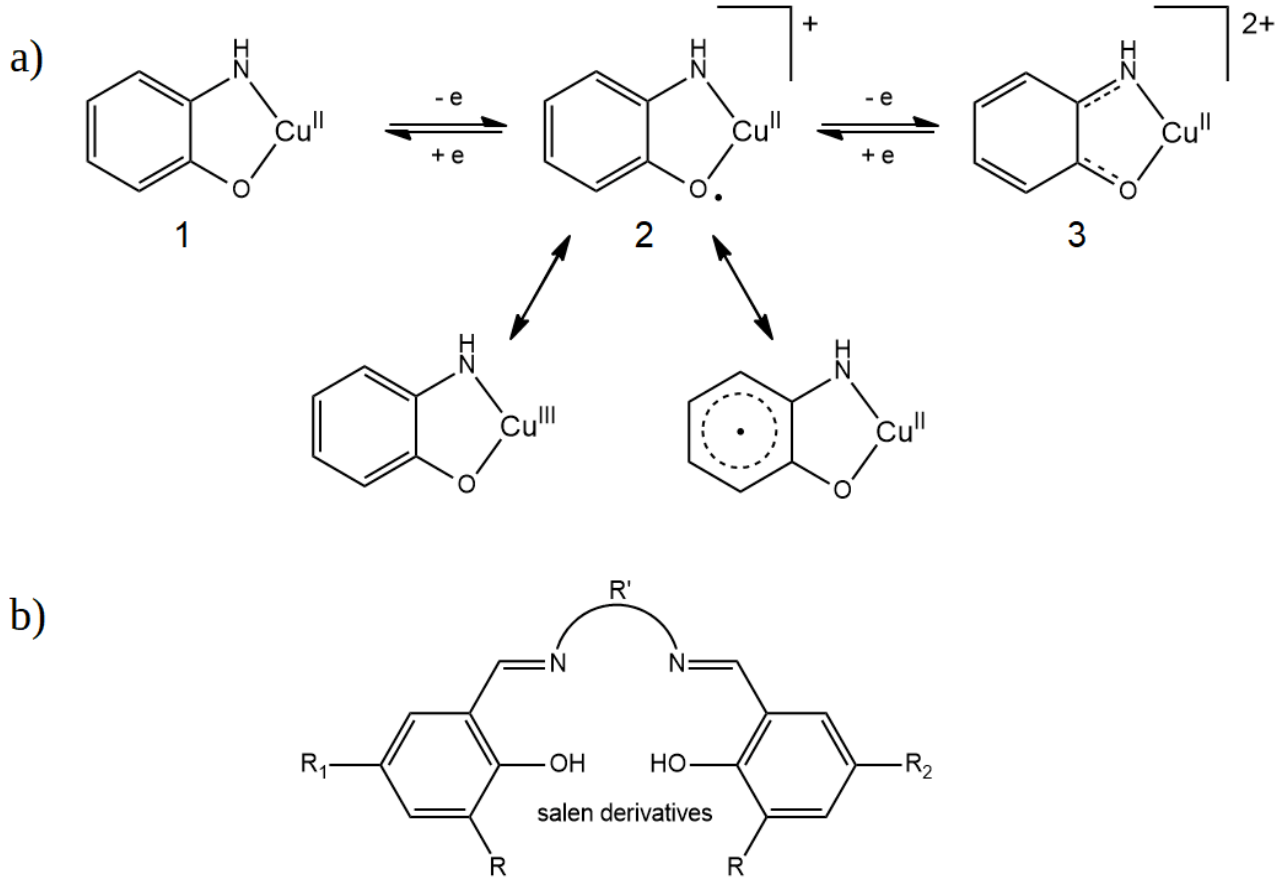

Figure 11: a) Aminophenol ligands as promising biomimetic ligands for mimicking GAO/GLO active sites. Intermediates:1 aminophenol, 2 iminosemiquinone, 3 iminoquinone. Mesomeric forms of iminosemiquinone are presented. b) General form of salen ligands, synthesized by condensation of a diamine (at the root of the NR'N part) and functionalized salicylaldehyde (left and right parts).

Electron Paramagnetic Resonance (EPR) is not a technique of choice, because oxidized GAO is EPR silent, due to antiferromagnetic coupling between Cu^{II} and phenoxyl radical, or because of large zero-field splitting parameter of ferromagnetic species. The character of the oxidized metal-ligand can be determined anyway, with the help of metal replacement (oxidized Ni-salen complex is EPR active), X-ray crystallography[39], X-ray absorption spectroscopy[40] and DFT calculations. For the stabilization of such metal radical character, different strategies were considered. As an analogous of the cross-bridged Cys228, the use of S groups in R_1 and R_2 positions stabilize the radical character on the phenoxyl groups. R' ligation chain can also have influence on the stability by slight distortion of the planar configuration[40]. Electron-donor groups in R, R_1, R_2 positions prevent dimerization.

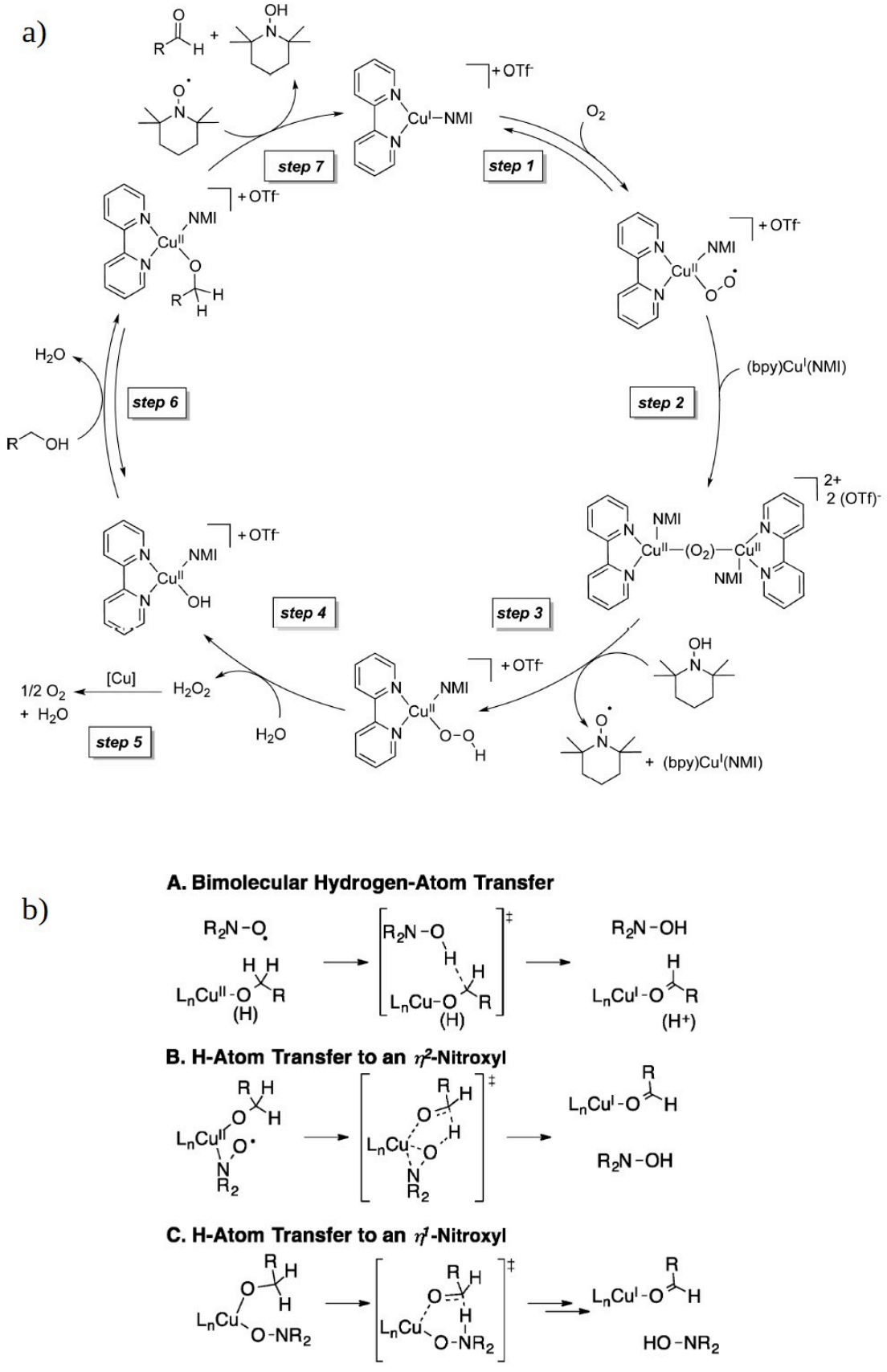

Figure 12: a) Proposed mechanism for the oxidation of alcohols by a [Cu$^{(II)}$(bpy)] complex, associated with TEMPO as co-catalyst. NMI stands for N-methyl-imidazole. Reproduced with permission from [134]. Copyright 2013 American Chemical Society. b) Proposals of mechanism for step 7. Reproduced with permission from [129]. Further permissions related to the material excerpted should be directed to the ACS.

The radical character can be fully delocalized on both cycles (class III, according Robin-Day classification[41]), when the ligand is symmetric, but can be also partly (class II), or fully (class I), localized on one phenoxyl group by the use of asymmetric ligands (R1 ≠ R_2, *e.g.* OMe, ^{t}Bu, S^{i}Pr, SMe, Cl) that differentiate the two phenoxyl groups. EPR, UV-Vis[42], IR[43] and resonance Raman[44] spectroscopies and electrochemistry, coupled with DFT calculations are good tools to determine the oxidation locus[45]. Class II complexes are widespread. They are particularly of interest, because a tight control on the ligand gives access to close inter-valence charge transfer (IVCT) to those observed with GAO. After oxidation, sulfur groups stabilize the radical character on one part of the ligand[43], such as in the GAO active site, where the tyrosyl radical is delocalized over O atom, the cycle and S atom. The planar conformation, with asymmetric sulfur-functionalized salen ligands, allows the partial delocalization electron on the sulfanyl group[46] as a reminder of the delocalization in GAO, that stabilizes the active form[45]. Other ligands designed to mimic GAO active site have been reported[38]. Some of them are presented in Figure 13, notably ligands with only one phenol group. S.S. Stahl and co-workers, through a well-detailed kinetic study[47] proposed a mechanism for the alcohol oxidation with Cu^{II}bpy, associated with a hydroxylamine co-catalyst (Figure 13.f), achieves in high yields the alcohol to aldehyde conversion (Figure 12.a). In the proposed mechanism, one can find similarities with the proposed mechanism of GAO (Figure 3.c). Firstly, the O_2 coordination, that leads to a Cu-hydroperoxo intermediate. Then, an acid-base reaction that deprotonates the alcohol of interest takes place. Finally, a copper-radical intermediate that allows the H-atom transfer from alcohol to the radical. Three different mechanisms were proposed to explain the process of step 7 (Figure 12.b). On the basis of DFT calculations, a H-atom transfer to an η^1-nitroxyl was found to be preferential, especially less encumbered co-catalyst that have a higher driving force (ABNO, AZADO, ACT)[48]. Primary and/or benzyl alcohols are preferentially oxidized with this class of catalysts. The regeneration of $Cu^{(II)}$ can be achieved electrochemically, in anoxic conditions[49].

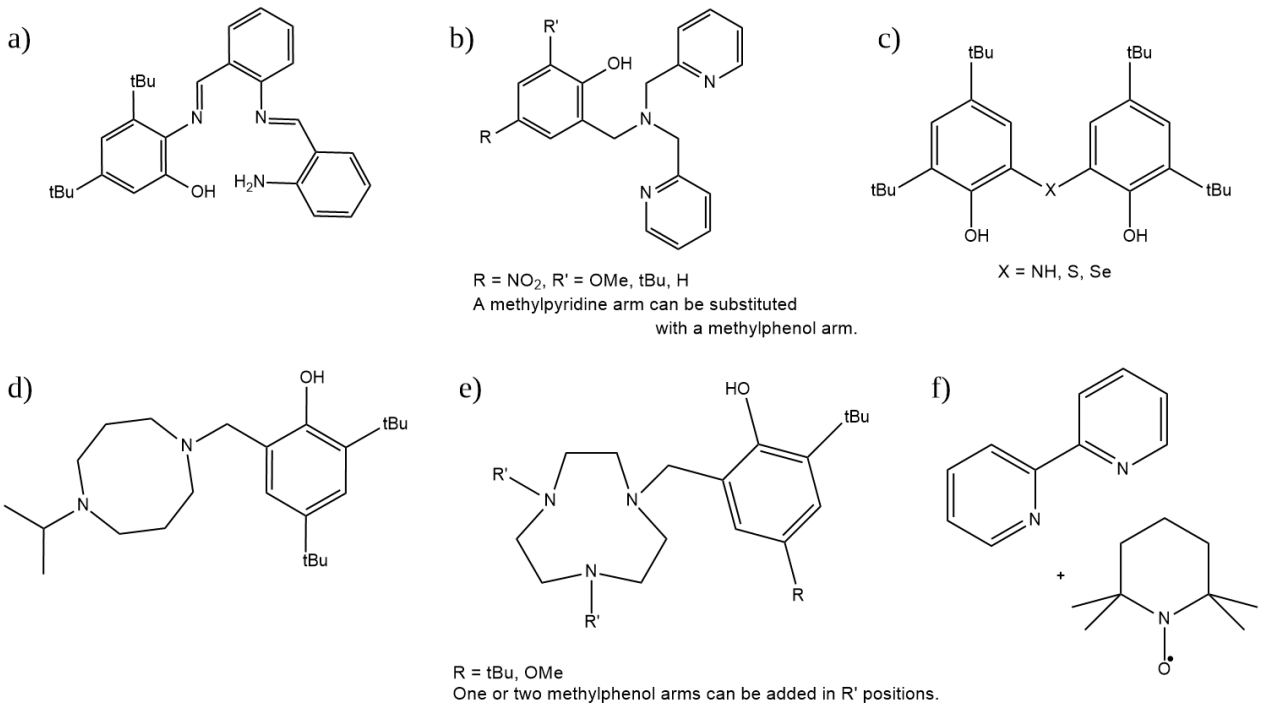

Figure 13: Other ligands designed to mimic the GAO active site. a) Salen-inspired N_3O ligand, very efficient towards benzyl alcohol oxidation (100 % in 4 h)[119]. b) Tripodal ligands, that offer a wide range of complexes. A steric hindrance (R' = tBu) prevents the dimerization of the complex (X-Ray structures show that the two copper ions are bridged by both O atoms of phenolate groupes). A c) Diphenol ligands. d) 1,5-Diazocane-based ligand. e) 1,4,7-Triazacyclononane (TACN)-based complexes[133]. f) bpy assisted by TEMPO as co-catalyst.

2.2. Models of LPMO

The "histidine brace" pattern has inspired models of LPMO (and pMMO)[50]. Bis(arylcarbox-amido)pyridine ligands (Figure 14.a) have been studied for a decade as efficient models[51]. The addition of charged functional groups in R' position leads to a better solubility of the complexes in water. It was previously shown that the species able to abstract a H atom from substrates (strong CH or OH bonds) is $Cu^{(III)}$-OH[52,53]. These complexes are able to stabilize $Cu^{(III)}$-OH after its formation, due to the anionic nature of the ligand. The complex of Castillo and co-workers (Figure 14.c) breaks the glycoside bond of polysaccharides in high yields[54]. Benzimidazole group appear to have suitable σ-donor/π -acceptor character towards Cu ions and to be sterically protective. The hydrogen atom of the amine group is likely to form hydrogen bond with the substrate. Interestingly, this complex works with a large panel of conditions. The co-catalyst can be O_2 (in combination with $Cu^{(I)}$ complex), H_2O_2 with a base (with $Cu^{(II)}$) or even KO_2 (which give superoxide anion) with $Cu^{(II)}$, in order to generate the final species $[LCu(OH)(H_2O)]^+$,

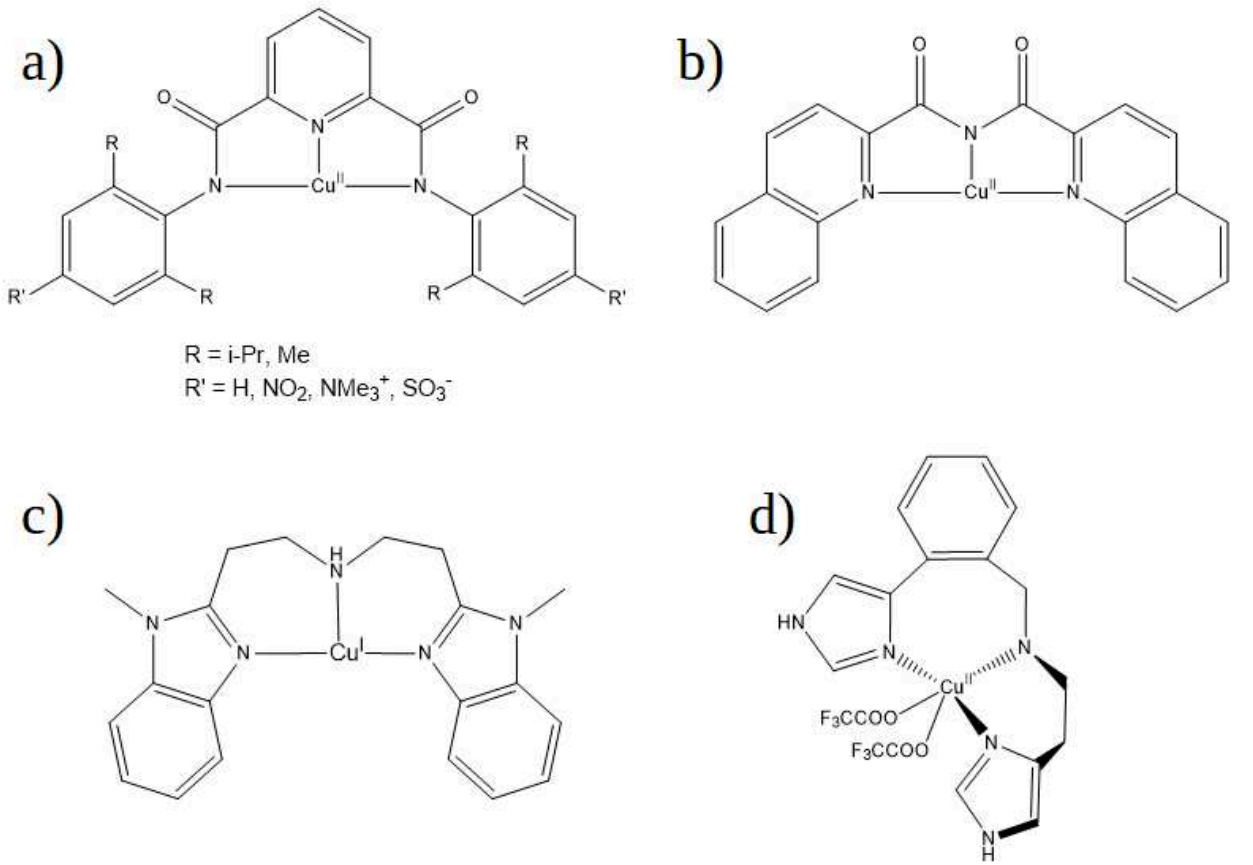

Figure 14: Designed ligands to mimic the active site of LPMO. One can note that none of them has tyrosine-like character. a) Anionic bis(arylcarboxamido)pyridine complex[51]. b) bis(quinolinyl-carbonyl)-amide. c) Bis(methylbenzoimidazolethyl)amine complex, able to form mononuclear dimers[54]. d) Complex from Itoh and co-workers[55]. Some of the ligands proposed as models of PHM are also used as models for LPMO (Figure 15).

detected by mass spectrometry. The $[LCuO_2]^+$ and $[LCuO]^+$ complexes are also stable enough to be detected by mass spectrometry. In water, above pH 7.5, the complex may dimerize, as shown by Raman spectroscopy. Cryoelectrospray mass spectrometry (CSI-MS, 243 K) has been necessary to detect the postulated oxygenated dinuclear species. The average value of the twist angle between the two histidine amino-acids (in the reported model of LPMOs) is 72°. A new model, designed by Itoh and coworkers (Figure 14.d) gives a twist angle value of 75°, which makes the complex very efficient in the presence of H2O2 for the glycoside bond breakage (Turn Over Number, TON = 58) and also, the oxidation of cyclohexane into cyclohexanol and cyclohexanone (TON = 26)[55].

2.3. Models of DβM and PHM

Tri- and tetradentate tripodal ligands are widely described in the literature as models for DβM and PHM[56,57]. They form very stable complexes with $Cu^{(II)}$ ions (e.g. log $K_{asso}(Cu^{(II)}Tren)$ = 18.5 at 25.0 °C, 0.1 M KNO_3). Hypodentate cases (in which the tripodal ligand does not bind only one metal) were reported with $Cu^{(I)}$ or $Cu^{(II)}$[58], and also with other metals ($Co^{(III)}$, $Pt^{(III)}$, $Cd^{(II)}$)[59]. Mononuclear CuO_2 complexes are not expected to be strong oxidants, but TMPA, Tren and N_3S derivatives exhibits capacities to abstract a H atom of weak CH bonds. $[Cu(N_3S)(\eta^2\text{-}O_2)]^+$ complex is able to oxidize dihydroanthracene (DHA)[60,61]. One can note that the hemilabile character of the methionine residue in PHM is reproduced with the help of a thioether functional group. The $Cu^{(II)}$-superoxo and -hydroperoxo intermediates were spectroscopically characterized. They are stable at –80 °C and at room temperature, respectively. The $Cu^{(II)}$-hydroperoxo species was excluded as an efficient H-atom agent, since only a low activity was observed towards DHA. Phenols were oxidized with the help of substituted TMPA, *via* an end-on $Cu^{(II)}$-superoxo species[62]. So, the key for the dioxygen activation is the improvement of the superoxide character in Cu-O_2 cores. In fact, di- or trinuclear complexes are stronger oxidants, due to a much better electron transfer from Cu centers to O_2. One can note that the substrate is not necessarily external to the system: the substrate to be oxidized is sometimes the ligand itself. In general, mononuclear complexes are still able to coordinate O_2, to form a $Cu^{(II)}$-superoxo species. The lack of stability and/or the low activation of O_2 of such superoxo species does not allow the hydrogen atom abstraction on strong CH bonds. Fortunately, some strategies have been set up to overcome that issue. Lateral chains (such as amide groups) can be added on the ligand, in order to stabilize $Cu^{(II)}$-superoxo species, by forming hydrogen bonds with the proximal atom of the superoxo ion, and are able to oxidize more challenging substrates, such as toluene[63]. Bulky and/or strong electron-donating substituents also favor the stabilization of $Cu^{(II)}\text{-}O_2^{\bullet-}$[64]. Nevertheless, di- or tri-copper systems are complexes of choice for the oxidation of strong C-H bonds[65]. Ligands can be designed in order to control the nuclearity of the system[66] (Figure 15.d). Some were designed on the basis of di-, tripodal ligands. Two different approaches coexist: Cu centers are held by different ligands (Figure 16.a) or by the same ligand (Figure 16.b). Both strategies can be used to efficiently activate O_2. Along reaction pathways, mixed-valence complexes can be obtained. The reaction mechanisms will not be more deepened here, and only the general reactivity of mononuclear complexes is described. Once O_2 is activated, it is able to capture a H atom, or a proton from its environment (inter-[67] and

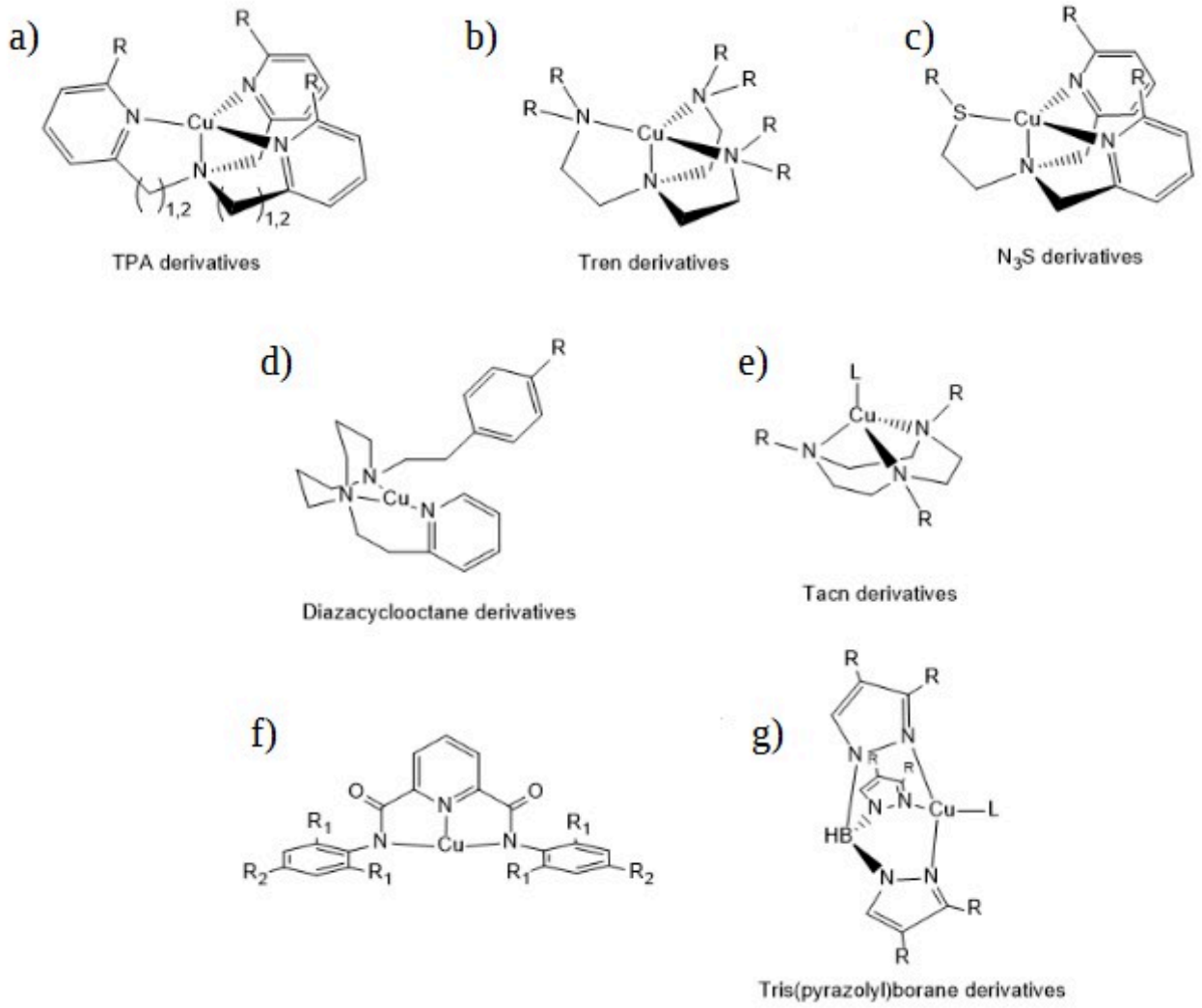

Figure 15: Some proposed models of DβM/PHM. A huge variety of these kinds of complexes were designed. TPA is called TMPA, when there is one carbon atom (methylpyridyl arm).

intramolecular[68] paths are reported). This step is often the rate limiting step of the mechanism. The stability of Cu-hydroperoxo species is enhanced by the presence of H bonds[69], like superoxo species. CuOOH species can be also generated in solution by adding H_2O_2 and a base[70]. Cu-hydroperoxo undergoes OO cleavage either by H atom addition (leading to the formation of a water molecule) or by OH radical abstraction (also called OH remigration, when the substrate is hydroxylated). A $Cu^{(II)}$-oxyl/$Cu^{(III)}$-oxo intermediate is then privileged, or even the protonated $Cu(OH)^{2+}$ core[71]. $Cu^{(II)}$-oxyl intermediate is expected to be a strong oxidant, even more than the analogous $Cu^{(II)}$-superoxo intermediate. $Cu^{(II)}$-oxyl can also be generated from the $Cu^{(I)}$ complex, by adding the strong oxidant PhIO in solution. However, only indirect evidences were collected: the high reactivity of such a structure does not allow its isolation.

2.4. Models of AO

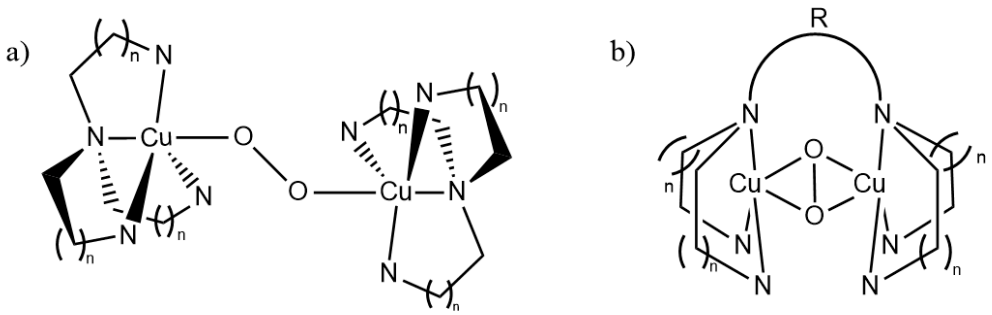

Figure 16: Different approaches for coordination of O_2. N designates a nitrogen donor atom, regardless of the real structure of the ligand.

Models of amine oxidase will not be deeply detailed here. They are basically similar to the proposed biomimetic models previously shown. Galactose oxidase models, for amine oxidase modeling, should be a field of research in future years, with respect to the tyrosine residue. However, metal-free oxidation of amines was observed with a wide class of substituted quinones, in high yields[72]. The regeneration of the active form of the quinone is done chemically or electrochemically.

To conclude, the biomimetic approach has been deepened to reproduce the active site of the considered enzymes as much as possible. Taking into account the smallest details (geometry, symmetry, conformation, electronic distribution, spectroscopic properties) has led to the development of efficient and sometimes specific catalytic systems, with a good understanding of reaction mechanisms. Models of GAO/GLO, LPMO and DβM/PHM were established on geometric, steric, electronic and oxidative properties of the corresponding enzyme. They exhibit a similar scheme of reaction, namely a pathway that can be decomposed in an oxidative half-reaction (activation of the catalyst) and a reductive half-reaction (oxidation of the substrate). At least for the activation of O_2 (oxidative half-reaction), the models mentioned have similar behavior. O_2 binds to the Cu center, associated with an electron transfer leading to Cu-superoxo or Cu-peroxo species that are able to abstract a H atom from their environment. This species might decompose to give a Cu-oxyl species, which is expected to be the most oxidative species (PHM, LPMO, AO models). The other possibility is the release of H_2O_2 with the participation of the ligand (GAO models). Then, the reductive pathway varies between enzymes.

3. Intermediates in copper-oxygen chemistry

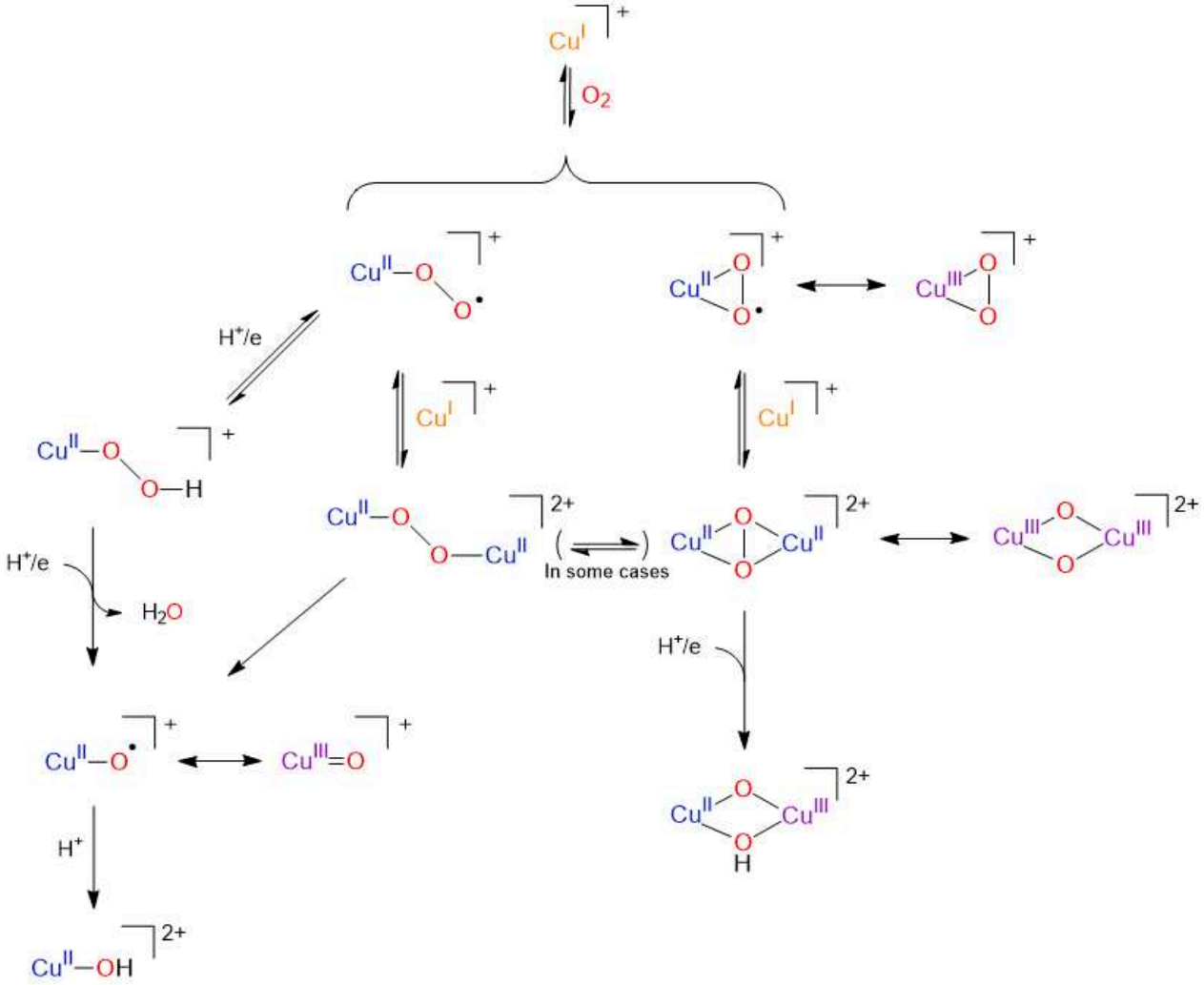

Figure 17: Identified reaction intermediates in the considered models.

We will mainly focus on the proposed intermediates for molecular catalysts, although there are many examples of O_2 activation and substrate oxidation using nanomaterials, oxides, metallic surfaces[73] or even organic catalysts[74]. Among molecular catalysts, late-transition metal based complexes are widespread. A few examples of Mn[75], Co[76] and Ni-based[77] O_2-activating catalysts are reported in the literature, but most of the catalysts have Fe and Cu centers. So, the general overview of CuO_2 chemistry identifies some key-intermediates that are proposed in the literature (Figure 17). As a consequence of the crucial influence of ligands, the reaction intermediates may be obtained or not.

3.1. Dioxygen coordination

The first step consists in the coordination of O_2 to $Cu^{(I)}$ center. Here, the usual +I formal oxidation degree of Cu (observed in most biologic and catalytic models, due to the reductive medium) is considered, even if extended studies led to the observation of neutral CuO_2 species[78]. Cu^+ is a medium electron-rich ion, corresponding to a soft acid in the Hard and Soft Acid and Base (HSAB) theory of Pearson. The limiting cases of mono-CuO_2 characters are reported in Table 1. The choice of a ligand is then a balancing act, in order to get the best reactivity of CuO_2 assembly. Three different properties are of first interest: the O_2 character, the coordination type and the spin state.

	$L_nCu^IO_2^+$	$L_nCu^{II}O_2^+$	$L_nCu^{III}O_2^+$
Cu-O_2 interaction	Weak	Medium	Strong
Donating power of ligand	Poor	Medium	High
Character of O_2	Biradical Dioxygen O_2	Radical Superoxide $O_2^{\bullet -}$	No radical Peroxide O_2^{2-}
OD(O)	0	- 1/2	- 1
d(OO)	1.207 Å[79]	≈ 1.35 Å	≈ 1.49 Å
ν(OO)	1580 cm^{-1}[79]	≈ 1100 cm^{-1}	≈ 877 cm^{-1}
Coordination type	End-on (η^1)	End-on/Side-on	Side-on (η^2)
Oxidizing power	Poor oxidant	Good oxidant	Poor oxidant
Spin state	Triplet	Singlet/Triplet	Singlet

Table 1: Limiting-case characterizations of $LCuO_2^+$ adducts. OD stands for Oxidation Degree, d for distance and ν for frequency. The roman exponent represents the formal oxidation degree of copper in such structures.

The general trend is the more donating the ligand, the lower the oxidation potential, the easier the reaction with O_2 and the higher the oxidation degree of Cu in CuO_2 species. The electron affinity of O_2 is 0.45 eV and the second ionization potential of Cu is 20.29 eV[4]. Therefore, in the absence of ligands, it is very unlikely that a strong dative bond can be established. An electrostatic (ion-dipole) interaction might take place. The $Cu^{(I)}$-O_2 case is obtained with low-donating ligands. No strong biomimetic effort was led on that type of adducts, because of the low activation of O_2. However, the existence in the nature of such pre-catalytic adducts was experimentally

4 The first ionization potential is 7.726 eV. Values are from the NIST[80].

measured[81]. The other extreme case, $Cu^{(III)}$-η^2-O_2^{2-}, was observed with strong-donating ligands, such as β-diketiminate or anilido-imine derivatives. $Cu^{(II)}$-superoxide species were the most studied species, because of their greater oxidizing power[82]. Superoxide character of O_2 in LCu-O_2^+ can be proven by adding KO_2 to the corresponding $LCu^{(II)}$ species[83]. X-Ray crystallography (for d(OO) determination), IR spectroscopy (ν(OO)), magnetic and kinetic experiments give meaningful information on the nature of the CuO_2 core[84].

3.1.1. Influence of the ligand

All three properties (coordination type, CuO_2 character, oxidizing power) strongly depend on the nature of the ligand. Reproducing the active sites of enzymes such as hemocyanin, tyrosinase (Type III copper proteins) or galactose oxidase, amine oxidase and dopamine β-monooxygenase (Type II) requires an environment with 3 or 4 coordinating atoms. In active sites of these enzymes, the coordinating atoms can be N (side-chain of histidine residue), O (from tyrosine, glutamate) and/or S (from cysteine, methionine). Histidine residues being the most popular coordinating amino-acid, biomimetic attempts widely use aromatic N ligands (pyridyl, pyrazole, imidazole, quinolyl) or even aliphatic amine ligands to enclose Cu. Also, O donor atoms are sometimes introduced. N-aromatic/N-aliphatic/O coordinating mixes are frequent. The geometry of $Cu^{(I)}$ complexes is quite free, and is in general dictated by steric and structural constraints. In general, $Cu^{(I)}$ complexes have two (linear or bent), three (T-shaped or Y-shaped) or four coordination atoms. A four-coordinating atom set is not flat. $Cu^{(I)}$ rarely exhibits five-coordinated geometry. $Cu^{(II)}$ complexes commonly adopt trigonal-bipyramidal, square-planar or square-pyramidal (with ligand poorly coordinated on axial position) geometries. The choice of a ligand appears to be preponderant for the following reactivity. Few parameters can play a non-negligible role in the coordination of O_2:

— Number of coordinating atoms in the coordinating sphere of the Cu;

— Steric hindrance;

— Electron-donor character;

— $Cu^{(II)}/Cu^{(I)}$ redox potential (not only dependent on the donating power);

— Arrangement of the orbitals.

One has to consider that all these parameters are strongly entangled. The higher the number of coordinating atoms, the more filled the coordination sphere of the copper. This simple assertion leads to consider that di- and tricoordinated Cu sites are able coordinate O_2 in a side-on manner. End-on coordination is more expected with tri- and tetra-coordinated Cu centers. Thus, the place left free by the ligand (which we could associate with a more or less large cone) in the Cu coordination sphere should be considered as the first criterion for the coordination of O_2[85].

In addition, both counter-ion and hydrophobicity of the ligand may play a role in the dioxygen coordination. An expressing example is given by a series of tripodal ligands (Table 2). In the solid state, encumbered counter-ions are able to protect the Cu_2O_2 core from reduction[86]. No such example of anion shielding was reported for mononuclear species, but some stable structures were isolated[64,87]. Secondly, the high donor power of the ligand allows efficient electron transfer from Cu to O_2. Even though a tetra-coordinating ligand can be considered to be a strong donor, Cu-peroxo species are very unlikely because side-on coordination is required to observe double electron transfer (O_2^{2-}).

Ligand	TMPA	BPQA	BQPA	TMQA
Coordinating arms	3 Py	2 Py, 1 Quin	1 Py, 2 Quin	3 Quin
$E_{1/2}(Cu^{II}/Cu^{I})$	-0.63 V	-0.55 V	-0.43 V	-0.26 V
$\Delta H_1°$ (kJ·mol^{-1})	- 34 ± 1	$[Cu(L)(O_2)]^+$ Reacts too fast	- 35 ± 6	$[Cu(L)(O_2)]^+$ Not observed
$\Delta S_1°$ (J·mol^{-1})	- 123 ± 4		- 125 ± 27	
$k_{1,183\,K}$ ($M^{-1}\cdot s^{-1}$)	$(1.8 \pm 0.1)\cdot 10^4$		18 ± 1	
$k_{-1,183\,K}$ ($M^{-1}\cdot s^{-1}$)	8 ± 1		$(6.1 \pm 0.7)\cdot 10^{-3}$	
$\Delta H_2°$ (kJ·mol^{-1})	- 81 ± 1	- 69 ± 2	- 50	$[Cu_2(L)_2(O_2)]^+$ Not observed
$\Delta S_2°$ (kJ·mol^{-1})	- 220 ± 11	- 181 ± 5	- 145	

Table 2: Properties of a series of tripodal ligands (with Py: pyridine and Quin: quinolyl arm). Redox potentials were measured in DMF, and are given vs Fc^+/Fc[85]. ΔH° and ΔS° values are from [88]. Refer to the text for the meaning of subscripts 1 and 2 (see Equations 1 and 2).

A series of complexes based on tripodal ligands were designed in order to determine the influence of the ligand on the coordination of dioxygen (Equation 1). Quinolyne is a less σ-donor group than pyridine. So, less electron density is provided to $Cu^{(I)}$ by quinolyl arms than by pyridyl arms. It results in a higher value of redox potential when the number of quinolyl arms increases. Another effect to take into account is the hydrophobicity of such quinolyl arms: a lower dielectric

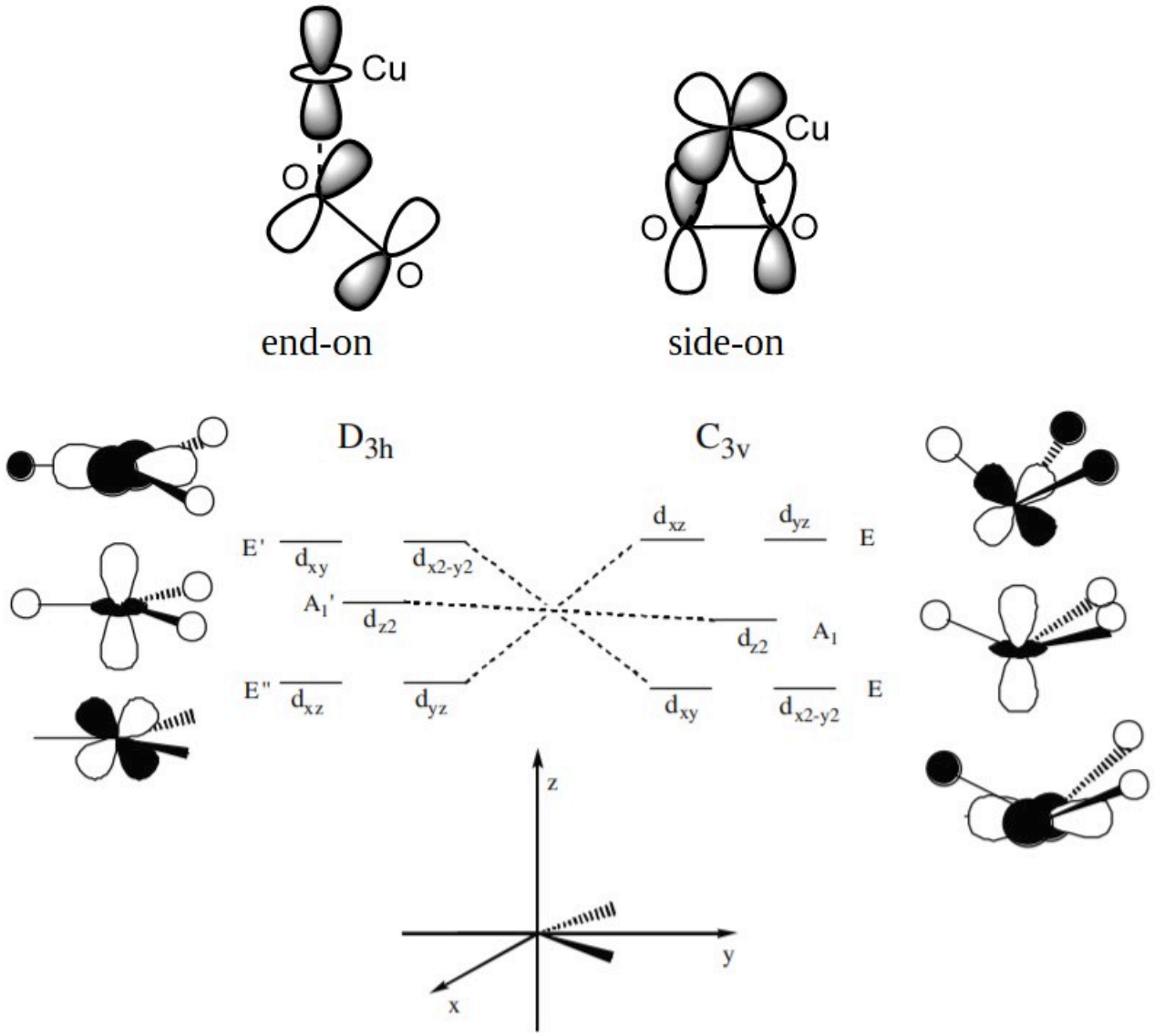

Figure 18: Upper part: End-on and side-on coordination of O_2 on Cu. Lower part: Stabilization of Cu d orbitals in D_{3h} (left) and C_{3v} (right) geometries. Reproduced by permission from Springer Nature Customer Service Centre GmbH: [89], Copyright (2006).

environment favors lower charges[85]. Thereby, for these reasons, $[Cu(TMQA)]^+$ ligand is unable to react with O_2. Comparison of $k_{1,183\ K}$ for TMPA and BQPA Cu complexes is explicit (strongly in favor of TMPA), due to the steric hindrance induced by quinolyl arms. The expectation for such CuO_2 complexes is to undergo dimerization with another $Cu^{(I)}$ complex (Equation 2).

$$[LCu(RCN)]^+ + O_2 \rightarrow [LCu(O_2)]^+ + RCN \qquad \text{Equation 1}$$

$$[LCu(O_2)]^+ + [LCu(RCN)]^+ \rightarrow [\{LCu\}_2(O_2)]^+ + RCN \qquad \text{Equation 2}$$

Decrease of $\Delta H_2°$ enthalpies along the series shows that bulky substituents disfavors the formation of $[\{LCu\}_2(O_2)]^+$. BQPA preferentially forms $[LCu(O_2)]^+$ complex after exposure to O_2.

However, $[\{(BPQA)Cu\}_2(O_2)]^+$ complex exhibits better stability than the TMPA analogous towards the addition of PPH_3, a strong ligand of $Cu^{(I)}$. Superoxo (in $[LCu(O_2)]^+$) and peroxo (in $[\{LCu\}_2(O_2)]^+$) ions are radicalophile (a species that can abstract a H atom from its environment). Their basic nature was also confirmed by the reaction with H^+, leading to H_2O_2 in both cases.

3.1.2. Molecular orbitals

The σ lone pairs of O_2 are low lying orbitals compared to the filled 3d orbitals of $Cu^{(I)}$ and do not participate to the CuO_2 bond (only polarization can take place). The 4s orbital of Cu is high lying and are even more destabilized by the ligand. Therefore, only half-filled π* of O_2 are involved in σ-bonding with Cu. Depending on the number of coordinating atoms and their relative orientation, the d orbitals of Cu involved in the coordination of O_2 vary. End-on coordination mode implies Cu d_{z^2} orbital, while side-on coordination involves four-lobe orbitals (Figure 18, upper part). Most ligands have three or four donor atoms, in the most common trigonal bipyramid or (distorted) tetrahedron geometries with a vacant site (or occupied by a solvent molecule). It is possible to predict, depending on the geometry of the ligand, what will be the mode of coordination of the oxygen. In D3h planar geometry (Figure 18, lower part, left), dxy and dx^2-y^2 orbitals are destabilized by their interaction with ligands and will not be involved in O2 bonding. The d_{z^2} orbital is moderately antibonding with ligands, and will be the orbital which allows the better σ-interaction with z-axis incoming O_2. The two other Cu orbitals, d_{xz} and d_{yz} are non-bonding with ligands but can lead to π-interaction with O_2. In the case that there is an axial ligand (in the apical position), this even destabilizes the d_{z^2} orbital above the d_{xy} and $d_{x^2-y^2}$ orbitals. In Figure 19 are reported three key CuO_2 structures, in triplet and singlet spin states, in end-on and side-on coordination modes[5]. As O_2 approaches, d_{z^2} orbital in D_{3h} symmetry group interacts with π_σ^* orbital of O_2 (Figure 19.A), leading to an end-on bonding interaction ($d_{z^2} + \pi_\sigma^*$) and to an antibonding interaction ($d_{z^2} - \pi_\sigma^*$). When the apical atom is non-coordinating, with respect to the relaxed geometric angles of such atoms, the complex is reduced to a C_{3v} representation (Figure 18, lower part, right). The bonding orbitals of the ligands do not point anymore in the direction of maximum bonding of Cu d orbitals. In that case, d_{xz} and d_{yz} orbitals are now the highest occupied orbitals and suit for side-on π-bonding with π_σ^* orbital of O_2. In some cases, d_{z^2} orbital is perpendicular to the O_2 axis: $d_{x^2-y^2}$ is implied in side-on bonding of O_2 (Figure 19.B). Geometric considerations, such as the dihedral angle drawn by atoms in the

5 These cases are not exhaustive. For example, side-on coordination in the triplet state can be also observed with bidentate ligands.

equatorial positions and Cu, can lead to unambiguous conclusions as to the mode of O_2 coordination[89]. In the case of bidentate ligands (C_{2v} symmetry group in case of a symmetric ligand), d_{xz} (xz plane containing the Cu and O atoms) orbital is destabilized. It is able to interact with π_σ^* of O_2 (Figure 19.C). To conclude, the geometry of the complex and chemical intuition can lead to reliable hypothesis on the coordination mode of O_2 on $Cu^{(I)}$. However, the spin state is difficult to handle at first glance. Further considerations are presented hereafter.

3.1.3. Spin state

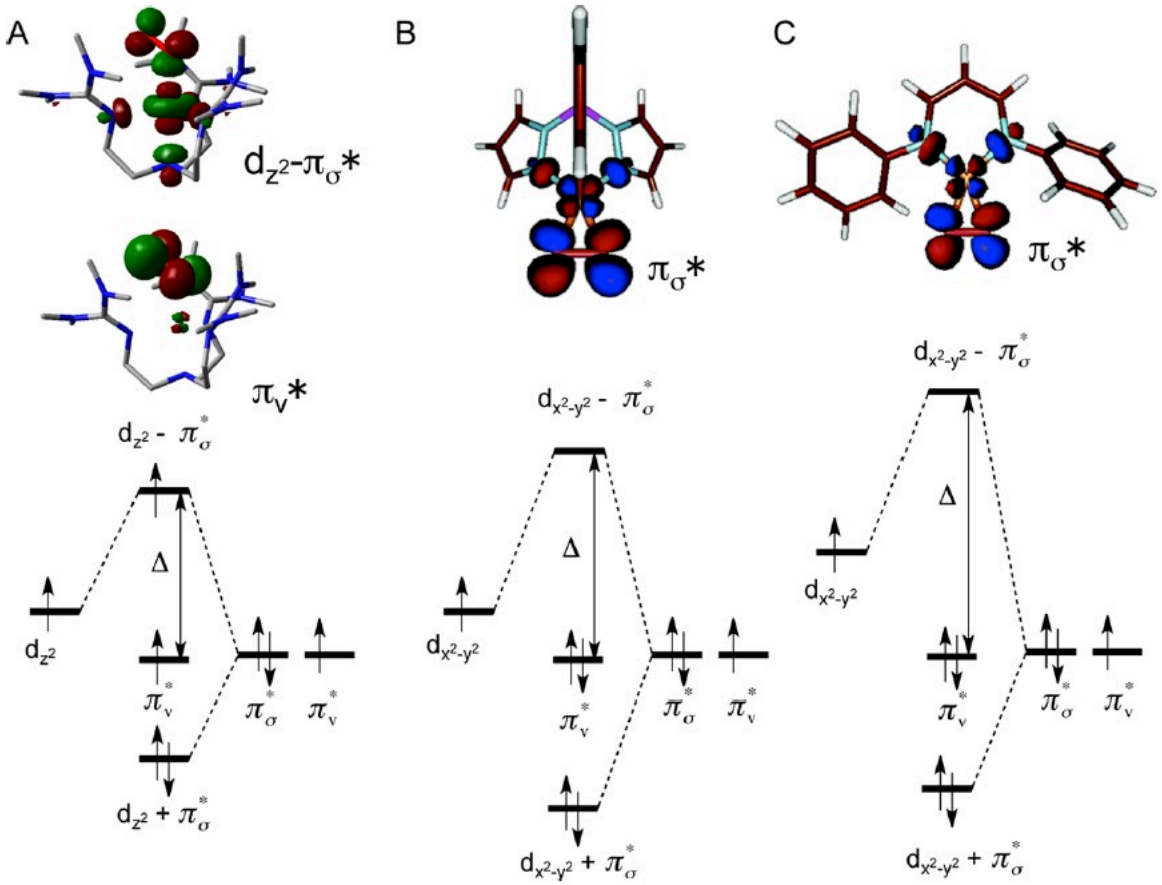

Figure 19: Molecular orbital diagrams for $Cu^{(II)}$-superoxo/$Cu^{(III)}$-peroxo species (A: TMG_3Tren as ligand, end-on coordination, triplet spin state; B: tris(pyrazolyl)hydroborate ligand, side-on coordination, singlet spin state) and $Cu^{(III)}$-peroxo species (C: β-diketiminate ligand, side-on coordination, singlet spin state). SOMOs/HOMOs are shown. Reproduced with permission from [123]. Copyright 2014 American Chemical Society.

The triplet ground state of O_2 imposes an in-depth search for the spin state of considered complex. In the low-interacting $Cu^{(I)}$-O_2 case, Cu is in the formal oxidation state +I, which

corresponds to an electronic configuration $4s^0\ 3d^{10}$, with no radical character. So, the triplet spin state of O_2 prevails, and is imposed to the whole structure. In the case of $Cu^{(II)}$-$O_2^{\bullet -}$, biradical singlet and triplet spin states are expected to have closer energies, because of the $4s^0\ 3d^9$ electronic configuration of $Cu^{(II)}$ and the radical character of $O_2^{\bullet -}$ (superoxide). Magnetic measurements (SQUID) on such species can help to determinate the spin state[6]. Finally, the $Cu^{(III)}$-O_2^{2-} assembly is expected to have a closed-shell singlet character, due to the dianion O_2^{2-} and the $4s^0\ 3d^8$ electronic configuration of $Cu^{(III)}$. The ground state depends on the ligand[90]. From left to right in Figure 20, the gap between πv* orbital of O2 and the upper orbital (composed by πσ* of O2 and d electrons of Cu) increases. That means that a low Δ value implies a low interaction between the d_{z^2} or $d_{x^2-y^2}$ orbital on Cu and the π* orbitals of O_2. With a tris(pyrazolyl)hydroborate ligand (case B), which give a $Cu^{(II)}$-superoxo character to the CuO_2 moiety, Δ is about 1500 cm^{-1}[91] and will favor a singlet spin state. $Cu^{(II)}$-$O_2^{\bullet -}$ can be also characterized as end-on singlet[89], and side-on[60]/end-on[92] triplet structures. The destabilization of the bonding d orbital of Cu by ligand orbitals is primordial to predict the spin state[89]. The increase of the energy of such orbital will also increase the mixing with π^*_σ orbital of O_2. The antibonding ($d_{z^2} + \pi_\sigma^*$) orbital will raise in energy. Singlet spin state is not favored until the mixing reaches the point where the energy difference Δε (Equation 3) between the stabilization due to the retrogradation of the electron from the d orbital to the lower πv* (Δ on Figure 20) and the repulsion relative to the spin-pairing (Epairing) becomes positive.

$$\Delta\varepsilon = \Delta - E_{pairing} \qquad \text{Equation 3}$$

The increase of the donating power of the appropriate ligands, associated with adapted symmetries will enable the obtaining of the singlet spin state. Nevertheless, the use of too strong donating ligands will eventually decrease their $Cu^{(II)}$-superoxo character. The determination of the ground state remains a challenging task, even with the help of extensive theoretical calculations. In general, the use of multi-determinantal or in-depth calculating methods (broken-symmetry, sometimes followed by spin purification[90], spin-flip TD-DFT[93]) is needed to accurately determine the spin state of $Cu_nO_2^{n+}$ species.

3.1.4. Influence of the second coordination sphere and dimer formation

In biological systems, the active sites are protected from the outside by the secondary, ternary and quaternary structures of enzymes. These high-ordering structures prevent the untimely arrival of undesired molecules, that can inhibit the activity. In general, only substrates that can be

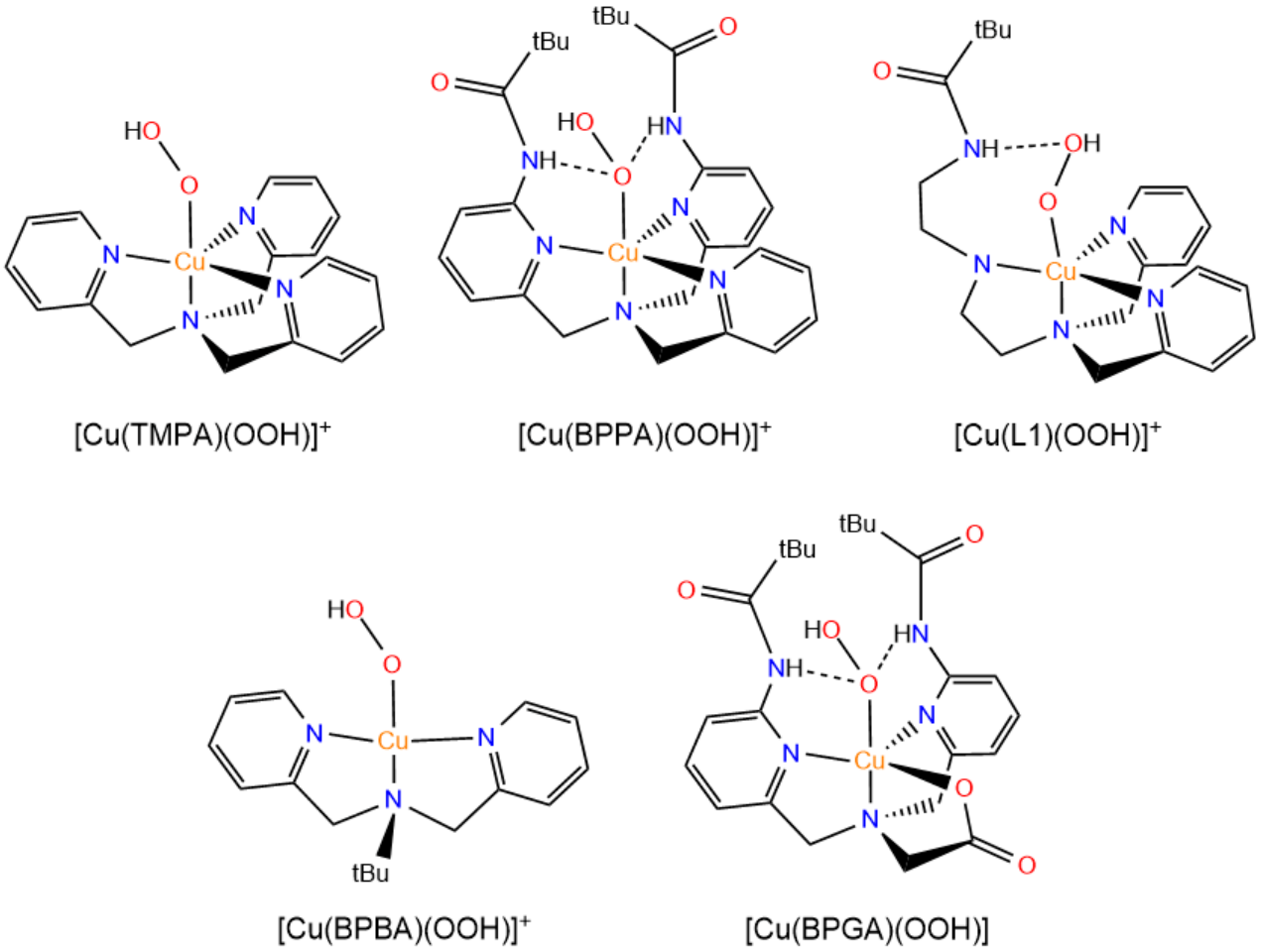

Figure 20: CuOOH complexes referring to Table 3. tBu stands for tertiobutyl group.

oxidized or solvent molecules (in biological environment, water) are able to come in the cavity. Biomimetic systems break free from this natural barrier that is the structure of the protein, at the risk of being deactivated or slowed down by undesired reaction pathways. In the liquid phase, the coordination of O_2 on $Cu^{(I)}$ complexes is consecutive – or maybe competitive – with the decoordination of the solvent[94]. The strength of bonding between Cu and the exogenous solvent molecule then defines the affinity for O_2. Counter-ions also have importance. Some studies about CuO_2 systems mainly discuss dimeric μ-peroxo- and bis(μ-oxo)-dinuclear complexes (as models for mononuclear enzymes), in which the initially formed CuO_2^+ species has attacked an other $Cu^{(I)}$ residue (Figure 17, right). The first crystallographic evidence for Cu_2O_2 core was obtained with TMPA (Tris(2-pyridylmethyl)amine) as ligand. Sufficiently bulky ligands prevent the formation of such dinuclear species, in both side-on and end-on O_2 coordination cases[64]. A lot of models were established on that pattern, they will not be discussed further here.

3.2. $Cu^{(II)}$-hydroperoxo

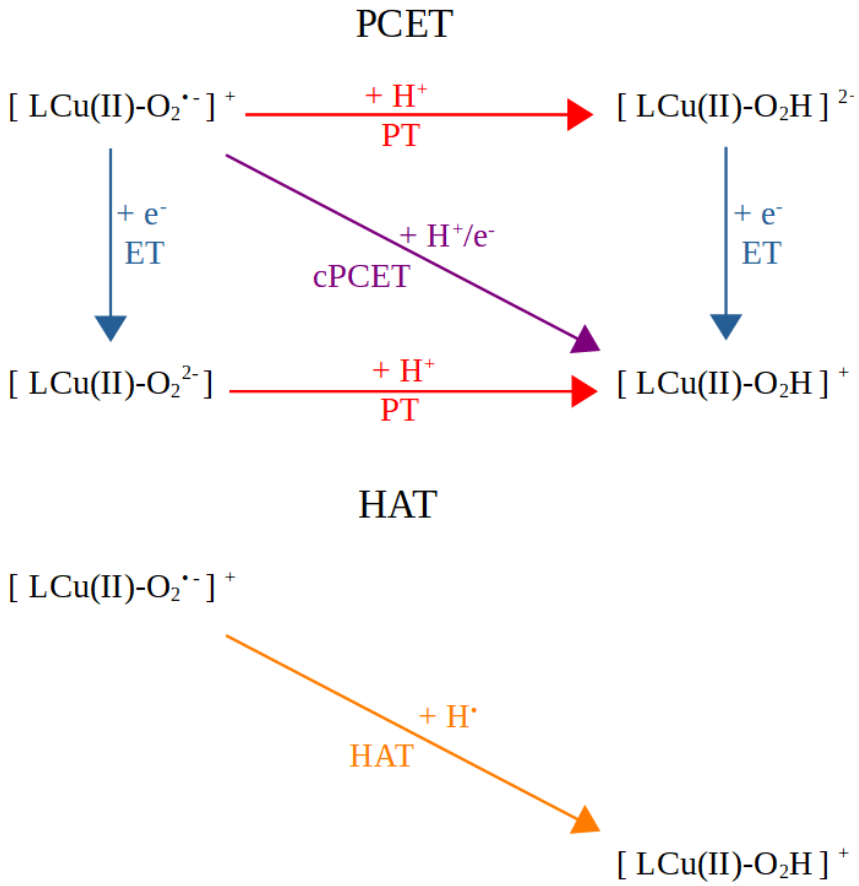

Figure 21: Two pathways for H abstraction : Proton Coupled Electron Transfer (PCET) or HAT (Hydrogen Atom Abstraction).

$Cu^{(II)}$-OOH or $Cu^{(II)}$-hydroperoxide species are key intermediates in the mechanisms of some enzymes, such as PHM, galactose oxidase or superoxide dismutase. $Cu^{(II)}$-superoxo is able, in given conditions, to capture a hydrogen in its environment. The nature of the transferred particle can be either a proton plus an electron ($H^+ + e^-$) or a hydrogen atom ($H^\bullet$). The pathways relative to these transfers are called Proton Coupled Electron Transfer (PCET) or Hydrogen Atom Transfer (HAT), respectively. A PCET corresponds to the transfer of a proton and an electron. It can be done in two steps by a proton transfer (PT), followed by an electron transfer (ET) or *vice versa* or in one step, by a concerted PCET (cPCET). When a H atom is transferred in one step, the mechanism is called Hydrogen Atom Transfer (HAT). HAT and cPCET are experimentally hard to distinguish. The analysis of the change of Intrinsic Bond Orbitals (IBO) along the Intrinsic Reaction Coordinate

(IRC) affords a good way to discriminate them[95]. Charge calculations were also used to differentiate both pathways[96].

The lifetime of hydroperoxo species is expected to be low because of their ability to capture a proton that lead to the loss of H_2O_2 and $Cu^{(II)}$ (Equation 4) or to the degradation of $Cu^{(II)}$-OOH in H_2O and $Cu^{(II)}$-O (Equation 5).

$$[LCu(OOH)]^+ + H^+ \rightarrow [LCu]^{2+} + H_2O_2 \qquad \text{Equation 4}$$

$$[LCu(OOH)]^+ + H^{\bullet} \rightarrow [LCu(O^{\bullet})]^+ + H_2O \qquad \text{Equation 5}$$

Some copper-hydroperoxide species were spectroscopically characterized, from CuO_2^+ species or from the reaction of a $Cu^{(II)}$ species with H_2O_2, in the presence of a base. The first example of a crystallographic isolated $Cu^{(II)}$-hydroperoxo was reported by Masuda and co-workers[69]. Using the BPPA (bis(6-pivalamide-2-pyridylmethyl)-(2-pyridylmethyl)amine) tripod as ligand, both superoxo[63] and hydroperoxo species are stabilized by pivalamide substituents on pyridine arms (at -135 °C and room temperature, respectively). H-bonds are formed with the proximal oxygen atom, and methyl groups prevent Cu-OOH from oxidation. Superoxo species (generated from Cu(I) and O_2) was spectroscopically characterized: three absorption bands were observed at 398, 614 and 716 nm. Hydroperoxo species (from $[LCu]^{2+}$ and H_2O_2) exhibits different features (380, 660 and 830 nm), which makes it possible to distinguish them. The former intense bond, in both cases, was assigned to the LMCT band, the two latter being d-d transition bands of $Cu^{(II)}$ in a bipyramidal trigonal geometry. MS spectrum exhibits a peak at m/z 584, corresponding to the $[LCu(OOH)]^+$ ion. EPR measurements are in favor of an end-on coordination of O_2H anion. Raman spectroscopy experiments showed an 856 cm^{-1} band, close to the 873 cm^{-1} band observed in free H_2O_2 (the OO value with superoxo complex is 1117 cm^{-1}). Reaction of Cu-superoxo with p-methoxyphenol leads to the formation of the Cu-hydroperoxo species (with a rate constant of $4.00 \cdot 10^{-3}$ s^{-1}, with 100 equivalents of substrate). At room temperature, similar example of Cu-hydroperoxo with Me_6Tren as ligand was also characterized by UV-Vis (375, 680 and 840 nm) and Raman (OO: 846 cm^{-1}) spectroscopy. The cumylperoxo ($[LCu(OO\text{-}C(CH_3)_2\text{-}Ph]^+$) equivalent was also synthesized and characterized (UV-Vis: 440, 680, 787 nm; Raman for OO: 839 and 887 cm^{-1}). Both of hydroperoxo and cumylperoxo are expected to undergo homolytic fragmentation of the OO bond. Unfortunately, no activity of both complexes was observed, in nucleophilic and electrophilic oxidation reactions. Other studies explain the reactivity of Cu-hydroperoxo species, by regulation of their stability. It was found that hydrogen bonding with the distal oxygen atom promotes the

reactivity, by activation of the OO bond[97]. It was also shown that the change of the coordination structure from bipyramidal trigonal to square planar geometry enhances the reactivity of the Cu(OOH) species. For example, $[Cu(BPBA)(OOH)]^+$ (BPBA: bis(2-pyridylmethyl)tert-butylamine), is able to oxidize sulfide to sulfoxide much faster than $[Cu(TMPA)(OOH)]^+$ ($15.2\cdot10^{-5}$ s^{-1} against $1.9\cdot10^{-4}$ s^{-1}, respectively, with 100 equivalents of sulfide), but the latter is also more stable in solution[98]. The nature of coordinating atoms has also its importance[99]. Replacing the simple pyridine arm of BPPA by a methylacetate group (BPGA ligand) leads to the stabilization of the hydroperoxo species. S-bearing arm, as an analogous of methionine residue in PHM active site, was found to raise even more the decomposition rate of OOH[100]. A general trend can be taken from Table 3, which gathers some spectroscopic and kinetic data for selected complexes (Figure 20). There is no evident relationship between the OO length and the stability of the complex. However, a strong correlation exists between the decomposition rate constant k_{obs} (determined from the monitoring of the lower UV-Vis band) and the stretching frequency of OO and CuO bonds (resonance Raman). The lower the ν(O-O) stretching frequency, the more the OO bond is activated and thus, the higher the decomposition rate constant k_{obs}.

Ligand	TMPA	BPPA[69]	L1[97]	BPBA[98]	BPGA[99]
H bond	No	Yes (2 on O_p)	Yes (1 on O_d)	No	Yes (2 on O_p)
d(OO)	1.458 Å [a]	1.460 Å	No crystal structure	No crystal structure	1.462 Å [a]
d(CuO)	1.867 Å [a]	1.888 Å			1.889 Å [a]
rRaman(OO)	879.0 cm^{-1} [a] 847 cm^{-1} (MeOH)	892.7 cm^{-1} [a] 856 cm^{-1} (MeCN)	853 cm^{-1} (MeOH)	834 cm^{-1} (MeCN)	890.2 cm^{-1} [a] 854 cm^{-1} (MeOH)
rRaman(CuO)	506.6 cm^{-1} [a]	464.2 cm^{-1} [a]	--	--	479.3 cm^{-1} [a] 501 cm^{-1} (MeOH)
UV-Vis bands	379, 668, 828 (MeCN)	380, 660, 830 nm (MeCN)	381, 635, 770 nm (MeCN)	350, 564, 790 nm (Me_2CO)	370, 675, 837 nm (MeCN)
k_{obs}	$8.3\cdot10^{-2}$ s^{-1} (Me_2CO, 10 °C)	$2.8\cdot10^{-5}$ s^{-1} (Me_2CO, 10 °C)	$4.03\cdot10^{-4}$ s^{-1} (MeCN, -30 °C)	1.88 s^{-1} (Me_2CO, 10 °C)	$1.2\cdot10^{-2}$ s^{-1} (MeCN, 10 °C)

Table 3: Properties of some LCu(OOH) complexes. O_p/O_d stands for proximal/distal oxygen atom. [a] Ab initio *calculated values. Values are from [100] and references herein.*

3.3. $Cu^{(II)}$-oxyl/$Cu^{(III)}$-oxo

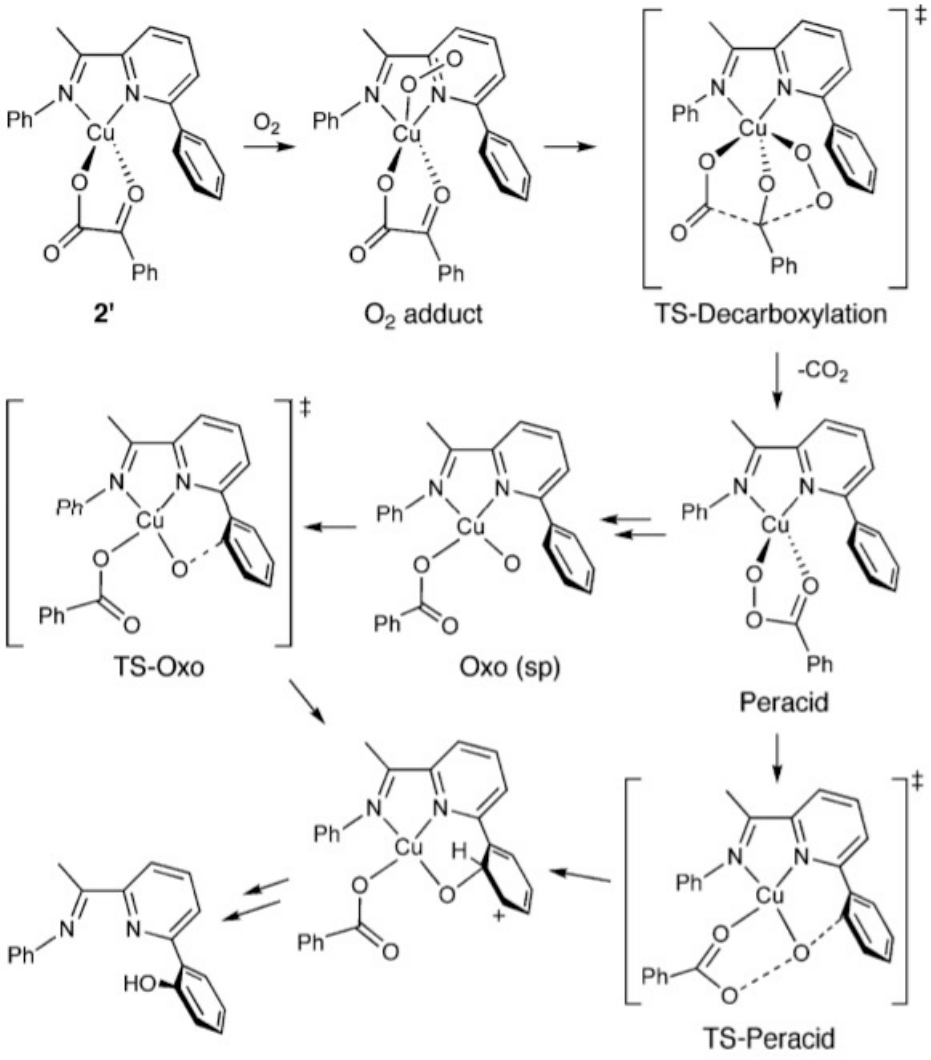

Figure 22: Postulated mechanism for the selective hydroxylation of phenyl group. Reprinted with permission from [102]. Copyright 2007 American Chemical Society.

Mononuclear Cu(II)-oxyl/Cu(III)-oxo species are formed from the decomposition of Cu-hydroperoxo (Figure 17), by reductive breakage of the OO bond (i.e. by homolytic cleavage). They are expected to have a higher oxidizing power than CuO_2 or CuO_2H cores, especially in the case where a given ligand induces a $Cu^{(III)}$-peroxo character[101]. Unfortunately, their expected high reactivity did not allow to observe them neither in the liquid phase (no spectroscopic evidence), nor in the solid phase (no crystallographic isolation). These species are able to react by intramolecular or intermolecular pathways. In general, the expected intramolecular pathway is the insertion of the

O atom into a CH bond of the ligand (often on an aryl ring). Hypothesis about the oxidation mechanism of aryl rings was proposed with the help of bidentate 6-phenyl-2-[(2,6-diisopropyl-phenyl)imino]pyridine ligands. The hydroxylation of the dangling phenyl group has been performed by adding O_2 to a [LCu(α-ketocarboxylate)] complex[102]. ^{18}O-tagged products revealed the incorporation of one oxygen on the ligand, and the other on benzoate by-product. Two pathways have been proposed in order to explain such results (Figure 22), one involving a CuO intermediate. The add of O_2 on Cu leads to the decarboxylation of the α-ketocarboxylate, leading to Cu(R-CO-OO) species. From that Cu-peracid species, either by the direct reaction (*TS-Peracid*) or by a supplementary square planar CuO intermediate (*Oxo (sp)*). The decarboxylation has been calculated to be the higher barrier. Thus, each pathway can be taken, even encountering spin crossing.

3.4. $Cu^{(III)}$-hydroxide intermediates

The intermolecular pathway is the capture of a proton from its environment (Equation 6), followed by the abstraction of a H-atom (Equation 7).

$$[LCu(O^{\bullet})]^{+} + H^{+} \rightarrow [LCu(OH)]^{2+} \qquad \text{Equation 6}$$

$$[LCu(OH)]^{2+} + R\text{-}H \rightarrow [LCu(OH_2)]^{2+} + R^{\bullet} \qquad \text{Equation 7}$$

The use of N,N'-bis(2,6-diisopropylphenyl)-2,6-pyridine-dicarboxamide (Figure 15.g, with R1 = iPr, R2 = H) or analogous as ligand is plebiscited to form the reactive Cu(III)-hydroxide intermediate. $[LCu(OH)]NBu_4$ precursor complex (which was isolated and characterized) has been reduced by electrochemical (~ 0.08 V vs Fc^{+}/Fc, in THF) or chemical (ferrocenium as oxidant) means. The resulting complex is stable at -80 °C. It has been characterized by XAS, showing the change of the oxidation degree of Cu. The H-atom abstraction reaction from CH bond of DHA exhibits a high constant rate of 1.1 $mol^{-1}{\cdot}s^{-1}$ at -80 °C[52]. The resulting $[LCu(H_2O)]$ has been successfully isolated and characterized. The same complex has shown activity towards diverse substrates (even against strong CH bond, such as cyclohexane) in DFB (1,2-difluorobenzene)[53].

As a conclusion, although $[LMO]^{+}$ stable species are reported in the literature (L and M being a ligand, and an other transition metal, such as Mn or Fe, respectively), mononuclear $[LCuO]^{+}/[LCuO]^{2+}/[LCu(OH)]^{2+}$ complexes are not expected to be stable in solution, but to be reliable intermediates in oxidation catalysis[71].

4. Gas phase intermediates

4.1. $[Cu(O_2)]^+$ in the gas phase

4.1.1. Bare CuO_2^+

CuO_2^+ is the simplest adduct between Cu^+ and O_2. High-level of theory calculations were led on this assembly. With single-reference completely renormalized coupled-cluster level of theory, the most stable conformer was found to be the end-on CuO_2 in the triplet state[90]. Side-on triplet, end-on singlet and side-on singlet were found to be 9.0, 14.1 and 23.1 kcal·mol^{-1} higher in energy, respectively. Calculated OO and CuO bond lengths have been calculated to be 1.240 and 1.909 Å, respectively, confirming the $Cu^{(I)}$-O_2 character of such assembly. Among the small number of publications treating the reactivity of CuO_2^+ in the gas phase, D. Caraiman and D.K. Bohme unveiled its low reactivity towards benzene, compared to other MO2+ in the gas phase (M: transition metal atom, from Ti to Au, excepted Tc, Ag and Cd), with the help of an ICP-SIFT apparatus (Figure 23). Unfortunately, only coordination of O_2 has been observed on $[Cu(benzene)]^+$ ion, with no subsequent reactivity[103]. Coordination of O_2 on Cu^+ has been also observed[104]. One has to note that Cu^+ is thermalized, due to the add of buffer gas He in the SIFT (about 0.35 torr). Thermalization corresponds to the equilibrium condition under which a system has a Boltzmann energy distribution, that is the same temperature in all degrees of freedom.

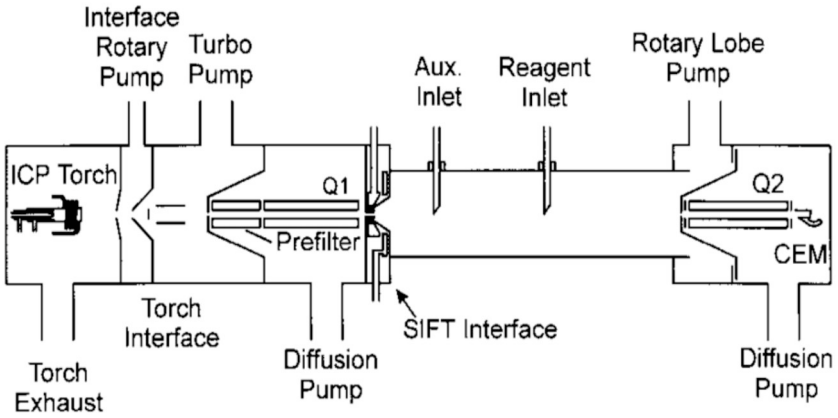

Figure 23: ICP-SIFT (Inductively Coupled Plasma - Selected Ion Flow Tube) apparatus used. Reproduced from [121], permission conveyed through Copyright Clearance Center, Inc.

4.1.2. With ligands, in the gas phase

In the gas phase, only a small number of publications deal with O_2 coordination in the gas phase, on transition metal bipyridyl (Co, Cr, Ni, Ru)[105], on Fe-carbonyl complexes[106], and on radical cationic peptides[107]. A recent study has evoked the coordination of O_2 on a Cu center. $[Cu(toluene\text{-}3,4\text{-}dithiolate)]^-$ complex was generated in the gas phase with the help of an electrospray (ESI) source[108]. Collisions with small traces of O_2 in a collision cell filled with Ar leads to the decoordination of one of the ligands (neutral) followed by the binding of O_2. Cu was calculated to be in the formal +III oxidation state, on the consideration of OO bond length (1.408 Å), obtained by DFT. This OO bond length as been found to be close of those obtained in $Cu^{(III)}$-peroxo characterized species[87,109]. Broken-symmetry calculations have indicated that the singlet spin state of $[LCu(O_2)]^-$ is favored by about 6 $kJ{\cdot}mol^{-1}$. Neither subsequent reactivity of such Cu(OO) nor Cu(OOH) adducts were observed in the gas phase.

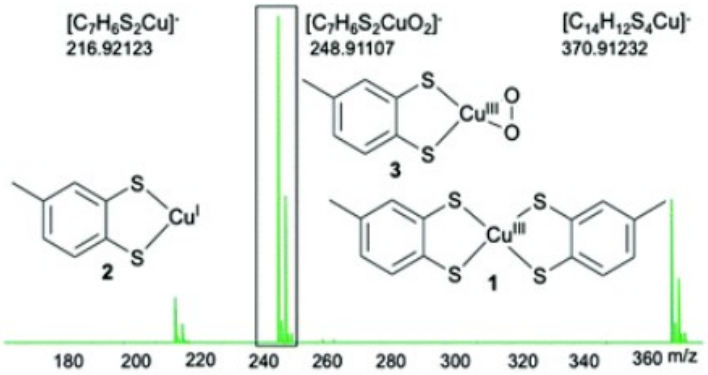

Figure 24: UHR-MSMS spectrum of [Cu(toluene(1,2)-dithiolate)]⁻, reprinted from [108].

4.2. $[CuO]^+$ and $[Cu(OH)]^{2+}$ in the gas phase

4.2.1. Bare CuO^+

Bare CuO^+ possesses the highest number of d electrons that are involved in antibonding interactions with the electrons of the oxygen atom. It leads to a weak, very reactive bond, with a 0.5 π bond order, within the triplet spin state. The BDE (Bond Dissociation Energy) of CuO^+ was experimentally determined to be 1.62 ± 0.15 eV (37.4 kcal·mol^{-1})[110]. The very high reactivity of CuO^+ does not allow it to be easily studied experimentally. Despite of this, spectroscopic data have been published recently on $[(CH_3CN)CuO]^+$, in order to calibrate theory on experience[111]. Vibronic absorption spectrum at very low temperature and the energy of the excited states were determined. Reliable MS-RASPT2 (Multi-State - 2nd order Perturbation Theory Restricted Active Space) calculations were in accordance with the experiments and extended to the bare $[CuO]^+$, the [(9,10-phenanthrenequinone)CuO]$^+$ and [(phenantroline)CuO]$^+$ species. The best electronic description of $[CuO]^+$ corresponds to 62 % of $Cu^{(I)}$-$O^{\bullet\bullet}$ and 26 % of $Cu^{(II)}$-$O^{\bullet -}$ valence bond characters. The addition of ligands increase the part of $Cu^{(II)}$-$O^{\bullet -}$ valence bond character. Then, the presence of ligands on CuO^+ reinforce the Cu-O bond. CuO^+ was evaluated to be even able to oxidize the most challenging CH bonds, such as methane into methanol (Equation 8).

$$CuO^+ + CH_3\text{-}H \rightarrow Cu^+ + CH_3\text{-}OH \qquad \text{Equation 8}$$

BDE(CH_3-H), BDE(CH_3-OH) and BDE(CH_3O-H) values were evaluated to be 103.3, 90.3 and 101.4 kcal·mol^{-1}, respectively[112]. The reaction between CuO^+ and CH_4 is thus expected to be exothermic, by about 51 kcal·mol^{-1}, and this value was confirmed by theoretical studies, with spin inversion from triplet to singlet spin states. This high reactivity is supported by the fact that the low-lying molecular orbitals of CuO^+ interfere easier with CH bonds than in early MO^+ cases (Sc, Ti, V)[113]. However, some studies has highlighted the fact that the triplet ground state configuration ($^3\Sigma^-$, corresponding to the $Cu^{(I)}$-$O^{\bullet\bullet}$ character) is unlikely to react, because of the two-electron occupancy of the orbital which should react. Hence, the first excited state ($^3\Pi$, 18.4 kcal·mol^{-1} higher[114], corresponding to the $Cu^{(II)}$-$O^{\bullet -}$ character) should be the reactive state, at the cost of an energetic excitation[115].

4.2.2. With ligands, in the gas phase

Few examples taken from the literature deal with the oxidation of substrates by CuO^+ complexes. Generation of such complexes in the gas phase is done either in the ion source of a mass spectrometer, by degradation of $[LCu(NO_3)]^+$ (or sometimes from $[LCu(ClO_3)]^+$) complexes, or in the collision cell. D. Schröder, M. Holthausen and H. Schwarz obtained interesting results with phenanthroline as ligand[116]. Firstly, $[(phen)Cu(NO_3)]^+$ was isolated and collided with Xe as inert collision gas (MSMS experiment). Pressure was fixed in single collision conditions. The increase of collision energy leads to the loss of 62 (loss of radical NO_3) and 46 (loss of radical NO_2). An uncertainty lies on the fact that one cannot know whether the loss of the NO_2 radical leads to $[(phen)CuO]^+$ or to an oxidized derivative such as $[(phenO)Cu]^+$. In order to solve this, the m/z 259 ion is formed in source, then mass-selected. The fragmentation shows the obtaining of two fragments. The first at m/z 243 which corresponds to $[(phen)Cu]^+$ (loss of a single oxygen atom). The other corresponds to the loss of 28, associated with CO, resulting from the degradation of the different $[(phenO)Cu]^+$. Finally, and even if some of the products are more stable (based on DFT calculations), it is accepted that there is a mixture of $[(phen)CuO]^+$/$[(phenO)Cu]^+$. $[(phen)CuO]^+$ was collided with different hydrocarbon substrates. Neutral gaseous reactants have been introduced in a collision cell, framed on both sides by quadrupoles, in the range ~ $2\text{-}10\cdot10^{-4}$ mbar. $[(Phen)CuO]^+$ ions are unlikely to react with hydrocarbons. Two competitive reactions, the abstraction of an atom on the substrate, or the transfer of an oxygen atom have been observed, depending on the substrate, without the need to bring any collision energy. The intramolecular and stereoselective oxidation of a chain born by the phen ligand was also evoked in the literature[117].

5. Objectives of the thesis

As we have seen, numerous studies around Cu enzymes and adapted models have enabled the scientific community to forge in-depth knowledge of these systems, with the help of different spectroscopic, electrochemical, magnetic and computational techniques. Strong biomimetic effort was made in order to get effective models, able to oxidize weak to moderate C-H and O-H bonds. This thesis is particularly focused on mononuclear CuO_2 complexes. Some of them were isolated and characterized at the solid state[64,67] and in enzymes[118]. This little review explains how the impact of the metallic center environment is responsible of the activation of O_2 and therefore, of the subsequent reactivity of CuO_2 core. As it was exposed, the activation of O_2 can be done using metal centers, generally surrounded by one or more ligands. The contribution of the ligand was discussed and it was shown that the character of the CuO_2 adduct and its characteristics strongly depend on the donor capacity of the ligand, on the number and on the geometry of its coordinating atoms. Enzymes and their analogous mononuclear complexes show similar reactivity. The first step of oxidation mechanism corresponds in almost all cases to the coordination of O_2 on Cu. The possible reorganization steps of the environment (conformational changes in the structure of the enzyme), and the exchange with the solvent (in two steps, or in one concerted step) were not deepened here. Then, the activation of O_2 leads to the abstraction in its environment of a hydrogen atom. The resulting Cu-hydroperoxo adduct is then decomposed towards the formation of a very oxidative CuO^+ species, or towards the loss of H_2O_2. In the latter case, the resulting $Cu^{(II)}$ species also possesses oxidative properties. Most of these studies were done in the condensed phase. Mass spectrometry is a tool of choice to work outside the solvent environment, especially since the copper species treated here have an ionic character. It also prevents the formation of polynuclear species. Computational techniques provide complementary information on the relative stability of the reaction intermediates, as well as on energy barriers.

The first idea was to start from the simplest system, Cu^+, and to evaluate its affinity towards O_2. Bare Cu^+, by itself, is not known to be a good activator of O_2. However, the formation of CuO_2^+ was already observed in the gas phase[104]. Then, we wanted to study the reactivity of the resulting CuO_2^+ towards a substrate. It did not show any kind of reactivity towards the strong CH bond of benzene[103]. In order to evaluate the way how CuO_2^+ may oxidize a substrate, the still challenging-to-oxidize C-H bond of methyl group of toluene was considered.

In order to form CuO_2^+ complexes in our mass spectrometer, the following idea was to add a ligand around Cu, to reinforce its electronic density. Actually, dioxygen adducts were obtained in the gas phase with two popular classes of Cu complexes, based on bidentate bipyrididyl and tetradentate tripodal ligands. $Cu^{(II)}$-superoxo character was confirmed with consistent DFT calculations. Bipyridyl ligands bearing different electron-donating and electron-withdrawing groups were also used in order to know if they have an influence on both O_2 coordination and electronic description.

The use of tetradentate tripodal ligands such as Me_6Tren and TMPA, in combination with the electrospray source, have made possible to observe $[Cu(L_{-H})]^+$ complexes ("-H" subscript designates the loss of a proton from the ligand). They were formed from their analogous $[Cu(L)(OH)]^+$ precursors. They were found to be approximately ten times more reactive towards O_2 than the corresponding $[Cu(L)]^+$, depending on the conditions. This chapter will try to explain that surprising result, with the help of DFT calculations.

References

1. Mason, H.S.; Fowlks, W.L.; Peterson, E. Oxygen Transfer and Electron Transport by the Phenolase Complex. *J. Am. Chem. Soc.* **1955**, *77*, 2914–2915, doi:10.1021/ja01615a088.

2. Bratsch, S.G. Standard Electrode Potentials and Temperature Coefficients in Water at 298.15 K. *J. Phys. Chem. Ref. Data* **2009**, *18*, 1, doi:10.1063/1.555839.

3. Furui, E.; Akai, N.; Ida, A.; Kawai, A.; Shibuya, K. Observation of Collision-Induced near-IR Emission of Singlet Oxygen O2 A1Δg Generated by Visible Light Excitation of Gaseous O2 Dimol. *Chem. Phys. Lett.* **2009**, *471*, 45–49, doi:10.1016/j.cplett.2009.02.020.

4. Lawton, S.A.; Phelps, A.V. Excitation of the b 1Σ+g State of O2 by Low Energy Electrons. *J. Chem. Phys.* **1978**, *69*, 1055–1068, doi:10.1063/1.436700.

5. de la Lande, A.; Salahub, D.R.; Maddaluno, J.; Scemama, A.; Pilme, J.; Parisel, O.; Gerard, H.; Caffarel, M.; Piquemal, J.-P. Spin-Driven Activation of Dioxygen in Various Metalloenzymes and Their Inspired Models. *J. Comput. Chem.* **2011**, *32*, 1178–1182, doi:10.1002/jcc.21698.

6. Chen, P.; Root, D.E.; Campochiaro, C.; Fujisawa, K.; Solomon, E.I. Spectroscopic and Electronic Structure Studies of the Diamagnetic Side-On CuII-Superoxo Complex Cu(O2)[HB(3-R-5-IPrpz)3]: Antiferromagnetic Coupling versus Covalent Delocalization. *J. Am. Chem. Soc.* **2003**, *125*, 466–474, doi:10.1021/ja020969i.

7. Landis, C.R.; Morales, C.M.; Stahl, S.S. Insights into the Spin-Forbidden Reaction between L2Pd0 and Molecular Oxygen. *J. Am. Chem. Soc.* **2004**, *126*, 16302–16303, doi:10.1021/ja044674b.

8. Bhagi-Damodaran, A.; Michael, M.A.; Zhu, Q.; Reed, J.; Sandoval, B.A.; Mirts, E.N.; Chakraborty, S.; Moënne-Loccoz, P.; Zhang, Y.; Lu, Y. Why Copper Is Preferred over Iron for Oxygen Activation and Reduction in Heme-Copper Oxidases. *Nat. Chem.* **2017**, *9*, 257–263, doi:10.1038/nchem.2643.

9. Ito, N.; Phillips, S.E.V.; Stevens, C.; Ogel, Z.B.; McPherson, M.J.; Keen, J.N.; Yadav, K.D.S.; Knowles, P.F. Novel Thioether Bond Revealed by a 1.7 Å Crystal Structure of Galactose Oxidase. *Nature* **1991**, *350*, 87–90, doi:10.1038/350087a0.

10. Whittaker, M.M.; Kersten, P.J.; Nakamura, N.; Sanders-Loehr, J.; Schweizer, E.S.; Whittaker, J.W. Glyoxal Oxidase from Phanerochaete Chrysosporium Is a New Radical-Copper Oxidase (∗). *J. Biol. Chem.* **1996**, *271*, 681–687, doi:10.1074/jbc.271.2.681.

11. Whittaker, M.M.; Kersten, P.J.; Cullen, D.; Whittaker, J.W. Identification of Catalytic Residues in Glyoxal Oxidase by Targeted Mutagenesis. *J. Biol. Chem.* **1999**, *274*, 36226–36232, doi:10.1074/jbc.274.51.36226.

12. Yin, D. (Tyler); Urresti, S.; Lafond, M.; Johnston, E.M.; Derikvand, F.; Ciano, L.; Berrin, J.-G.; Henrissat, B.; Walton, P.H.; Davies, G.J.; et al. Structure–Function Characterization Reveals New Catalytic Diversity in the Galactose Oxidase and Glyoxal Oxidase Family. *Nat. Commun.* **2015**, *6*, 10197, doi:10.1038/ncomms10197.

13. *Handbook of Metalloproteins*; Messerschmidt, A., Huber, R., Poulas, T., Wieghardt, K., Cygler, M., Bode, W., Eds.; John Wiley & Sons, Ltd: Chichester, 2006; ISBN 978-0-470-86981-9.

14. Whittaker, J.W. Galactose Oxidase. In *Advances in Protein Chemistry*; Copper-Containing Proteins; Academic Press, 2002; Vol. 60, pp. 1–49 ISBN 10.1016/S0065-3233(02)60050-6.

15. Whittaker, M.M.; Ballou, D.P.; Whittaker, J.W. Kinetic Isotope Effects as Probes of the Mechanism of Galactose Oxidase. *Biochemistry* **1998**, *37*, 8426–8436, doi:10.1021/bi980328t.

16. Chaudhuri, P.; Hess, M.; Flörke, U.; Wieghardt, K. From Structural Models of Galactose Oxidase to Homogeneous Catalysis: Efficient Aerobic Oxidation of Alcohols. *Angew. Chem. Int. Ed.* **1998**, *37*, 2217–2220, doi:10.1002/(SICI)1521-3773(19980904)37:16<2217::AID-ANIE2217>3.0.CO;2-D.

17. Pedersen, J.Z.; Finazzi-Agrò, A. Protein-Radical Enzymes. *FEBS Lett.* **1993**, *325*, 53–58, doi:10.1016/0014-5793(93)81412-S.

18. O'Dell, W.B.; Agarwal, P.K.; Meilleur, F. Oxygen Activation at the Active Site of a Fungal Lytic Polysaccharide Monooxygenase. *Angew. Chem. Int. Ed.* **2017**, *56*, 767–770, doi:10.1002/anie.201610502.

19. Munzone, A.; El Kerdi, B.; Fanuel, M.; Rogniaux, H.; Ropartz, D.; Réglier, M.; Royant, A.; Simaan, A.J.; Decroos, C. Characterization of a Bacterial Copper-Dependent Lytic Polysaccharide Monooxygenase with an Unusual Second Coordination Sphere. *FEBS J.* **2020**, *287*, 3298–3314, doi:10.1111/febs.15203.

20. Kim, S.; Ståhlberg, J.; Sandgren, M.; Paton, R.S.; Beckham, G.T. Quantum Mechanical Calculations Suggest That Lytic Polysaccharide Monooxygenases Use a Copper-Oxyl, Oxygen-Rebound Mechanism. *Proc. Natl. Acad. Sci.* **2014**, *111*, 149–154, doi:10.1073/pnas.1316609111.

21. Paradisi, A.; Johnston, E.M.; Tovborg, M.; Nicoll, C.R.; Ciano, L.; Dowle, A.; McMaster, J.; Hancock, Y.; Davies, G.J.; Walton, P.H. Formation of a Copper(II)–Tyrosyl Complex at the Active Site of Lytic Polysaccharide Monooxygenases Following Oxidation by H2O2. *J. Am. Chem. Soc.* **2019**, *141*, 18585–18599, doi:10.1021/jacs.9b09833.

22. Wallace, E.F.; Krantz, M.J.; Lovenberg, W. Dopamine-Beta-Hydroxylase: A Tetrameric Glycoprotein. *Proc. Natl. Acad. Sci. U. S. A.* **1973**, *70*, 2253–2255, doi:10.1073/pnas.70.8.2253.

23. Siebert, X.; Eipper, B.A.; Mains, R.E.; Prigge, S.T.; Blackburn, N.J.; Amzel, L.M. The Catalytic Copper of Peptidylglycine α-Hydroxylating Monooxygenase Also Plays a Critical Structural Role. *Biophys. J.* **2005**, *89*, 3312–3319, doi:10.1529/biophysj.105.066100.

24. Francisco, W.A.; Blackburn, N.J.; Klinman, J.P. Oxygen and Hydrogen Isotope Effects in an Active Site Tyrosine to Phenylalanine Mutant of Peptidylglycine α-Hydroxylating Monooxygenase: Mechanistic Implications. *Biochemistry* **2003**, *42*, 1813–1819, doi:10.1021/bi020592t.

25. Miller, S.M.; Klinman, J.P. Secondary Isotope Effects and Structure-Reactivity Correlations in the Dopamine .Beta.-Monooxygenase Reaction: Evidence for a Chemical Mechanism. *Biochemistry* **1985**, *24*, 2114–2127, doi:10.1021/bi00330a004.

26. Evans, J.P.; Ahn, K.; Klinman, J.P. Evidence That Dioxygen and Substrate Activation Are Tightly Coupled in Dopamine β-Monooxygenase: Implications for the Reactive Oxygen Species. *J. Biol. Chem.* **2003**, *278*, 49691–49698, doi:10.1074/jbc.M300797200.

27. Prigge, S.T.; Eipper, B.A.; Mains, R.E.; Amzel, L.M. Dioxygen Binds End-On to Mononuclear Copper in a Precatalytic Enzyme Complex. *Science* **2004**, *304*, 864–867, doi:10.1126/science.1094583.

28. de la Lande, A.; Salahub, D.; Moliner, V.; Gérard, H.; Piquemal, J.-P.; Parisel, O. Dioxygen Activation by Mononuclear Copper Enzymes: Insights from a Tripodal Ligand Mimicking Their CuM Coordination Sphere. *Inorg. Chem.* **2009**, *48*, 7003–7005, doi:10.1021/ic900567z.

29. Francisco, W.A.; Merkler, D.J.; Blackburn, N.J.; Klinman, J.P. Kinetic Mechanism and Intrinsic Isotope Effects for the Peptidylglycine α-Amidating Enzyme Reaction. *Biochemistry* **1998**, *37*, 8244–8252, doi:10.1021/bi973004y.

30. Chen, P.; Bell, J.; Eipper, B.A.; Solomon, E.I. Oxygen Activation by the Noncoupled Binuclear Copper Site in Peptidylglycine α-Hydroxylating Monooxygenase. Spectroscopic Definition of the Resting Sites and the Putative CuIIM−OOH Intermediate. *Biochemistry* **2004**, *43*, 5735–5747, doi:10.1021/bi0362830.

31. Miller, S.M.; Klinman, J.P. Magnitude of Intrinsic Isotope Effects in the Dopamine .Beta.-Monooxygenase Reaction. *Biochemistry* **1983**, *22*, 3091–3096, doi:10.1021/bi00282a011.

32. Abad, E.; Rommel, J.B.; Kästner, J. Reaction Mechanism of the Bicopper Enzyme Peptidylglycine α-Hydroxylating Monooxygenase. *J. Biol. Chem.* **2014**, *289*, 13726–13738, doi:10.1074/jbc.M114.558494.

33. Karlin, K.D.; Itoh, S.; Rokita, S. *Copper-Oxygen Chemistry*; John Wiley & Sons, 2011; ISBN 978-1-118-09435-8.

34. Rokhsana, D.; Shepard, E.M.; Brown, D.E.; Dooley, D.M. Amine Oxidase and Galactose Oxidase. In *Copper-Oxygen Chemistry*; John Wiley & Sons, Ltd, 2011; pp. 53–106 ISBN 978-1-118-09436-5.

35. Ruggiero, C.E.; Smith, J.A.; Tanizawa, K.; Dooley, D.M. Mechanistic Studies of Topa Quinone Biogenesis in Phenylethylamine Oxidase. *Biochemistry* **1997**, *36*, 1953–1959, doi:10.1021/bi9628836.

36. Shepard, E.M.; Okonski, K.M.; Dooley, D.M. Kinetics and Spectroscopic Evidence That the Cu(I)−Semiquinone Intermediate Reduces Molecular Oxygen in the Oxidative Half-Reaction of Arthrobacter Globiformis Amine Oxidase. *Biochemistry* **2008**, *47*, 13907–13920, doi:10.1021/bi8011516.

37. Pedersen, J.Z.; Finazzi-Agrò, A. Protein-Radical Enzymes. *FEBS Lett.* **1993**, *325*, 53–58, doi:10.1016/0014-5793(93)81412-S.

38. Thomas, F. Ten Years of a Biomimetic Approach to the Copper(II) Radical Site of Galactose Oxidase. *Eur. J. Inorg. Chem.* **2007**, *2007*, 2379–2404, doi:10.1002/ejic.200601091.

39. Orio, M.; Jarjayes, O.; Kanso, H.; Philouze, C.; Neese, F.; Thomas, F. X-Ray Structures of Copper(II) and Nickel(II) Radical Salen Complexes: The Preference of Galactose Oxidase for Copper(II). *Angew. Chem. Int. Ed.* **2010**, *49*, 4989–4992, doi:10.1002/anie.201001040.

40. Wang, Y.; DuBois, J.L.; Hedman, B.; Hodgson, K.O.; Stack, T.D.P. Catalytic Galactose Oxidase Models: Biomimetic Cu(II)-Phenoxyl-Radical Reactivity. *Science* **1998**, *279*, 537–540, doi:10.1126/science.279.5350.537.

41. Robin, M.B.; Day, P. Mixed Valence Chemistry-A Survey and Classification. In *Advances in Inorganic Chemistry and Radiochemistry*; Emeléus, H.J., Sharpe, A.G., Eds.; Academic Press, 1968; Vol. 10, pp. 247–422.

42. Kurahashi, T.; Fujii, H. One-Electron Oxidation of Electronically Diverse Manganese(III) and Nickel(II) Salen Complexes: Transition from Localized to Delocalized Mixed-Valence Ligand Radicals. *J. Am. Chem. Soc.* **2011**, *133*, 8307–8316, doi:10.1021/ja2016813.

43. Pratt, R.C.; Lyons, C.T.; Wasinger, E.C.; Stack, T.D.P. Electrochemical and Spectroscopic Effects of Mixed Substituents in Bis(Phenolate)–Copper(II) Galactose Oxidase Model Complexes. *J. Am. Chem. Soc.* **2012**, *134*, 7367–7377, doi:10.1021/ja211247f.

44. McGlashen, M.L.; Eads, D.D.; Spiro, T.G.; Whittaker, J.W. Resonance Raman Spectroscopy of Galactose Oxidase: A New Interpretation Based on Model Compound Free Radical Spectra. *J. Phys. Chem.* **1995**, *99*, 4918–4922, doi:10.1021/j100014a008.

45. Lyons, C.T.; Stack, T.D.P. Recent Advances in Phenoxyl Radical Complexes of Salen-Type Ligands as Mixed-Valent Galactose Oxidase Models. *Coord. Chem. Rev.* **2013**, *257*, 528–540, doi:10.1016/j.ccr.2012.06.003.

46. Verma, P.; Pratt, R.C.; Storr, T.; Wasinger, E.C.; Stack, T.D.P. Sulfanyl Stabilization of Copper-Bonded Phenoxyls in Model Complexes and Galactose Oxidase. *Proc. Natl. Acad. Sci.* **2011**, *108*, 18600–18605, doi:10.1073/pnas.1109931108.

47. Hoover, J.M.; Ryland, B.L.; Stahl, S.S. Mechanism of Copper(I)/TEMPO-Catalyzed Aerobic Alcohol Oxidation. *J. Am. Chem. Soc.* **2013**, *135*, 2357–2367, doi:10.1021/ja3117203.

48. Rafiee, M.; Miles, K.C.; Stahl, S.S. Electrocatalytic Alcohol Oxidation with TEMPO and Bicyclic Nitroxyl Derivatives: Driving Force Trumps Steric Effects. *J. Am. Chem. Soc.* **2015**, *137*, 14751–14757, doi:10.1021/jacs.5b09672.

49. Badalyan, A.; Stahl, S.S. Cooperative Electrocatalytic Alcohol Oxidation with Electron-Proton-Transfer Mediators. *Nature* **2016**, *535*, 406–410, doi:10.1038/nature18008.

50. Concia, A.L.; Beccia, M.R.; Orio, M.; Ferre, F.T.; Scarpellini, M.; Biaso, F.; Guigliarelli, B.; Réglier, M.; Simaan, A.J. Copper Complexes as Bioinspired Models for Lytic Polysaccharide Monooxygenases. *Inorg. Chem.* **2017**, *56*, 1023–1026, doi:10.1021/acs.inorgchem.6b02165.

51. Donoghue, P.J.; Gupta, A.K.; Boyce, D.W.; Cramer, C.J.; Tolman, W.B. An Anionic, Tetragonal Copper(II) Superoxide Complex. *J. Am. Chem. Soc.* **2010**, *132*, 15869–15871, doi:10.1021/ja106244k.

52. Donoghue, P.J.; Tehranchi, J.; Cramer, C.J.; Sarangi, R.; Solomon, E.I.; Tolman, W.B. Rapid C–H Bond Activation by a Monocopper(III)–Hydroxide Complex. *J. Am. Chem. Soc.* **2011**, *133*, 17602–17605, doi:10.1021/ja207882h.

53. Dhar, D.; Tolman, W.B. Hydrogen Atom Abstraction from Hydrocarbons by a Copper(III)-Hydroxide Complex. *J. Am. Chem. Soc.* **2015**, *137*, 1322–1329, doi:10.1021/ja512014z.

54. Neira, Andrea.C.; Martínez-Alanis, P.R.; Aullón, G.; Flores-Alamo, M.; Zerón, P.; Company, A.; Chen, J.; Kasper, J.B.; Browne, W.R.; Nordlander, E.; et al. Oxidative Cleavage of Cellobiose by Lytic Polysaccharide Monooxygenase (LPMO)-Inspired Copper Complexes. *ACS Omega* **2019**, *4*, 10729–10740, doi:10.1021/acsomega.9b00785.

55. Fukatsu, A.; Morimoto, Y.; Sugimoto, H.; Itoh, S. Modelling a ‘Histidine Brace’ Motif in Mononuclear Copper Monooxygenases. *Chem. Commun.* **2020**, *56*, 5123–5126, doi:10.1039/D0CC01392G.

56. Mirica, L.M.; Ottenwaelder, X.; Stack, T.D.P. Structure and Spectroscopy of Copper−Dioxygen Complexes. *Chem. Rev.* **2004**, *104*, 1013–1046, doi:10.1021/cr020632z.

57. Lewis, E.A.; Tolman, W.B. Reactivity of Dioxygen−Copper Systems. *Chem. Rev.* **2004**, *104*, 1047–1076, doi:10.1021/cr020633r.

58. Zhang, C.X.; Kaderli, S.; Costas, M.; Kim, E.; Neuhold, Y.-M.; Karlin, K.D.; Zuberbühler, A.D. Copper(I)−Dioxygen Reactivity of [(L)Cu]+ (L = Tris(2-Pyridylmethyl)Amine): Kinetic/Thermodynamic and Spectroscopic Studies Concerning the Formation of Cu−O2 and Cu2−O2 Adducts as a Function of Solvent Medium and 4-Pyridyl Ligand Substituent Variations. *Inorg. Chem.* **2003**, *42*, 1807–1824, doi:10.1021/ic0205684.

59. Blackman, A.G. The Coordination Chemistry of Tripodal Tetraamine Ligands. *Polyhedron* **2005**, *24*, 1–39, doi:10.1016/j.poly.2004.10.012.

60. Sánchez-Eguía, B.N.; Flores-Alamo, M.; Orio, M.; Castillo, I. Side-on Cupric–Superoxo Triplet Complexes as Competent Agents for H-Abstraction Relevant to the Active Site of PHM. *Chem. Commun.* **2015**, *51*, 11134–11137, doi:10.1039/C5CC02332G.

61. Kim, S.; Lee, J.Y.; Cowley, R.E.; Ginsbach, J.W.; Siegler, M.A.; Solomon, E.I.; Karlin, K.D. A N3S(Thioether)-Ligated CuII-Superoxo with Enhanced Reactivity. *J. Am. Chem. Soc.* **2015**, *137*, 2796–2799, doi:10.1021/ja511504n.

62. Maiti, D.; Fry, H.C.; Woertink, J.S.; Vance, M.A.; Solomon, E.I.; Karlin, K.D. A 1:1 Copper−Dioxygen Adduct Is an End-on Bound Superoxo Copper(II) Complex Which Undergoes Oxygenation Reactions with Phenols. *J. Am. Chem. Soc.* **2007**, *129*, 264–265, doi:10.1021/ja067411l.

63. Diaz, D.E.; Quist, D.A.; Herzog, A.E.; Schaefer, A.W.; Kipouros, I.; Bhadra, M.; Solomon, E.I.; Karlin, K.D. Impact of Intramolecular Hydrogen Bonding on the Reactivity of Cupric Superoxide Complexes with O−H and C−H Substrates. *Angew. Chem. Int. Ed.* **2019**, *58*, 17572–17576, doi:https://doi.org/10.1002/anie.201908471.

64. Würtele, C.; Gaoutchenova, E.; Harms, K.; Holthausen, M.C.; Sundermeyer, J.; Schindler, S. Crystallographic Characterization of a Synthetic 1:1 End-On Copper Dioxygen Adduct Complex. *Angew. Chem. Int. Ed.* **2006**, *45*, 3867–3869, doi:10.1002/anie.200600351.

65. Trammell, R.; Rajabimoghadam, K.; Garcia-Bosch, I. Copper-Promoted Functionalization of Organic Molecules: From Biologically Relevant Cu/O2 Model Systems to Organometallic Transformations. *Chem. Rev.* **2019**, *119*, 2954–3031, doi:10.1021/acs.chemrev.8b00368.

66. Abe, T.; Morimoto, Y.; Tano, T.; Mieda, K.; Sugimoto, H.; Fujieda, N.; Ogura, T.; Itoh, S. Geometric Control of Nuclearity in Copper(I)/Dioxygen Chemistry. *Inorg. Chem.* **2014**, *53*, 8786–8794, doi:10.1021/ic501461n.

67. Fujii, T.; Yamaguchi, S.; Funahashi, Y.; Ozawa, T.; Tosha, T.; Kitagawa, T.; Masuda, H. Mononuclear Copper(Ii)–Hydroperoxo Complex Derived from Reaction of Copper(i) Complex with Dioxygen as a Model of DβM and PHM. *Chem. Commun.* **2006**, *0*, 4428–4430, doi:10.1039/B609673E.

68. Álvarez, M.; Molina, F.; Fructos, M.R.; Urbano, J.; Álvarez, E.; Sodupe, M.; Lledós, A.; Pérez, P.J. Aerobic Intramolecular Carbon–Hydrogen Bond Oxidation Promoted by Cu(I) Complexes. *Dalton Trans.* **2020**, *49*, 14647–14655, doi:10.1039/D0DT03198D.

69. Wada, A.; Harata, M.; Hasegawa, K.; Jitsukawa, K.; Masuda, H.; Mukai, M.; Kitagawa, T.; Einaga, H. Structural and Spectroscopic Characterization of a Mononuclear Hydroperoxo-Copper(II) Complex with Tripodal Pyridylamine Ligands. *Angew. Chem. Int. Ed Engl.* **1998**, *37*, 798–799, doi:10.1002/(SICI)1521-3773(19980403)37:6<798::AID-ANIE798>3.0.CO;2-3.

70. Choi, Y.J.; Cho, K.-B.; Kubo, M.; Ogura, T.; Karlin, K.D.; Cho, J.; Nam, W. Spectroscopic and Computational Characterization of CuII–OOR (R = H or Cumyl) Complexes Bearing a Me6-Tren Ligand. *Dalton Trans.* **2011**, *40*, 2234, doi:10.1039/c0dt01036g.

71. Gagnon, N.; Tolman, W.B. [CuO]+ and [CuOH]2+ Complexes: Intermediates in Oxidation Catalysis? *Acc. Chem. Res.* **2015**, *48*, 2126–2131, doi:10.1021/acs.accounts.5b00169.

72. Rinaldi, A.C.; Rescigno, A.; Rinaldi, A.; Sanjust, E. Modeling Novel Quinocofactors: An Overview. *Bioorganic Chem.* **1999**, *27*, 253–288, doi:10.1006/bioo.1998.1130.

73. Montemore, M.M.; van Spronsen, M.A.; Madix, R.J.; Friend, C.M. O2 Activation by Metal Surfaces: Implications for Bonding and Reactivity on Heterogeneous Catalysts. *Chem. Rev.* **2018**, *118*, 2816–2862, doi:10.1021/acs.chemrev.7b00217.

74. Wang, X.; Liu, R.; Jin, Y.; Liang, X. TEMPO/HCl/NaNO2 Catalyst: A Transition-Metal-Free Approach to Efficient Aerobic Oxidation of Alcohols to Aldehydes and Ketones Under Mild Conditions. *Chem. - Eur. J.* **2008**, *14*, 2679–2685, doi:10.1002/chem.200701818.

75. Deville, C.; Padamati, S.K.; Sundberg, J.; McKee, V.; Browne, W.R.; McKenzie, C.J. O2 Activation and Double C-H Oxidation by a Mononuclear Manganese(II) Complex. *Angew. Chem.* **2016**, *128*, 555–559, doi:10.1002/ange.201508372.

76. Jing, Y.; Jiang, J.; Yan, B.; Lu, S.; Jiao, J.; Xue, H.; Yang, G.; Zheng, G. Activation of Dioxygen by Cobaloxime and Nitric Oxide for Efficient TEMPO-Catalyzed Oxidation of Alcohols. *Adv. Synth. Catal.* **2011**, *353*, 1146–1152, doi:10.1002/adsc.201100067.

77. Kieber-Emmons, M.T.; Riordan, C.G. Dioxygen Activation at Monovalent Nickel. *Acc. Chem. Res.* **2007**, *40*, 618–625, doi:10.1021/ar700043n.

78. Güell, M.; Luis, J.M.; Rodríguez-Santiago, L.; Sodupe, M.; Solà, M. Structure, Bonding, and Relative Stability of the Ground and Low-Lying Electronic States of CuO2. The Role of Exact Exchange. *J. Phys. Chem. A* **2009**, *113*, 1308–1317, doi:10.1021/jp8031379.

79. Herzberg, G. Molecular Spectra and Molecular Structure. I. Spectra of Diatomic Molecules. *Am. J. Phys.* **1951**, *19*, 390–391, doi:10.1119/1.1932852.

80. National Institute of Standards and Technology Available online: https://www.nist.gov/ (accessed on 24 October 2021).

81. Prigge, S.T.; Eipper, B.A.; Mains, R.E.; Amzel, L.M. Dioxygen Binds End-On to Mononuclear Copper in a Precatalytic Enzyme Complex. *Science* **2004**, *304*, 864–867, doi:10.1126/science.1094583.

82. de la Lande, A.; Gérard, H.; Parisel, O. How to Optimize a C-H Cleavage with a Mononuclear Copper–Dioxygen Adduct? *Int. J. Quantum Chem.* **2008**, *108*, 1898–1904, doi:https://doi.org/10.1002/qua.21679.

83. Nappa, M.; Valentine, J.S.; Miksztal, A.; Schugar, H.J.; Isied, S.S. Reactions of Superoxide in Aprotic Solvents. A Superoxo Complex of Copper(II) Rac-5,7,7,12,14,14-Hexamethyl-1,4,8,11-Tetraazacyclotetradecane. *J. Am. Chem. Soc.* **1979**, *101*, 7744–7746, doi:10.1021/ja00520a034.

84. Lanci, M.P.; Smirnov, V.V.; Cramer, C.J.; Gauchenova, E.V.; Sundermeyer, J.; Roth, J.P. Isotopic Probing of Molecular Oxygen Activation at Copper(I) Sites. *J. Am. Chem. Soc.* **2007**, *129*, 14697–14709, doi:10.1021/ja074620c.

85. Wei, N.; Murthy, N.N.; Chen, Q.; Zubieta, J.; Karlin, K.D. Copper(I)/Dioxygen Reactivity of Mononuclear Complexes with Pyridyl and Quinolyl Tripodal Tetradentate Ligands: Reversible Formation of Cu:O2 = 1:1 and 2:1 Adducts. *Inorg. Chem.* **1994**, *33*, 1953–1965, doi:10.1021/ic00087a036.

86. Würtele, C.; Sander, O.; Lutz, V.; Waitz, T.; Tuczek, F.; Schindler, S. Aliphatic C−H Bond Oxidation of Toluene Using Copper Peroxo Complexes That Are Stable at Room Temperature. *J. Am. Chem. Soc.* **2009**, *131*, 7544–7545, doi:10.1021/ja902327s.

87. Aboelella, N.W.; Kryatov, S.V.; Gherman, B.F.; Brennessel, W.W.; Young, Victor G.; Sarangi, R.; Rybak-Akimova, E.V.; Hodgson, K.O.; Hedman, B.; Solomon, E.I.; et al. Dioxygen Activation at a Single Copper Site: Structure, Bonding, and Mechanism of Formation of 1:1 Cu−O2 Adducts. *J. Am. Chem. Soc.* **2004**, *126*, 16896–16911, doi:10.1021/ja045678j.

88. Karlin, K.D.; Wei, N.; Jung, B.; Kaderli, S.; Niklaus, P.; Zuberbuehler, A.D. Kinetics and Thermodynamics of Formation of Copper-Dioxygen Adducts: Oxygenation of Mononuclear Copper(I) Complexes Containing Tripodal Tetradentate Ligands. *J. Am. Chem. Soc.* **1993**, *115*, 9506–9514, doi:10.1021/ja00074a015.

89. de la Lande, A.; Gérard, H.; Moliner, V.; Izzet, G.; Reinaud, O.; Parisel, O. Theoretical Modelling of Tripodal CuN3 and CuN4 Cuprous Complexes Interacting with O2, CO or CH3CN. *JBIC J. Biol. Inorg. Chem.* **2006**, *11*, 593–608, doi:10.1007/s00775-006-0107-8.

90. Cramer, C.J.; Gour, J.R.; Kinal, A.; Włoch, M.; Piecuch, P.; Moughal Shahi, A.R.; Gagliardi, L. Stereoelectronic Effects on Molecular Geometries and State-Energy Splittings of Ligated Monocopper Dioxygen Complexes. *J. Phys. Chem. A* **2008**, *112*, 3754–3767, doi:10.1021/jp800627e.

91. Chen, P.; Root, D.E.; Campochiaro, C.; Fujisawa, K.; Solomon, E.I. Spectroscopic and Electronic Structure Studies of the Diamagnetic Side-On CuII-Superoxo Complex Cu(O2)[HB(3-R-5-IPrpz)3]: Antiferromagnetic Coupling versus Covalent Delocalization. *J. Am. Chem. Soc.* **2003**, *125*, 466–474, doi:10.1021/ja020969i.

92. Bonniard, L.; de la Lande, A.; Ulmer, S.; Piquemal, J.-P.; Parisel, O.; Gérard, H. Competitive Ligand/Chelate Binding in [Cu(TMPA)]+ and [Cu(Tren)]+ Based Complexes. *Catal. Today* **2011**, *177*, 79–86, doi:10.1016/j.cattod.2011.07.015.

93. de la Lande, A.; Moliner, V.; Parisel, O. Singlet-Triplet Gaps in Large Multireference Systems: Spin-Flip-Driven Alternatives for Bioinorganic Modeling. *J. Chem. Phys.* **2007**, *126*, 035102, doi:10.1063/1.2423010.

94. Weitzer, M.; Schindler, S.; Brehm, G.; Schneider, S.; Hörmann, E.; Jung, B.; Kaderli, S.; Zuberbühler, A.D. Reversible Binding of Dioxygen by the Copper(I) Complex with Tris(2-Dimethylaminoethyl)Amine (Me6tren) Ligand. *Inorg. Chem.* **2003**, *42*, 1800–1806, doi:10.1021/ic025941m.

95. Klein, J.E.M.N.; Knizia, G. CPCET versus HAT: A Direct Theoretical Method for Distinguishing X–H Bond-Activation Mechanisms. *Angew. Chem. Int. Ed.* **2018**, *57*, 11913–11917, doi:10.1002/anie.201805511.

96. Sirjoosingh, A.; Hammes-Schiffer, S. Proton-Coupled Electron Transfer versus Hydrogen Atom Transfer: Generation of Charge-Localized Diabatic States. *J. Phys. Chem. A* **2011**, *115*, 2367–2377, doi:10.1021/jp111210c.

97. Yamaguchi, S.; Nagatomo, S.; Kitagawa, T.; Funahashi, Y.; Ozawa, T.; Jitsukawa, K.; Masuda, H. Copper Hydroperoxo Species Activated by Hydrogen-Bonding Interaction with Its Distal Oxygen. *Inorg. Chem.* **2003**, *42*, 6968–6970, doi:10.1021/ic035080x.

98. Fujii, T.; Naito, A.; Yamaguchi, S.; Wada, A.; Funahashi, Y.; Jitsukawa, K.; Nagatomo, S.; Kitagawa, T.; Masuda, H. Construction of a Square-Planar Hydroperoxo-Copper(II) Complex Inducing a Higher Catalytic Reactivity. *Chem. Commun.* **2003**, 2700–2701, doi:10.1039/B308073K.

99. Yamaguchi, S.; Kumagai, A.; Nagatomo, S.; Kitagawa, T.; Funahashi, Y.; Ozawa, T.; Jitsukawa, K.; Masuda, H. Synthesis, Characterization, and Thermal Stability of New Mononuclear Hydrogenperoxocopper(II) Complexes with N3O-Type Tripodal Ligands Bearing Hydrogen-Bonding Interaction Sites. *Bull. Chem. Soc. Jpn.* **2005**, *78*, 116–124, doi:10.1246/bcsj.78.116.

100. Yamaguchi, S.; Masuda, H. Basic Approach to Development of Environment-Friendly Oxidation Catalyst Materials. Mononuclear Hydroperoxo Copper(II) Complexes. *Sci. Technol. Adv. Mater.* **2005**, *6*, 34, doi:10.1016/j.stam.2004.06.004.

101. Gherman, B.F.; Tolman, W.B.; Cramer, C.J. Characterization of the structure and reactivity of monocopper–oxygen complexes supported by β-diketiminate and anilido-imine ligands. *J. Comput. Chem.* **2006**, *27*, 1950–1961, doi:10.1002/jcc.20502.

102. Hong, S.; Huber, S.M.; Gagliardi, L.; Cramer, C.C.; Tolman, W.B. Copper(I)−α-Ketocarboxylate Complexes: Characterization and O2 Reactions That Yield Copper−Oxygen Intermediates Capable of Hydroxylating Arenes. *J. Am. Chem. Soc.* **2007**, *129*, 14190–14192, doi:10.1021/ja0760426.

103. Caraiman, D.; Bohme, D.K. Periodic Trends in Reactions of Benzene Clusters of Transition Metal Cations, M(C6H6)1,2+ with O2. *J. Phys. Chem. A* **2002**, *106*, 9705–9717, doi:10.1021/jp0208900.

104. Koyanagi, G.K.; Caraiman, D.; Blagojevic, V.; Bohme, D.K. Gas-Phase Reactions of Transition-Metal Ions with Molecular Oxygen: Room-Temperature Kinetics and Periodicities in Reactivity. *J. Phys. Chem. A* **2002**, *106*, 4581–4590, doi:10.1021/jp014145j.

105. Molina-Svendsen, H.; Bojesen, G.; McKenzie, C.J. Gas-Phase Reactivity of Coordinatively Unsaturated Transition Metal Complex Ions toward Molecular Oxygen. *Inorg. Chem.* **1998**, *37*, 1981–1983, doi:10.1021/ic970345r.

106. Schroeder, D.; Fiedler, A.; Schwarz, J.; Schwarz, H. Generation and Characterization of the Anionic, Neutral, and Cationic Iron-Dioxygen Adducts [FeO2] in the Gas Phase. *Inorg. Chem.* **1994**, *33*, 5094–5100, doi:10.1021/ic00100a039.

107. Xia, Y.; Chrisman, P.A.; Pitteri, S.J.; Erickson, D.E.; McLuckey, S.A. Ion/Molecule Reactions of Cation Radicals Formed from Protonated Polypeptides via Gas-Phase Ion/Ion Electron Transfer. *J. Am. Chem. Soc.* **2006**, *128*, 11792–11798, doi:10.1021/ja063248i.

108. Donnelly, J.M.; Lermyte, F.; Wolny, J.A.; Walker, M.; Breeze, B.G.; Needham, R.J.; Müller, C.S.; O'Connor, P.B.; Schünemann, V.; Collingwood, J.F.; et al. Cu(III)–Bis-Thiolato Complex Forms an Unusual Mono-Thiolato Cu(III)–Peroxido Adduct. *Chem. Commun.* **2021**, *57*, 69–72, doi:10.1039/D0CC06921C.

109. Reynolds, A.M.; Gherman, B.F.; Cramer, C.J.; Tolman, W.B. Characterization of a 1:1 Cu−O2 Adduct Supported by an Anilido Imine Ligand. *Inorg. Chem.* **2005**, *44*, 6989–6997, doi:10.1021/ic050280p.

110. Fisher, E.R.; Elkind, J.L.; Clemmer, D.E.; Georgiadis, R.; Loh, S.K.; Aristov, N.; Sunderlin, L.S.; Armentrout, P.B. Reactions of Fourth-period Metal Ions (Ca+−Zn+) with O2: Metal-oxide Ion Bond Energies. *J. Chem. Phys.* **1990**, *93*, 2676–2691, doi:10.1063/1.458906.

111. Srnec, M.; Navrátil, R.; Andris, E.; Jašík, J.; Roithová, J. Experimentally Calibrated Analysis of the Electronic Structure of CuO+: Implications for Reactivity. *Angew. Chem. Int. Ed.* **2018**, *57*, 17053–17057, doi:10.1002/anie.201811362.

112. Meunier, B. *Metal-Oxo and Metal-Peroxo Species in Catalytic Oxidations*; Springer, 2003; ISBN 978-3-540-46592-8.

113. Shiota, Y.; Yoshizawa, K. Methane-to-Methanol Conversion by First-Row Transition-Metal Oxide Ions: ScO+, TiO+, VO+, CrO+, MnO+, FeO+, CoO+, NiO+ and CuO+. *J. Am. Chem. Soc.* **2000**, *122*, 12317–12326, doi:10.1021/ja0017965.

114. Fiedler, A.; Schroeder, D.; Shaik, S.; Schwarz, H. Electronic Structures and Gas-Phase Reactivities of Cationic Late-Transition-Metal Oxides. *J. Am. Chem. Soc.* **1994**, *116*, 10734–10741, doi:10.1021/ja00102a043.

115. Clemmer, D.E.; Aristov, N.; Armentrout, P.B. Reactions of ScO+, TiO+, and VO+ with D2: M+-OH Bond Energies and Effects of Spin Conservation. *Phys. Inorg. Chem.* **1993**, *24*, doi:10.1002/chin.199316003.

116. Schröder, D.; Holthausen, M.C.; Schwarz, H. Radical-Like Activation of Alkanes by the Ligated Copper Oxide Cation (Phenanthroline)CuO+. *J. Phys. Chem. B* **2004**, *108*, 14407–14416, doi:10.1021/jp0496452.

117. Shaffer, C.J.; Schröder, D.; Gütz, C.; Lützen, A. Intramolecular C-H Bond Activation through a Flexible Ester Linkage. *Angew. Chem. Int. Ed.* **2012**, *51*, 8097–8100, doi:10.1002/anie.201203163.

118. Siebert, X.; Eipper, B.A.; Mains, R.E.; Prigge, S.T.; Blackburn, N.J.; Amzel, L.M. The Catalytic Copper of Peptidylglycine α-Hydroxylating Monooxygenase Also Plays a Critical Structural Role. *Biophys. J.* **2005**, *89*, 3312–3319, doi:10.1529/biophysj.105.066100.

119. Safaei, E.; Bahrami, H.; Pevec, A.; Kozlevčar, B.; Jagličić, Z. Copper(II) Complex of New Non-Innocent O-Aminophenol-Based Ligand as Biomimetic Model for Galactose Oxidase Enzyme in Aerobic Oxidation of Alcohols. *J. Mol. Struct.* **2017**, *1133*, 526–533, doi:10.1016/j.molstruc.2016.11.076.

120. Wilce, M.C.; Dooley, D.M.; Freeman, H.C.; Guss, J.M.; Matsunami, H.; McIntire, W.S.; Ruggiero, C.E.; Tanizawa, K.; Yamaguchi, H. Crystal Structures of the Copper-Containing Amine Oxidase from Arthrobacter Globiformis in the Holo and Apo Forms: Implications for the Biogenesis of Topaquinone. *Biochemistry* **1997**, *36*, 16116–16133, doi:10.1021/bi971797i.

121. Koyanagi, G.K.; Baranov, V.I.; Tanner, S.D.; Bohme, D.K. An Inductively Coupled Plasma/Selected-Ion Flow Tube Mass Spectrometric Study of the Chemical Resolution of Isobaric Interferences. *J. Anal. At. Spectrom.* **2000**, *15*, 1207–1210, doi:10.1039/B000989J.

122. Lewis, E.A.; Tolman, W.B. Reactivity of Dioxygen−Copper Systems. *Chem. Rev.* **2004**, *104*, 1047–1076, doi:10.1021/cr020633r.

123. Solomon, E.I.; Heppner, D.E.; Johnston, E.M.; Ginsbach, J.W.; Cirera, J.; Qayyum, M.; Kieber-Emmons, M.T.; Kjaergaard, C.H.; Hadt, R.G.; Tian, L. Copper Active Sites in Biology. *Chem. Rev.* **2014**, *114*, 3659–3853, doi:10.1021/cr400327t.

124. Frandsen, K.E.H.; Simmons, T.J.; Dupree, P.; Poulsen, J.-C.N.; Hemsworth, G.R.; Ciano, L.; Johnston, E.M.; Tovborg, M.; Johansen, K.S.; von Freiesleben, P.; et al. The Molecular Basis of Polysaccharide Cleavage by Lytic Polysaccharide Monooxygenases. *Nat. Chem. Biol.* **2016**, *12*, 298–303, doi:10.1038/nchembio.2029.

125. Yoshizawa, K.; Kihara, N.; Kamachi, T.; Shiota, Y. Catalytic Mechanism of Dopamine β-Monooxygenase Mediated by Cu(III)−Oxo. *Inorg. Chem.* **2006**, *45*, 3034–3041, doi:10.1021/ic0521168.

126. McEvoy, A.; Creutzberg, J.; Singh, R.K.; Bjerrum, M.J.; Hedegård, E.D. The Role of the Active Site Tyrosine in the Mechanism of Lytic Polysaccharide Monooxygenase. *Chem. Sci.* **2021**, *12*, 352–362, doi:10.1039/D0SC05262K.

127. Kumar, V.; Dooley, D.M.; Freeman, H.C.; Guss, J.M.; Harvey, I.; McGuirl, M.A.; Wilce, M.C.; Zubak, V.M. Crystal Structure of a Eukaryotic (Pea Seedling) Copper-Containing Amine Oxidase at 2.2 å Resolution. *Structure* **1996**, *4*, 943–955, doi:10.1016/S0969-2126(96)00101-3.

128. Kim, M.; Okajima, T.; Kishishita, S.; Yoshimura, M.; Kawamori, A.; Tanizawa, K.; Yamaguchi, H. X-Ray Snapshots of Quinone Cofactor Biogenesis in Bacterial Copper Amine Oxidase. *Nat. Struct. Biol.* **2002**, *9*, 591–596, doi:10.1038/nsb824.

129. McCann, S.D.; Stahl, S.S. Copper-Catalyzed Aerobic Oxidations of Organic Molecules: Pathways for Two-Electron Oxidation with a Four-Electron Oxidant and a One-Electron Redox-Active Catalyst. *Acc. Chem. Res.* **2015**, *48*, 1756–1766, doi:10.1021/acs.accounts.5b00060.

130. Wendt, F.; Rolff, M.; Thimm, W.; Näther, C.; Tuczek, F. A Small-Molecule Model System of Galactose Oxidase: Geometry, Reactivity, and Electronic Structure. *Z. Für Anorg. Allg. Chem.* **2013**, *639*, 2502–2509, doi:10.1002/zaac.201300475.

131. (a) Bank, R.P.D. RCSB PDB: Homepage Available online: https://www.rcsb.org/ (accessed on 17 September 2021). (b) Sehnal D., Bittrich S., Deshpande M., Svobodová R., Berka K., Bazgier V., Velankar S., Burley S.K., Koča J., Rose A.S. Mol* Viewer: modern web app for 3D visualization and analysis of large biomolecular structures, *Nucleic Acids Res*. **2021**, *49*, W431-W437.

132. Klinman, J.P. The Copper-Enzyme Family of Dopamine β-Monooxygenase and Peptidylglycine α-Hydroxylating Monooxygenase: Resolving the Chemical Pathway for Substrate Hydroxylation. *J. Biol. Chem.* **2006**, *281*, 3013–3016, doi:10.1074/jbc.R500011200.

133. Halfen, J.A.; Jazdzewski, B.A.; Mahapatra, S.; Berreau, L.M.; Wilkinson, E.C.; Que, L.; Tolman, W.B. Synthetic Models of the Inactive Copper(II)−Tyrosinate and Active Copper(II)−Tyrosyl Radical Forms of Galactose and Glyoxal Oxidases. *J. Am. Chem. Soc.* **1997**, *119*, 8217–8227, doi:10.1021/ja9700663.

134. Hoover, J.M.; Ryland, B.L.; Stahl, S.S. Mechanism of Copper(I)/TEMPO-Catalyzed Aerobic Alcohol Oxidation. *J. Am. Chem. Soc.* **2013**, *135*, 2357–2367, doi:10.1021/ja3117203.

135. Messerschmidt, A. 8.14 - Copper Metalloenzymes. In *Comprehensive Natural Products II*; Liu, H.-W. (Ben), Mander, L., Eds.; Elsevier: Oxford, 2010; pp. 489–545 ISBN 978-0-08-045382-8.

Chapter 2

A Model Reaction for the Understanding of Enzymatic Mechanisms – The Oxidation of Toluene by CuO_2^+

Introduction

Since the 1980s and 1990s, certain copper enzymes have been in the limelight. Their efficiency and their specificity in oxidizing substrates with medium to strong C-H bonds have attracted much attention. Nowadays, the oxidation of strong C-H, C-C or O-H bonds is still an important challenge to produce sustainable fuels. Their mechanisms were partly elucidated at that time. Setting up a production of fuels on the sole basis of the production of enzymes remains difficult due to their limited operating conditions. Thus, models have been set up, reproducing the structure of the Cu_nO_2 active sites at the heart of enzymes. In the liquid phase, biomimetic mono-, di- or trinuclear Cu^+-based complexes are well-known to activate O_2 and to achieve the oxidation of such C-C or C-H bonds[1,2]. Specifically, mononuclear CuO_2 species have been proven to participate in enzymatic oxidations, in the mechanisms of PHM/DβM[3,4], quercetinase[5], galactose and amine oxidases[6], superoxide dismutase[7]... CuO_2^+ core is a usual pattern in the copper enzyme chemistry: in many enzymatic mechanisms, the first step is the co-activation of O_2 and of the $Cu^{(I)}$ resting state. The O_2 coordination has several characteristics: the bonding-type, the overall spin state (singlet or triplet) and the degree of electron transfer from $Cu^{(I)}$ to O_2. The stability and the reactivity of CuO_2 core is set by the environment of the active site, which means that in biomimetic models, the characteristics of CuO_2 are mainly governed by the ligands. Crystallographic studies, completed by modelization, have shown that the bonding-type of O2 (end-on or side-on) depends on the coordination sphere, on the orbital arrangement and on the bulk of the ligand[8]. The character of CuO_2 bonding depends on the electron richness of the ligand. The more electron-donating the ligand is, the stronger the electron transfer from Cu to O_2. CuO_2^+ can take on three extreme cases: $Cu^{(I)}$-O_2, $Cu^{(II)}$-$O_2^{\bullet-}$ and $Cu^{(III)}$-O_2^{2-}. $Cu^{(I)}$-O_2 may lead to an end-on coordination in the triplet spin state, due to the triplet character of O_2,while $Cu^{(II)}$-$O_2^{\bullet-}$ can be either triplet or singlet, with side-on or end-on coordination type. $Cu^{(III)}$-O_2^{2-} is observed with side-on coordination, in the singlet state[9]. Concerning the spin state of mononuclear CuO_2 within enzymes, despite some experimental methods[10,11], it is difficult to obtain information, due to the reactivity of such adduct. The main considerations on spin state are essentially based on reliable theoretical considerations[12–15]. In the absence of ligand, the main character of CuO_2^+ is $Cu^{(I)}$-dioxygen, with an end-on coordination[16,17]. Bare Cu^+ poorly activates O_2, but the adduct is enough stable to be observed in the gas phase[18]. In that study, Cu^+ was generated in the gas phase via an Inductively Coupled Plasma (ICP) torch. Then, ions were conducted in a SIFT (Selected-Ion Flow Tube)

apparatus, in which they are cooled down by collisions with He to a temperature of 295 K. Introduction of O_2 in the flow tube leads to the formation of CuO_2^+ ions, with a low rate coefficient ($2.4 \cdot 10^{-13}$ $cm^3.molecule^{-1}.s^{-1}$). With the same ICP-SIFT apparatus, the oxidation of benzene C-H bonds (BDE = 472 ± 3 $kJ.mol^{-1}$[19]) was only observed with other transition metal cations[20]. CuO_2^+ does not have any kind of influence on such a strong CH bond and no subsequent reaction has been observed. However, the reactivity of CuO_2^+ has not been tested towards weaker CH bonds in the gas phase.

In this chapter is presented a new approach for biomimetism, based on a mechanistic point of view. The main idea is to establish a model mechanism, which would put together the reactants (the oxidant O_2, a substrate and a metal center) and to compare it with well-informed, although not necessarily complete reaction mechanisms. The objective is to identify the intermediates of the model mechanism and compare them with the structures proposed in the enzymes/synthetic catalysts, to obtain clues on the role of ligands to favor an intermediate, to lower energy barriers... The different influences of metal center, ligand, substrate, counter-ion and solvent form a real network, in which the different factors influence each other. We propose here to separate these different influences:

— by first removing the solvent and counter-ions, working in the gas phase;

— by removing the ligand, which allows us to know the intrinsic properties of the metal center and of the CuO_2 adduct, and by comparison, to understand the role of the ligand;

— by choosing a coordinating substrate (but weak donor), difficult to oxidize.

In the present chapter, we are studying the possibility for bare CuO_2^+ to oxidize toluene, which is undoubtedly one of the most challenging substrates to oxidize in spite of a lower BDE of the methyl CH bond that amounts to 375 ± 3 $kJ.mol^{-1}$[19]). Some catalysts have been designed on that purpose, for example metal-enriched[21] or metal-free[22] mesoporous surfaces, metals[23], metal oxides[24–26] or molecular catalysts[1,27] in combination with molecular oxygen or H_2O_2 as oxidant. However, the intrinsic role of Cu center in enzymes was never completely described. Bare $Cu^{(I)}$ is not able to properly activate O_2. In an attempt to rationalize the role of Cu^+ in the oxidation of various substrates, we studied the model system of bare $Cu^{(I)}$ with O_2 and the details of the putative oxidation mechanism of toluene. In particular, the oxidation of substrate goes through the use of electron-donating ligands that increase the electron transfer between $Cu^{(I)}$ and O_2. Bare Cu^+ is

the simplest model that can be studied to mimic the active site of cuproenzymes. The two-electron oxidation is preponderant in enzymes, from CH to OH bond, or from primary (and secondary) alcohols to aldehydes (ketones). As a consequence, our model mechanism covers both of these ranges from CH bond of toluene to CO bond of benzaldehyde, via a four-electron oxidation. The idea, beyond knowing whether this reaction is possible or not, is also to show the influence of ligand and of Cu in the enzymatic mechanisms. A comparison is made between the proposed model mechanism to the mechanisms of cuproenzymes throughout the reaction, to reveal common points and divergences. The studies on enzymatic mechanisms reveal a sequence of steps, which is more or less the same with different mononuclear enzymes. The first step is the coordination of O_2 on the $Cu^{(II)}$ center. It is followed by the abstraction of a H atom in its environment. The third step is the decomposition of the resulting Cu-hydroperoxo species, either into an oxidative CuO^+ species or by the loss of H_2O_2. The final step corresponds to the oxidation of the substrate.

The computed mechanism of toluene oxidation is first structurally described. Emphasis is on similarities/differences with biomimetic catalysts and enzymes. Follow then energetic aspects, comparison with different levels of theory and shedding light on the switching from triplet-to-singlet spin states (two-state reactivity). Our efforts to find a crossing point between spin surfaces are briefly described. Molecular orbitals (MO) and Fukui functions, atomic charges (Bader) and bond critical points (BCP) are then presented to discuss the very nature of interactions between the copper metal center and the reactants and to investigate the nature of intermediates.

1. Methods

DFT calculations were carried out with the help of Gaussian16 suite of programs[28]. Gaussview 3[29] and Chemcraft trial version[30] were used as visualization tools. Energy minimized geometries were obtained at the B3LYP/6-31+G(d,p) level of theory and all structural data in the following discussion will refer to it. The B3LYP[31] (hybrid GGA), CAM-B3LYP[32], ωB97, ωB97X[33], ωB97X-D[34] (range-separated hybrid GGA), PW6B95[35], M05[36], M06[37], τ-HCTHhyb[38] (hybrid meta-GGA), M06-L[39] (local meta-GGA), MN15[40] and MN15-L[41](hybrid meta-NGA) functionals were used. They are recommended for their good performances to predict barrier heights. Energetic data are given in terms of electronic energy corrected with ZPE. Bader charges were calculated with the Henkelman's code[42] using the Bader definition of the charge. This code was run on Gaussian cube files, generated with cubegen program (included in Gaussian16), with a medium grid (6 points/Bohr) on parallelepipedic simulation boxes (adapted for each structure). The analysis of bonding was carried out with the help of one scalar field, ρc, the electronic density. The relevant information from these fields is extracted with the gradient of the respective scalar field. The electron density envelopes the molecules and the topological analysis of specific point of this envelope is very relevant. In between atoms when a chemical bond is engaged, one can find a Bond Critical Point (BCP)[43]. This BCP is the point where the gradient of ρ_c cancels and it is characterized by a minimum in the direction of the bond and two maxima in the perpendicular directions. At this point, one can extract the value of the electronic density, the energetic contribution and the laplacian of the density at this point. With these three features, the nature of the chemical bond can be identified. Unless necessary we will only use the value of the density at the critical point or selected bonds that are formed or broken during the reaction pathway. The analysis was performed with the help of DGrid5.1 software[44]. Fukui functions, that provide information on reactive sites, have been previously defined in the literature[45]. f^+ and f^- are related to the reactivity towards nucleophiles and electrophiles, respectively. They are calculated as the difference between $\rho_{N+1}(r)$ and $\rho_N(r)$, or between $\rho_N(r)$ and $\rho_{N-1}(r)$, respectively, where ρ is the electronic density and N the number of electrons of the considered species. $\rho_{N+1}(r)$ and $\rho_{N-1}(r)$ are calculated with single-point calculations, within the geometry of the considered species.

2. Results and discussion

2.1. Formation of the reactant complex

Starting from the bare Cu^+ ion, it is possible to coordinate first the toluene or O_2. The stabilization energy of $[Cu(toluene)]^+$ is -258 kJ.mol^{-1}. This high bonding energy between Cu^+ and toluene is explained by the short distance between Cu and the cycle (2.10 Å with B3LYP, with other functionals: min 2.10, max 2.26), due to the interaction between the π orbitals of the cycle and the Cu d orbitals. CuC_{cycle} bond lengths are longer when Cu is centered on the cycle. The stabilization energy of $[Cu(toluene)]^+$ complex is consistent with the $[Cu(benzene)]^+$ bonding energy (209 kJ.mol^{-1}[46]). The bonding energy of O_2 in the triplet spin state on Cu^+ has been calculated to be -74 kJ.mol^{-1}. The triplet-to-singlet gap is evaluated to be 125 kJ.mol^{-1}. According the literature on the simple CuO_2^+ structure, the singlet spin state is also higher in energy (about 101 kJ.mol^{-1}, on the basis of CR-CC(2,3) high level of theory[16]). The coordination of triplet dioxygen on $[Cu(toluene)]^+$ ion is exothermic by about 66 kJ.mol^{-1}. Although the toluene-Cu interaction strongly stabilizes the complex, it does not change so much the CuO_2 bonding energy. Triplet spin state might be naturally considered at the starting spin state of the mechanism, taking into account the triplet ground-state of dioxygen. The end-on coordination of O_2 on $[Cu(toluene)]^+$ in the triplet state was found to be 112 kJ.mol^{-1} more stable than the side-on coordination and 104 kJ.mol^{-1} more stable than reactants in the singlet state (side-on). These values are in accordance with the literature on free CuO_2^+[16]. The O-O distance remains close to that of the free O_2 in triplet state (1.215 Å against 1.224 Å in the complex). This is reminiscent of the mechanism of PHM/DβM enzyme proposed by J. Klinman and co-workers[47] and confirmed by crystallographic study[3], in which the first step corresponds to the formation of a pre-catalytic $Cu^{(I)}$-O_2 adduct. Here, O_2 is badly activated by bare Cu^+ or by $[Cu(toluene)]^+$. Only 5 % of the triplet spin density (Mulliken) lays on Cu, which is consistent with the low electron transfer rate between Cu and O_2. $Cu^{(I)}$-O_2 character is obtained in both cases, as confirmed by charge calculations (see p.107). The singly occupied orbitals of O_2 are in low occupied orbitals, so they are not easily available to react. The TS 1 barrier height is then expected to be high and the influence of Cu to be weak. However, in the enzymatic mechanisms, $Cu^{(I)}$-O_2 pre-catalytic complex is then activated in a $Cu^{(II)}$-superoxo species, which is the reactive species able to abstract a hydrogen atom in its environment.

2.2. First step: abstraction of a hydrogen atom on the methyl group

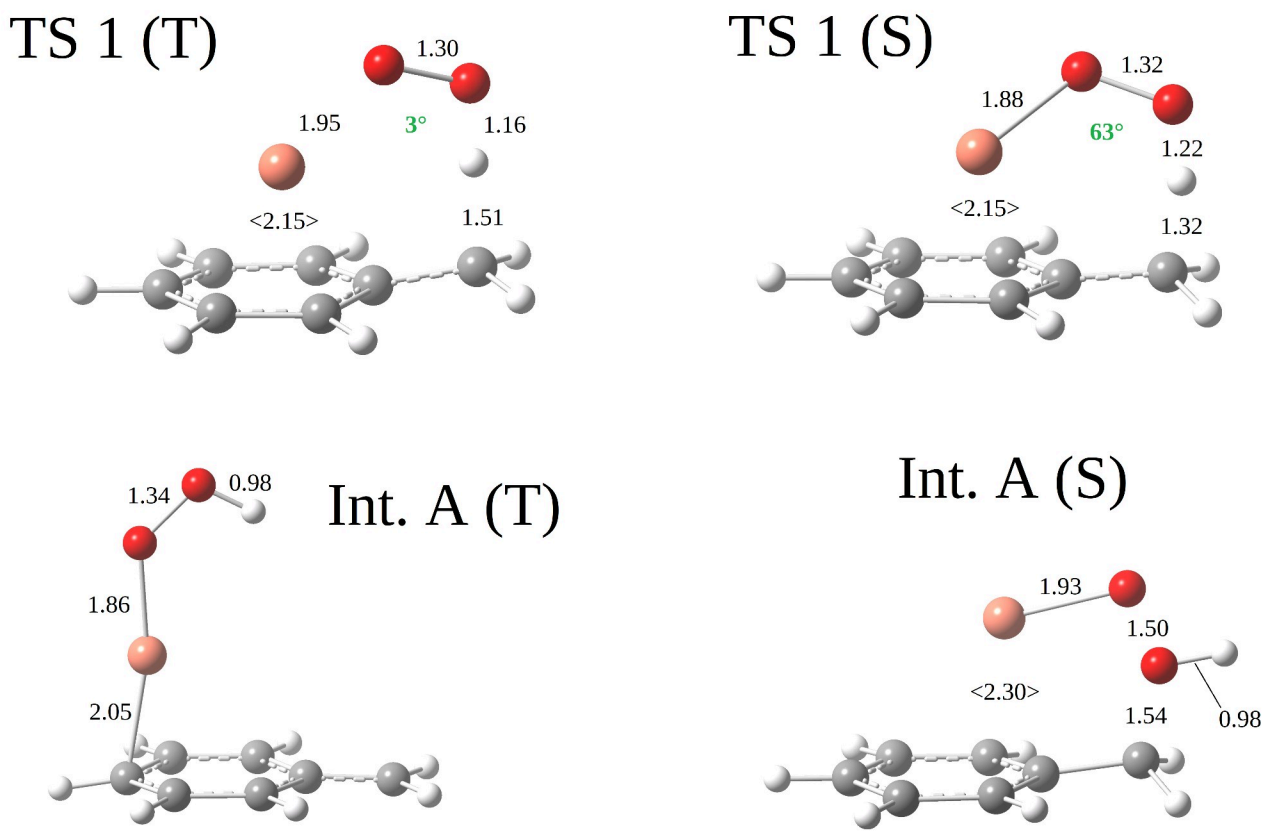

Figure 1: Singlet and triplet geometries of TS 1, which corresponds to the abstraction of a H atom on the methyl group and of Int. A, obtained by following the corresponding IRC. All distances are given in Å. Values between <> are mean values between Cu and the two closer C atoms. C: grey, O: red, H: white, Cu: orange, CuOOH dihedral angles (in °) are indicated in bold green. S and T stand for singlet and triplet, respectively.

With ligands, the reactivity of Cu-O_2 systems has been debated for a long time. After coordination of O_2, the following step corresponds to the abstraction of a hydrogen atom in the environment of the active site, either on a substrate (DβM), or on a close amino-acid (galactose oxidase). Many hypothesis were formulated about the abstracting species: CuO_2^+ (with a $Cu^{(II)}$-$O_2^{\bullet-}$ character[47,48]) and CuO_2H^{2+}[49] have been proposed. The abstraction of a hydrogen atom leads to a $Cu^{(II)}$-hydroperoxo intermediate. Cu-hydroperoxo species is very usual in a lot of mechanisms of cuproenzymes and generally reacts with the environment, leading to the formation of CuO^+ intermediates. MO^+ catalysts, and especially CuO^+, are well-known to be strong oxidants, able to oxidize methane to methanol[25,50]. $Cu^{(II)}$-oxyl is often proposed as intermediate in the mechanism

of DβM/PHM[48], pMMO[51] and LPMO[52]. CuO^+ is sometimes proposed as the oxidative (and H abstracting) species on the substrate[53].

In our case, the hydrogen atoms the most likely to undergo a chemical reaction are the atoms of the methyl group, because of their lower bond dissociation energy[54]. Bringing closer the terminal oxygen atom and the methyl group and looking for a TS in triplet state leads to the TS 1 (T) geometry (Figure 1 and 2 for the imaginary frequency mode). Oxygen atoms are named p (proximal, bound to Cu throughout the reaction) and d (distal). The first hydrogen to be transferred is H8, while the second is H7. The TS 1 (T) energy barrier is 129 $kJ.mol^{-1}$, which may be due to the low reactivity of O_2 (poorly activated) and the strength of toluene CH bond. Mulliken spin density of TS 1 (T) clearly shows that the triplet spin state is partly delocalized (25.1 %) on the carbon atom of the methyl group. In our case, O_2 is not electron-rich enough to have a superoxide character, which is expected to lead to an increase in reactivity compared to $Cu^{(I)}$-O_2 or $Cu^{(III)}$-O_2^{2-} species[55,56]. A similar geometry, namely TS 1 (S), however with a distorted CuOOH dihedral angle (63° - min: 58°, max: 75° - in place of 3° - min: 0°, max: 4° - for the triplet state), was obtained in the singlet state with a somewhat higher energy (151 $kJ.mol^{-1}$). Its structure is presented in Figure 1 and its imaginary frequency mode in Figure 2. Both singlet and triplet cases recalls the expected reactivity for such an end-on superoxo structure[47], even though there is no ligand on Cu. Stable structures bracketing each TS found were obtained by following the intrinsic Reaction Coordinates (IRC)[57] both in forward and reverse directions. The IRC from TS 1 (T) leads to Int. A (T) (see Figure 1), which can be identified as a Cu-hydroperoxo species, with the spin state concentrated on both C (0.75) and CuOOH (1.27) moieties. The OO distance is 1.34 Å in Int. A (T), which is consistent with a superoxide character[58]. Without ligand(s), Cu-hydroperoxo is not stable (Cu is not electron-rich enough to stabilize it) in the triplet spin state (destabilized by more than 100 $kJ.mol^{-1}$ compared to the starting reactant complex). Indeed, it is necessary to activate O_2 properly to stabilize also the following Cu-hydroperoxo species.

Concerning the singlet spin state, following the IRC revealed the insertion of one oxygen atom in the CH bond in four steps:

— shortening of the OH bond (formation of a covalent OH bond);

— rotation around the OO bond introducing the distal oxygen atom O_d in CH bond (the remaining Ph-CH_2 adopting a planar conformation);

— CO bond formation (with the shortening of the CO distance);

— smooth rotation around CC bond (reorganization).

This surprising pathway was observed whatever the functional used. The rotation around the OO bond might be explained by the fact that the single electron of CH_2 radical must be paired. Thus, Int. A (S) is not a biradical species (the wave function was found to be stable), and the formation of the CO bond is necessary to remain on the singlet surface. The singlet intermediate Int. A (S) is 47 kJ.mol^{-1} more stable in energy than the triplet Int. A (T) species.

It seems like Int. A (S) is a mix between two different intermediates, in the singlet spin state, with a global charge of + 1:

— a benzyl-alcohol like structure, in interaction with CuO. From TS 1 (S) to Int. A (S), the OO bond is elongated by 0.18 Å (min: 0.14, max: 0.19), which means that the bond is partially broken (see Bond Critical point analysis, p.107). The OO distance of Int. A (S) is 1.50 Å (min: 1.44, max: 1.51), close to the OO bond length of peroxide ion (1.49 Å) and much longer than the OO bond length of a hydroperoxide (1.32 Å in the free CuOOH structure). The π(CO) bonding orbital is low-lying and confirm the strong CO bonding.

— a Cu-hydroperoxo species, in interaction with $C_6H_5CH_2$. This form can be identified thanks to the long CuO bond (1.93 Å), which is close to the CuO bond length of the free Cu-hydroperoxo (1.91 Å). Moreover, the CO distance remains relatively long (1.54 Å – min: 1.51, max: 1.56 –, against 1.45 Å in alcohols). The OO bond is weakened, but do not cancel out, as revealed by the little π* orbital lobes on both O atoms. The total break of OO bond (departure of CuO^+) is strongly unfavorable: it was calculated to be 222 kJ.mol^{-1} higher than Int. A (S).

Strong π and d_{z^2}-p_z interactions are visible between Cu and $O_{p.}$ The considered MOs show the CuO bonding character and the stabilization of the global structure. CuO remains on the cycle because of the π electrons of the cycle are delocalized towards Cu.

The hydroxylation of a substrate is sometimes proposed to be done in two steps (abstraction of H atom on the substrate, followed by OH radical rebound, also called remigration[48]). In this no-ligand/solvent-free case, both seem to happen in the same step, on the singlet surface, by the remarkable rotation around the OO bond. Nevertheless, the OO is so strong that it is not possible to break directly. There is no equivalent of Int. A (S) structure in the literature, to our knowledge. Even

if CuO distance (1.93 Å) is much longer than the one of free CuO^+ (estimated: 1.76 Å[59]) and does not have a high charge (see Charge analysis, p.105), one can make the assumption that CuO moiety is able to react.

Since TS 1 (T) is more stable than TS 1 (S), and Int. A (S) is lower in energy than Int. A (T), we emit the hypothesis of a crossing between these two spin state surfaces (see Crossing spin state surfaces, p.102), without us being able to precisely localize it.

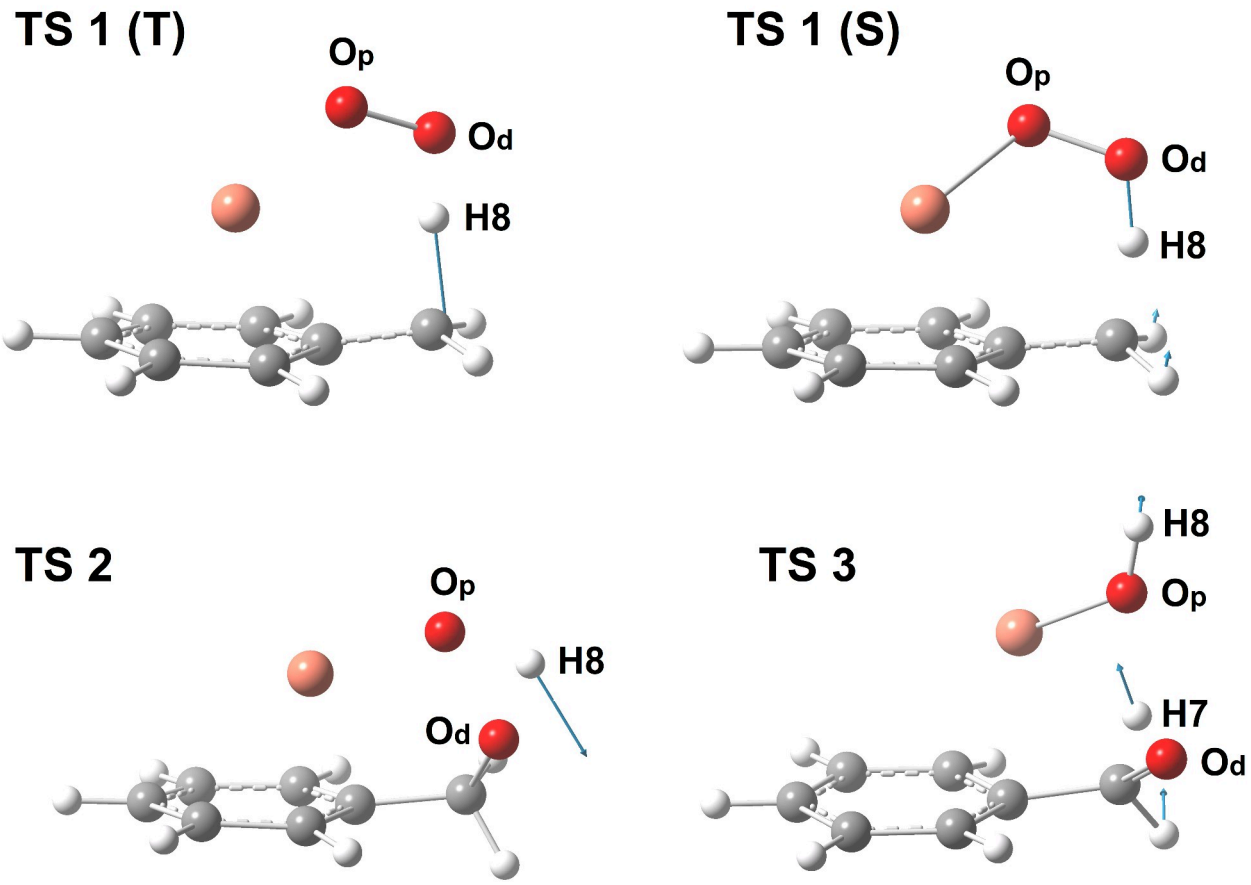

Figure 2: Imaginary frequency mode (indicated with the help of blue arrows) of TS 1 (T), TS 1 (S), TS 2 and TS 3, calculated at the B3LYP/6-31+G(d,p) level of theory. Cu: orange, C: grey, O: red, H: white. The direction and the lenght of the arrows depends on the forces on the considered atoms.

2.3. Second step: hydrogen transfer from one oxygen atom to the other

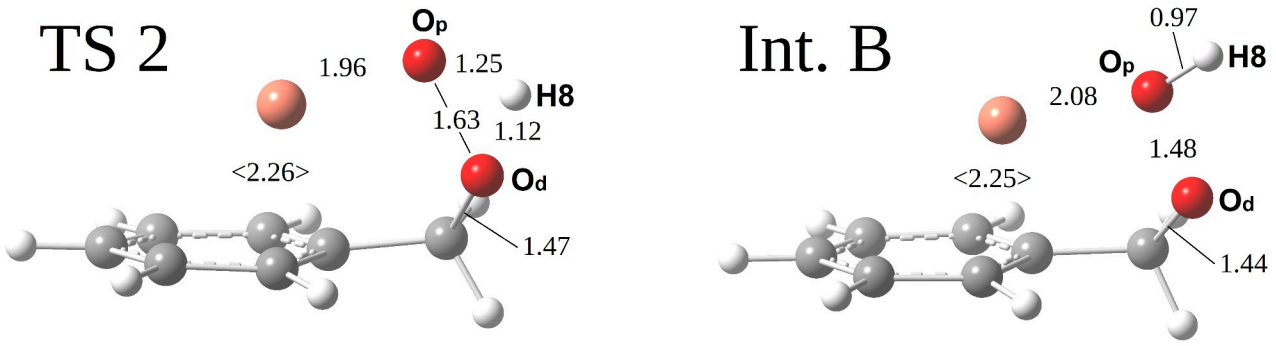

Figure 3: Singlet geometries of TS 2 and Int. B, obtained by following the IRC. All values are given in Å. Numbers with <> are mean distance values of Cu and the two closest C atoms. C: grey, O: red, H: white, Cu: orange.

For the molecular system in the triplet spin state studied herein, no structures were found leading from Int. A (T) to further reactivity (Cu-OOH and $PhCH_2$ radicals may react together to form Int. B). Therefore, only singlet state reactivity is discussed from this point. One can expect than the CuO moiety have still the ability to abstract a proton, or a hydrogen atom, from the O_dH hydroxyle group. The postulated TS 2 corresponds to the hydrogen transfer between the two oxygen atoms (Figure 3 and 2 for imaginary frequency mode). In other words, it may be seen as the insertion of O_p into the O_dH bond, or as a hydrogen transfer followed by OH remigration, like in the first step. The imaginary frequency mode of TS 2 explicitly exhibits the transfer of hydrogen atom. The energy barrier to reach TS 2 is 123 $kJ.mol^{-1}$ and the peroxide-like structure obtained after TS 2 is 95 $kJ.mol^{-1}$ more stable than Int. A (S). The IRC path from Int. A (S) to TS 2 shows an increase in the OO distance. It corresponds to the last part of the OH remigration. Although no shoulder is visible along the IRC path, there are two elementary steps, i.e. the transfer of the hydrogen atom which must be followed by the O_dO_p bond formation. The transfer of H leads to the strengthening of the CO bond. This reinforcement is visible thanks to the decrease of the length of the CO bond (which goes from 1.54 to 1.47 Å). The OO distance is decreased by 0.15 Å to reach 1.48 Å (min: 1.44, max: 1.50), which is close to the typical OO distance for peroxides (1.44 Å in methyl peroxide[60]). Thus, Int. B may be seen as a peroxide-like structure. A concerted process is taking place. The decrease in the length of the CO bond and, the increase in the OO bond strengthens the reactivity of the proximal oxygen, especially as the length of the CuO bond increases sharply. The expected reactivity for CuO^+ is the capture of two hydrogen, which leads to the formation of H_2O.

2.4. Third step: peroxide decomposition by a second hydrogen transfer

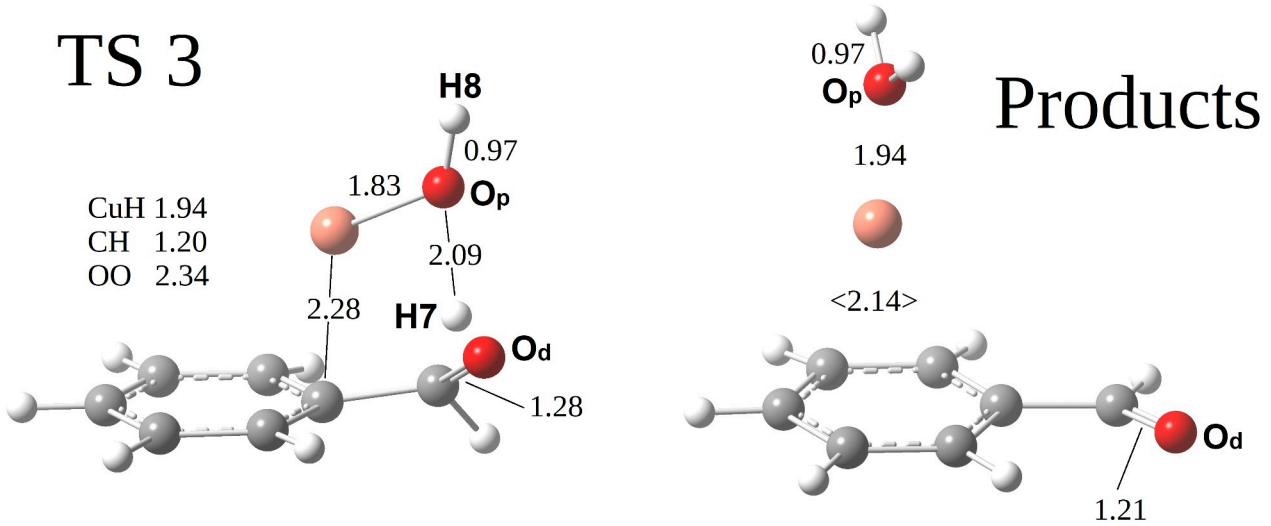

Figure 4: Singlet geometries of TS 3 and Products, obtained by IRC. All distances are given in Å. Values between <> are mean values between Cu and the two closer C atoms. C: grey, O: red, H: white, Cu: orange.

Analogously to other peroxides, benzylperoxide species may decompose. The expectation is the homolytic cleavage of OO bond, that leads to $OH^{\bullet}$ and to benzoyl radical. Thus, once OO breakage is engaged, a hydrogen atom is transferred from the carbon atom, in order to stay on the singlet spin surface. No reliable geometries were obtained in the triplet state, pushing aside the hypothesis of an other spin crossing. On TS 3 geometry (Figure 4 and Figure 2 for imaginary frequency mode), one can recognize CuOH and benzoyl radical moieties. After the TS, H atom is transferred from the C atom to the O_p atom, the whole process remaining on the singlet surface. The wave function found was tested for stability. The singlet spin state enforces the H atom transfer. The energy barrier was calculated to be 134 $kJ.mol^{-1}$. IRC calculation finds the Int. A (reverse direction) and leads directly to the product structure, without other TS. OO bond is first broken, and the OH group is stabilized by the decrease of the CuO bond length. After TS 3, the second H atom is transferred from the benzylperoxide to the OH ligand with the mediation of copper: Cu bond length decreases from 1.94 Å (min: 1.92, max: 2.21) to 1.64 Å and, with the stronger attraction of the oxygen atom, the hydrogen atom is captured in a concerted process. At least two of the considered MOs reveals a CuH interaction. Cu^{+} serves as a hook that grabs the second H before its capture by OH (which leads to H_2O formation). The formation of an oxidized product, PhCHO, is expected to strongly stabilize the global structure. Water is expected to have a low oxidizing power.

2.5. Comparison of methods on geometric criteria

Several DFT functionals have been compared in this study (B3LYP, CAM-B3LYP, ωB97, ωB97X, ωB97X-D, PW6B95, M05, M06, M06-L, τ-HCTHhyb, MN15 and MN15-L). The structures of reactant complex, intermediates and product complex are very similar with all functionals. The standard deviation is lower than 0.03 Å for all considered bond lengths, except for the CuO bond length in the reactant complex (0.05 Å). Thus, the bigger differences are concentrated on TS geometries. A dramatic divergence is observed at TS 2 step, with local functionals (M06-L and MN15-L). With these functionals, the CuO bond was calculated to be 1.73 and 1.74 Å, respectively, far from the 2.08 Å bond length obtained with B3LYP. On the other hand, the OO bond is elongated, to reach a bond length of 2.25 and 2.24 Å, respectively (1.63 Å with B3LYP). Moreover, IRC procedure led on these TS 2 were unsuccessful and did not lead to the expected intermediates. The distance between O_p and the second transferred hydrogen at TS 3 step is also overestimated with M06-L (2.42 Å) and MN15-L (2.38, against 2.09 Å with B3LYP). OO distances are also overestimated in respect to the other methods. The use of these local functionals influences also the energetic values (see Energetics, p.109). So, it seems important to include a part of HF exchange to get consistent geometries. As we have seen, the CuH interaction seems to be important in the evolution of the third step. ωB97 and ωB97X give a CuH distance of 2.21 and 2.04 Å (1.94 Å with B3LYP), which is out of the standard deviation interval. Moreover, they underestimate the OH bond length (as well as MN15). Here again, the energetic results obtained with these functionals have to be treated with caution. No other strong divergence were observed.

2.6. Influence of the add of ligands

Toluene was chosen because it has a cycle that can binds Cu, and bring together the substrate and the oxidant. It was also selected because of its strong CH bond, but weaker than the methane or benzene CH bond, which are too strong to be oxidized by CuO_2^+[20]. Toluene is a bulky substrate, that strongly binds Cu. Adding ligands on Cu would result in making the O_2 coordination more difficult. Obviously, some tests which are not detailed here had shown that O_2 coordination is jeopardized when toluene is used as substrate.

The add of ligands on Cu may have to important consequences on the first step. First, ligand(s) should reinforce the electronic density on Cu. Then, Cu^+ becomes more able to activate O_2, by improving the electron transfer between Cu and O_2. $Cu^{(II)}$-$O_2^{\bullet-}$ was found to be more reactive towards substrates than $Cu^{(I)}$-O_2[55,56]. The single-occupied orbital of superoxo ion is then high-lying and more likely to react with a substrate. So, the add of ligands may decrease the energy barrier needed for the first step, as proposed in the literature[13,48,53]. In other words, ligands decrease the OO bond order, improving its reactivity towards substrates. In our case, which may be seen as a H abstraction/OH remigration mechanism, the add of ligands on Cu would favor the break of the OO bond. Then, the $Cu^{(II)}$ is expected to favor the radical reactions within the catalytic system, because of its $4s^0$ $3d^9$ character. The second step of our model mechanism (the insertion of O_p in O_dH bond) is very unlikely to happen with ligands. In this no-ligand case, the CuO moiety interacts with the hydroxyle group O_dH, that gives it the possibility to react. Indeed, with ligands, the tendency is to break the OO bond. Moreover, as proposed by J. Roithova and co-workers[61], the add of ligands on CuO^+ stabilizes it (in the triplet spin state) by reinforcing the CuO bond (but decreasing its abstracting power).

On the other hand, the ligand(s) may have an influence on the spin state, by decreasing the gap between the two spin state surfaces or even by favoring TS 1 in the singlet state at the beginning of the reaction, mainly by orbital arrangement. The peroxylation of a substrate was never proposed to happen in the enzymatic mechanisms considered here. Thus, it is difficult to evaluate the role of ligands on Cu on the third step. However, its higher oxidation state and its congested environment (ligands, solvent molecules) should not allow the $Cu^{(II)}$ to help the transfer of hydrogen atoms/protons. So, the second and the third step are very specific of our model mechanism.

3. Energetics

3.1. Comparison between different DFT functionals

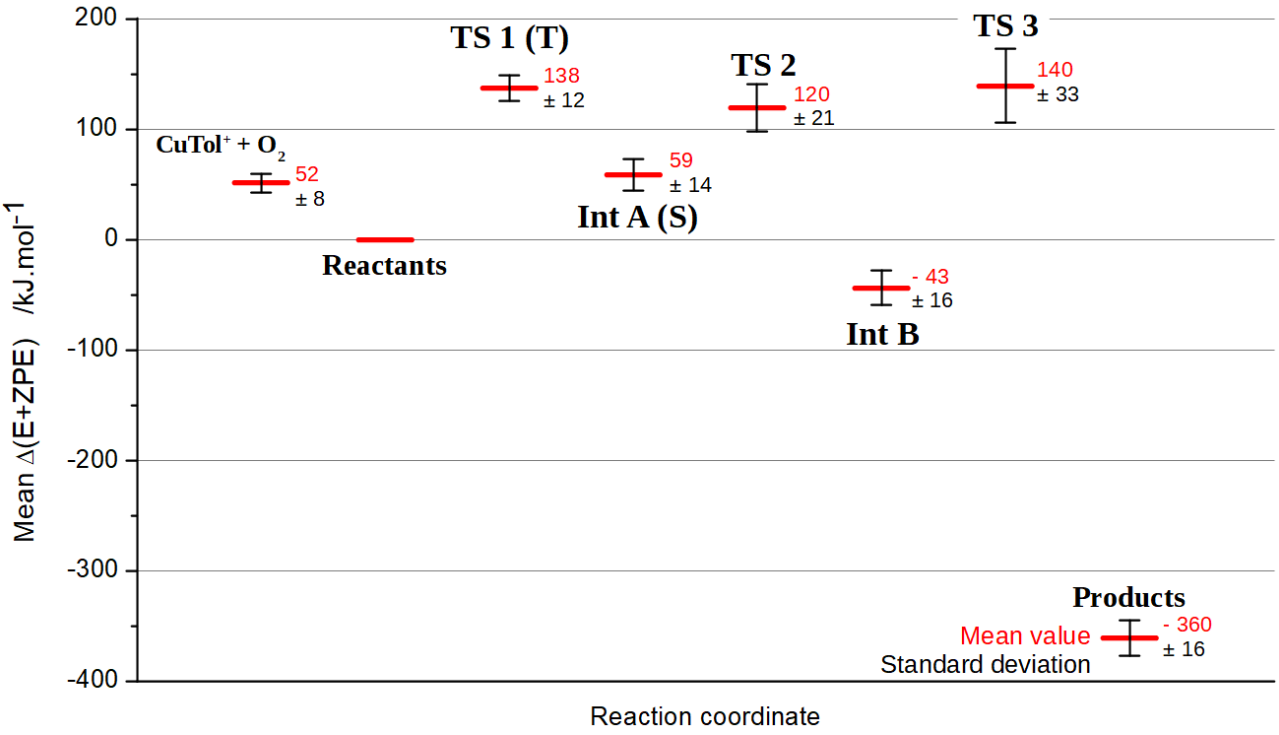

Figure 5: Scaled mean Δ(E+ZPE) energies of minimal energy pathway (in red), with relative errors (standard deviations, in black). The dashed line represents the crossing of spin state surfaces from triplet to singlet.

Figure 5 presents the calculated mean energies with all functionals for the minimal energy pathway. Full table of data is presented hereafter (p.98). The standard deviation varies between 8 kJ.mol^{-1} ($CuTol^+ + O_2$) and 33 kJ.mol^{-1} (TS 3). The latter is the witness of a difficult case. Nonetheless, some trends can be put in evidence. With all functionals, TS 1 (T) was found to be lower in energy than TS 1 (S) (excepted for MN15-L, that predicts the singlet spin state to be lower in energy for TS 1 – by about 35 kJ.mol^{-1} – which is surprising). The crossing of spin state surfaces is then expected to happen between TS 1 and Int. A. Despite the large amount of energy needed to transfer the first hydrogen atom, the first barrier is not the limiting step. Indeed, although TS 2 was calculated to be slightly lower in energy, TS 3 is higher than TS 1 (T) for most functionals. In addition, the reactions reactant complex → Int. B and Int. A → Int. B reactions are exothermic,

therefore stabilizing. The formation of benzaldehyde and water products is also hugely exothermic. As we have seen before, local functionals M06-L and MN15-L do not give consistent geometries with the rest of the functionals. Quite logically, they underestimate the energy barrier height of TS 2 and TS 3. Moreover, Int. A and Int. B are destabilized with M06-L as functional. B3LYP, that does not take well into account the dispersion forces, always underestimates the barrier heights, especially for long-range H atom transfers (TS 1 and TS 3). On the other hand, B3LYP seems to give consistent relative stability of reaction intermediates. M06 and MN15, that are highly parameterized functionals (the latter being a functional of choice for evaluating barrier heights[62]), apparently stabilize Int. A, TS 2 and Int. B from the mean energy pathway. MN15 predicts a barrier height of 144 $kJ.mol^{-1}$ for TS 3, which is consistent with the values obtained with PBE0, PW6B95 and M05. However, M06 gives a much lower energy (103 $kJ.mol^{-1}$). ωB97 and ωB97X functionals seem to strongly overestimate the energy of TS 1 (T) and TS 3, and are in the three higher values for TS 2. CAM-B3LYP and ω-B97X-D, whose definition takes into account long-range corrections, and to a lesser extent PW6B95 and PBE0, gave remarkably consistent results (compared to the other tested methods). B3LYP and τ-HCTHhyb are also in good agreement between them. The use of a bigger basis set (DGDZVP2, with add of p diffuse functions on O atoms) does not impact the conclusions made here. Extreme values are concentrated on the Minnesota and on the ωB97 and ωB97X functionals (Table 1). It is an additional argument to discard local functionals.

Functional	S. React.	TS 1 (T)	TS 1 (S)	Int. A (S)	TS 2	Int. B	TS 3	Prod.
B3LYP	51	128	151	55	123	-41	126	-358
M05	40	140	176	74	140	-35	143	-368
M06	51	125	149	32	101	-70	103	-395
M06-L	70	129	146	80	86	-14	91	-333
MN15	53	138	160	38	100	-74	144	-384
MN15-L	61	135	100	59	82	-47	94	-365
PBE0	46	133	169	65	132	-39	147	-347
PW6B95	44	141	177	67	132	-37	148	-356
CAM-B3LYP	48	139	185	50	124	-49	160	-366
τ-HCTH-hyb	56	124	141	57	121	-39	118	-349
ωB97	60	165	229	75	151	-28	203	-348
ωB97X	48	155	210	64	139	-40	183	-355
ωB97X-D	44	140	181	55	128	-49	158	-362
Mean	52	138	167	59	120	43	140	-360
Standard dev.	8	12	32	14	21	16	33	16

Table 1: Δ(E+ZPE) values of intermediates and TS (in kJ.mol^{-1}, relative to reactant complex) are indicated for the different functionals used in this study (in combination with the 6-31+G(d,p) level of theory). Higher and lower values of each column are highligthed in yellow and orange, respectively. The two last lines contain the mean energy value and the standard deviation for each intermediate/TS.

3.2. Influence of the basis set

Basis set	S. React.	TS 1 (T)	TS 1 (S)	Int. A (S)	TS 2	Int. B	TS 3	Prod.
BS1	51	128	151	55	123	-41	126	-358
BS1 - D3	54	118	140	46	114	-49	119	-364
BS2	40	130	157	54	120	-48	135	-360
BS2 - D3	43	120	146	46	111	-56	127	-365
BS3	49	130	155	58	129	-36	127	-357
Mean value	47	125	150	52	120	-46	127	-361
Standard dev.	6	6	7	5	7	8	6	4

Table 2: Δ(E+ZPE) values for each intermediate and TS (in kJ.mol^{-1}, in respect with Reactant complex) are indicated for the different basis sets used for comparison (in combination with the B3LYP functional). BS1 stands for 6-31+G(d,p) basis set, used in this study. BS2 stands for LANL2DZ pseudopotential on Cu, 6-31+G(d,p) basis set on all other atoms. BS3 stands for the extended def2QZVP (these energies were calculated with the 6-31+G(d,p) geometries). D3 stands for D3 version of Grimme's dispersion[67]. The two last lines contain the mean energy value and the standard deviation for each intermediate/TS.

The standard deviations vary between 4 and 8 kJ.mol^{-1}, which is much lower than the standard deviations observed with different functionals. It means that the choice of a good functional prevails on the choice of a basis set. Moreover, the energy differences are not significant with the different basis sets. The add of D3 Grimme's dispersion[67] tends to reduce barrier heights (by 7 ~ 10 kJ.mol^{-1}) and to stabilize intermediates (by 6 ~ 8 kJ.mol^{-1}). The use of pseudopotential on Cu is more difficult to analyze: TS 1 and TS 3 are heightened with pseudopotential, while TS 2 and Int. B are lowered. The use of a bigger basis set does not change so much the energy.

3.3. Influence of the toluene cycle

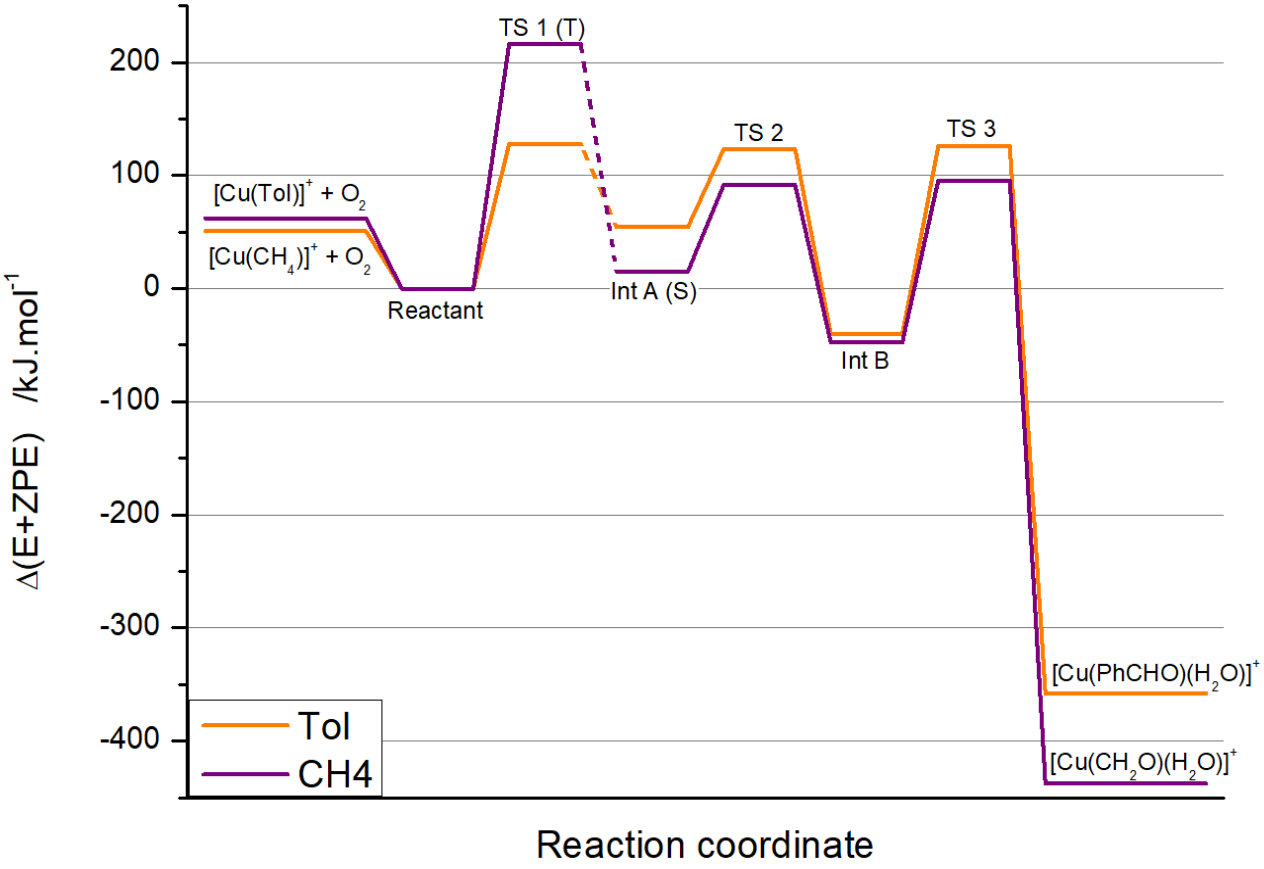

Figure 6: Optimized methane oxidation pathway, calculated at the B3LYP/6-31+G(d,p) level of theory. Tol stands for toluene, PhCHO for benzaldehyde.

Toluene was chosen for its lower CH bond dissociation energy than benzene or methane and for its ability to bind Cu^+ (or CuO_2^+). However, one can legitimately ask about the influence of the cycle as a ligand on the coordination of O_2, and then, on the different reaction steps. All initial guesses of geometries of the 'methane pathway' were postulated from their 'toluene pathway' analogous and were optimized at the B3LYP/6-31+G(d,p) level of theory, with the same spin state. IRC procedures were led on TS 1 (S), TS 2 and TS 3 and were able to find the products or the reactants of each TS. The coordination of O_2 is 11 kJ.mol^{-1} more favorable on $[Cu(CH_4)]^+$ than on $[Cu(toluene)]^+$. The first TS is much higher with CH_4, in respects to the strength of the CH bond of methane (432 kJ.mol^{-1}[66]). It seems like the cycle exerts a hold over Cu, and destabilizes the Int. A (S) structure (39 kJ.mol^{-1}/Int. A with CH_4). In the methane pathway, the Cu is not under the influence of the cycle: it is free to rotate. Cu is placed in an *anti* position and reduce steric

hindrance. Then, the cycle has only a low influence on TS 2 barrier. It favors (by about 8 kJ.mol^{-1} relative to Int. A) the H transfer from O_d to O_p. Cycle is not expected to act directly on this step. It is consistent with the fact that, from Int. A to TS 2, the O_pO_d bond is a little bit elongated, to permit the O_p insertion in the O_dH bond. So, the cycle smoothly stabilizes the CuO moiety during this step. Int. B is not influenced by the cycle, which means that Cu interacts mainly with O_p atom. The third step is also influenced by the presence of the cycle: the abstraction of a second H atom is 30 kJ.mol^{-1} harder with toluene than with methane. It does not grab the transferred hydrogen atom. So, the influence of the cycle is reduced all over the pathway. Cycle might be considered as a ligand that has low-influence.

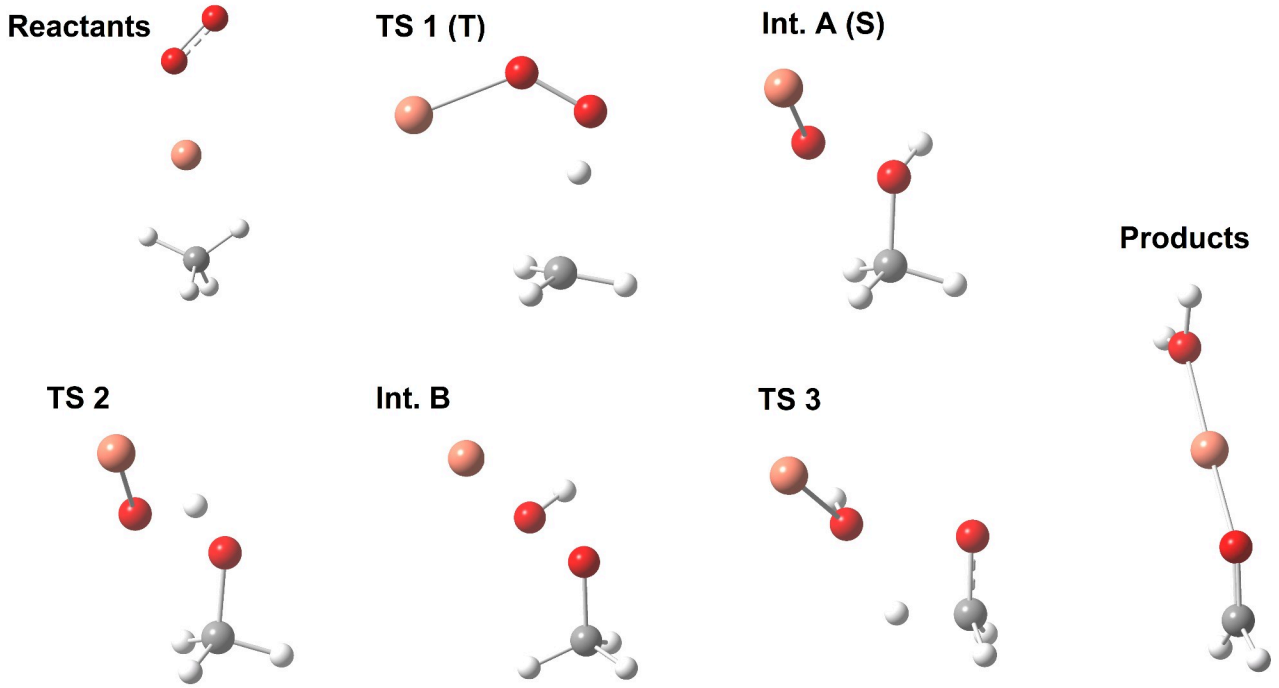

Figure 7: Structures obtained with methane as substrate, at the B3LYP/6-31+G(d,p) level of theory.

4. Crossing spin state surfaces

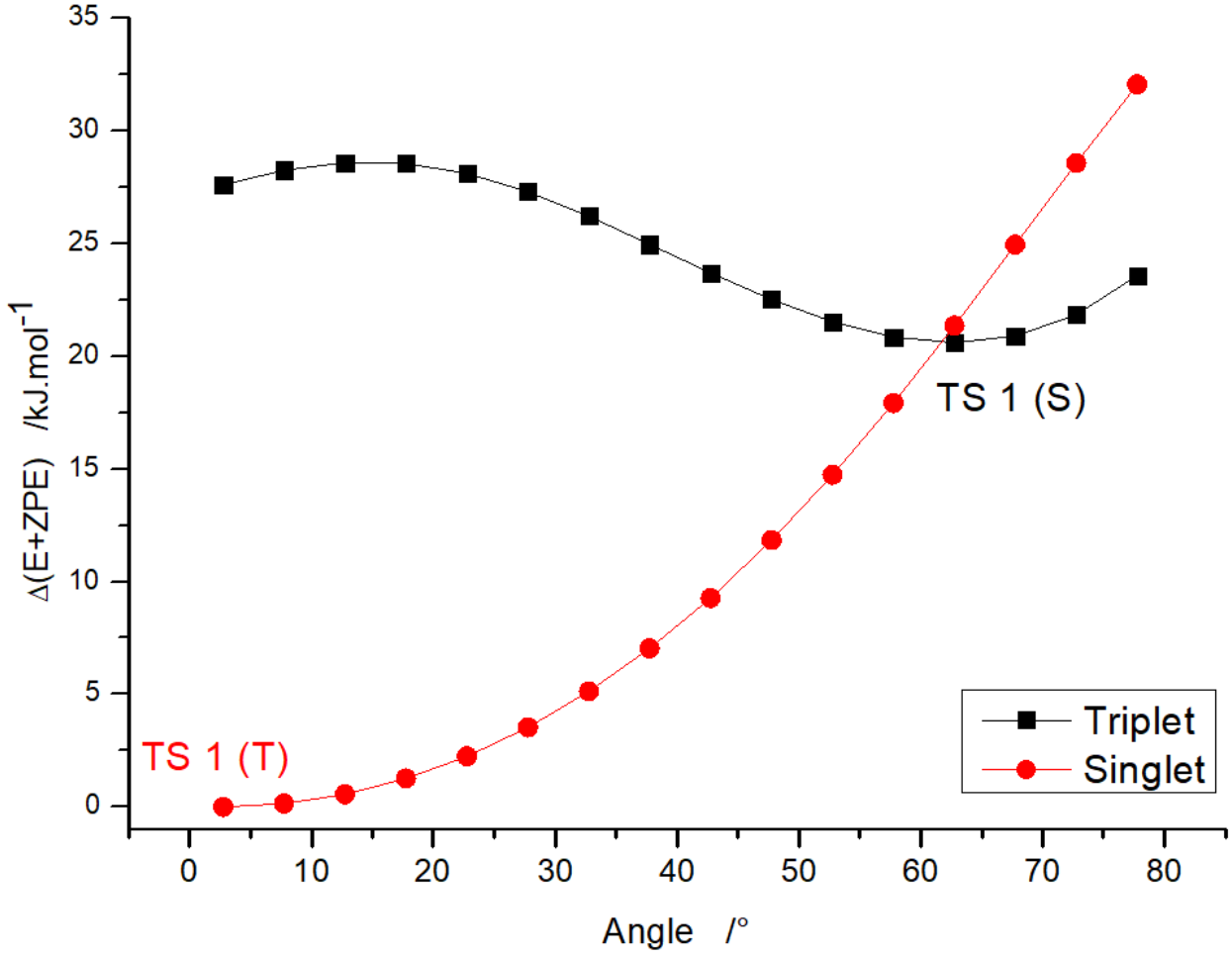

Figure 8: Plotted energies of optimized (constrained) TS in the triplet and singlet spin states, as a function of the CuOOH dihedral angle.

TS 1 was calculated in both singlet and triplet spin states. The triplet TS 1 was found to be 23 kJ.mol^{-1} more stable in energy than its singlet equivalent. After following their respective IRC pathways, the triplet Cu-hydroperoxo is 51 kJ.mol^{-1} higher in energy than the surprising Int. A (S). Although the two TS are relatively close, both in terms of geometry and energy, their products are very different. Therefore, they a priori go in different directions, and in this case, it is necessary to locate a spin-crossing point (CP) to know if the full toluene oxidation reaction can be achieved or not. So, from the reactants complex to TS 1, the gap between triplet and singlet spin state surfaces is reduced by about 80%, consolidating the idea that a spin crossing can take place around TS 1. Having say that, we identified the main difference between the two TS structures to be the CuOOH

dihedral angle. The rotation of the OO bond after TS 1 (S) is the key point of the singlet state mechanism to obtain Int. A (S). Without any rotation (i.e. in the triplet state), only the formation of the hydroperoxo happens. The search for a spin crossing point was done first considering the change in the CuOOH dihedral angle. A vibrational mode was identified as a torsion of the CuOOH moiety, for both singlet (206 cm^{-1}) and triplet (152 cm^{-1}) TSs. The potential wells associated with each vibration are more or less formalized in the Figure 8. The energy plots were obtained optimization for a TS with a given CuOOH dihedral angle. The torsion of the dihedral angle theoretically leads to an intersection of the surface near to the geometry of TS 1 (S), since the two structures are very similar at that point. On the other hand, if the intersection of surfaces seems to be accessible, the statistical part of the molecules which would remain on the singlet surface would be extremely low.

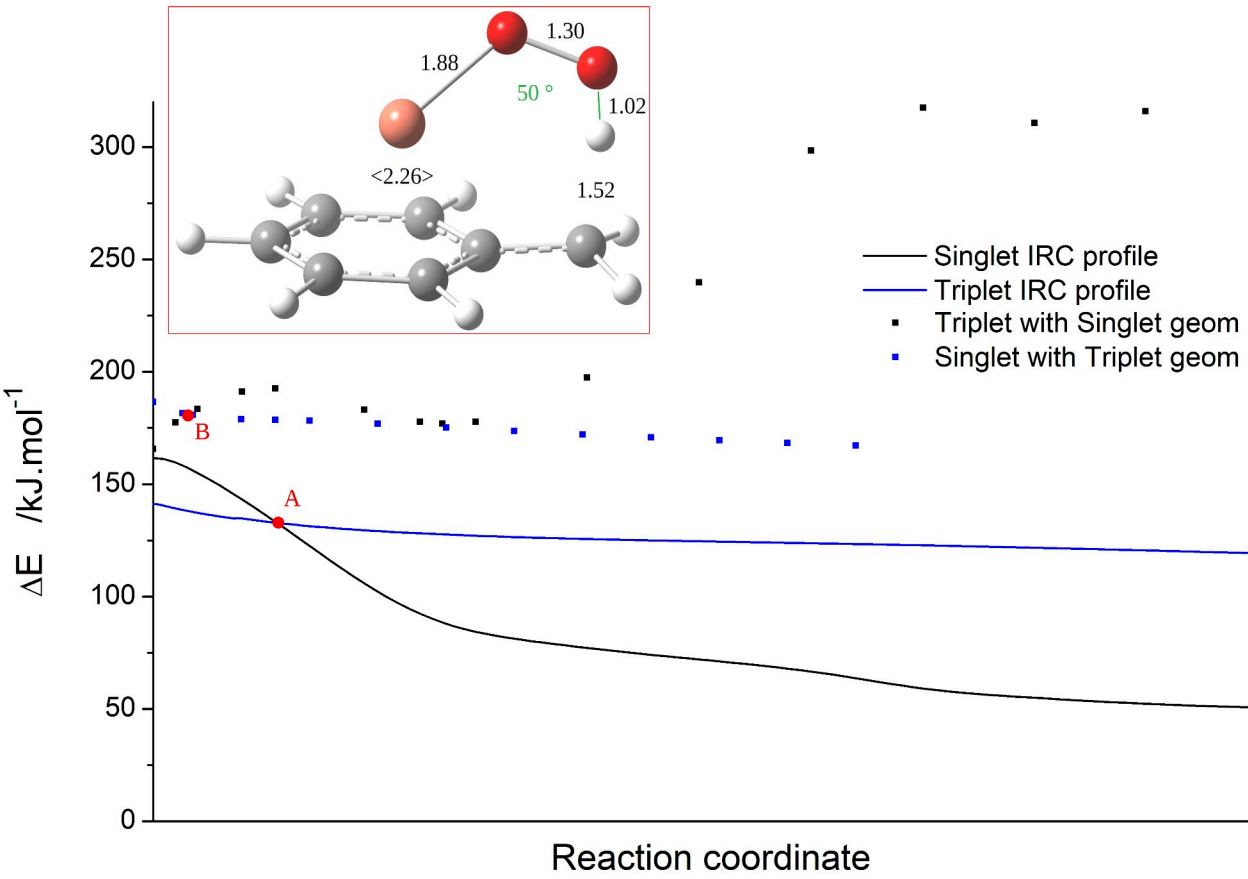

Figure 9: Singlet (black line) and triplet (blue line) IRC profiles after TS 1, with triplet (from singlet geometries, black dots) and singlet (from triplet geometries, blue dots) single point energies. The energies are plotted with respect to the reactant complex.

An other approach has been tested in order to take into account all the degrees of freedom of the system (Figure 9). The IRC profiles were plotted towards their relative reaction coordinate. An intersection between the two IRC curves has been found (point A). However, at that point, geometries are much more different than between the two TS, and point A is not a crossing-point (same geometry and energy in both spin states). It is necessary to look closer from the TS to find an adequate crossing-point. Single-point calculations from IRC geometries have shown an other intersection between excited profiles (point B). At point B, the energies are equal, but the geometry are different (especially the CuOOH dihedral angle). The geometry into the red box was obtained by weight-averaging the two close geometries obtained at point B. Thus, it possesses some of the characteristics of a crossing-point (same geometry, same energy in both spin states). Its energy was found to be 166 $kJ.mol^{-1}$, which is only 25 $kJ.mol^{-1}$ higher than TS 1 (T). Optimization of our putative crossing-point, although it is not on the lowest energy surfaces, leads to reactant complex when optimized in the triplet spin state and to Int. A (S), when optimized in the singlet spin state.

5. Nature of TS and intermediates

5.1. Charge analysis

In Figure 10 is presented the evolution of the Bader charges during the reaction, considering only the lowest energy TS or intermediate (i.e. with a spin crossing between TS 1 and Int. A). The charge of Cu does not change so much during the reaction. It indicates that the Cu is not strongly implied in the mechanism. The charge of the carbon atom of the methyl group strongly increases and the charge of O atoms hardly decreases during the reaction, as a witness of the growing oxidation. C atom is strongly oxidized at TS 3: its charge is doubled from reactants, and multiplied by three for the product complex. It corresponds to the formation of the CO double-bond (aldehyde group). The transferred H atoms see their charge increase when they are transferred from the C atom to the O atom. Each intermediate and TS is detailed below. Some points of attention are mentioned, in order to support the discussion. The Bader charge of Cu varies only by + 0.04 (the global charge of O_2 becomes -0.02) through the coordination of O_2. So, as proposed, O_2 is low-activated ($Cu^{(I)}$-O_2 character). From the reactant complex to TS 1, the charge of the first transferred H increases strongly (0.449 at TS step): it has an intermediate character between hydrogen atom and proton. The carbon and oxygen atoms recover negative charge from that $H^+/H^\bullet$. At Int. A step, the CO bond formation is well shown by the strong increase of the C charge (from 0.022 to 0.356). The charge on the CuO fragment is only 0.237: the next oxidative species cannot be completely assessed to be CuO^+. For TS 2, here again, the transferred H has an intermediate $H^+/H^\bullet$ character, but somewhat more protonic: the charge has increased from 0.449 (TS 1) to 0.673 (TS 2). The CO bond is even more stronger with the charge on C that is delocalized on the close O_d atom. During this step, C atom gains charge, in favor of oxygen atoms: it explains why the distance OO is slightly increased allowing the transfer of H. In Int. B, the charge of Cu is 0.693: almost 70 % of the positive charge of the overall complex remains on Cu, which confirm the benzylperoxide nature of Int. B. The ‘hydrogen atom’ nature of the second transferred H (TS 3) is without contest: its charge is only 0.191. This step is the scene of huge changes in the molecule charges, as a witness of the high barrier height. The charge of both oxygen atoms decreases strongly: the CO_d bond is totally formed as the OO bond is broken.

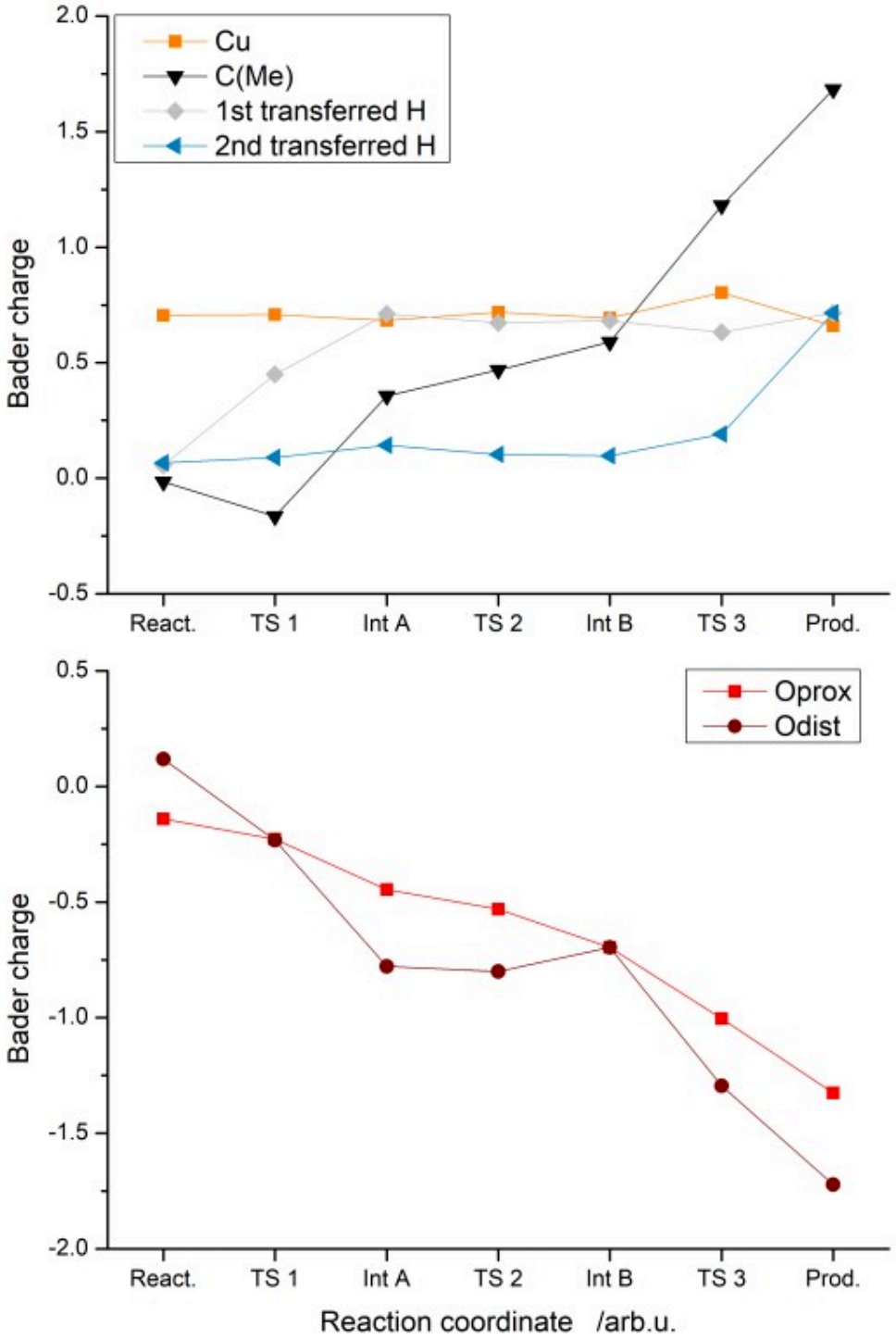

Figure 10: Bader charge calculated on some atoms with the help of a medium grid (6 pts/Bohr). The geometries from B3LYP/6-31+G(d,p) were used. Only low-lying intermediates and TSs are considered.

5.2. Bond Critical point (BCP) analysis

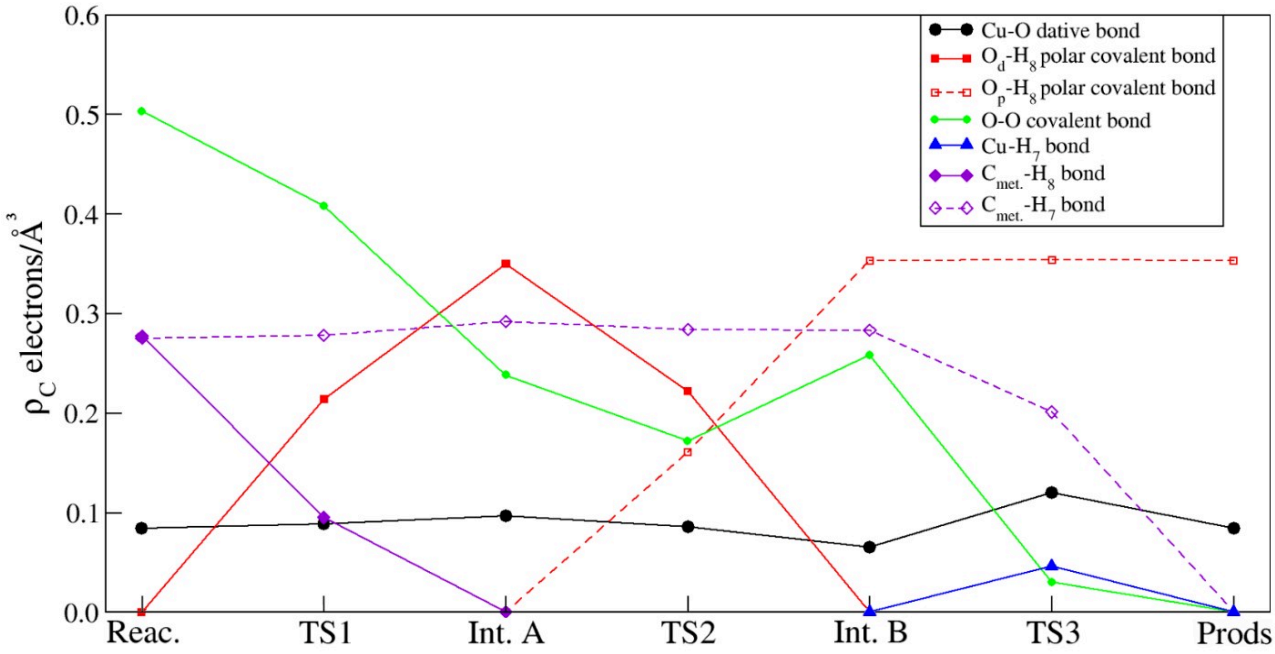

Figure 11: Electron density monitoring by BCP analysis on some bonds during the process. H8 is the first H to be transferred, H7 is the second.

Figure 11 depicts the behavior of the electronic density at the BCP for the most relevant chemical bonds intervening in the reaction process. From Reactants to TS 1, the strong increase of ρc at the BCP of the O_d-H8 bond combined with the drop of the electronic density at the BCP of C-H8 and O_p-O_d bonds illustrates the H abstraction process stemming from the O_d atom. At Int. A point, the C-H8 bond is totally broken, and the O_dH8 bond totally formed. There is a strong interaction between both oxygen atoms and between C and O_d, confirming the proposed nature of the intermediate. The ground state of CuO^+ is expected to be triplet, but the interaction between O atoms (0.23 electrons.Å^{-3}) and the global charge of CuO moiety (0.237, see Charge analysis p.87) allow the whole structure to be on the singlet surface. The transfer process corresponding to TS 2 is well visible on Figure 9: the O_dH7 bond density drops (from Int. A to Int. B: -0.35 electrons.Å-3), while O_pH7 bond density raises (from Int. A to Int. B: +0.35 electrons.Å-3). Bond density of O_pO_d is at a local minimum: the bond is elongated by 0.14 Å. OO bond is weakened, in order to allow the transfer of H. During TS 2 → Int. B transition, the evolution of Cu, H, O_p and O_d charges shows that Cu is not strongly bounded to O_p, because it does not give nor take back electrons. At Int. B point, the value of the CuO bond density is the lowest of all the pathway, showing that the benzylperoxide

fragment is real. The O_p-H8 bond is as strong as the precedent O_d-H7: it means that this O_d-H7 was a strong bond, and explain why the OO bond was elongated at this step (as a complement of charge analysis). The second intermediate Int. B has a peroxide character: the O_p-O_d bond density goes up again, whilst O_pH bond is now totally formed. BCP analysis was led on TS 3 geometry: two remarkable BCPs appear between the second H to be transferred, O_p and Cu, respectively (Figure 12). O_p-O_d and C-H7 bonds collapse, because they are breaking, while Cu-O_p dative bond density slightly increases. In a concerted way, O_p recovers electron density from the OO bond and gives electron density to Cu, which is able to interact with H7. Notwithstanding the long 1.94 Å and 2.09 Å distances between Cu and H, and O and H, respectively, here there are very weak and non-covalent bondings, that can be described as a hydrogen or Van der Waals bonds, according Matta's table[43]. The assertion of the influence of Cu^+ has been verified with the other functionals: each of them shows a non-negligible interaction between Cu and the transferred H atom. Both Cu charge and CuO_p bond density remain stable (around 0.70 and 0.09 electron.$Å^{-3}$, respectively), except for TS 3, in which Cu is directly involved.

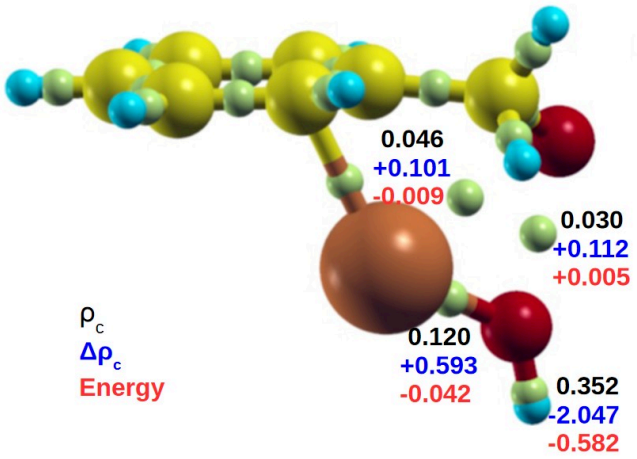

Figure 12: BCP analysis on TS 3 geometry. BCPs are green dots, H: blue, O: dark red, Cu: brown, C: yellow. ρ_c stands for density and $\Delta\rho_c$ for its derivative.

6. Comparison without Cu^+

6.1. Energetics

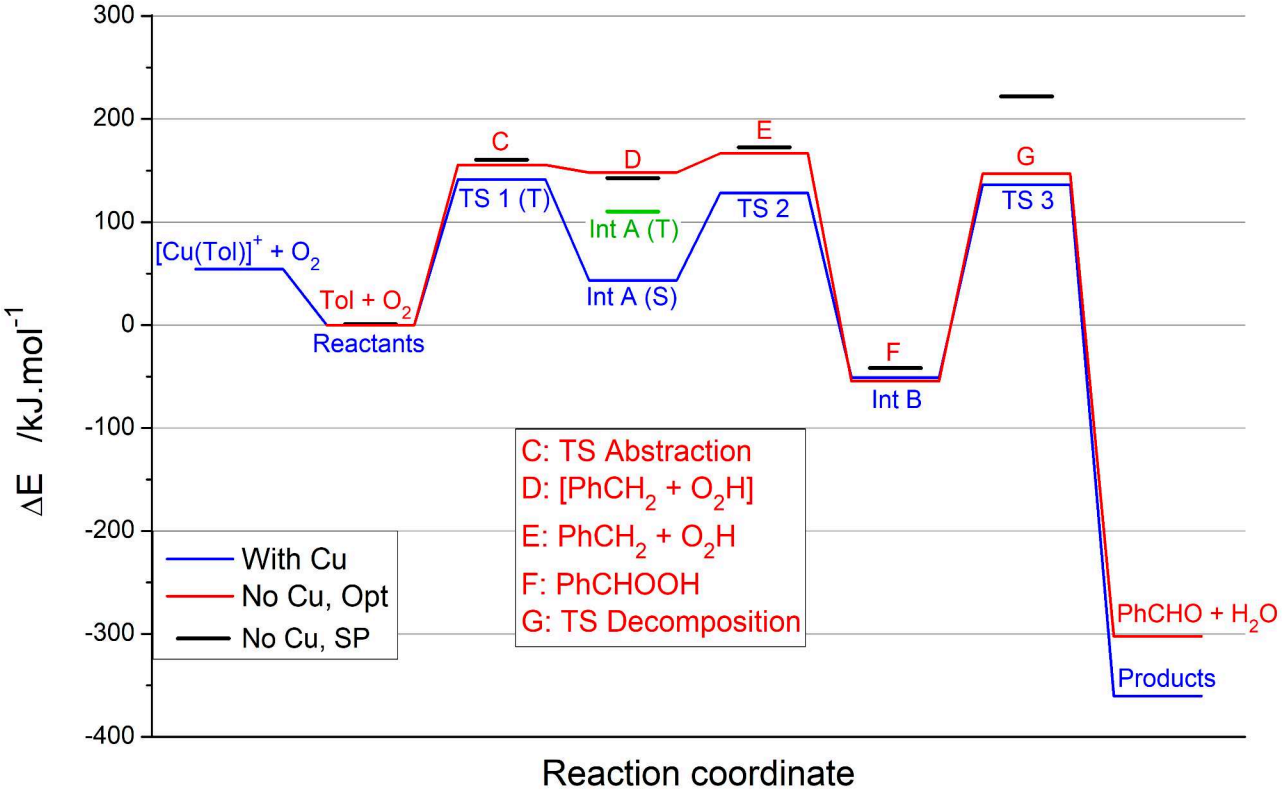

Figure 13: Comparison between our postulated mechanism (blue, and green for Int. A (T)), expected mechanism without Cu (red) and single point energies on the geometries obtained in our mechanism, but without Cu^+ (black, on the geometries obtained at the B3LYP/6-31+G(d,p) level of theory, with the same spin state (until TS 1, triplet spin state; after TS 1, singlet spin state).

It seems also important to discuss the influence of Cu on the mechanism, in order to complete the proposals made before. The pathway we have determined (blue line, Figure 13) is compared in one hand to the energies of the structures without Cu^+ (black dashes, Figure 13) and in the other hand, to a postulated mechanism without Cu^+, that can lead to benzaldehyde and water (red line, Figure 13). As a reminder, bare Cu^+ is expected to be a poor-activator of O_2. The triplet spin state leads to the formation of a Cu-hydroperoxo species. The singlet spin state imposes a rearrangement after the formation of the hydroperoxo species, which is the remigration of the OH group on the dehydrogenated toluene. This intermediate evolves towards a benzylperoxide species, which is even more stable than the reactant complex. The final stage of our model mechanism is the concerted two-step degradation of the peroxide into benzaldehyde and water. Single point

calculations were led after removal of Cu on the geometries obtained at the B3LYP/6-31+G(d,p) level of theory (Figure 13). The same spin state was found to be lower in energy for each TS and intermediate. In fact, the graph shows the influence of Cu on the energy barriers and on the stability of intermediates. The energetic gaps might be cautiously considered, since the structures are not optimized. All three TS are higher in energy without Cu. O_2 is low-activated by bare Cu^+: the first energy barrier is only 10 % lower in the presence of Cu^+. It might be seen as the "activation power" of Cu^+ on O_2. It is consistent with the low spin density found on Cu. Cu strongly stabilizes the Int. A (by about 170 %). It confirms the presence of a relatively strong CuO bond (stronger than CuO^+ bond and weaker than a CuO bond, for which BDE of 54 and 273 $kJ.mol^{-1}$ were established, respectively[63]). The second energy barrier is about 30 % higher without Cu. However, it does not mean really that Cu stabilizes Int. A (S), TS 2 and TS 3. The differences are mainly due to structural reasons (single oxygen atom/radical hydroxyle group are energetically unfavorable). Int. B is not stabilized, nor destabilized by Cu^+, confirming the nature of Int. B (benzylperoxide + Cu, with a global +1 charge). The only possible reaction between toluene and triplet O_2 (red line) is the endothermic abstraction of a hydrogen atom on the methyl group, that leads to the formation of OOH and C_6H_5-CH_2 radicals (intermediate E). The absence of Cu increases the first energy barrier by only 10 %. Radical O_2H is stabilized by the presence of Cu^+ (by 58 $kJ.mol^{-1}$). The radical reaction between $OOH^\bullet$ and $PhCH_2^\bullet$ might happen, which leads to the formation of benzylperoxide (intermediate F), that can also decompose into benzaldehyde and water, via a second TS (G). The third energy barrier is reduced by about 8 % with Cu. The influence of Cu appears to be limited over the catalytic cycle, even for TS 3, for which we have shown that the Cu establishes a van der Waals interaction with the transferred hydrogen atom.

6.2. Molecular orbitals and Fukui functions

The general order of molecular orbitals with and without Cu^+ (excepted its d orbitals), from SOMO/HOMO to low-lying orbitals is the following:

— Two π orbitals of the cycle, in interaction with d orbitals of Cu;

— Two or three orbitals relative to O_p, O_d and the C atom of the methyl group, also in interaction with Cu d orbitals;

— One or two innocent d orbitals of Cu, followed by cycle σ orbitals.

Similar shapes are observed with low-lying orbitals once d orbitals are no more implied. The single electrons of O_2 are not in the two SOMOs. The fact that these orbitals are low-lying, both in the presence and in the absence of Cu, justify the high energy barriers of the model reaction. Both cycle and O_2 orbitals are shared with Cu^+, when it is present. Then, the orbitals of TS 1 (T) are quite similar in the presence or in the absence of Cu. They have more or less the same shape, the only difference being the d orbitals of Cu that are not strongly involved in interactions with O_2. For Int. A (S), without Cu, the high-lying molecular orbitals are concentrated on the single oxygen O_p. These orbitals are strongly stabilized by the d orbitals of Cu, confirming the statement given in the previous part. Molecular orbitals of Int. B confirm the peroxide character of the structure: Cu orbitals are well-defined, and inserted between the high-lying π orbitals (bonding orbitals of cycle and anti-bonding of O_2) and σ orbitals. TS 3 orbitals expose the interaction between the two oxygen atoms, despite the 2.34 Å distance between them. Here also, Cu stabilizes the single oxygen atom (hydroxyle group).

Fukui functions[45] have been calculated according a previously published procedure[64]. f^- Fukui function shows the sites of the system that are nucleophilic (susceptible to attack an electrophile), while f^+ Fukui function is the witness of electrophilic zones (susceptible to be attacked by a nucleophile). Fukui functions are mainly concentrated on CuO_2 moiety in the structures of intermediates (Figure 14). The cycle has a very low influence on the reactivity. The reactant complex has an O_2 moiety that is very electrophilic: it is consistent with the small electron transfer form Cu^+ to O_2 and with the electron requirement of O_2 to be activated. The methyl group is neither electrophile, nor nucleophile. The height of the first barrier is related to its inertness. The proximal O atom in Int. A (S) structure is a radicalophile: it confirms its reactivity for the abstraction of H atom from O_d. The transfer of the H atom from one oxygen to the other (Int. A to Int. B) strongly decreases the size of f^+ and f^- lobes. It is consistent with the energy stabilization of benzylperoxide. At Int. B step, f^+ shows the slight electrophilicity of O_d (formation of C=O bond) and f^- the nucleophilicity of O_p (abstraction of H atom): it is compatible with the two-step mechanism of TS 3 (OO bond break, followed by H migration). Similar results are obtained with the geometries in the absence of Cu (Figure 15). O_2 is very electrophilic (it is an oxidant). The f^- function of Int. A is mainly concentrated on the single oxygen, underlying its low-stability.

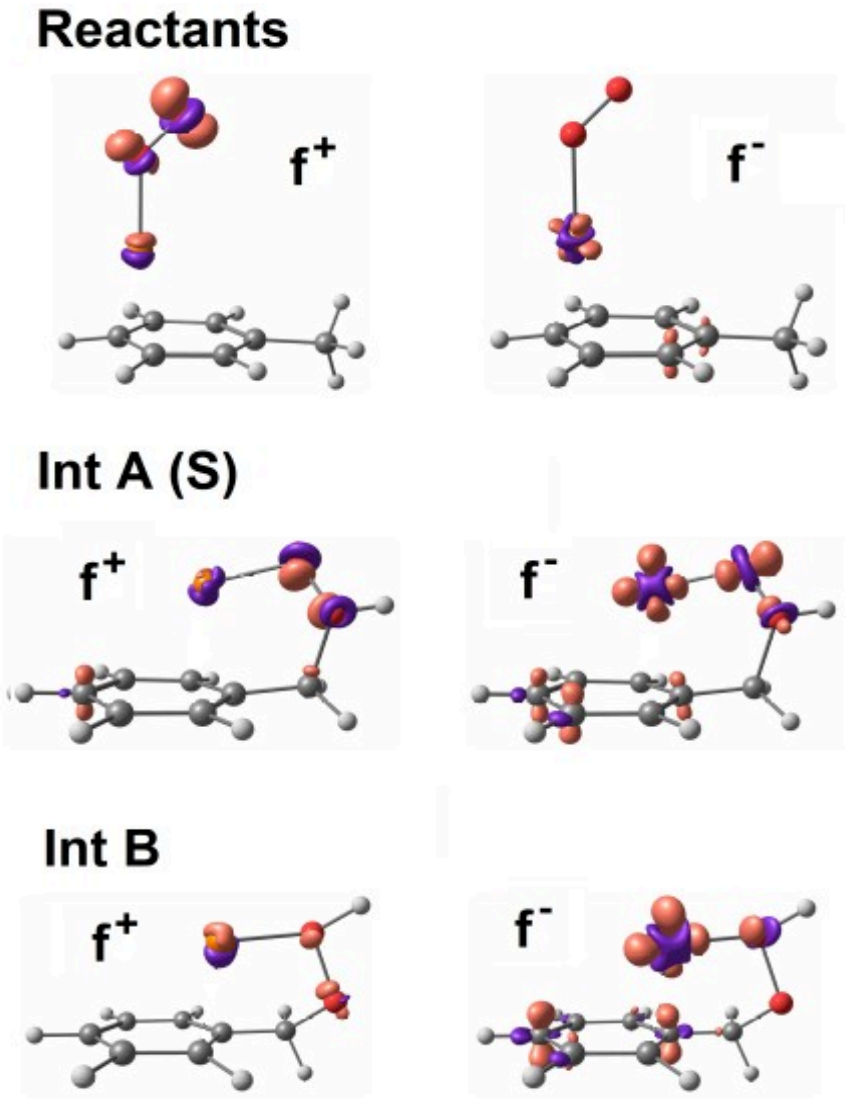

Figure 14: Fukui isosurfaces (f^+, f^-) for Reactants, Int. A (S) and Int. B, in the presence of Cu^+ (isovalues 0.01). Positive and negative values are indicated by light orange and violet lobes, respectively. C: grey, O: red, H: light grey, Cu: orange.

As a conclusion, Cu has only a limited role on the reaction. It never acts as a driving force of the reaction. It does not activate properly the dioxygen, does not take charge during the reaction, does not help the transfer of the first hydrogen atom/proton. It only stabilizes the proximal oxygen atom (Int. A) and has a low interaction with the second H atom transferred (TS 3). It also transmits excess electrons from O_2 moiety to cycle, and inversely. In other words, Cu acts as a buffer between O_2 and cycle moieties.

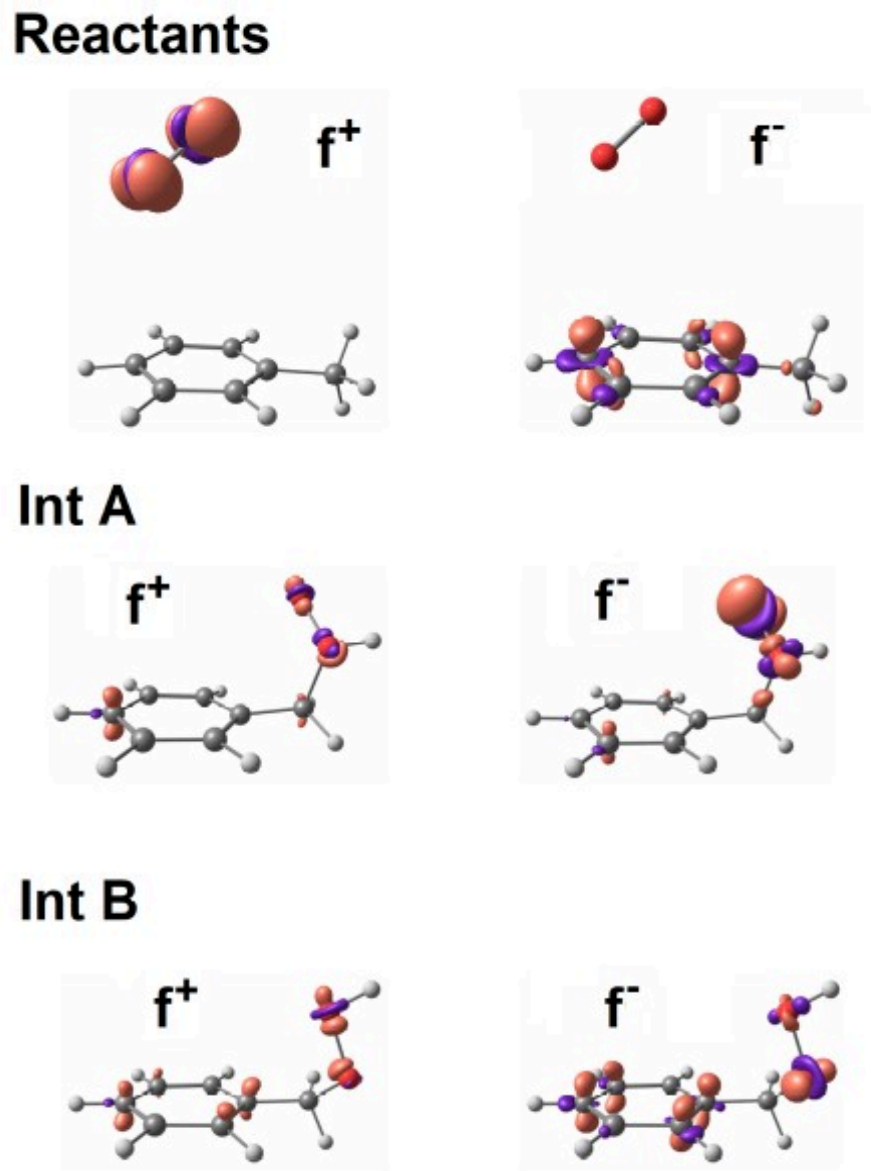

Figure 15: Fukui isosurfaces (f^+ and f^-) for Reactants, Int. A and Int. B, without Cu^+ (isovalues 0.01). Positive and negative values are indicated by light orange and violet lobes, respectively. C: grey, O: red, H: light grey.

Conclusions

The model mechanism for toluene oxidation by CuO_2^+ was determined theoretically, going through three steps. The first step of the mechanism (H abstraction followed by OH rebound, in the singlet spin state) is reminiscent of oxidation mechanisms proposed in the literature. The oxidation reaction of toluene presented here can be seen as the attack of CuO_2 on the methyl group of toluene, followed by the intramolecular degradation of CuOOH (due to the absence of solvent, that generally has a role in oxidation reactions).

The oxidation reaction of toluene by CuO_2^+ is very unlikely to happen in the gas phase because of the high energetic demand and of the spin-forbidden character of the reaction. Bare Cu^+ does not activated sufficiently O_2 to overcome these issues. However, this model reaction shows that ligands are necessary for oxidation reactions to reduce both the triplet-singlet spin state gap[16] and the height of the first barrier by reinforcing the $Cu^{(II)}$-$O_2^{\bullet -}$ character, the best oxidizing species. With ligand(s), the OO bond is then expected to be broken. The structure of ligands can influence the spin state of CuO_2^+ complexes. For example, some models of PHM / DβM have shown that their oxygenated copper complexes are in the singlet spin state[15,65]. Removing the solvent from this model reaction allows the intramolecular CuOOH degradation reaction to happen.

This innovative outlook helped us to understand the role of both the ligand and the metal center on the reaction. Similarities were found by comparison with mechanisms proposed in the literature. The influence of small ligands on barrier heights and on geometries of intermediates could be considered. Finally, this approach may be applied to a large range of enzymatic systems, in order to obtain information on the way they work, or for the design of biomimetic models.. A lot of mechanisms are still intensely debated. Our approach is promising to obtain reliable information: by varying the ligand without quite sticking to the structure or the activity of an enzyme, we make sure to play on the reaction, by introducing such a ligand on the metal center, or such a transformation on the ligand. Thus, it would become possible to favor such and such a reaction intermediate, which will facilitate the obtaining of a given substrate.

References

1. Elwell, C.E.; Gagnon, N.L.; Neisen, B.D.; Dhar, D.; Spaeth, A.D.; Yee, G.M.; Tolman, W.B. Copper–Oxygen Complexes Revisited: Structures, Spectroscopy, and Reactivity. *Chem. Rev.* **2017**, *117*, 2059–2107, doi:10.1021/acs.chemrev.6b00636.

2. Lee, J.Y.; Karlin, K.D. Elaboration of Copper–Oxygen Mediated C–H Activation Chemistry in Consideration of Future Fuel and Feedstock Generation. *Curr. Opin. Chem. Biol.* **2015**, *25*, 184–193, doi:10.1016/j.cbpa.2015.02.014.

3. Prigge, S.T.; Eipper, B.A.; Mains, R.E.; Amzel, L.M. Dioxygen Binds End-On to Mononuclear Copper in a Precatalytic Enzyme Complex. *Science* **2004**, *304*, 864–867, doi:10.1126/science.1094583.

4. Klinman, J.P. The Copper-Enzyme Family of Dopamine β-Monooxygenase and Peptidylglycine α-Hydroxylating Monooxygenase: Resolving the Chemical Pathway for Substrate Hydroxylation. *J. Biol. Chem.* **2006**, *281*, 3013–3016, doi:10.1074/jbc.R500011200.

5. Siegbahn, P.E.M. Hybrid DFT Study of the Mechanism of Quercetin 2,3-Dioxygenase. *Inorg. Chem.* **2004**, *43*, 5944–5953, doi:10.1021/ic0498541.

6. Whittaker, M.M.; Ballou, D.P.; Whittaker, J.W. Kinetic Isotope Effects as Probes of the Mechanism of Galactose Oxidase. *Biochemistry* **1998**, *37*, 8426–8436, doi:10.1021/bi980328t.

7. Smirnov, V.V.; Roth, J.P. Mechanisms of Electron Transfer in Catalysis by Copper Zinc Superoxide Dismutase. *J. Am. Chem. Soc.* **2006**, *128*, 16424–16425, doi:10.1021/ja066369r.

8. Cramer, C.J.; Tolman, W.B. Mononuclear Cu–O2 Complexes: Geometries, Spectroscopic Properties, Electronic Structures, and Reactivity. *Acc. Chem. Res.* **2007**, *40*, 601–608, doi:10.1021/ar700008c.

9. Solomon, E.I.; Heppner, D.E.; Johnston, E.M.; Ginsbach, J.W.; Cirera, J.; Qayyum, M.; Kieber-Emmons, M.T.; Kjaergaard, C.H.; Hadt, R.G.; Tian, L. Copper Active Sites in Biology. *Chem. Rev.* **2014**, *114*, 3659–3853, doi:10.1021/cr400327t.

10. Ettinger, M.J.; Kosman, D.J. Circular Dichroism Spectra of the Copper Enzyme, Galactose Oxidase, in the Presence of Its Substrates and Products. *Biochemistry* **1974**, *13*, 1247–1251, doi:10.1021/bi00703a030.

11. Bennett, B.; Kowalski, J. EPR Methods for Biological Cu(II): L-Band CW and NARS. *Methods Enzymol.* **2015**, *563*, 341–361, doi:10.1016/bs.mie.2015.06.030.

12. Aboelella, N.W.; Kryatov, S.V.; Gherman, B.F.; Brennessel, W.W.; Young, Victor G.; Sarangi, R.; Rybak-Akimova, E.V.; Hodgson, K.O.; Hedman, B.; Solomon, E.I.; et al. Dioxygen Activation at a Single Copper Site: Structure, Bonding, and Mechanism of Formation of 1:1 Cu−O2 Adducts. *J. Am. Chem. Soc.* **2004**, *126*, 16896–16911, doi:10.1021/ja045678j.

13. de la Lande, A.; Parisel, O.; Gérard, H.; Moliner, V.; Reinaud, O. Theoretical Exploration of the Oxidative Properties of a [(TrenMe1)CuO2]+ Adduct Relevant to Copper Monooxygenase Enzymes: Insights into Competitive Dehydrogenation versus Hydroxylation Reaction Pathways. *Chem. - Eur. J.* **2008**, *14*, 6465–6473, doi:10.1002/chem.200701595.

14. Woertink, J.S.; Tian, L.; Maiti, D.; Lucas, H.R.; Himes, R.A.; Karlin, K.D.; Neese, F.; Würtele, C.; Holthausen, M.; Bill, E.; et al. Spectroscopic and Computational Studies of an End-on Bound Superoxo-Cu(II) Complex: Geometric and Electronic Factors That Determine the Ground State. *Inorg. Chem.* **2010**, *49*, 9450–9459, doi:10.1021/ic101138u.

15. de la Lande, A.; Salahub, D.R.; Maddaluno, J.; Scemama, A.; Pilme, J.; Parisel, O.; Gerard, H.; Caffarel, M.; Piquemal, J.-P. Spin-Driven Activation of Dioxygen in Various Metalloenzymes and Their Inspired Models. *J. Comput. Chem.* **2011**, *32*, 1178–1182, doi:10.1002/jcc.21698.

16. Cramer, C.J.; Gour, J.R.; Kinal, A.; Włoch, M.; Piecuch, P.; Moughal Shahi, A.R.; Gagliardi, L. Stereoelectronic Effects on Molecular Geometries and State-Energy Splittings of Ligated Monocopper Dioxygen Complexes. *J. Phys. Chem. A* **2008**, *112*, 3754–3767, doi:10.1021/jp800627e.

17. Zapata-Rivera, J.; Caballol, R.; Calzado, C.J. Electronic Structure and Relative Stability of 1:1 Cu-O2 Adducts from Difference-Dedicated Configuration Interaction Calculations. *J. Comput. Chem.* **2011**, *32*, 1144–1158, doi:10.1002/jcc.21697.

18. Koyanagi, G.K.; Caraiman, D.; Blagojevic, V.; Bohme, D.K. Gas-Phase Reactions of Transition-Metal Ions with Molecular Oxygen: Room-Temperature Kinetics and Periodicities in Reactivity. *J. Phys. Chem. A* **2002**, *106*, 4581–4590, doi:10.1021/jp014145j.

19. Blanksby, S.J.; Ellison, G.B. Bond Dissociation Energies of Organic Molecules. *Acc. Chem. Res.* **2003**, *36*, 255–263, doi:10.1021/ar020230d.

20. Caraiman, D.; Bohme, D.K. Periodic Trends in Reactions of Benzene Clusters of Transition Metal Cations, M(C6H6)1,2+ with O2. *J. Phys. Chem. A* **2002**, *106*, 9705–9717, doi:10.1021/jp0208900.

21. Subrahmanyam, Ch.; Louis, B.; Rainone, F.; Viswanathan, B.; Renken, A.; Varadarajan, T.K. Partial Oxidation of Toluene by O2 over Mesoporous Cr–AlPO. *Catal. Commun.* **2002**, *3*, 45–50, doi:10.1016/S1566-7367(01)00070-X.

22. Li, X.-H.; Wang, X.; Antonietti, M. Solvent-Free and Metal-Free Oxidation of Toluene Using O2 and g-C3N4 with Nanopores: Nanostructure Boosts the Catalytic Selectivity. *ACS Catal.* **2012**, *2*, 2082–2086, doi:10.1021/cs300413x.

23. Wang, F.; Xu, J.; Li, X.; Gao, J.; Zhou, L.; Ohnishi, R. Liquid Phase Oxidation of Toluene to Benzaldehyde with Molecular Oxygen over Copper-Based Heterogeneous Catalysts. *Adv. Synth. Catal.* **2005**, *347*, 1987–1992, doi:10.1002/adsc.200505107.

24. Schröder, D.; Schwarz, H. C-H and C-C Bond Activation by Bare Transition-Metal Oxide Cations in the Gas Phase. *Angew. Chem. Int. Ed. Engl.* **1995**, *34*, 1973–1995, doi:10.1002/anie.199519731.

25. Butschke, B.; Schwarz, H. Thermal C−H Bond Activation of Benzene, Toluene, and Methane with Cationic [M(X)(Bipy)]+ (M = Ni, Pd, Pt; X = CH3, Cl; Bipy = 2,2′-Bipyridine): A Mechanistic Study. *Organometallics* **2011**, *30*, 1588–1598, doi:10.1021/om101138d.

26. Dietl, N.; van der Linde, C.; Schlangen, M.; Beyer, M.K.; Schwarz, H. Diatomic [CuO]+ and Its Role in the Spin-Selective Hydrogen- and Oxygen-Atom Transfers in the Thermal Activation of Methane. *Angew. Chem. Int. Ed.* **2011**, *50*, 4966–4969, doi:10.1002/anie.201100606.

27. Würtele, C.; Sander, O.; Lutz, V.; Waitz, T.; Tuczek, F.; Schindler, S. Aliphatic C−H Bond Oxidation of Toluene Using Copper Peroxo Complexes That Are Stable at Room Temperature. *J. Am. Chem. Soc.* **2009**, *131*, 7544–7545, doi:10.1021/ja902327s.

28. M. J. Frisch; G. W. Trucks; H. B. Schlegel; G. E. Scuseria; M. A. Robb; J. R. Cheeseman; G. Scalmani; V. Barone; G. A. Petersson; H. Nakatsuji; et al. *Gaussian16*; Gaussian, Inc.: Wallingford CT, 2016;

29. Roy Dennington; Todd A. Keith; John M. Millam *GaussView*; Semichem Inc.: Shawnee Mission, KS, 2016;

30. Andreienko, G. Chemcraft - Graphical Program for Visualization of Quantum Chemistry Computations Available online: https://www.chemcraftprog.com/ (accessed on 29 April 2020).

31. Becke, A.D. Density-functional Thermochemistry. III. The Role of Exact Exchange. *J. Chem. Phys.* **1993**, *98*, 5648–5652, doi:10.1063/1.464913.

32. Yanai, T.; Tew, D.; Handy, N. A New Hybrid Exchange-Correlation Functional Using the Coulomb-Attenuating Method (CAM-B3LYP). *Chem. Phys. Lett.* **2004**, *393*, 51–57, doi:10.1016/j.cplett.2004.06.011.

33. Chai, J.-D.; Head-Gordon, M. Systematic Optimization of Long-Range Corrected Hybrid Density Functionals. *J. Chem. Phys.* **2008**, *128*, 084106, doi:10.1063/1.2834918.

34. Chai, J.-D.; Head-Gordon, M. Long-Range Corrected Hybrid Density Functionals with Damped Atom–Atom Dispersion Corrections. *Phys. Chem. Chem. Phys.* **2008**, *10*, 6615–6620, doi:10.1039/B810189B.

35. Zhao, Y.; Truhlar, D.G. Design of Density Functionals That Are Broadly Accurate for Thermochemistry, Thermochemical Kinetics, and Nonbonded Interactions. *J. Phys. Chem. A* **2005**, *109*, 5656–5667, doi:10.1021/jp050536c.

36. Zhao, Y.; Schultz, N.E.; Truhlar, D.G. Exchange-Correlation Functional with Broad Accuracy for Metallic and Nonmetallic Compounds, Kinetics, and Noncovalent Interactions. *J. Chem. Phys.* **2005**, *123*, 161103, doi:10.1063/1.2126975.

37. Zhao, Y.; Truhlar, D.G. Density Functionals with Broad Applicability in Chemistry. *Acc. Chem. Res.* **2008**, *41*, 157–167, doi:10.1021/ar700111a.

38. Boese, A.D.; Handy, N.C. New Exchange-Correlation Density Functionals: The Role of the Kinetic-Energy Density. *J. Chem. Phys.* **2002**, *116*, 9559–9569, doi:10.1063/1.1476309.

39. Zhao, Y.; Truhlar, D. A New Local Density Functional for Main-Group Thermochemistry, Transition Metal Bonding, Thermochemical Kinetics, and Noncovalent Interactions. *J. Chem. Phys.* **2006**, doi:10.1063/1.2370993.

40. Yu, H.S.; He, X.; Li, S.L.; Truhlar, D.G. MN15: A Kohn–Sham Global-Hybrid Exchange–Correlation Density Functional with Broad Accuracy for Multi-Reference and Single-Reference Systems and Noncovalent Interactions. *Chem. Sci.* **2016**, *7*, 5032–5051, doi:10.1039/C6SC00705H.

41. Yu, H.S.; He, X.; Truhlar, D.G. MN15-L: A New Local Exchange-Correlation Functional for Kohn–Sham Density Functional Theory with Broad Accuracy for Atoms, Molecules, and Solids. *J. Chem. Theory Comput.* **2016**, *12*, 1280–1293, doi:10.1021/acs.jctc.5b01082.

42. Henkelman, G.; Arnaldsson, A.; Jónsson, H. A Fast and Robust Algorithm for Bader Decomposition of Charge Density. *Comput. Mater. Sci.* **2006**, *36*, 354–360, doi:10.1016/j.commatsci.2005.04.010.

43. Matta, C.F. Hydrogen–Hydrogen Bonding: The Non-Electrostatic Limit of Closed-Shell Interaction Between Two Hydro. In *Hydrogen Bonding—New Insights*; Grabowski, S.J., Ed.; Springer Netherlands: Dordrecht, 2006; pp. 337–375 ISBN 978-1-4020-4853-1.

44. Kohout, M. *DGrid*; V 5.1, Dresden, **2019**.

45. Parr, R.G.; Yang, W. Density Functional Approach to the Frontier-Electron Theory of Chemical Reactivity. *J. Am. Chem. Soc.* **1984**, *106*, 4049–4050, doi:10.1021/ja00326a036.

46. Bauschlicher, C.W.; Partridge, H.; Langhoff, S.R. Theoretical Study of Transition-Metal Ions Bound to Benzene. *J. Phys. Chem.* **1992**, *96*, 3273–3278, doi:10.1021/j100187a018.

47. Evans, J.P.; Ahn, K.; Klinman, J.P. Evidence That Dioxygen and Substrate Activation Are Tightly Coupled in Dopamine β-Monooxygenase: Implications for the Reactive Oxygen Species. *J. Biol. Chem.* **2003**, *278*, 49691–49698, doi:10.1074/jbc.M300797200.

48. Chen, P.; Solomon, E.I. Oxygen Activation by the Noncoupled Binuclear Copper Site in Peptidylglycine α-Hydroxylating Monooxygenase. Reaction Mechanism and Role of the Noncoupled Nature of the Active Site. *J. Am. Chem. Soc.* **2004**, *126*, 4991–5000, doi:10.1021/ja031564g.

49. Abad, E.; Rommel, J.B.; Kästner, J. Reaction Mechanism of the Bicopper Enzyme Peptidylglycine α-Hydroxylating Monooxygenase. *J. Biol. Chem.* **2014**, *289*, 13726–13738, doi:10.1074/jbc.M114.558494.

50. Maiti, D.; Lee, D.-H.; Gaoutchenova, K.; Würtele, C.; Holthausen, M.C.; Narducci Sarjeant, A.A.; Sundermeyer, J.; Schindler, S.; Karlin, K.D. Reactions of a Copper(II) Superoxo Complex Lead to C-H and O-H Substrate Oxygenation: Modeling Copper-Monooxygenase C-H Hydroxylation. *Angew. Chem.* **2008**, *120*, 88–91, doi:10.1002/ange.200704389.

51. Ross, M.O.; Rosenzweig, A.C. A Tale of Two Methane Monooxygenases. *JBIC J. Biol. Inorg. Chem.* **2017**, *22*, 307–319, doi:10.1007/s00775-016-1419-y.

52. Walton, P.H.; Davies, G.J. On the Catalytic Mechanisms of Lytic Polysaccharide Monooxygenases. *Curr. Opin. Chem. Biol.* **2016**, *31*, 195–207, doi:10.1016/j.cbpa.2016.04.001.

53. Yoshizawa, K.; Kihara, N.; Kamachi, T.; Shiota, Y. Catalytic Mechanism of Dopamine β-Monooxygenase Mediated by Cu(III)−Oxo. *Inorg. Chem.* **2006**, *45*, 3034–3041, doi:10.1021/ic0521168.

54. Emdee, J.L.; Brezinsky, K.; Glassman, I. A Kinetic Model for the Oxidation of Toluene near 1200 K. *J. Phys. Chem.* **1992**, *96*, 2151–2161, doi:10.1021/j100184a025.

55. Cramer, C.J.; Tolman, W.B.; Theopold, K.H.; Rheingold, A.L. Variable Character of O—O and M—O Bonding in Side-on (H2) 1:1 Metal Complexes of O2. *Proc. Natl. Acad. Sci.* **2003**, *100*, 3635–3640, doi:10.1073/pnas.0535926100.

56. de la Lande, A.; Gérard, H.; Parisel, O. How to Optimize a C-H Cleavage with a Mononuclear Copper–Dioxygen Adduct? *Int. J. Quantum Chem.* **2008**, *108*, 1898–1904, doi:https://doi.org/10.1002/qua.21679.

57. Fukui, K. The Path of Chemical Reactions - the IRC Approach. *Acc. Chem. Res.* **1981**, *14*, 363–368, doi:10.1021/ar00072a001.

58. Abrahams, S.C.; Kalnajs, J. The Crystal Structure of α-Potassium Superoxide. *Acta Crystallogr.* **1955**, *8*, 503–506, doi:10.1107/S0365110X55001540.

59. Shaik, S.; Danovich, D.; Fiedler, A.; Schröder, D.; Schwarz, H. Two-State Reactivity in Organometallic Gas-Phase Ion Chemistry. *Helv. Chim. Acta* **1995**, *78*, 1393–1407, doi:10.1002/hlca.19950780602.

60. Bach, R.D.; Schlegel, H.B. Bond Dissociation Energy of Peroxides Revisited. *J. Phys. Chem. A* **2020**, *124*, 4742–4751, doi:10.1021/acs.jpca.0c02859.

61. Srnec, M.; Navrátil, R.; Andris, E.; Jašík, J.; Roithová, J. Experimentally Calibrated Analysis of the Electronic Structure of CuO+: Implications for Reactivity. *Angew. Chem. Int. Ed.* **2018**, *57*, 17053–17057, doi:10.1002/anie.201811362.

62. Mardirossian, N.; Head-Gordon, M. How Accurate Are the Minnesota Density Functionals for Noncovalent Interactions, Isomerization Energies, Thermochemistry, and Barrier Heights Involving Molecules Composed of Main-Group Elements? *J. Chem. Theory Comput.* **2016**, *12*, 4303–4325, doi:10.1021/acs.jctc.6b00637.

63. Daoudi, A.; Touimi Benjelloun, A.; Flament, J.P.; Berthier, G. Potential Energy Curves and Electronic Structure of Copper Nitrides CuN and CuN+Versus CuO and CuO+. *J. Mol. Spectrosc.* **1999**, *194*, 8–16, doi:10.1006/jmsp.1998.7596.

64. Keith, J.A.; Grice, K.A.; Kubiak, C.P.; Carter, E.A. Elucidation of the Selectivity of Proton-Dependent Electrocatalytic CO2 Reduction by Fac-Re(Bpy)(CO)3Cl. *J. Am. Chem. Soc.* **2013**, *135*, 15823–15829, doi:10.1021/ja406456g.

65. de la Lande, A.; Gérard, H.; Moliner, V.; Izzet, G.; Reinaud, O.; Parisel, O. Theoretical Modelling of Tripodal CuN3 and CuN4 Cuprous Complexes Interacting with O2, CO or CH3CN. *JBIC J. Biol. Inorg. Chem.* **2006**, *11*, 593–608, doi:10.1007/s00775-006-0107-8.

Chapter 3

O_2 Coordination on Cu-bipyridyl Complexes in the Gas Phase – Influence of Functionalization

Introduction

The development by a biomimetic approach of efficient catalytic systems for the oxidation of organic substrates oxidation or for the four-electron reduction of O_2 represents an appealing approach to produce "green fuels" or energy. Numerous studies based on crystallographic[1,2], kinetic[3] and spectroscopic[4] experiments have provided valuable data on the structure and the chemical environment of the active sites of enzymes capable of catalyzing these reactions with high efficiency under mild conditions. In parallel, synthetic studies also led to the development of a wide variety of metal-based models that are able to activate O_2 and to oxidize organic substrates in high yields. The coordination of O_2 on the active metallic center is the first step of oxidation mechanisms. Its activation, although it is challenging, can be performed at electron-rich metal centers, such as $Fe^{(II)}$ or $Cu^{(I)}$, surrounded by electron-donor ligands that allow a metal-to-ligand charge transfer[5]. The formation of mononuclear CuO_2 species is favored when the ligand stabilizes these intermediates with the help of H-bonds[6], electron-donating[7] or bulky groups[8] that prevent dimerization. In this situation, mononuclear $Cu^{(II)}$-superoxo species have been characterized by crystallography. However, mononuclear CuO_2 intermediates bearing no bulky ligands undergo both reverse dissociation reaction and fast dimerization, even at low temperature[9]. Working in the gas phase may prevent from dimerization, due to the high dispersion of ions. Molina-Svendsen and coworkers summarize well the interest of the study of the formation of complexes with O_2 in the gas phase:

The study of reactions of coordinatively unsaturated transition metal ions with dioxygen is useful since such processes are often essential in the activation of molecular oxygen for its subsequent utilization in oxidation reactions in biological and other systems. The four-electron conversion of dioxygen to oxide (or water/hydroxide) ligands, and the reverse of this process, is a subject under considerable debate in the field of bioinorganic chemistry, due to metalloenzyme involvement in oxygen-utilizing and -generating processes. Studies of molecular activation under well-controlled conditions can contribute to the elucidation of the mechanisms of molecular oxygen activation.[10]

As an extension of Chapter II, we have tried to experimentally study the oxidation reaction of toluene by CuO_2^+, using mass spectrometry. No coordination of O_2 on bare Cu^+ (generated by the electrospray source) or on the $[Cu(toluene)]^+$ complex has been observed with both triple

quadrupole and ion trap devices. The O_2 pressure used was $5 \cdot 10^{-5}$ mbar in the transfer hexapole preceding the first quadrupole, and between $1 \cdot 10^{-3}$ and $1 \cdot 10^{-2}$ mbar in the collision cell, well below the O_2 pressure used (~ 0.47 mbar of O_2 mixed with He) by Schwarz and coworkers on similar systems (M^+ and $[M(benzene)]^+$, with M being a transition metal)[11,12]. So, it is quite naturally that we have tried to add ligands on Cu^+, in order to increase the collisional cross-section and as a consequence, the inertia of the system and the probability to collide the complex with O_2 molecules. No coordination of O_2 was observed on $Cu^{(I)}$ ion complexed with one or two CH_3CN or N-methylimidazole molecules. We have chosen to use 2,2'-bipyridyl (see Figure 1) as ligand. The choice of bidentate ligand is justified with the fact that it strongly binds transition metals ions, including $Cu^{(I)}$ and $Cu^{(II)}$. Thus, no competitive decoordination of the ligand will happen when it is collided with O_2 (at low collision voltages). Bipyridyl ligands are also interesting because they are constrained ligands. The two nitrogen atoms are not from either side of the Cu ion, and predisposes its d orbitals to bind O_2 (see p.143). Moreover, the catalysis of the two-electron oxidation of primary and secondary alcohols into their corresponding aldehydes by metal bipyridyl (bpy) complexes in combination with hydroxylamines (R_2NOH) as a co-catalyst and a base has been the subject of numerous studies. The mechanism using $[Cu(bpy)]^+$ as a catalyst has been discussed on the basis of electrochemical, spectroscopic and kinetic experiments[13–16]. The oxidation of alcohols was investigated both in the presence of O_2 or in anoxic conditions. The oxidation of alcohols was also studied using hydroxylamines as the only catalyst being regenerated by a strong oxidant, such as NaOCl or Br_2, or by electrochemical oxidation[14]. In the absence of O_2, the proposed mechanism involves the deprotonation of alcohol by hydroxylamine prior to its coordination from the $Cu^{(II)}$ center. After further coordination of hydroxylamine, an inner-sphere H atom transfer takes place from the carbon atom bearing the OH group of alcohol to the OH group of hydroxylamine. The remaining electron is then transferred back to the $Cu^{(II)}$ center leading to the release of aldehyde. The re-oxidation of the catalyst can then be achieved chemically or electrochemically to close the catalytic cycle[17]. Other mechanisms have also been proposed, implying action of the fully oxidized form of hydroxylamine ($R\text{-}N{=}O^+$). According to the mechanism proposed by Stahl and coworkers[18], in the presence of O_2, the formation of a $Cu^{(II)}$-superoxo or $Cu^{(III)}$-peroxo intermediates is favored, most likely followed by the coordination of a second $Cu^{(I)}$ complex, leading to a $\mu\text{-}\eta^1\text{-}\eta^1$ O_2 coordination. The putative Cu_2O_2 core would be able to abstract the weakly bonded H atom of the hydroxylamine leading to a $Cu^{(II)}$-hydroperoxo intermediates which is able to deprotonate water. At this point, bidendate ligands seems not to be strong enough electron donors to

ensure efficient coordination and activation of O_2. Additional donor ligands, such as N-methylimidazole (NMI), need to be added to the solution in order to strengthen the electron transfer between the metal center and O_2[19]. The oxidation mechanism of alcohols by mononuclear Cu complex with bidentate ligand (biquinolyl) is also theoretically discussed, with a reasonable energy barrier of CH bond activation (69 $kJ \cdot mol^{-1}$)[20]. However, there are no direct proofs of existence of CuO_2 (superoxo) intermediates with bidentate ligands in solution, because of their high reactivity (instantaneous dimerization)[21]. Only grafted Cu-phenanthroline complexes have shown remarkable activity for O_2 reduction into H_2O (four-electron reduction) or H_2O_2 (two-electron reduction), depending on the nuclearity of the active species (binuclear and mononuclear, respectively)[22]. Systematic studies have shown that electron-withdrawing groups favor the electro-reduction of $Cu^{(II)}$-phenanthroline complexes but decrease the rate of O_2 reduction[23].

The Collision Activated Reactions (CAR) technique, which is affiliated with ion-molecule reactions, is able to provide analytical[24] and mechanistic[25–30] information. Using this technique, the gas-phase coordination of O_2 was reported for mono-charged cations of transition metals produced by ICP[11] and also reported for doubly-charged $[M(bpy)_{1,2}]^{2+}$ with M = Co, Ni, Ru, Cr, Os, generated by ESI source[10]. Conclusions drawn from these studies suggested that O_2 forms low-energy bonds with first row transition metals, whereas with heavier transition metals, such as Os and possibly Ru, a four-electron reduction of O_2 is proposed to occur, leading to $M(O)_2$ adducts. The reactivity of Cu-O_2 adducts is expected to follow that of other first row transition metals. However, no coordination of O_2 in the gas phase was ever reported with $[Cu(R_2bpy)]^+$ complexes. Very recently, Donnelly *et al.* reported evidences for the coordination of O_2 at trace pressure by $[Cu(tdt)]^-$ (tdt = toluene-3,4-dithiolate) in the gas phase[31], the formation of which occurred by ligand exchange. Based on this experimental work and on DFT calculations, it was proposed that the Cu ion is in the +III oxidation state and the bounded O_2 to have a peroxo character, consistent with the strong electron-donor properties of the dianionic tdt ligand.

In this chapter is reported a mass spectrometric and DFT study about the gas phase reactivity of $[Cu(R_2bpy)]^+$ (R_2bpy = bipyridine or bipyridyl, R = -H, -Me, -OMe, $-CO_2Me$, -tBu or $-NO_2$) and $[Cu(phen)]^+$ (phen = phenanthroline) complexes towards O_2 (Figure 1). We were able to show, for the first time, that $[Cu(R_2bpy)]^+$ has the intrinsic capacity to coordinate and activate O_2 without any collaboration of additional ligands or solvent molecules. Hammett's approach, which is based on the electronic contributions of a substituent on a given reaction, was applied in our case to determine the influence of R on the coordination of O_2. The influence of electron-donating (R = -OMe, -tBu and -Me) and electron-withdrawing (R = $-CO_2Me$ and $-NO_2$) groups both on O_2 coordination and Bond Dissociation Energies are evaluated by gas-phase tandem mass spectrometry and DFT computations respectively. Data are then compared with reported Hammett parameters and discussed in light of solvent contributions also. Finally, DFT calculations, Bader charge and Mulliken spin density analysis, are carried out to discuss O_2 coordination its superoxo character.

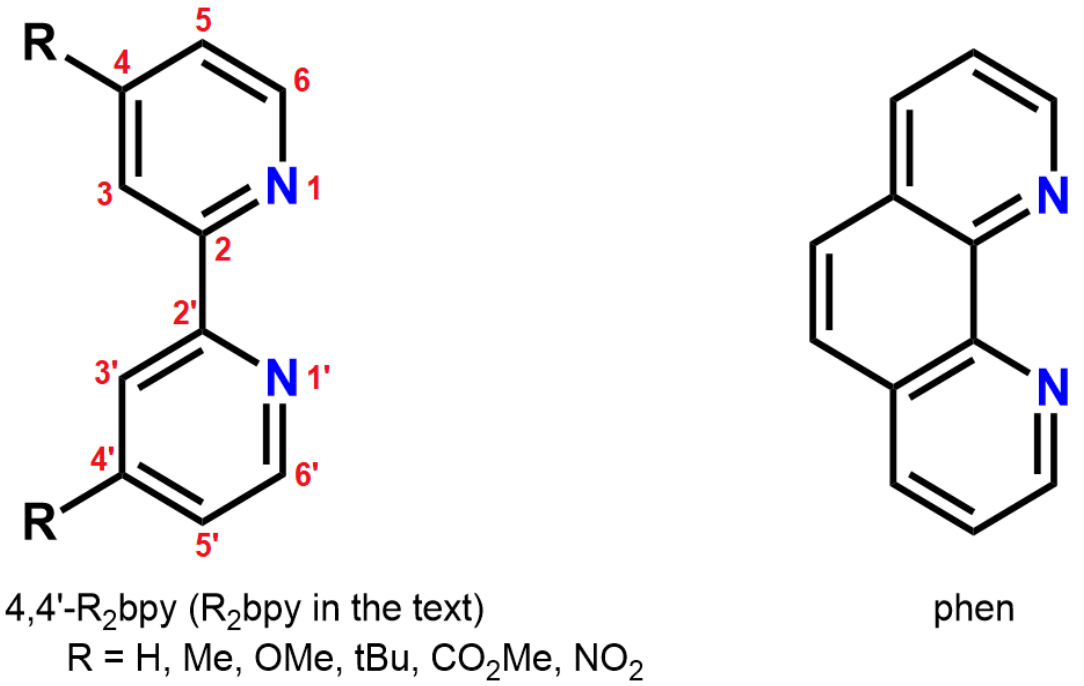

Figure 1: Structures of substituted 4,4'- bipyridyl and phenanthroline ligands.

1. Experimental section

1.1. Mass spectrometry

Mass spectrometry experiments were performed in positive ion mode using a triple quadrupole (Quattro II, Waters/Micromass Co., Manchester UK) equipped with an electrospray source (Z-spray ESI, Waters Co.). Pressures were measured in the collision cell thanks to a Pirani pressure gauge (AGP-L, Edwards Ltd.). MS/MS experiments were performed with O_2 (Alphagaz 2 grade with 99.9995% purity, Air Liquide France Industrie) as collision gas at pressures ranging from $3 \cdot 10^{-3}$ to $1 \cdot 10^{-2}$ mbar (uncorrected gauge reading) depending on the experiments. The source parameters were fixed as follows: capillary 3.50 kV, cone 35 V, extractor 10 V, drying gas flux 300 $L \cdot min^{-1}$, desolvation gas flux 20 $L \cdot min^{-1}$, desolvation temperature 20 °C, HM/LM resolution 15.0 (15.0/15.0 in MS/MS mode). In the ESI source, the $Cu^{(II)}$ complexes can be reduced in their $Cu^{(I)}$ analogous by electron capture from the solvent[32,33]. This is why more stable $Cu^{(II)}$ complexes were used, although $[Cu(R_2bpy)]OTf$ are relatively stable under air. Adduct ions corresponding to $[Cu(R_2bpy)(CH_3CN)]^+$ were mass-selected before collisions with O_2 occurred in the collision cell at collision voltages ranging from 3 to 10 V. $[Cu(R_2bpy)(CH_3CN)]^+$ adduct was mass-selected because of its strong intensity compared to the less intense signal of $[Cu(R_2bpy)]^+$ ion. To coordinate O_2, MS/MS experiments allowed for a ligand exchange between acetonitrile and O_2. Direct coordination on $[Cu(R_2bpy)]^+$ was also observed after its mass-selection, albeit in lower yields. The reactivity of $[Cu(R_2bpy)(O_2)]^+$ adducts towards various substrates was also probed thanks to home-made modifications on the QqQ instrument[28]. Acquisition time was set to 2 minutes at a scan rate of 90 $Th \cdot s^{-1}$ over a window of 90 Th. The baseline has been subtracted from all spectra and data presented in this chapter (80 %, with 2 parameters).

1.2. Samples

Phenanthroline (phen) and 4-4'-functionalized bipyridine ligands (R_2bpy) (Figure 1) were purchased from Sigma-Aldrich or TCI Europe and used as received. The corresponding Cu complexes were prepared by adding 1 equivalent of ligand to a solution of $Cu^{(II)}OTf_2$ in acetonitrile (CH_3CN). Solutions of $[Cu(R_2bpy)](OTf)_2$ were prepared in CH_3CN/H_2O (4:1 v/v) at $5 \cdot 10^{-5}$ M.

$Cu^{(I)}$- or $Cu^{(II)}$-bipyridyl complexes are formed very quickly in solution. With $[Cu(CH_3CN)_4]OTf$ as salt, the solution turns orange in a second. Structures of the complexes studied were characterized by direct injection ESI-MS at a flow rate of 20 µL.min^{-1}. Mass spectra for all solutions were recorded with parameters specified hereafter, and the spectra made with H_2bpy can be found as an example together with the modeling of isotopic distributions (Figures 2 and 3). Higher extractor voltages were used in order to fragment the more intense $[Cu(H_2bpy)(CH_3CN)]^+$ and observe the peaks corresponding to $[Cu(H_2bpy)]^+$, $[Cu(H_2bpy)(H_2O)]^+$ and $[Cu(H_2bpy)(N_2)]^+$ (the latter two were formed by association of H_2O and N_2 on $[Cu(H_2bpy)]^+$, respectively). They have been identified thanks to isotopic models. At lower source temperature, and lower extractor voltage, the peaks corresponding to $[Cu(H_2bpy)]^+$, $[Cu(H_2bpy)(H_2O)]^+$ and $[Cu(H_2bpy)(N_2)]^+$ ions are no longer observed. MS spectrum for each R_2bpy/phen compound are presented below, as well as the characterization of the $[Cu(R_2bpy)(CH_3CN)]^+$ and $[Cu(R_2bpy)(OTf)]^+$ adducts, which have been observed for each complex. Tested substrates for reactivity (phenol, 4-methoxyphenol, 2,5-ditertiobutylphenol, dihydroanthracene, isopropanol, benzyl alcohol) were purchased from Sigma-Aldrich. Benzyl alcohol was stored in glove box.

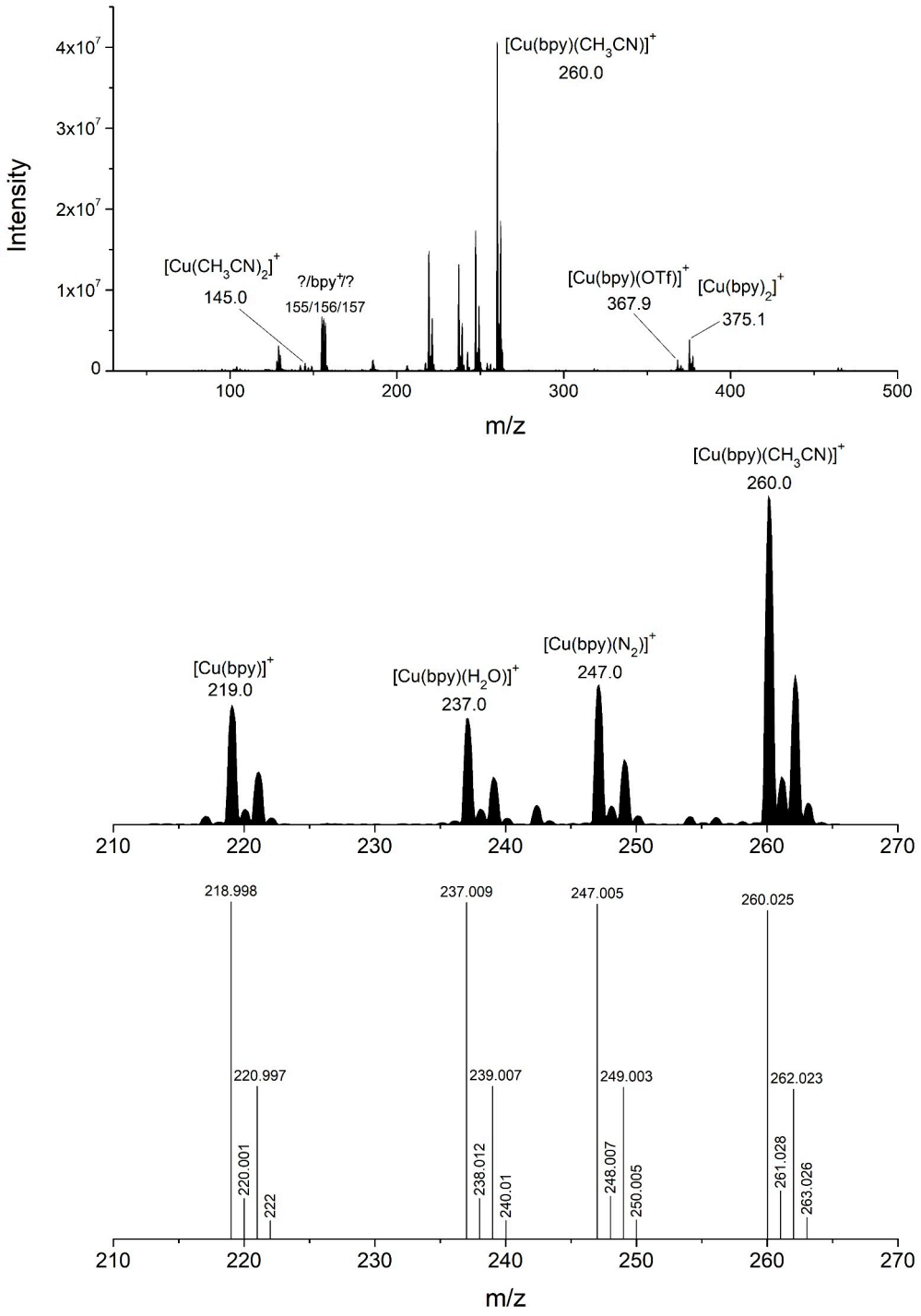

Figure 2: MS spectrum of a mixture of $Cu(OTf)_2$ ($5 \cdot 10^{-5}$ M) and one equivalent of H_2bpy (in CH_3CN/H_2O 4:1), and corresponding isotopic models. T source: 90°C, Extractor: 17 V.

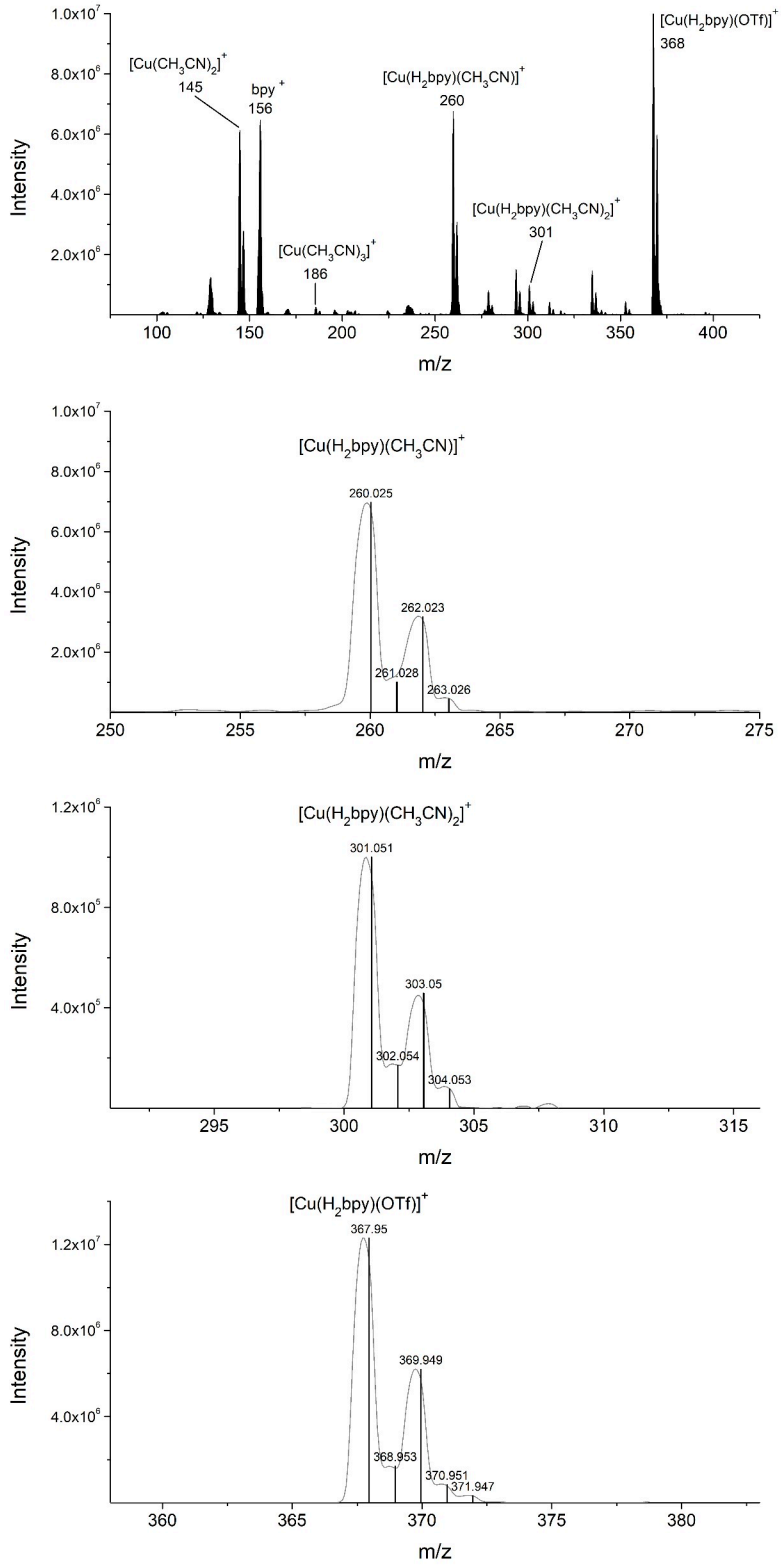

Figure 3: MS spectrum of a mixture of $Cu(OTf)_2$ ($5 \cdot 10^{-5}$ M) and one equivalent of H_2bpy (in CH_3CN/H_2O 4:1), and corresponding isotopic models. T source: 20°C, Extractor: 10 V.

1.3. Characterization of adducts

$[Cu(R_2bpy)(CH_3CN)]^+$ and $[Cu(R_2bpy)(OTf)]^+$ have been observed for each R_2bpy and phen ligand. In the following section, the measured m/z are compared to theoretical values. L stands for R_2bpy in the following paragraph.

H_2bpy: $[Cu(L)(CH_3CN)]^+$ found m/z 260.0 (theoretical 260.025), $[Cu(L)(OTf)]^+$ fd 367.9 (th 367.950)
$(OMe)_2bpy$: $[Cu(L)(CH_3CN)]^+$ fd m/z 320.0 (th 320.046), $[Cu(L)(OTf)]^+$ fd m/z 427.9 (th 427.971)
Me_2bpy: $[Cu(L)(CH_3CN)]^+$ fd m/z 288.1 (th 288.056), $[Cu(L)(OTf)]^+$ fd m/z 396.0 (th 395.982)
tBu_2bpy: $[Cu(L)(CH_3CN)]^+$ fd m/z 372.2 (th 320.150), $[Cu(L)(OTf)]^+$ fd m/z 480.2 (th 480.076)
$(NO_2)_2bpy$: $[Cu(L)(CH_3CN)]^+$ fd m/z 350.0 (th 349.995), $[Cu(L)(OTf)]^+$ fd m/z 458.0 (th 457.921)
$(CO_2Me)_2bpy$: $[Cu(L)(CH_3CN)]^+$ fd m/z 375.9 (th 376.036), $[Cu(L)(OTf)]^+$ fd m/z 483.8 (th 483.961)
phen: $[Cu(L)(CH_3CN)]^+$ fd m/z 284.0 (th 284.025), $[Cu(L)(OTf)]^+$ fd m/z 391.9 (th 391.950)

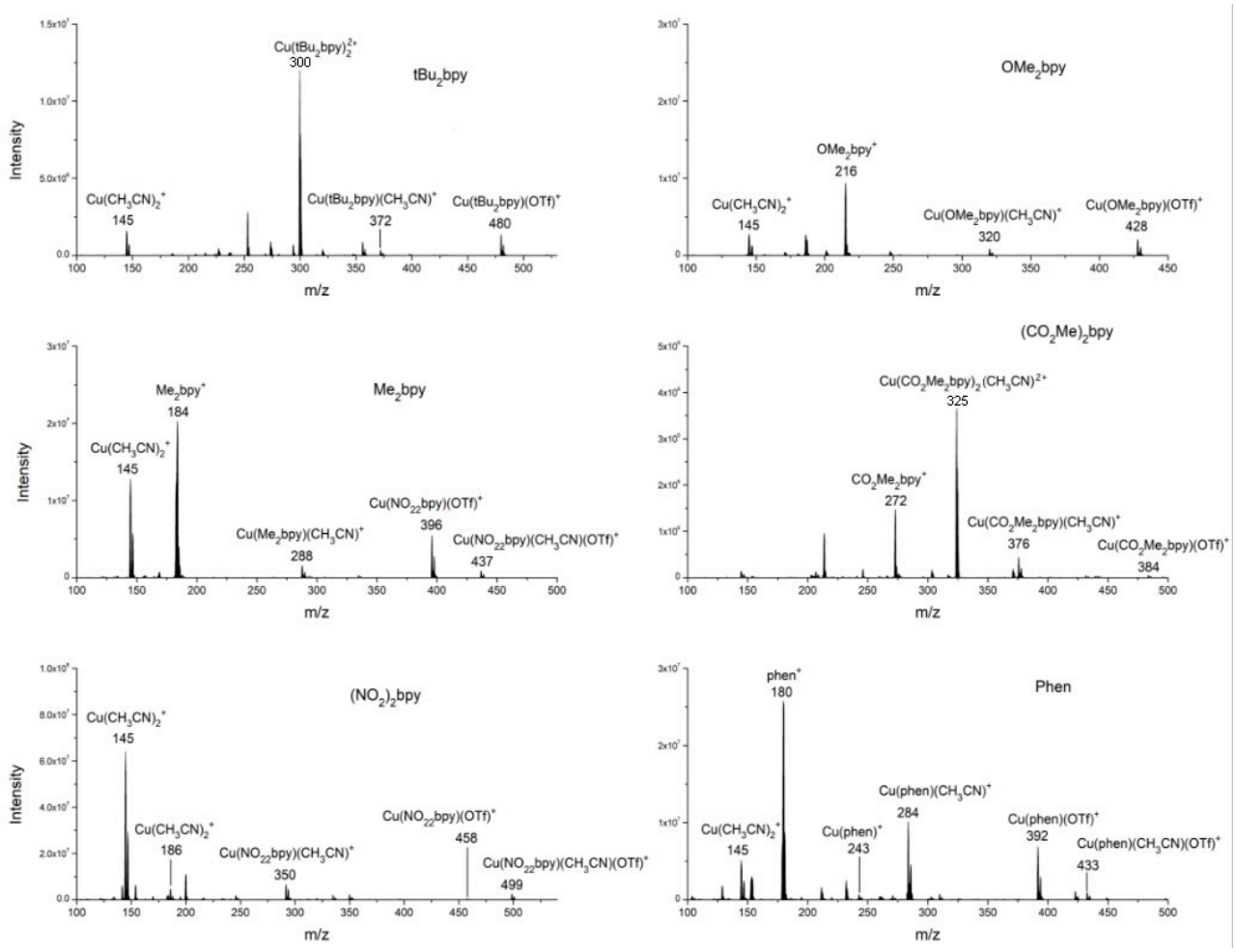

Figure 4: MS spectra of the Cu-bipyridyl complexes used in this study.

1.4. DFT calculations

Geometry optimization and frequency calculations were performed at the B3LYP/6-31+G(d,p) level of theory[34]. B3LYP has proven its ability to give reliable coordination energies of ligands on $Cu^{(I)}$ and was used many times on that purpose[35,36]. The Gaussian16 software package[37] was used for all calculations. Forces have been computed at the first point of optimization process and default parameters have been used for convergence. Due to the $(4s)^0$ $(3d)^{10}$ configuration of $Cu^{(I)}$, singlet state was considered for all Cu complexes. Triplet state was considered as ground state for all O_2 adducts[20]. Side-on coordination of O_2 is proposed for R_2bpy complexes, by taking into account the low steric hindrance of the ligands. A planar geometry was validated by preliminary calculations. End-on triplet spin state as well as side-on and end-on singlet spin state coordination have also been tested, and were found less stable in energy. Calculated Bond Dissociation Energies (BDEs) are presented in terms of Δ(E+ZPE), according to the following equation:

$$BDE = \Delta(E+ZPE)_{calc,\,L} = (E_{LCu+} + ZPE_{LCu+} + E_{O2} + ZPE_{O2}) - (E_{LCuO2+} + ZPE_{LCuO2+})$$

Bader charges were calculated with the help of the Henkelman's code[38]. We used a medium grid (6 points/Bohr) to generate files in Gaussian cube format.

2. Results and discussion

2.1. Gas phase coordination of O_2 by $[Cu(R_2bpy)]^+$ complexes

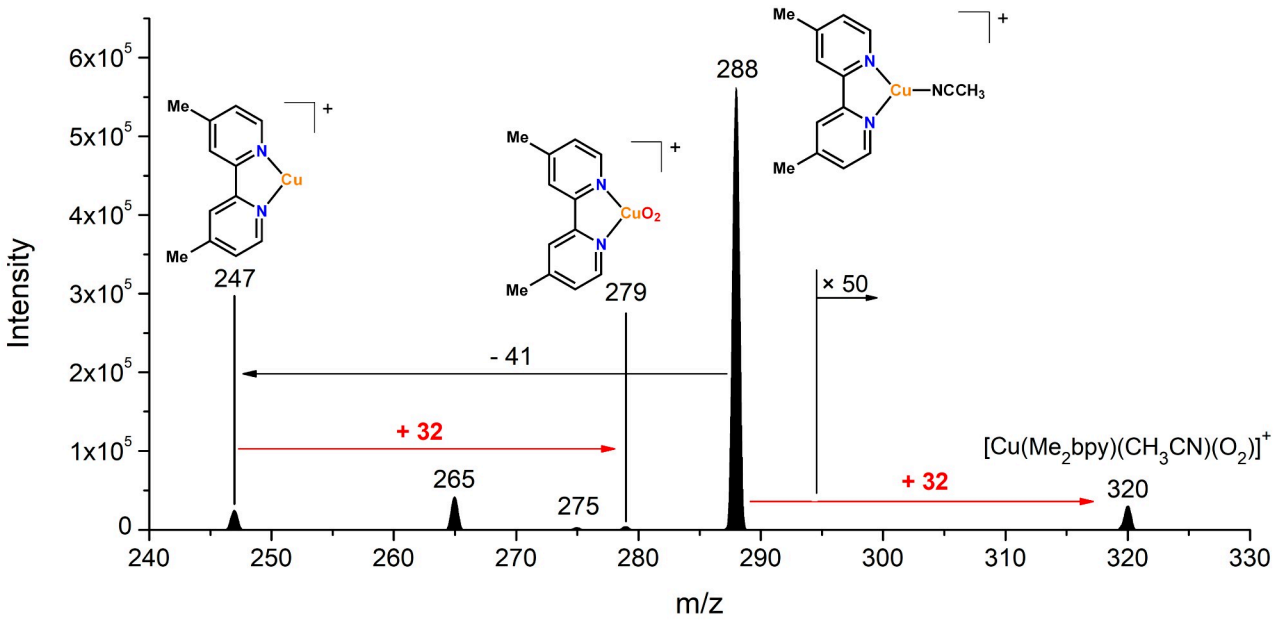

Figure 5: MS/MS spectrum of $[Cu(Me_2bpy)(CH_3CN)]^+$ with $P(O_2) = 5 \cdot 10^{-3}$ mbar and $V_{coll} = 5$ V in the collision cell.

The coordination of O_2 on $[Cu(R_2bpy)]^+$ complexes was observed after mass-selection of the $[Cu(R_2bpy)(CH_3CN)]^+$ complexes. The collision of these precursors with O_2 led to the release of CH_3CN and the coordination of O_2 by the supposedly resulting $[Cu(R_2bpy)]^+$ ion. We observed a higher peak intensity of $[Cu(R_2bpy)(O_2)]^+$ when the temperature of the ESI source was set at room temperature (20 °C) even if signal intensity for the precursor ion was lower. Coordination with traces of H_2O (+18, m/z 265) and N_2 (+28, m/z 275), coming from the solvent and the ionization source, were also detected. Cu-bipyridyl complexes seem to be a good sensor of the presence of small ligands in the gas phase and could be used on that purpose. One may also expect gas-phase back coordination of CH_3CN as it was used as solvent, however with low yields as the residual pressure in the collision chamber without insertion of O_2 was $2.4 \cdot 10^{-5}$ mbar. The coordination of O_2 was also observed on the precursor ion (Figure 5), albeit with low peak intensity. So, the formation of $[Cu(R_2bpy)(O_2)]^+$, the complex of interest, can occur either by the coordination of O_2 on $[Cu(R_2bpy)(CH_3CN)]^+$ followed by decoordination of acetonitrile, or by the decoordination of CH_3CN, followed by O_2 coordination on $[Cu(R_2bpy)]^+$. Considering the low intensity of the M+32

adduct, the first pathway seems to be energetically less favorable. Moreover, our DFT calculations have shown that the dissociation energy of $(R_2bpy)Cu\text{-}CH_3CN$ is between 2.1 and 2.8 times larger than that of$(R_2bpy)Cu\text{-}O_2$, depending on the nature of the R group, being higher with R an electron-withdrawing group (see Table 1, p.142). The one-step exchange mechanism, through a TS, might also be considered. However, no TS structure was found despite our efforts. Moreover, the low intensity of $[Cu(R_2bpy)(O_2)]^+$ peak compared to the intensity of M-41 peak allows to dismiss this mechanism.

2.2. Optimal O_2 pressure and collision voltage for $[Cu(R_2bpy)(O_2)]^+$ formation

Variations of the intensities of some selected peaks relative to the TIC (Total Ion Current corresponding to the sum of intensities of all peaks) as a function of the collision voltage Vcoll at different O2 pressures are presented in Figure 6 (given in percentage on the diagrams). Variations of the TIC (Figure 6.a) and of the ratio of peaks intensities $[Cu(R_2bpy)(O_2)]^+/[Cu(R_2bpy)]^+$ (Figure 6.f) against V_{coll} are also presented at different O_2 pressures. For the sake of clarity, results obtained with Me_2bpy ligand only are presented here as all other ligands exhibit similar behavior. In the case of R = NO_2, results were also similar, except the much lower peak intensity observed for the $[Cu(R_2bpy)(CH_3CN)(O_2)]^+$ complex.

The TIC is representative of the peak intensities and thus of the quality of signal (see Figure 2.a). Its value may be affected by mass-dependent ion scattering leading to erroneous relative peak intensities. It is therefore important to keep it at its highest value and ensure no distortion is observed. At the lowest pressure ($3\cdot10^{-3}$ mbar), the TIC decreases as the collision voltage is increased, which is the sign of ion loss (either precursor or some fragment ions). At higher pressures, one observes more stable TIC as a function of collision voltage although it is accompanied by a global decrease when the O_2 pressure is increased. Slightly higher TIC is obtained at 5 V, which may be attributed to the refocusing of ion beam towards the optical line and the detector without producing much scattering. Accordingly, best experimental conditions should then be $5\cdot10^{-3}$ mbar and 5 V collision voltage.

The collision voltage, which is applied to the ions by an electric potential in the collision cell, results in the acceleration of the precursor ions. As a consequence of this acceleration,

collisions with the O_2 gas are more energetic, leading to an increase in the energy transferred into the adducts and, eventually, to a larger amount of fragmentation. This is clearly observed for the precursor ion peak at all pressures of O_2 (see Figure 6.b) leading ultimately to $[Cu(R_2bpy)]^+$ fragment ions (see Figure 6.e). Increasing O_2 pressure essentially, but not only, decreases the amount of fragmentation: on the one hand, the multiple collisions experienced by the precursor ions indeed cool down the ions by energy transfer from internal to kinetic energy of O_2 (see Figures 2.b and 2.e) but, on the other hand, there is also association with O_2 to form $[Cu(R_2bpy)(CH_3CN)(O_2)]^+$ or $[Cu(R_2bpy)(O_2)]^+$ (Figures 6.c and 6.d) that is increased due to 1) more numerous collisions and 2) precursor ions that are slowed and cooled down by successive collisions.

$[Cu(R_2bpy)(CH_3CN)(O_2)]^+$ remains in low abundance relative to other peaks (I_{peak} = 0.15 %, see Figure 6.d) and, it even totally disappears at low pressure and high voltage. The largest peak intensity was observed at largest pressure and lowest voltage whatever the ligand substituent. The most intense peak was obtained with R = tBu (I_{peak} = 0.86 %). This confirms the complex is of quite low stability (determined by DFT to be endoenergetic by ~24-26 $kJ \cdot mol^{-1}$ at 0 K, depending on the substituent R). As discussed above, when considered separately, the coordination of CH_3CN on Cu is stronger than the coordination of O_2. Then, high collision voltage applied in the reaction cell prevents the formation of/tend to dissociate $[Cu(R_2bpy)(CH_3CN)(O_2)]^+$ adduct ions to regenerate precursor ions, because the Cu-O_2 bond is more easily broken than the Cu-CH_3CN bond. This is partly compensated by the multiple collisions with O_2 at larger pressures, although a similar decrease in intensity is observed at larger collision voltages. This result suggests cooler conditions are obtained at $1 \cdot 10^{-2}$ mbar and 3 V collision voltage[39–41].

On the contrary, the intensity of the $[Cu(R_2bpy)]^+$ peak increases with the applied collision voltage (Figure 2.e), while the intensity of the $[Cu(R_2bpy)(CH_3CN)]^+$ precursor ion peak decreases corresponding to an increase in the fragmentation at higher collision voltage (Figure 2.b). This process is less efficient at larger O_2 pressure in the collision cell. Once again, it suggests that high pressure facilitates ion cooling and thermalization by increasing the number of collisions[39–41] but also association reaction with O_2. The $[Cu(R_2bpy)(O_2)]^+$ peak indeed increases with the pressure and the collision voltage, except for $P(O_2) = 3 \cdot 10^{-3}$ mbar (see Figure 6.c). Similar observations can be made with other functional groups.

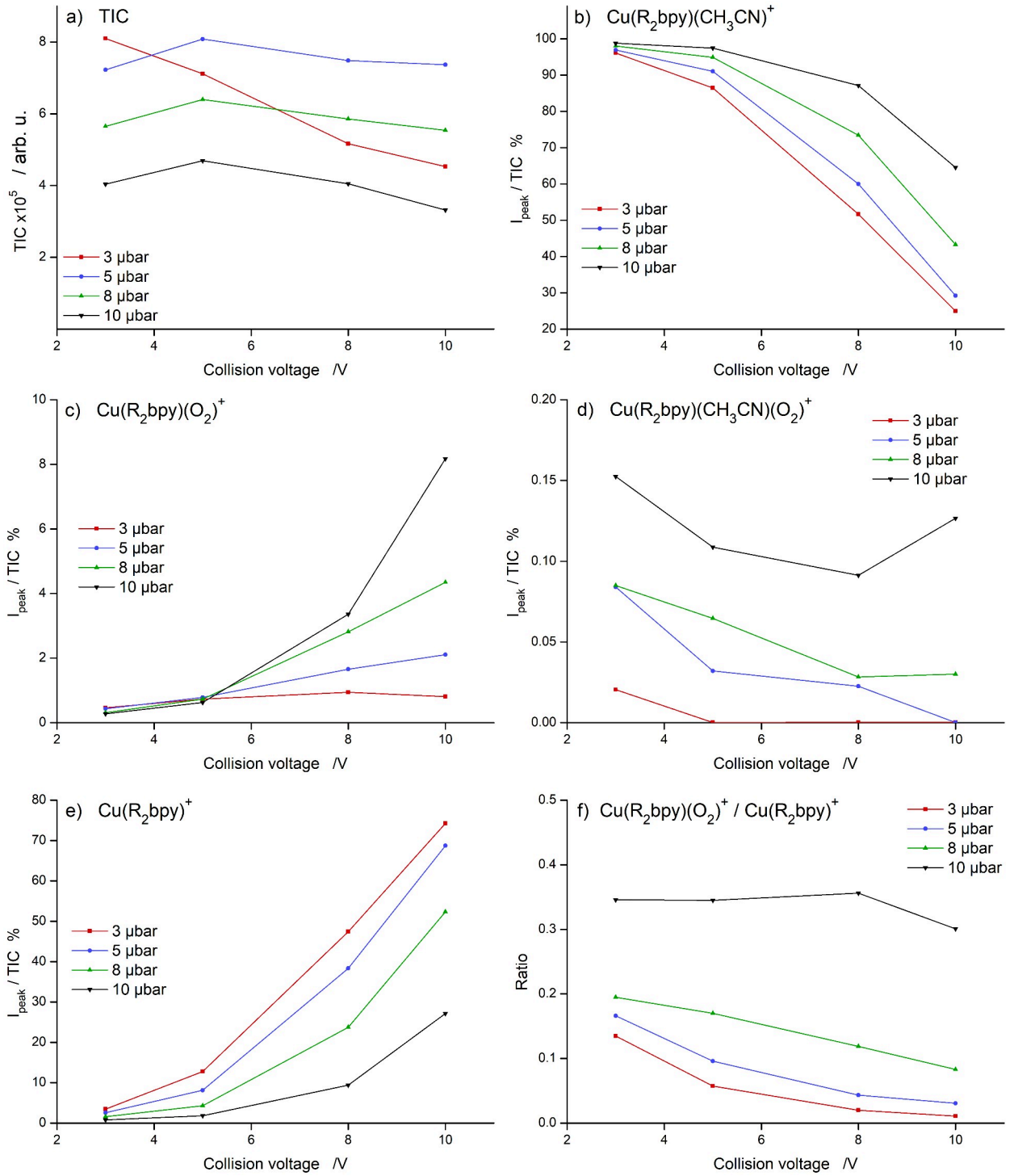

Figure 6: Variations of MS/MS peak intensities over TIC (in %) of some ions as a function of collision voltage (from 3 to 10 V) at different O_2 pressures (from 3 to 10 µbar). R stands for Me. Diagrams (a) and (f) show the Total Ion Current (TIC) and $[Cu(R_2bpy)(O_2)]^+/[Cu(R_2bpy)]^+$ ratio of peak intensities.

These observations are consistent with the fact that a high pressure of O_2 combined with high V_{coll} favors the CH_3CN/O_2 exchange via a two-step ligand-exchange mechanism: $[Cu(R_2bpy)(CH_3CN)(O_2)]^+$ complex is formed under soft conditions (Figure 2.d) but quickly dissociates to regenerate the precursor ion, which in turn dissociates to form $[Cu(R_2bpy)]^+$ eventually coordinating O_2 at large enough O_2 pressures. However, 4,4'-dinitro-bipyridyl ligand gave only small O_2 adduct ion peaks due to their electron-withdrawing character that destabilizes the CuO_2 bonding. Poor signal for this compound did not permit it to be considered in the following of this study.

Finally, concerning the choice of experimental conditions to study the influence of functional groups on O_2 coordination, a compromise has to be made. Peak intensities of $[Cu(R_2bpy)(O_2)]^+$ and $[Cu(R_2bpy)]^+$ were thus measured at rather large pressure of O_2 ($8 \cdot 10^{-3}$ mbar) and low collision voltage (5 V) in order to maximize both the TIC and the ratio of peak intensities $[Cu(R_2bpy)(O_2)]^+/[Cu(R_2bpy)]^+$.

2.3. Linear energy relationship

Hammett's equation has been successfully applied to derive structure-activity relationships in various chemical systems[42]. Therefore, we have evaluated the gas-phase affinity towards O_2 of our list of substituted ligands (R = $-NO_2$, $-CO_2Me$, -H, -Me, -tBu, -OMe, phen) coordinating Cu^+ using this approach. Tandem MS experiments were then performed in the previously determined optimal conditions (see above), namely MS/MS at 5 V acceleration voltage and 8 µbar O_2 pressure in the collision chamber and, after mass-selection of $[Cu(R_2bpy)(CH_3CN)]^+$. However, in the case of NO_2 group, the ion peak intensity corresponding to $[Cu(R_2bpy)(O_2)]^+$ was too weak and the background noise difficult to remove leading to unreliable experimental data (see Table 1 for a full dataset). According to the above discussion, one may reasonably assume the ratio bpy^R of MS/MS peak intensities for $[Cu(R_2bpy)(O_2)]^+$ and $[Cu(R_2bpy)]^+$ is informative of a gas-phase equilibrium constant for O_2 association (thermalization of ions inside the collision chamber[40]. Then, by comparing, at constant experimental conditions, bpy^R ratio with the same ratio obtained with L = H_2bpy, namely bpy^H, one obtains some indications on the gas phase O_2 affinity of $[Cu(R_2bpy)]^+$ normalized to the O_2 affinity of $[Cu(H_2bpy)]^+$. This is confirmed with the direct linear correlation obtained between the $\log(bpy^R/bpy^H)$ and Hammett parameter (see Figure 7, left-hand side diagram): a high coefficient of determination ($R^2 = 0.975$) and well-balanced data dispersion (homoscedastic distribution) are obtained together with a correct sequencing of data according to electron-donating

power (R = -OMe > -tBu > -Me > -H). However, when considering an electron-withdrawing group such as $-CO_2Me$ (other groups were not evaluated due to poor signal quality), one observes a significant deviation from the previously determined linearity. At this stage of the discussion, we anticipate that the latter deviation from linearity may be attributed to solvation effect. Hammett's parameters were indeed obtained in aqueous medium while our MS/MS measurements were performed with isolated molecules and relate more closely to intrinsic molecular properties. DFT calculations were therefore performed to evaluate Bond Dissociation Energies (BDEs) for $[(R_2bpy)Cu\text{-}O_2]^+$. Considering the thermalization hypothesis holds for fragment and O_2 adduct ions, the above-mentioned ratio bpy^R/bpy^H may directly be related to the computed BDEs.

The gas-phase equilibrium constant for the association reaction between O_2 and $[Cu(R_2bpy)]^+$ complexes can be written as a function of partial pressures P of the species:

$$K_{eq}^{R} = \frac{P([Cu(R_2bpy)(O_2)]^+)}{P([Cu(R_2bpy)]^+).P(O_2)} \qquad \text{Equation 1}$$

Considering the MS/MS peak intensities are in a simple proportion with the abundance in the gas-phase of the considered species (the proportionality constant being equivalent for different species), one may then write it as:

$$K_{eq}^{R} = \frac{I([Cu(R_2bpy)(O_2)]^+)}{I([Cu(R_2bpy)]^+).P(O_2)} \qquad \text{Equation 2}$$

The quantity bpy^R/bpy^H is defined as the following ratio (with H corresponding to the simple bipyridyl ligand and R a 4,4'-di-functionalized one) in which MS/MS peak intensities were obtained from the same experimental conditions (pressure of O_2 in the collision chamber and collision voltage):

$$\frac{bpy^R}{bpy^H} = \frac{I([Cu(R_2bpy)(O_2)]^+) \,/\, I([Cu(R_2bpy)]^+)}{I([Cu(H_2bpy)(O_2)]^+) \,/\, I([Cu(H_2bpy)]^+)} \qquad \text{Equation 3}$$

Assuming we are in a thermal conditions, bpy_R/bpy_H is then also the ratio of equilibrium constants (after cancellation of O_2 pressure in Equation 1) and can be written accounting for the Van't Hoff equation:

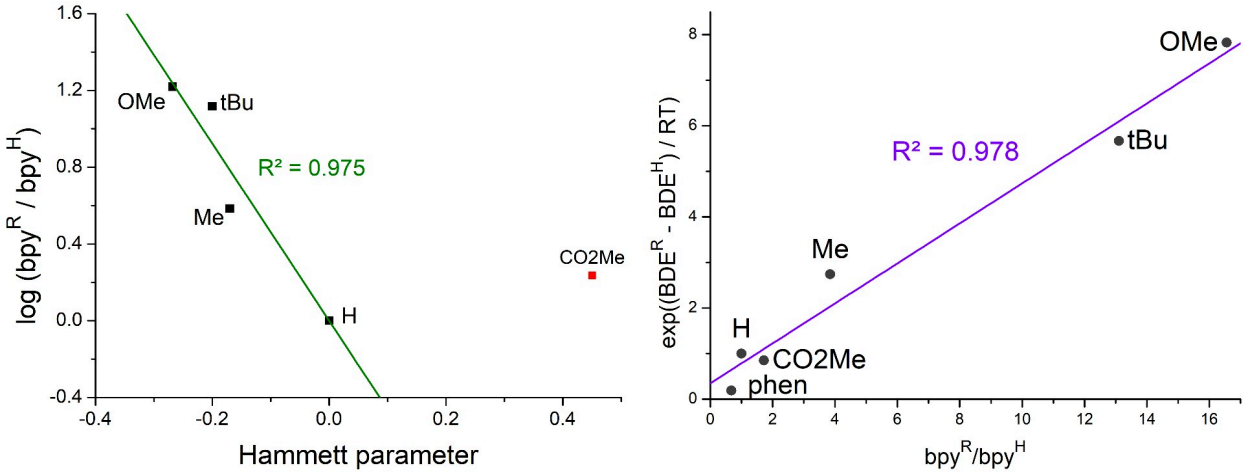

Figure 7: Left: Hammett plot of bpy^R/bpy^H ratio with consideration of electron-donating R groups only (red). Right: exp((BDE^R-BDE^H)/RT) against bpy^R/bpy^H ratio of MS/MS peak intensities, obtained at $P(O_2) = 8 \cdot 10^{-3}$ mbar and $V_{coll} = 5$ V.

$$\frac{bpy^R}{bpy^H} = \frac{K_{eq}^R}{K_{eq}^H} = \frac{\exp(-\Delta G^R / R_{pg} T)}{\exp(-\Delta G^H / R_{pg} T)} \qquad \text{Equation 4}$$

with ΔG^R corresponding to the Gibbs free energy for the coordination of O_2 on the $[Cu(R_2bpy)]^+$ complexes. Then:

$$\frac{K_{eq}^R}{K_{eq}^H} = \frac{\exp(-\Delta H^R / R_{pg} T + T \Delta S^R / R_{pg})}{\exp(-\Delta H^H / R_{pg} T + T \Delta S^H / R_{pg})} \qquad \text{Equation 5}$$

$$\frac{K_{eq}^R}{K_{eq}^H} = \frac{\exp(-\Delta((E_{elec} + ZPE)^R + \Delta E_{corr}^R) / R_{pg} T + T \Delta S^R / R_{pg})}{\exp(-\Delta((E_{elec} + ZPE)^H + \Delta E_{corr}^H) / R_{pg} T + T \Delta S^H / R_{pg})} \qquad \text{Equation 6}$$

with $\Delta(E_{elec} + ZPE)^R$ the coordination energy at 0 K (including the electronic energy and the Zero-Point vibrational Energy ZPE for the ligand with R as substituent), E_{corr}^R the thermal corrections to the electronic energy (including translational, rotational and vibrational), T the temperature of ion population, ΔS^R the corresponding activation entropy and R_{pg} the perfect gas constant. $\Delta(E_{elec} + ZPE)^R$ is the opposite of the BDE for the ligand with R substituent. Assuming variations in the thermal corrections to the electronic energies for the coordination of O_2 on $[Cu(H_2bpy)]^+$ and $[Cu(R_2bpy)]^+$ complexes are similar ($\Delta E_{corr}^H \approx \Delta E_{corr}^R$) and that the difference in the entropy of coordination, $\Delta S^R - \Delta S^H$, is negligible, Equation 6 can be simplified to Equation 7.

$$\frac{bpy^R}{bpy^H} = \frac{K_{eq}^R}{K_{eq}^H} = \exp\left(\frac{BDE^R - BDE^H}{R_{pg}T}\right) \qquad \text{Equation 7}$$

With the above expression there is a simple direct linear correlation between measured association reactions (left-hand side) and calculated electronic energies (right-hand side). More precisely, a direct linear correlation is expected to be found between $exp[(BDE^R\text{-}BDE^H)/RT]$ and the MS/MS peak intensities ratio bpy^R/bpy^H.

As shown in Figure 7 (right-hand side diagram), the resulting plot exhibits a linear trend (R^2 = 0.978), demonstrating that a simple correlation can indeed be made between gas-phase experimental measurements of O_2 affinity and calculated BDEs (see Table 1 for a full dataset). However, by using T = 298.15 K (ambient temperature), the linear correlation was found with the slope a = 0.44. Adjusting the temperature parameter T (the unique parameter of the model), the linear regression line was optimized to achieve a slope a = 1 that corresponds to our model prediction. Interestingly, it optimized to T = 215 K (and R^2 = 0.980), which suggests there is significant cooling of the ions in our analysis. A more detailed kinetic modeling of the collisions would be necessary to investigate this effect. Calculated BDE for $[(phen)Cu\text{-}O_2]^+$ was found 3 $kJ{\cdot}mol^{-1}$ lower than that of $[(H_2bpy)Cu\text{-}O_2]^+$, which is consistent with the expected lower electron-donor strength of the phen vs. bpy ligand[43] and in agreement with our experiments. As a conclusion, it appears gas-phase experimental data are well in line with DFT computed O_2 affinities and, it does not show any significant sign of deviation from the expected linear correlation from our model.

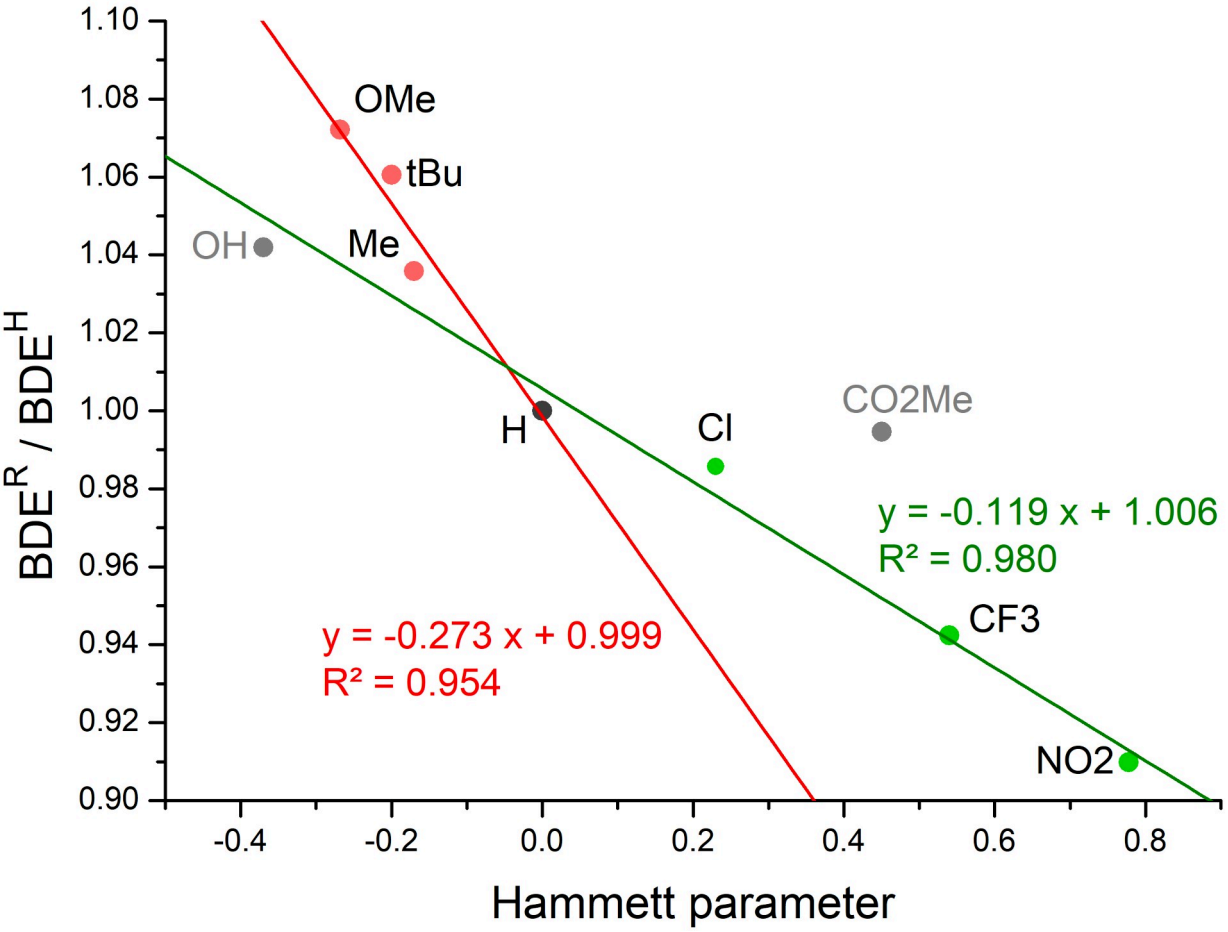

Figure 8: DFT computed Bond Dissociation Energies (BDEs), for different R substituents, relative to BDE for R = H, as a function of Hammett parameter. Substituents are separated into electron-donating and electron-withdrawing groups and linear correlations are plotted accordingly (-OH and -CO_2Me groups are not considered, see text).

Going a step further, we evaluated the results of our DFT calculations with reported Hammett's parameters for a larger set of R substituents by including the electron-withdrawing group -OH and electron-donor groups -Cl, -CF_3 and -NO_2. Computed BDEs of $[(R_2bpy)Cu\text{-}O_2]^+$, normalized to data with R = H, namely BDE^R/BDE^H, are reported as a function of Hammett's parameter in Figure 8. The plot clearly shows two different trends according to the ability of the substitution for electrodonation, however, with two outliers: -OH and -CO_2Me groups (not included in the linear regression presented herein). Not surprisingly, those two groups are expected to interact strongly by hydrogen-bonding with water solvent, which may lead to deviation from the intrinsic electronic properties. In the case of R = -CO_2Me, the larger reported Hammett parameter suggests hydrogen-bonding increases the affinity for O_2 by drawing out the electronic density from O atoms and the pyridine groups. On the contrary, in the case of -OH, the lower reported Hammett value

suggests this effect is strongly compensated by the hydrogen-bonding towards alcoholic H atom. The two linear trends observed are: i) for electron-donating groups (R^2 = 0.980, without -CO_2Me) and ii) for electron-withdrawing groups (R^2 = 0.954, without -OH) resulting in different slopes but identical intercepts corresponding to R = H. When enforcing the intercept to 1, the coefficients of determination are increased to 0.988 and 0.986 respectively. The deviation observed experimentally with R = -CO_2Me in Figure 7 (left diagram), is confirmed with our DFT analysis of Hammett parameters and may be due, on one hand, to solvent effect (and hydrogen-bonding) but also, on the other hand, to a different trend in the correlation between the BDEs and Hammett parameters for the two groups of substituents according to the two trend lines obtained in Figure 8.

Substituent	Hammett value	BDE(Cu-O_2)	BDE(Cu-$NCCH_3$)	exp(BDE^R-BDE^H)/RT)	bpy^R/bpy^H
OMe	-0.27	76.7	162.2	7.83	16.56
tBu	-0.20	75.9	162.9	5.67	13.11
Me	-0.17	74.1	165.6	2.74	3.84
H	0.00	71.6	169.3	1.00	1.00
Cl	0.23	70.6	--	0.67	--
CO_2Me	0.45	71.2	169.5	0.85	1.72
CF_3	0.54	67.5	--	0.19	--
NO_2	0.78	65.1	182.3	0.07	--
phen	---	67.5	165.7	0.19	0.68

Table 1: Calculated vs experimental data for the coordination of O_2 on $[Cu(R_2bpy)]^+$ complexes. Bond Dissociation Energies are given in $kJ{\cdot}mol^{-1}$.

2.4. Electronic structures of the $[Cu(R_2bpy)(O_2)]^+$ complexes

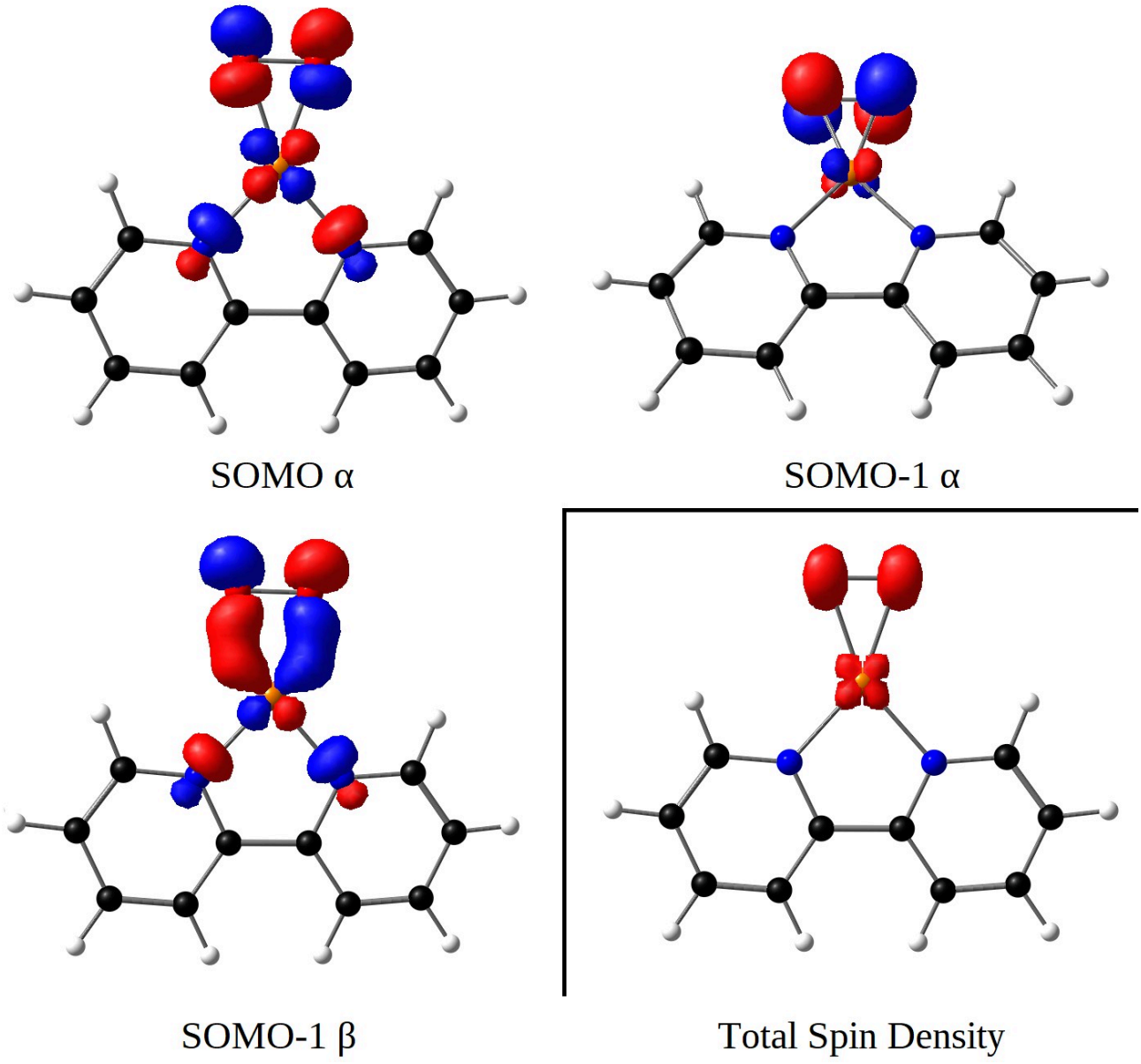

Figure 9: Chosen molecular orbitals of $[Cu(H_2bpy)(O_2)]^+$. Total Spin Density of the complex is also shown (bottom, right). An isovalue of 0.07 was chosen for all orbitals.

According to DFT calculations, side-on triplet geometry for $[Cu(H_2bpy)(O_2)]^+$ is 22 kJ·mol^{-1} more stable than end-on triplet geometry. It is also 53 kJ·mol^{-1} more stable than the side-on singlet geometry. Some molecular orbitals of $[Cu(H_2bpy)(O_2)]^+$ are presented in Figure 9. They show the bonding interaction of π_σ^* (O_2) and $d_{x^2-y^2}$ (Cu) (SOMO-1 β) and the antibonding interactions between π_σ^* (O_2) and $d_{x^2-y^2}$ (Cu) (SOMO α) and π_v^* (O_2) and d_{xy} (Cu) (SOMO-1 α). The Mulliken spin density (total spin density on Figure 9) is mainly located on the $Cu(O_2)$ moiety (0.354 on the Cu

atom and 0.770 on each O atom). The totally planar conformation is explained by the antibonding interaction between π_σ* of O_2 and $d_{x^2-y^2}$ orbital of Cu, itself involved in the coordination with the lone pairs of N donor atoms. The same behavior was observed for all other ligands. The Bader charge on the Cu atom increases from 0.545 e in $[Cu(H_2bpy)]^+$ to 0.982 e in $[Cu(H_2bpy)(O_2)]^+$. Cu charge doubling can be associated with the increase in the formal oxidation state from +I to +II, usually expected with the binding of O_2 on a $Cu^{(I)}$ center. The O_2 charge indeed amounts to -0.378 e. The O-O bond length is 1.294 Å, close to the O-O bond length in the superoxo ($O_2^{\bullet-}$) anion (1.28 Å)[44]. The charge distribution in the $Cu(O_2)$ moiety is hence $[Cu^{2+}][O_2^{\bullet-}]$.

Considering the other $[Cu(R_2bpy)(O_2)]^+$ derivatives, going from the most electron-withdrawing NO_2 to the very electron-donating OMe groups, one observe than the Bader charge on the Cu atom is increased by 0.022 e while it is decreased by 0.036 for O_2. The O-O distance varies from 1.289 Å to 1.297 Å. The Mulliken spin density on Cu atom is reduced by 0.036, while it is increased by 0.060 on O_2 moiety (see Table 2 for a full dataset). These changes are small, indicating that the electronic variation induced by the nature of the R groups in R_2bpy ligand mainly influence the strength of O_2 binding on the Cu center. However, a higher absolute Bader charge and Mulliken spin density on O atoms reveal that O_2 is more efficiently activated with electron-donating groups.

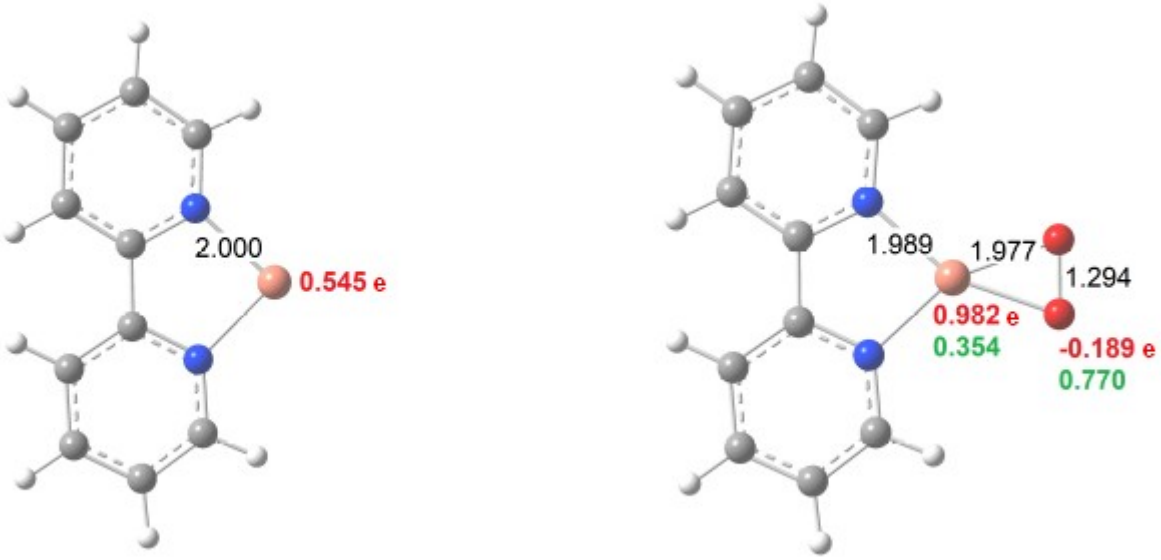

Figure 10: Structures of $[Cu(H_2bpy)]^+$ (left), $[Cu(H_2bpy)(O_2)]^+$ (right) calculated at the B3LYP/6-31+G(d,p) level of theory. Some important distances (in Å, black), Bader charges (bold red) and Mulliken spin densities (bold green) are indicated.

R	OO (Å)	CuO (Å)	CuN (Å)	Cu charge	O_2 charge	MSD Cu	MSD O_2
OMe	1.297	1.976	1.979	0.997 e	-0.388 e	0.3719	1.5158
tBu	1.297	1.977	1.982	0.981 e	-0.394 e	0.3635	1.5216
Me	1.296	1.977	1.985	0.995 e	-0.379 e	0.3579	1.5289
H	1.294	1.977	1.989	0.982 e	-0.377 e	0.3537	1.5394
CO_2Me	1.294	1.978	1.990	0.979 e	-0.369 e	0.3571	1.5409
NO_2	1.289	1.981	2.001	0.975 e	-0.315 e	0.3359	1.5756
phen	1.292	1.982	2.002	0.979 e	-0.348 e	0.3468	1.5518

Table 2: Some bond lengths, Bader charges and Mulliken spin densities along the series of R_2bpy and phen ligands.

2.5. Reactivity of the $Cu^{(II)}(O_2^{\bullet-})$ adducts

In the condensed phase, the expected reactivity of the unencumbered $Cu^{(II)}(O_2^{\bullet-})$ (i.e. superoxo) model complexes is the reaction with a second $[Cu(L)]^+$ moiety leading to the formation of a dinuclear complex $[L_2Cu_2^{(II)}(\mu-O_2)]$ [9]. The O_2 ligand can be found in η^1-η^1 or in η^2-η^2 binding mode, depending on the steric hindrance of the L ligand. Working in the gas phase prevents the formation of a μ-O_2 dinuclear complex. The mass spectrometer we used has been home-modified in order to perform reactivity experiments in the gas phase[25]. In our mass spectrometer, the $Cu^{(II)}(O_2^{\bullet-})$ adducts could be formed before the first quadrupole by introducing a suitable pressure of O_2 in the first hexapole. Further reactivity of the superoxo intermediates towards various substrates known as radical scavengers or having a weak C-H or O-H bond could thus be evaluated. The good affinity of $[Cu(R_2bpy)]^+$ for O_2 allowed the formation of $[Cu(R_2bpy)(O_2)]^+$ in sufficient yields in the first hexapole. The reactivity of $[Cu(R_2bpy)(O_2)]^+$ with various substrates such as isopropanol, benzyl alcohol, phenol, p-methoxy-phenol, 2,5-ditertiobutylphenol and dihydroanthracene were thus investigated. However, substrate coordination was sometimes observed on $[Cu(R_2bpy)(O_2)]^+$ (for example with alcohols), but with no subsequent reactivity, except the release of O_2. Most of the time, nothing was observed at all. This result may indicate that the substrate is in too low concentration in the gas phase to observe its coordination (DHA, phenols), or that it just played the role of a collision gas. These observations are consistent with the fact that the calculated Cu-O_2 bond dissociation energies are lower than the C-H or the O-H bond dissociation energy of the considered substrates, and accordingly the Cu-O_2 bond should thus break first.

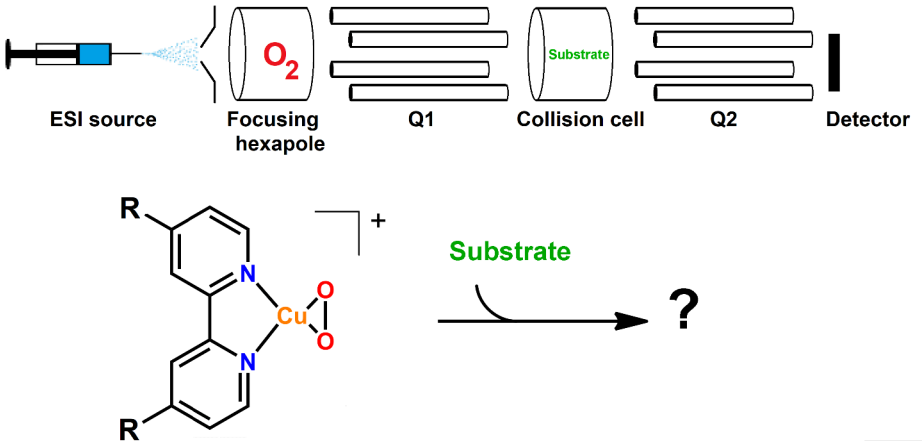

Figure 11: Reactivity studies on our home-modified apparatus.

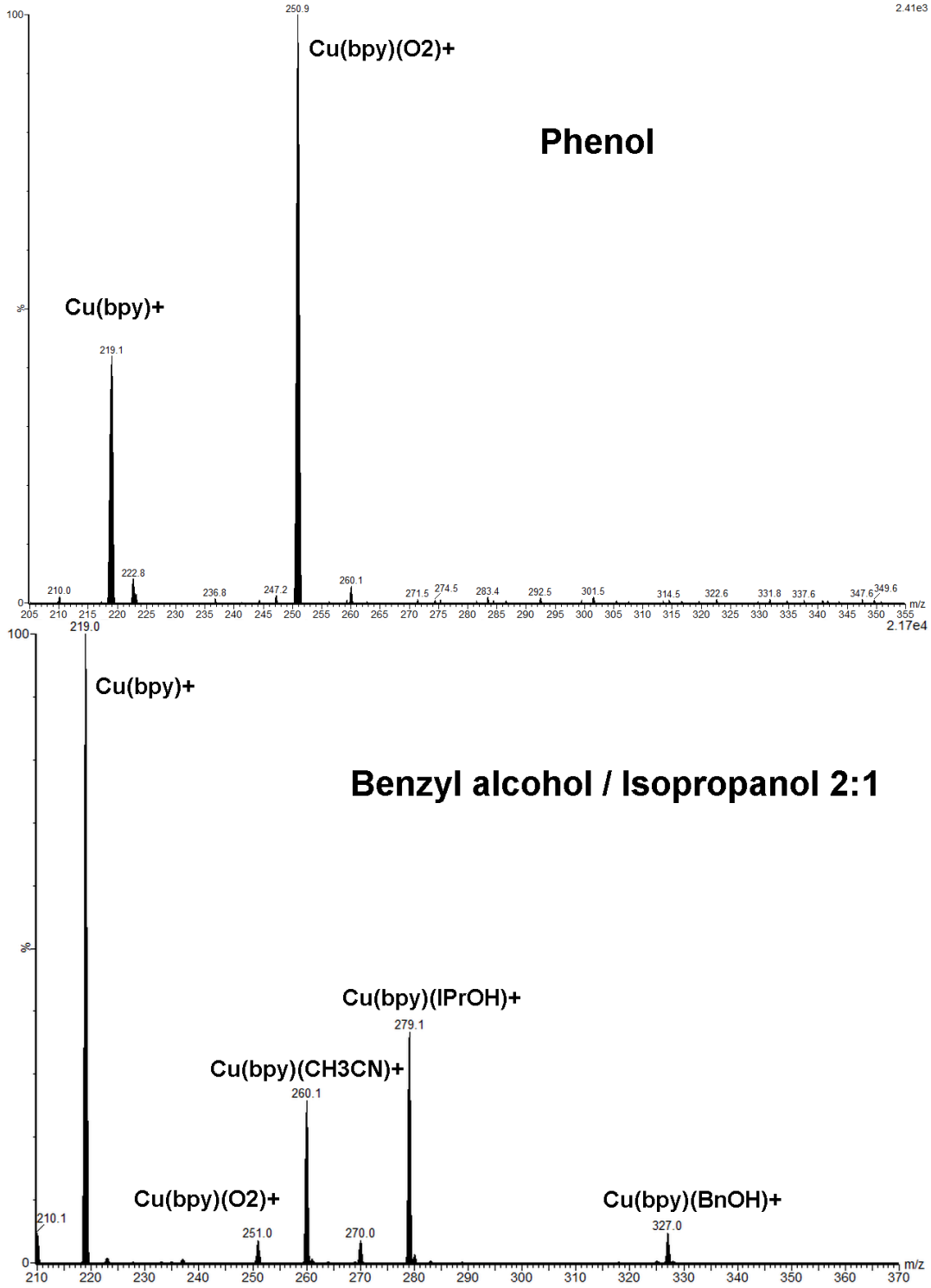

Figure 12: MS/MS spectra of $[Cu(H_2bpy)(O_2)]^+$, using phenol (top) and alcohols (bottom) as collision/reactive gas.

Conclusions

The activation of O_2 by $[Cu(R_2bpy)]^+$ and $[Cu(phen)]^+$ complexes has been studied in a triple quadrupole mass spectrometer by ligand-exchange from ESI generated $[Cu(R_2bpy)(CH_3CN)]^+$ precursor ions. The ligands used in this study are electron-donor enough to observe the coordination of O_2 by $Cu^{(I)}$ center in the gas phase. O_2 collision gas pressure and acceleration voltage were optimized in the collision chamber to achieve simultaneously large signal intensity and thermalisation of the complexes formed. The electronic effect of R groups in R_2bpy ligands was investigated by a Hammett-like model. Experimentally determined reactivity of $[Cu(R_2bpy)]^+$ complexes towards O_2 showed a linear trend as a function of the Hammett parameter values reported in the literature: as expected, O_2 is more strongly bound to the Cu with the help of electro-donating ligands and is also more easily activated. However, strong deviation from linearity was observed for the electron-withdrawing $-CO_2Me$ substituent. DFT calculations of Bond Dissociation Energies (BDEs) of $[(R_2bpy)Cu\text{-}O_2]^+$ demonstrated an excellent agreement with experimental data whatever the nature of the ligand. By comparing normalized BDEs for a larger set of R substituents with reported Hammett parameters, it appeared two different linear trends for electron-donor on one hand and electron-withdrawing R groups on the other hand. Anomalous behaviors of -OH and $-CO_2Me$ substituents were attributed to hydrogen-bonding with the solvent leading to solvent-dependent reported Hammett parameters. The results obtained suggest the proposed methodology may provide intrinsic, solvent-free, Hammett parameters, which may be used as absolute indicator of the electronic influence of various substituent groups.

The structures of $[Cu(R_2bpy)(O_2)]^+$ complexes is also discussed from DFT calculations. Bader charge analyses are consistent with a CuO_2 moiety having a $Cu^{(II)}(O_2^{\bullet-})$ (superoxo) electronic character. Mulliken spin densities have shown that CuO_2 moiety has a stronger $Cu^{(II)}$-superoxide character when electron-donating groups are used. The coordination of small molecules have been observed on $[Cu(R_2bpy)(O_2)]^+$, by performing gas-phase reactive collisions. However, no sign of gas-phase oxidation was observed in our experimental setup and conditions used.

References

1. Prigge, S.T.; Kolhekar, A.S.; Eipper, B.A.; Mains, R.E.; Amzel, L.M. Substrate-Mediated Electron Transfer in Peptidylglycine Alpha-Hydroxylating Monooxygenase. *Nat. Struct. Biol.* **1999**, *6*, 976–983, doi:10.1038/13351.

2. Prigge, S.T.; Eipper, B.A.; Mains, R.E.; Amzel, L.M. Dioxygen Binds End-On to Mononuclear Copper in a Precatalytic Enzyme Complex. *Science* **2004**, *304*, 864–867, doi:10.1126/science.1094583.

3. Evans, J.P.; Ahn, K.; Klinman, J.P. Evidence That Dioxygen and Substrate Activation Are Tightly Coupled in Dopamine β-Monooxygenase: Implications for the Reactive Oxygen Species. *J. Biol. Chem.* **2003**, *278*, 49691–49698, doi:10.1074/jbc.M300797200.

4. Solomon, E.I.; Pavel, E.G.; Loeb, K.E.; Campochiaro, C. Magnetic Circular Dichroism Spectroscopy as a Probe of the Geometric and Electronic Structure of Non-Heine Ferrous Enzymes. *Coord. Chem. Rev.* **1995**, *144*, 369–460, doi:10.1016/0010-8545(95)01150-N.

5. Karlin, K.D.; Itoh, S.; Rokita, S. *Copper-Oxygen Chemistry*; John Wiley & Sons, 2011; ISBN 978-1-118-09435-8.

6. Würtele, C.; Sander, O.; Lutz, V.; Waitz, T.; Tuczek, F.; Schindler, S. Aliphatic C−H Bond Oxidation of Toluene Using Copper Peroxo Complexes That Are Stable at Room Temperature. *J. Am. Chem. Soc.* **2009**, *131*, 7544–7545, doi:10.1021/ja902327s.

7. Maiti, D.; Fry, H.C.; Woertink, J.S.; Vance, M.A.; Solomon, E.I.; Karlin, K.D. A 1:1 Copper−Dioxygen Adduct Is an End-on Bound Superoxo Copper(II) Complex Which Undergoes Oxygenation Reactions with Phenols. *J. Am. Chem. Soc.* **2007**, *129*, 264–265, doi:10.1021/ja067411l.

8. Würtele, C.; Gaoutchenova, E.; Harms, K.; Holthausen, M.C.; Sundermeyer, J.; Schindler, S. Crystallographic Characterization of a Synthetic 1:1 End-On Copper Dioxygen Adduct Complex. *Angew. Chem. Int. Ed.* **2006**, *45*, 3867–3869, doi:10.1002/anie.200600351.

9. Weitzer, M.; Schindler, S.; Brehm, G.; Schneider, S.; Hörmann, E.; Jung, B.; Kaderli, S.; Zuberbühler, A.D. Reversible Binding of Dioxygen by the Copper(I) Complex with Tris(2-Dimethylaminoethyl)Amine (Me6tren) Ligand. *Inorg. Chem.* **2003**, *42*, 1800–1806, doi:10.1021/ic025941m.

10. Molina-Svendsen, H.; Bojesen, G.; McKenzie, C.J. Gas-Phase Reactivity of Coordinatively Unsaturated Transition Metal Complex Ions toward Molecular Oxygen. *Inorg. Chem.* **1998**, *37*, 1981–1983, doi:10.1021/ic970345r.

11. Koyanagi, G.K.; Caraiman, D.; Blagojevic, V.; Bohme, D.K. Gas-Phase Reactions of Transition-Metal Ions with Molecular Oxygen: Room-Temperature Kinetics and Periodicities in Reactivity. *J. Phys. Chem. A* **2002**, *106*, 4581–4590, doi:10.1021/jp014145j.

12. Caraiman, D.; Bohme, D.K. Periodic Trends in Reactions of Benzene Clusters of Transition Metal Cations, M(C6H6)1,2+ with O2. *J. Phys. Chem. A* **2002**, *106*, 9705–9717, doi:10.1021/jp0208900.

13. Munakata, M.; Nishibayashi, S.; Sakamoto, H. Copper(I) Complex-Catalysed Reduction of Dioxygen to Water and Oxidation of Alcohols: A Model of Copper(I)-Containing Oxidase. *J. Chem. Soc. Chem. Commun.* **1980**, 219–220, doi:10.1039/C39800000219.

14. Cheung, K.; Wong, W.; Ma, D.; Lai, T.; Wong, K. Transition Metal Complexes as Electrocatalysts—Development and Applications in Electro-Oxidation Reactions. *Coord. Chem. Rev.* **2007**, *251*, 2367–2385, doi:10.1016/j.ccr.2007.04.004.

15. Hoover, J.M.; Ryland, B.L.; Stahl, S.S. Mechanism of Copper(I)/TEMPO-Catalyzed Aerobic Alcohol Oxidation. *J. Am. Chem. Soc.* **2013**, *135*, 2357–2367, doi:10.1021/ja3117203.

16. Badalyan, A.; Stahl, S.S. Cooperative Electrocatalytic Alcohol Oxidation with Electron-Proton-Transfer Mediators. *Nature* **2016**, *535*, 406–410, doi:10.1038/nature18008.

17. Ryland, B.L.; McCann, S.D.; Brunold, T.C.; Stahl, S.S. Mechanism of Alcohol Oxidation Mediated by Copper(II) and Nitroxyl Radicals. *J. Am. Chem. Soc.* **2014**, *136*, 12166–12173, doi:10.1021/ja5070137.

18. Rafiee, M.; Miles, K.C.; Stahl, S.S. Electrocatalytic Alcohol Oxidation with TEMPO and Bicyclic Nitroxyl Derivatives: Driving Force Trumps Steric Effects. *J. Am. Chem. Soc.* **2015**, *137*, 14751–14757, doi:10.1021/jacs.5b09672.

19. Bhaduri, S.; Sapre, N.Y.; Basu, A. Activation of Dioxygen by CuI Complexes Containing 2,2′-Bipyridine or 1,10-Phenanthroline and 2-Methylimidazole. *J. Chem. Soc. Chem. Commun.* **1986**, 197–198, doi:10.1039/C39860000197.

20. Polestshuk, P.M.; Magdesieva, T.V. Computational Exploration of the Mechanism of Alcohol Oxidation by Dioxygen Activated with Biquinolyl-Containing Cu Complexes Available online: https://pubs.acs.org/doi/pdf/10.1021/ic9024537 (accessed on 4 February 2022).

21. Mirica, L.M.; Ottenwaelder, X.; Stack, T.D.P. Structure and Spectroscopy of Copper−Dioxygen Complexes. *Chem. Rev.* **2004**, *104*, 1013–1046, doi:10.1021/cr020632z.

22. McCrory, C.C.L.; Devadoss, A.; Ottenwaelder, X.; Lowe, R.D.; Stack, T.D.P.; Chidsey, C.E.D. Electrocatalytic O2 Reduction by Covalently Immobilized Mononuclear Copper(I) Complexes: Evidence for a Binuclear Cu2O2 Intermediate. *J. Am. Chem. Soc.* **2011**, *133*, 3696–3699, doi:10.1021/ja106338h.

23. McCrory, C.C.L.; Ottenwaelder, X.; Stack, T.D.P.; Chidsey, C.E.D. Kinetic and Mechanistic Studies of the Electrocatalytic Reduction of O2 to H2O with Mononuclear Cu Complexes of Substituted 1,10-Phenanthrolines. *J. Phys. Chem. A* **2007**, *111*, 12641–12650, doi:10.1021/jp076106z.

24. Brodbelt, J.S. Analytical Applications of Ion-Molecule Reactions. *Mass Spectrom. Rev.* **1997**, *16*, 91–110, doi:10.1002/(SICI)1098-2787(1997)16:2<91::AID-MAS3>3.0.CO;2-4.

25. Chen, P. Electrospray Ionization Tandem Mass Spectrometry in High-Throughput Screening of Homogeneous Catalysts. *Angew. Chem. Int. Ed.* **2003**, *42*, 2832–2847, doi:10.1002/anie.200200560.

26. Lesage, D.; Memboeuf, A.; Gimbert, Y.; Tabet, J.-C. RRKM Modeling of Collision Activated Reaction/Collision Induced Dissociation Experiments: Energy Profile Determination for Phenylethyne Incorporation on Palladium (II)–Phosphinous Acid Complex. *Int. J. Mass Spectrom.* **2012**, *319–320*, 31–39, doi:10.1016/j.ijms.2012.05.002.

27. Lesage, D.; Milet, A.; Memboeuf, A.; Blu, J.; Greene, A.E.; Tabet, J.-C.; Gimbert, Y. The Pauson-Khand Mechanism Revisited: Origin of CO in the Final Product. *Angew. Chem. Int. Ed.* **2014**, *53*, 1939–1942, doi:10.1002/anie.201307745.

28. Iacobucci, C.; Lebon, A.; De Angelis, F.; Memboeuf, A. CuAAC Click Reactions in the Gas Phase: Unveiling the Reactivity of Bis-Copper Intermediates. *Chem. - Eur. J.* **2016**, *22*, 18690–18694, doi:10.1002/chem.201603518.

29. Schröder, D. Applications of Electrospray Ionization Mass Spectrometry in Mechanistic Studies and Catalysis Research. *Acc. Chem. Res.* **2012**, *45*, 1521–1532, doi:10.1021/ar3000426.

30. Chen, P. Electrospray Ionization Tandem MS for High Throughput Screening of Katalysator Libraries. *Angew Chem* **2003**, *115*, 2938–2954, doi:10.1002/ange.200200560.

31. Donnelly, J.M.; Lermyte, F.; Wolny, J.A.; Walker, M.; Breeze, B.G.; Needham, R.J.; Müller, C.S.; O'Connor, P.B.; Schünemann, V.; Collingwood, J.F.; et al. Cu(III)–Bis-Thiolato Complex Forms an Unusual Mono-Thiolato Cu(III)–Peroxido Adduct. *Chem. Commun.* **2021**, *57*, 69–72, doi:10.1039/D0CC06921C.

32. Lavanant, H.; Virelizier, H.; Hoppilliard, Y. Reduction of Copper(II) Complexes by Electron Capture in an Electrospray Ionization Source. *J. Am. Soc. Mass Spectrom.* **1998**, *9*, 1217–1221, doi:10.1016/S1044-0305(98)00100-7.

33. Gianelli, L.; Amendola, V.; Fabbrizzi, L.; Pallavicini, P.; Mellerio, G.G. Investigation of Reduction of Cu(II) Complexes in Positive-Ion Mode Electrospray Mass Spectrometry. *Rapid Commun. Mass Spectrom.* **2001**, *15*, 2347–2353, doi:10.1002/rcm.510.

34. Becke, A.D. Density-functional Thermochemistry. III. The Role of Exact Exchange. *J. Chem. Phys.* **1993**, *98*, 5648–5652, doi:10.1063/1.464913.

35. Ducéré, J.-M.; Goursot, A.; Berthomieu, D. Comparative Density Functional Theory Study of the Binding of Ligands to Cu+ and Cu2+: Influence of the Coordination and Oxidation State. *J. Phys. Chem. A* **2005**, *109*, 400–408, doi:10.1021/jp047971b.

36. Bonniard, L.; de la Lande, A.; Ulmer, S.; Piquemal, J.-P.; Parisel, O.; Gérard, H. Competitive Ligand/Chelate Binding in [Cu(TMPA)]+ and [Cu(Tren)]+ Based Complexes. *Catal. Today* **2011**, *177*, 79–86, doi:10.1016/j.cattod.2011.07.015.

37. M. J. Frisch; G. W. Trucks; H. B. Schlegel; G. E. Scuseria; M. A. Robb; J. R. Cheeseman; G. Scalmani; V. Barone; G. A. Petersson; H. Nakatsuji; et al. *Gaussian16*; Gaussian, Inc.: Wallingford CT, 2016;

38. Henkelman, G.; Arnaldsson, A.; Jónsson, H. A Fast and Robust Algorithm for Bader Decomposition of Charge Density. *Comput. Mater. Sci.* **2006**, *36*, 354–360, doi:10.1016/j.commatsci.2005.04.010.

39. Plattner, D.A. Electrospray Mass Spectrometry beyond Analytical Chemistry: Studies of Organometallic Catalysis in the Gas Phase. *Int. J. Mass Spectrom.* **2001**, *207*, 125–144, doi:10.1016/S1387-3806(01)00371-2.

40. Ichou, F.; Lesage, D.; Machuron-Mandard, X.; Junot, C.; Cole, R.B.; Tabet, J.-C. Collision Cell Pressure Effect on CID Spectra Pattern Using Triple Quadrupole Instruments: A RRKM Modeling: Pressure Effect on CID Spectra Pattern Using TQ. *J. Mass Spectrom.* **2013**, *48*, 179–186, doi:10.1002/jms.3143.

41. Maroto, A.; Jeanne Dit Fouque, D.; Memboeuf, A. Ion Trap MS Using High Trapping Gas Pressure Enables Unequivocal Structural Analysis of Three Isobaric Compounds in a Mixture by Using Energy-Resolved Mass Spectrometry and the Survival Yield Technique. *J. Mass Spectrom.* **2020**, *55*, e4478, doi:10.1002/jms.4478.

42. Hansch, Corwin.; Leo, A.; Taft, R.W. A Survey of Hammett Substituent Constants and Resonance and Field Parameters. *Chem. Rev.* **1991**, *91*, 165–195, doi:10.1021/cr00002a004.

43. Maqsood, S.R.; Islam, N.; Bashir, S.; Khan, B.; Pandith, A.H. Sigma Donor and Pi Acceptor Characteristics of Certain NN-Bidentate Ligands: A DFT Study. *J. Coord. Chem.* **2013**, *66*, 2308–2315, doi:10.1080/00958972.2013.800866.

44. Abrahams, S.C.; Kalnajs, J. The Crystal Structure of α-Potassium Superoxide. *Acta Crystallogr.* **1955**, *8*, 503–506, doi:10.1107/S0365110X55001540.

Chapter IV

Use of Tripodal Ligands for Dioxygen Coordination in the Gas Phase

Introduction

The biomimetic approach has been deepened for a long time on galactose oxidase (GO), peptidyl hydroxylating monooxygenase (PHM)/dopamine beta-hydroxylase (DBH) or lytic polysaccharide monooxygenases (LPMOs). A lot of molecular models have been designed in order to copy the mononuclear (or uncoupled dinuclear) active site of these cuproenzymes and mimic their behavior towards substrates. The first idea was to reproduce the coordination sphere of Cu center in the heart of these enzymes, based on the nature and number of coordinating atoms, the donating power of the ligand, the geometric constraints... Thus, copper complexes such as $[Cu(HB(3\text{-}R\text{-}5\text{-}iPrpz)_3)]^+$ ($HB(3\text{-}R\text{-}5\text{-}iPrpz)_3$: hydrotris(3-tert-butyl-5-isopropyl-1-pyrazolyl)-borate)[1], salen derivatives[2] or complexes based on 'histidine brace' pattern[3] have been designed. The geometry of these models has been sometimes finely tuned, with respect to experimental data[4,5]. The number and the nature of the coordinating atoms[6,7] (and/or nature of the group that binds Cu[8,9]) have also been discussed. As an example, end-on superoxo was proposed as an intermediate in PHM/DβM[10], while pyramidal models (such as $[Cu(HB(3\text{-}R\text{-}5\text{-}iPrpz)_3)]^+$) have only shown side-on coordination (Figure 1[1]).

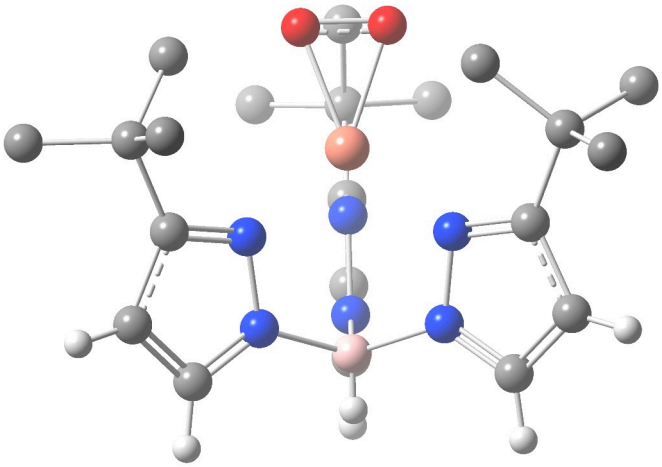

Figure 1: Structure of $CuO_2[HB(3\text{-}tBu\text{-}5\text{-}iPrpz)_3]$[1]. H of tertiobutyl groups are removed for the sake of clarity.

Adding an axially coordinating atom allows the end-on coordination of O_2, which explains why N_3N tripodal ligands have been widely studied as basic patterns to model the active sites of PHM/DβM. Most enzymatic mechanisms starts with the activation of dioxygen by electron transfer

1 The color code for atoms in the Figures is C: grey, N: blue, O: red, H: white, Cu: orange, B: light pink, Cl: flashy green.

from $Cu^{(I)}$ to O_2. The expected reactivity for resulting $Cu^{(II)}$-superoxo complexes is the abstraction of a hydrogen atom or a proton from its environment by intra-molecular or extra-molecular reactions.

However, it is still a challenge to obtain mononuclear CuO_2 adducts, because in the presence of O_2, these $Cu^{(I)}$ complexes quickly form $[\{LCu\}_2(O_2)]^{2+}$ dimers, even it was shown that the use of low temperatures or the addition of basic/bulky substituents stabilize the mononuclear superoxo species and prevents dimerization[11–15]. Gas phase is also suitable to study mononuclear CuO_2 species, since no dimerization can happen. The gas phase coordination of O_2 has been only observed a few times, on bare transition metal ions in the +I oxidation state[16], on monocharged transition metal-benzene complexes[17] and $[Cu(tdt)]^+$ (tdt: toluene-3,4-dithiolate)[18]. It has been also found to happen on $[M(R_2bpy)]^+$ (M: Cr, Co, Ni, Ru, Os[19], Cu (see Chapter III); R_2bpy: functionalized 4,4'-bipyridines) complexes.

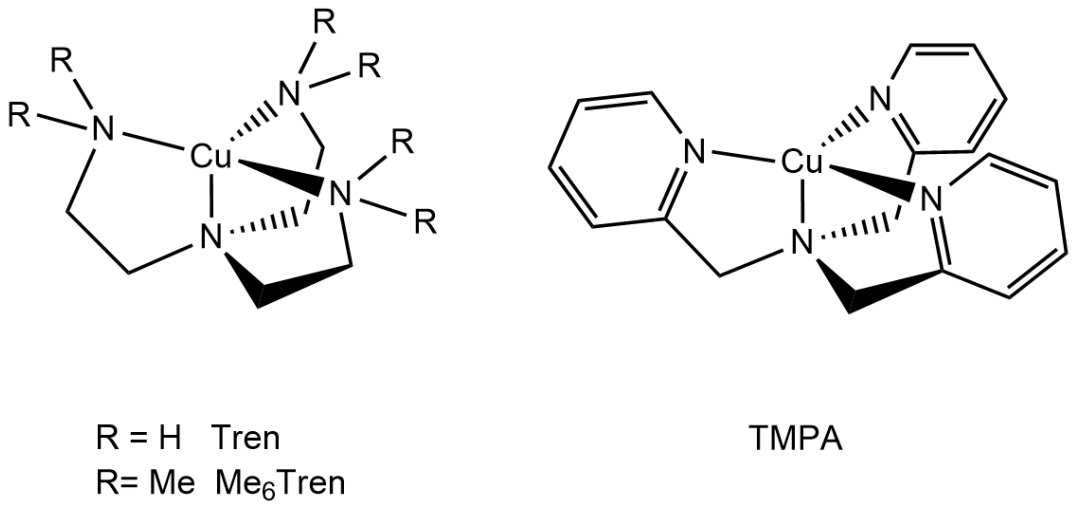

R = H Tren TMPA
R= Me Me_6Tren

Figure 2: Structures of Tren, Me_6Tren and TMPA Cu complexes.

Here, we study the coordination of O_2 on Cu complexes with N_3N tripodal ligands (Me_6Tren: tris[2-(dimethylamino)ethyl]amine, TMPA: tris(2-pyridylmethyl)amine, Figure 2) by mass spectrometry and DFT calculations. Mass spectrometry experiments, performed with other $Cu^{(II)}$ complexes, have shown the formation of both $[Cu(L)]^+$ and $[Cu(L_{-H})]^+$, in addition to the $[Cu(L)(X)]^+$ ion (L designates the ligand, L_{-H} the same but deprotonated ligand, X a counter-ion). Such behavior has been reported previously in some publications[20]. Monocharged $[Cu(L)]^+$ have been observed, despite the fact that the ESI source has been set in the positive ion mode (so the analytes should undergo oxidation). This reduction was explained by outer-sphere electron capture from solvent molecules which have relatively low ionization potential. This change of oxidation

degree is proposed to happen in the gas phase, during the last step of desolvatation process, in the nozzle-skimmer zone. Inner-sphere processes are also proposed elsewhere, from diverse precursors, depending on the ligand[21,22]. The appearance of peaks that correspond to $Cu^{(I)}$ complexes is favored with easy-to-reduce $Cu^{(II)}$ complexes. On the other hand, deprotonated $[Cu(L_{-H})]^+$ complexes have been generated by varying solvents, voltages and/or temperature of the electrospray ionization source (ESI), in addition to the $[Cu(L)]^+$ peak. This kind of complexes has already been observed in the gas phase, with relatively acidic[23] and non-acidic[22] ligands. This original reactivity has been explained as the acido-basic reaction that takes place between $Cu^{(II)}$ complex and a counter-ion. In fact, gas phase favours the reduction of the number of charges[24].

In enzymes, the existence of Cu-radical intermediates is also proposed. For example, the well-deepened mechanism of galactose oxidase involves the loss of a hydrogen atom by a tyrosine amino-acid residue, that binds to Cu, leading to a Cu-tyrosyl intermediate, able to oxidize alcohols after H_2O_2 departure[25]. EPR experiments on the relative models of galactose oxidase (or glyoxal oxidase), such as $[Cu^{(II)}(salen)]$ complexes (synthetized by condensation from salicylaldehyde and ethylenediamine), have shown that Cu remains in its formal +II oxidation state.

The formation of $Cu^{(I)}$-radical species was never intensely discussed in previous studies, to our knowledge. One publication emit the hypothesis of the formation of $Cu^{(I)}$ with an uncoordinated radical center[26]. A mechanism was proposed to explain the oxidation of the ligand bearing a $Cu^{(II)}$ center. After the deprotonation of a carbon atom on the ligand, the addition of O_2 is proposed to happen on the same C atom. O_2 is a radicalophile, due to its incomplete π orbitals. It reacts with the radical center more than with the $Cu^{(I)}$ center, leading to the oxidation of the ligand and to the loss of 1-butanal as a by-product. The flexibility of N-ethyl-N,N-dimethylamine arms of Me_6Tren ligand allows it to form an uncommon CuC bond. Cu-carbenes are generally formed by reaction between stabilized carbene ligand, from diazo compounds that lose N_2 or from alkynes (as substrates) in the presence of a base in the condensed[27] or in the gas phase[28]. No such direct formation of CuC bonds were reported from the ligand. Concerning the more rigid TMPA ligand, the formation of a close carboradical allows the reaction of O_2 with both $Cu^{(I)}$ and C radical centers. The reactivity of these $[Cu(L_{-H})]^+$ complexes towards O_2 was evaluated with the help of MSMS experiments and DFT calculations. It was found that these new species, probably not involved in the mechanism of enzymes, are yet extremely sensitive to O_2. The structures of these $[Cu(L_{-H})(O_2)]^+$ complexes were determined and the nature of the adducts has been defined.

1. Methods

1.1. Mass spectrometry

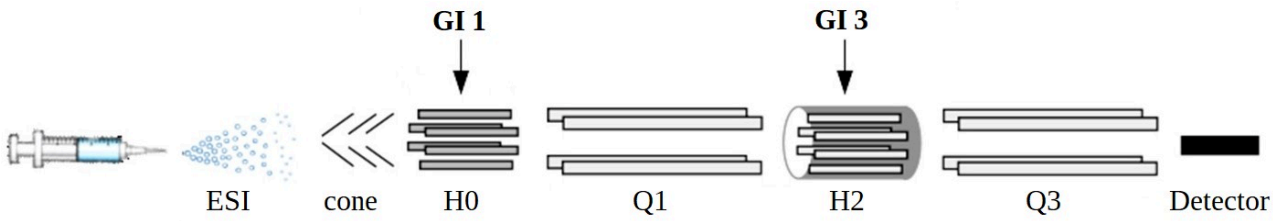

Figure 3: General scheme of the ESI-Quattro II. ESI stands for ElectroSpray Ionization source, H for hexapole, Q for quadrupole and GI for gas inlet.

Mass spectrometry experiments were performed on a home-modified Quattro II (triple quadrupole from Waters, Figure), equipped with an electrospray source (ESI, Agilent) working in the positive ion mode. The drying gas temperature was set at 150 °C. O_2 (Alphagaz 2 grade with 99.9995% purity, Air Liquide France Industrie) can be introduced in the focusing hexapole (before the first quadrupole) or in the collision cell (from $1{\cdot}10^{-3}$ to $1{\cdot}10^{-2}$ mbar). The source parameters were fixed as follows: capillary 3.60 kV, cone 35 V, extractor 5 V, drying gas flux 300 $L.min^{-1}$, desolvation gas flux 20 $L.min^{-1}$, desolvation temperature 150 °C, HM/LM resolution 15.0 (15.0/15.0 in MS/MS). Tris(2-aminoethyl)amine (Tren), tris[2-(dimethylamino)ethyl]amine (Me_6Tren) and tris[(2-piridyl)methyl]amine (TMPA) were purchased from Sigma-Aldrich and used as received. Synthesis of [Cu(Tren)(H_2O)](OTf)$_2$, [Cu(Me_6Tren)(H_2O)](ClO_4)$_2$ and [Cu(TMPA)(H_2O)](OTf)$_2$ (OTf stands for CF_3SO_3 anion) were adapted from previously reported procedures[29]. Partially deuterated Tren complex was generated by letting the complex in D_2O over night. The deuterium atoms are expected to be on amine groups, because of the modest basicity of D_2O. [Cu($^{d6\text{-}DMM}$TMPA)(CO)](ClO_4) (deuterated on methylenic positions) was synthesized according to previously reported procedure[30]. High-grade CH_3CN and H_2O milliQ were used to prepare solutions of copper complexes at concentrations of $5{\cdot}10^{-5}$ $mol{\cdot}L^{-1}$. Solutions were infused at a flow rate of 20 $\mu L{\cdot}min^{-1}$. Resolution parameters were set to obtain monoisotopic peaks. Collision Activated Reactions (CAR) between monocharged Cu complexes and O_2 have taken place in the collision cell. Suitable pressures of O_2 (~ $1{\cdot}10^{-3}$ to $7{\cdot}10^{-3}$ mbar) were used to observe CuO_2 adducts. In general, low collision voltage (~ 2-3 V) allows the coordination of O_2 on Cu complexes, but with higher pressures (> $6{\cdot}10^{-3}$ mbar), a slightly higher value of collision voltage is needed to allow the ions

going through the gas cell. O_2 can also act as a classical CID gas in the collision cell and fragmentation is observed with high collision voltages (~ 10-15 V).

1.2. DFT calculations

DFT calculations were run with the help of Gaussian16 package. Minimum energy structures were obtained by optimization from crystallographically determined structures[29,31]. B3LYP, in combination with the basis set designed as 6-31+G(d,p) in Gaussian16 on all atoms, was used to calculate geometries and frequencies. B3LYP was found to furnish remarkable results of BDEs with $Cu^{(I)}$ metal center[32], and was used many times on that purpose[33,34]. Nevertheless, other methods (M06, MN15, CAM-B3LYP) have been tested. Precise BDE values were established with single point calculations with 6-311++G(3df,2pd) and def2-QZVP basis sets on the previously 6-31+G(d,p) optimized structures. The stability of the wavefunction has been checked to validate the global spin state of the complexes. Presented pathways were checked with the help of the Intrinsic Reaction Coordinate (IRC) procedure[35]. Bond Dissociation Energies (BDE) are calculated as the difference of E+ZPE between reactants (CuO_2 complex) and the products (Cu complex and O_2).

Bond Critical Point (BCP) analysis was used to evaluate the nature of bonds formed. ρ is an indicator of the strength of a bond (a high ρ value for a given BCP specifies that the corresponding bond is strong), while Δρ gives a hint about the character of the bond. The more negative the value of Δρ, the more covalent the corresponding bond is. On the contrary, a positive value indicates the dative character of the bond[36].

2. General description of mass spectra

Mass spectra obtained for $[Cu(Tren)(H_2O)](X)_2$, $[Cu(Me_6Tren)(H_2O)](X)_2$ and $[Cu(TMPA)(H_2O)](X)_2$ solutions (with X being a monocharged counter-anion) are similar to what was previously in the literature with $Cu^{(II)}$ complexes[22]. First of all, it is important to note the absence of doubly-charged species. Thus, $[Cu(Me_6Tren)]^{2+}$ (m/z 146.6) and $[Cu(TMPA)]^{2+}$ (m/z 176.5) or relative adducts with a solvent molecule do not appear on mass spectra. However, five-coordinated $Cu^{(II)}$ complexes were observed: $[Cu(Me_6Tren)(X)]^+$ and $[Cu(TMPA)(X)]^+$ were observed with different counter-anions, and, in particular, with $X = OH^-$ when water is used as solvent. Also, $[Cu(Me_6Tren)]^+$ (m/z 293) and $[Cu(TMPA)]^+$ (m/z 353) are observed. No $Cu^{(I)}$ adducts with a solvent molecule were observed, in accordance with the usual four-coordination pattern of $Cu^{(I)}$. It is surprising that $Cu^{(I)}$ complexes have been observed from $[Cu(Me_6Tren)]^{2+}$ and $[Cu(TMPA)]^{2+}$ for two reasons:

— They have lower reduction potentials than the $Cu^{(II)}$ complexes previously studied[22].

— Both acetonitrile and water have relatively high ionization energies (12.20 and 12.64 eV, respectively) compared to methanol (10.83 eV).

Notwithstanding the nature of the solvent, it might be explained by the bipyramidal trigonal geometry of our complexes, while the complexes studied previously have planar to tetrahedral geometries. These considerations are beyond the goal of this study and will not be discussed further. The intensity ratios between $Cu^{(II)}$ and $Cu^{(I)}$ species vary with the ionization parameters of the ESI source, and the same trends as in the literature were observed. Finally, when water is used as solvent, and with specific source conditions, peaks at m/z 292 (Me_6Tren) and 352 (TMPA) were observed. We emit the hypothesis that the lack of 1 Da is associated to the loss of a proton relative to the close m/z 293 (Me_6Tren) and 353 (TMPA), respectively. MSMS experiments of m/z 293 (Me_6Tren) and 353 (TMPA) do not show the loss of a proton. Obviously, parent peak experiments and MS/MS experiments confirm that $[Cu(L_{-H})]^+$ is formed by the loss of HX acid from $[Cu(L)(X)]^+$ analogous ion (X being ClO_4^-, OTf^-, Cl^- or OH^-). As an example, the loss of H_2O was observed from $[Cu(Me_6Tren)(OH)]^+$ (m/z 310.0, Figure 4, top) and the loss of $HClO_4$ was observed from $[Cu(Me_6Tren)(ClO_4)]^+$ (m/z 392.1, Figure 4, bottom). The loss of H_2O is favored compared to the loss of $HClO_4$ (or HOTf) as indicated by the ratio of $[Cu(Me_6Tren_{-H})]^+/[Cu(Me_6Tren_{-H})(X)]^+$ which is much higher with OH^- than with ClO_4^- (or OTf^-) as counter-ion, with the same ionization

conditions. The use of pure acetonitrile as solvent does not favor the appearance of $[Cu(L_{-H})]^+$: only the addition of a given amount of water does (Figure 5). In a 4:1 mixture with acetonitrile, $[Cu(L)(OH)]^+$ peak is observed and $[Cu(L_{-H})]^+$ emerges, enhanced by the increase of temperature and source parameters (especially the extractor voltage). When H_2O is added, and after an equilibration time, the $[Cu(L)(OH)]^+$ ion is formed. The use of bigger, low-coordinating anions (such as BPh_4^-) increase the intensity of $[Cu(L)(OH)]^+$, $[Cu(L)]^+$ and $[Cu(L_{-H})]^+$ signals (Figure 6). $[Cu(Me_6Tren)]^{2+}$ perchlorate aqueous solution is stable over time, while tetraphenylboron solution turns light pink after few hours, revealing the presence of $[Cu(L)(OH)]^+$ complexes.

First approach (i.e. in the condensed phase) is counter-intuitive: despite the low acidity of H atoms in Me_6Tren and TMPA (pKa ~ 40-50) and the low basicity of counter-ion (unfavorable reaction), we have also observed that OH^- (as counter-ion) is able to take off a proton from these ligands. Simple DFT calculations of gas phase pKa have shown that deprotonation reactions from $[Cu(Me_6Tren)]^{2+}$ or $[Cu(TMPA)]^{2+}$ are energetically favorable (by 926 and 803 $kJ{\cdot}mol^{-1}$, respectively, with OH^- as a base). Nevertheless, these observations are consistent with the theoretical calculations of abstraction energies OH^-, ClO_4^- and OTf^- counter-ions (Figure 8).

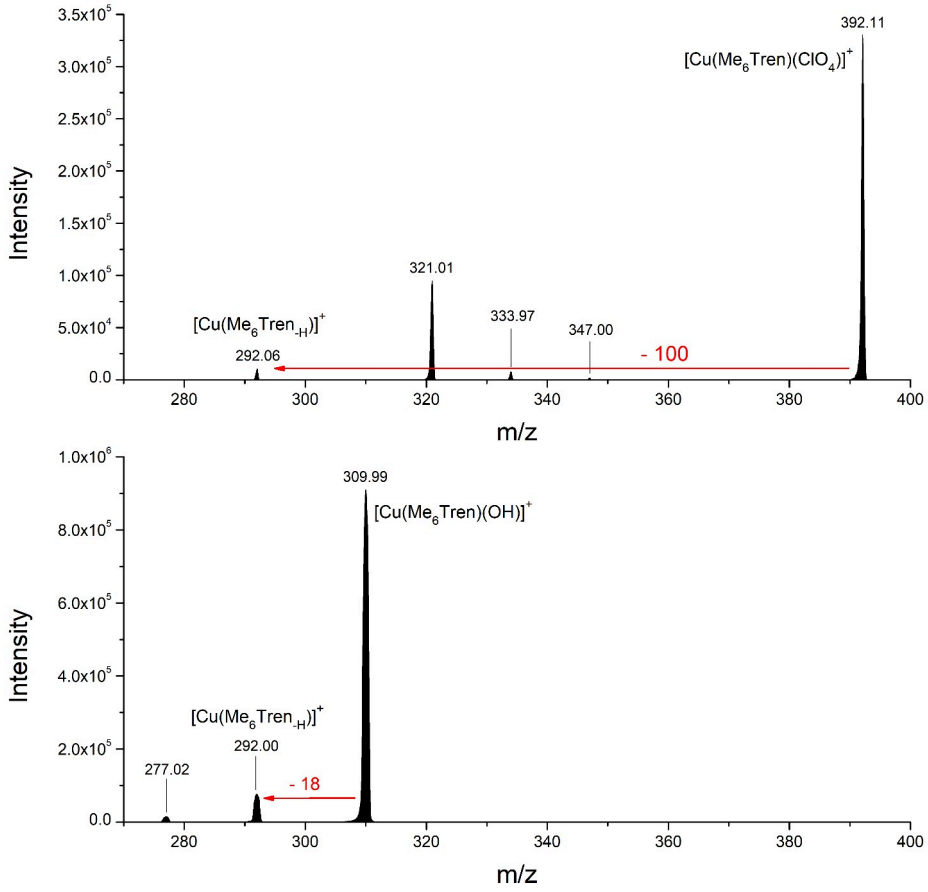

Figure 4: MSMS spectra of $Cu(Me_6Tren)(ClO_4)]^+$ (m/z 392, top) and $[Cu(Me_6Tren)(OH)]^+$ (m/z 310, bottom). P(Ar) = $1{\cdot}10^{-3}$ mbar, ramping V_{coll}.

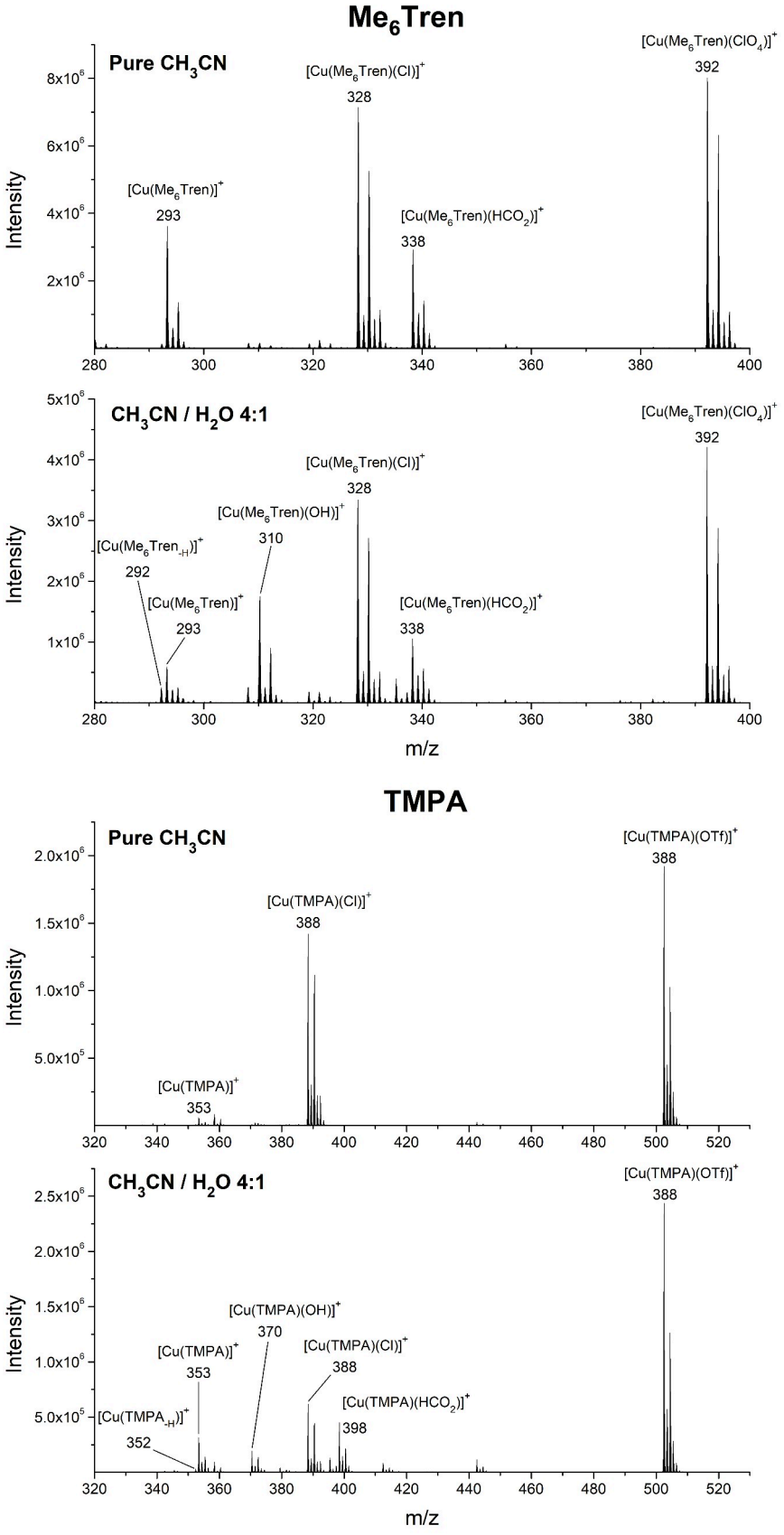

Figure 5: MS spectra of $[Cu(Me_6Tren)(H_2O)](ClO_4)_2$ and $[Cu(TMPA)(H_2O)](OTf)_2$ ($5 \cdot 10^{-5}$ M) in pure CH_3CN and in CH_3CN/H_2O 4:1, all other settings being equal.

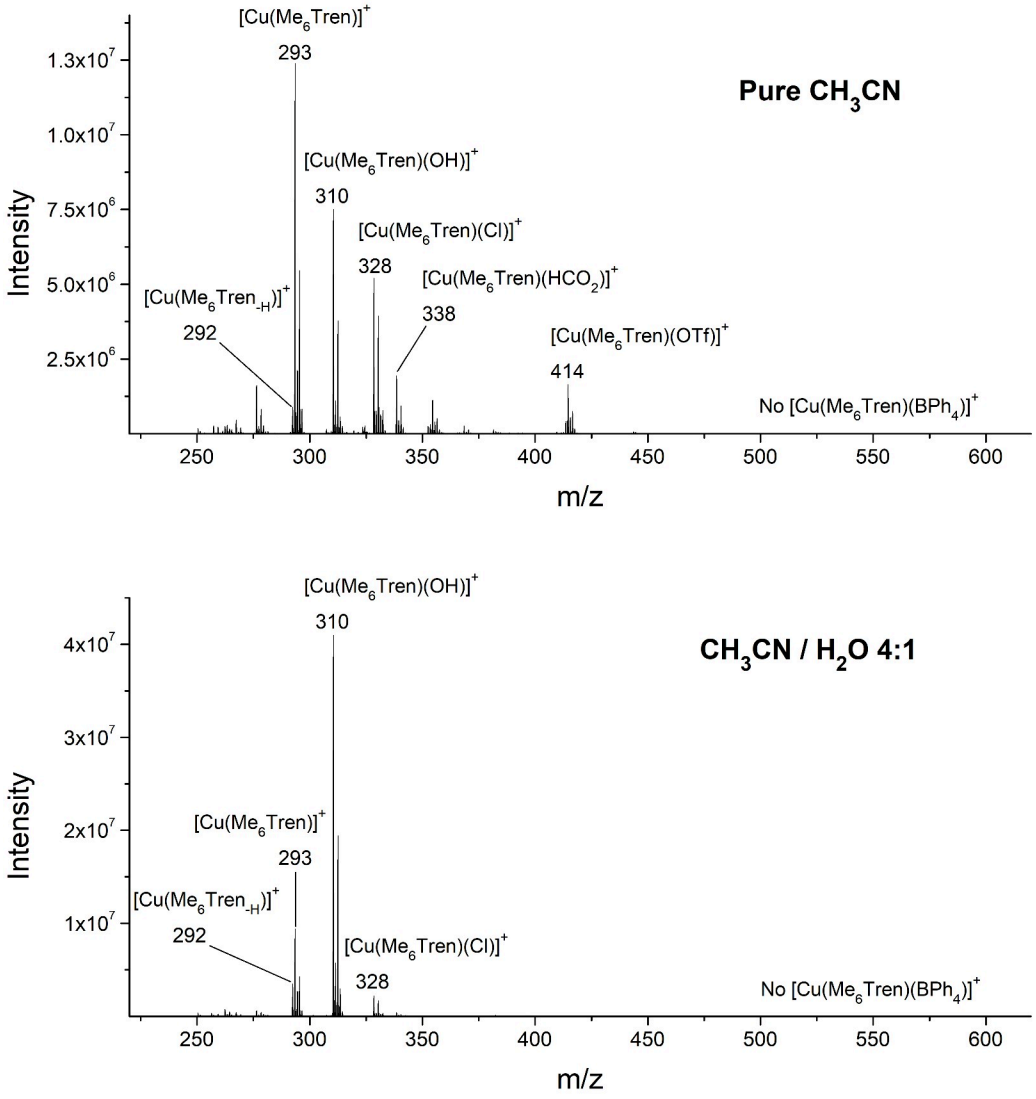

Figure 6: MS spectra of $[Cu(Me_6Tren)(H_2O)](BPh_4)_2$ ($5 \cdot 10^{-5}$ M) in pure CH_3CN (top) and in CH_3CN/H_2O 4:1 (bottom), all other settings being equal. The empty coordination site of $Cu^{(II)}$ is occupied by diverse counter-ions (triflate comes from the synthesis precursor).

3. Where H^+ is abstracted from?

The place where H^+ is lost is of first importance to determine the geometry of the $[Cu(L_{-H})]^+$ complexes, the reactivity of such complexes towards O_2 (see Part IV.2.) and mechanistic insights. A proton can be abstracted from different positions. If the arm of the tripodal ligand stays bound to the Cu center, the proton would be abstracted from the amine (Tren), the methyl (Me_6Tren) or the pyridine (TMPA) groups. On the contrary, if the arm decoordinates the metallic center, protons of the methylene groups might be also abstracted. Deuterated ligands were used in order to know if the arm stays coordinated or not on the metallic center. We emit the hypothesis if the arm of the tripodal ligand is coordinated to the Cu at the end of the ionization process, it will stay bound to it all the time. MS and MSMS experiments have shown that it is easier to form the $[Cu(L_{-H})]^+$ species in the source than in the collision cell. In the latter, a lot of energy is needed to fragment the precursor ion, while a slight increase of cone voltage is enough to generate more $[Cu(L_{-H})]^+$ species.

3.1. Tren ligand

In the $[Cu(Tren)(X)]^+$ case, the proton is very likely to be abstracted from the amine groups, for two reasons. First, the protons of the amine are more acidic than the ones of methylene groups, even in the gas phase. Secondly, the loss of 151 was observed from $[Cu(^{d6}Tren)(OTf)]^+$ (m/z 366, the amines were deuterated by H/D exchange). It means that the arms stay coordinated to the Cu ion. The structures of $[Cu(Tren)]^+$ and $[Cu(Tren_{-H})]^+$ are presented further after (Figure 9.a and b).

3.2. TMPA ligand

$[Cu(TMPA_{-H})]^+$ was also obtained from $[Cu(TMPA)(OTf)]^+$ and especially from $[Cu(TMPA)(OH)]^+$. Crystallographic studies of $[Cu(TMPA)]^+$ complexes confirm that the four nitrogen atoms are coordinated to the Cu[37,38]. Previous publications proposed that one of the three methylpyridyl arms can decoordinate the Cu[33], like in the active site of the PHM: a methionine moiety binds or not the Cu to favor the $Cu^{(I)}$ state by giving it the adequate number of coordinating atoms[39,40]. The loss of proton might happen on the four positions of the pyridine group, and also on the methylene group. However, the distance between the counter-ion and the proton and the acidity of the proton have to be considered. If the pyridine arm stays coordinated on the Cu center,

the only proton that can be abstracted is the closest to the N atom of the pyridine group. The other protons are expected to be too far from the counter-ion. On the contrary, if the arms does not stay coordinated on the Cu center, it becomes possible to abstract a proton on the methylene group, or on the pyridine cycle. The use of partially deuterated DMM-TMPA ligand (structure inserted in Figure 7) will help us to overcome this issue. All hydrogen atoms of methylene groups were exchanged with deuterium atoms. Only the loss of 18 (i.e. the loss of H_2O) is observed from the $[^{65}Cu(^{d6\text{-}DMM}TMPA)(OH)]^+$ complex. Hence, we assume that no arm decoordination happens in the ESI source and that the proton is abstracted from the pyridyl group (position 'a'). Moreover, this proton is expected to be a little bit acidic. Positions 'b' to 'e' are unattainable or too far from the hydroxyde counter-ion to envisage a proton transfer. In the case of arm decoordination, the deprotonation on 'd' and 'e' sites should be competitive. Moreover, the CH bonds are weaker in 'e' case that in 'd' case (see the synthesis procedure). H^+ abstraction from 'b' and 'c' positions is still unlikely, on a distance criterion. TMPA is a rigid ligand, that cannot reorganize as Me_6Tren does (see Part III.3). The deprotonated C atom is not able to bind Cu. So, the final structure (both geometries and charges) is not so much modified compared to the $[Cu(TMPA)]^+$ ion (see Figure 9.c and d).

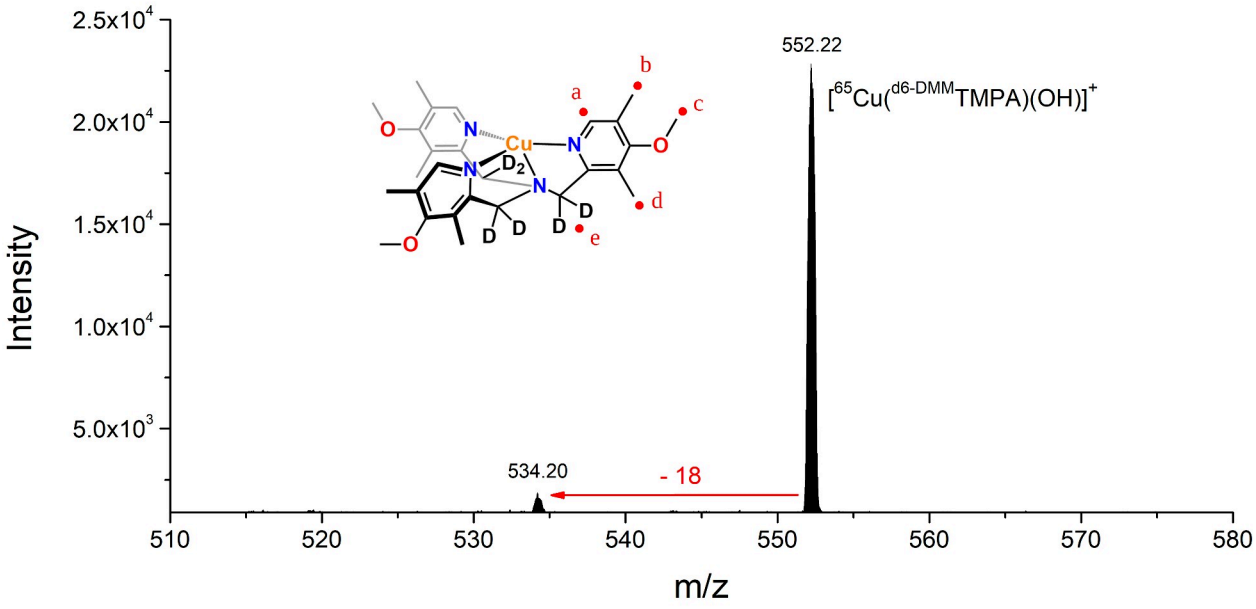

Figure 7: MSMS spectrum of $[^{65}Cu(^{d6\text{-}DMM}TMPA)(OH)]^+$ (m/z 552), P(Ar) = $1{\cdot}10^{-3}$ mbar, ramping collision voltage. The M+8 peak was selected in order to avoid cross-contamination with non-fully deuterated complexes. The five possibilities to abstract H^+ (loss of 18) are notated from 'a' to 'e' on the complex structure.

3.3. Me_6Tren ligand

In the case of Me_6tren ligand, the abstraction of a proton by the counter-ion is proposed to happen on the methyl groups. The decoordination of one arm from the Cu has also been considered. However, no decoordination has been proven to happen with Tren and TMPA as ligands. Since they are less donor than Me_6Tren, we expected the arms of the Me_6Tren remain coordinated on Cu ion. Then, two different cases have been examined, depending on the nature of the counter-ion. With large counter-ions, the deprotonation is made in one step. The departure of $HClO_4$ leads to the deprotonation of the methyl group, and a reorganization step happens just next (Figure 8, red and blue surfaces). The Intrinsic Reaction Coordinate (IRC) procedure has shown that the deprotonated C* carbon atom directly binds Cu to form a CuC bond. With smaller counter-ion, the decoordination is made in two steps (Figure 8, black surface). The first step is the abstraction of a proton on the methyl group: it leads to the formation of a Cu-O(H)-H-C "bridged" stable intermediate. The abstraction of H_2O causes then the formation of the CuC bond. So, the structure of the final $[Cu(Me_6Tren_{-H})]^+$ does not depend on the counter-ion. The TS corresponding to the abstraction has been calculated to be around 75 $kJ{\cdot}mol^{-1}$ lower with OH^- than with ClO_4^-/OTf^-. In the case of a bulky anion, having several oxygen atoms, one oxygen atom is pointing in the direction of methyl group and the other binds the counter-ion to the Cu (1.94 Å). At TS stage, the CuO distance increases (to 2.47 Å) and a hydrogen from a methyl group is transferred to the counter-ion, leading to the formation of $HClO_4$ (good leaving group). The Intrinsic Reaction Coordinate (IRC) procedure recovers the starting structure and the final $[Cu(Me_6Tren_{-H})]^+$. This product has an unusual Cu-C bond (2.00 Å against 2.17/2.21 Å for CuN_{eq}). In the OH^- case, only one oxygen atom is implied both in the binding of the counter-ion and in the abstraction of a proton on the methyl group. The structure of the 'TS abstraction' clearly shows that the equatorial nitrogen atom is progressively decoordinated from the Cu, just to allow the H from the methyl group to be abstracted. This lead to the so-called 'Intermediate bridged', which consists in the inclusion of OH between Cu and C. The release of H_2O, which was found to be lower in energy than the first TS, is concomitant with the recoordination of the deprotonated arm to the copper. The departure of H_2O leads to $[Cu(Me_6Tren_{-H})]^+$. The IRC procedure has also been applied here, and validate the pathway. We suppose the recoordination of the C* to be fast, because of the relative instability of a dangling CH_2 radical[41].

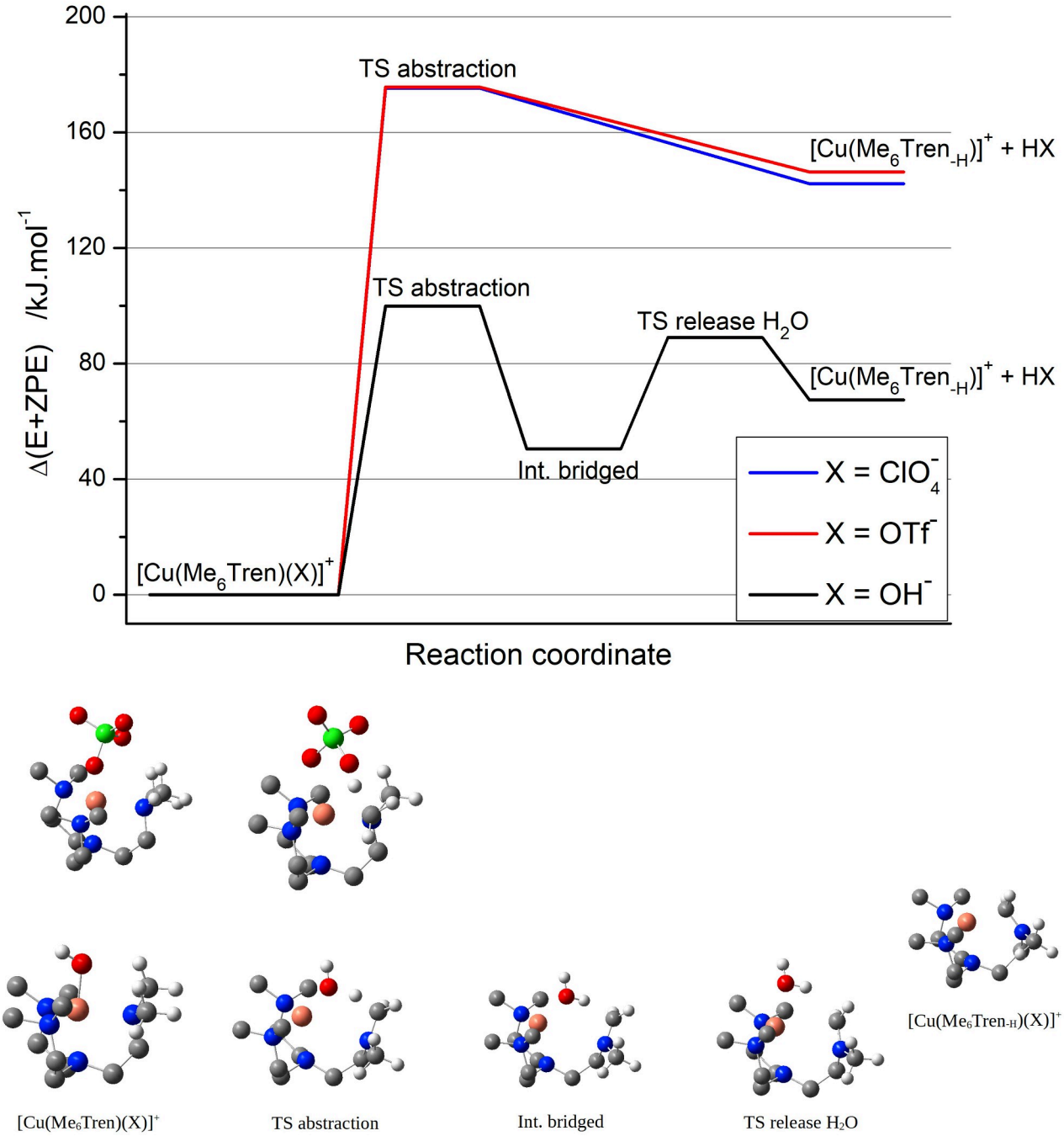

Figure 8: Energetic pathways for the one-step high-energy path of deprotonation with massive counter-ions (ClO_4^- and OTf^-), and for the two-step low-energy path of deprotonation with OH^- as counter-ion. Geometries and energies were computed at the B3LYP/6-31+G(d,p) level of theory.

3.4. Structures of Cu complexes

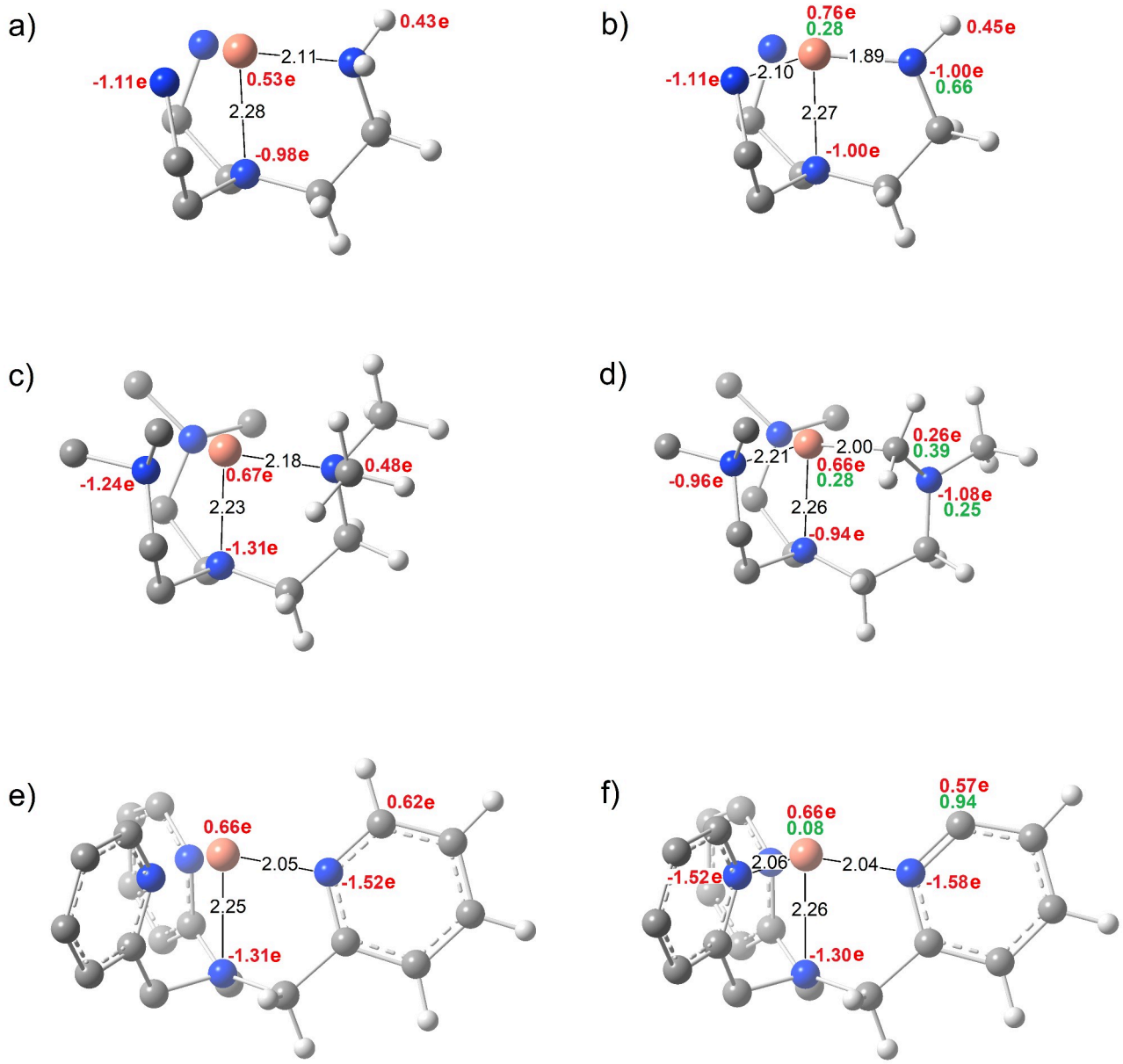

Figure 9: Geometries of $[Cu(Tren)]^+$ (a), $[Cu(Tren_{-H})]^+$ (b), $[Cu(Me_6Tren)]^+$ (c) and $[Cu(Me_6Tren_{-H})]^+$ (d), $[Cu(TMPA)]^+$ (e) and $[Cu(TMPA_{-H})]^+$ (f) calculated at the B3LYP/6-31+G(d,p) level of theory. Some distances (given in Å, black), Bader charges (bold red) and Mulliken spin densities (bold green) are indicated. Some H atoms were removed for the sake of clarity. Only conformers with coordinated arms were considered.

Some important distances and charges of $[Cu(L)]^+$ and $[Cu(L_{-H})]^+$ precursors are indicated in Figure 9. In the following discussion, N* designates the N atom of the deprotonated arm (or the deprotonated nitrogen atom), and C* designates the C atom that have undergone deprotonation. As

it has been discussed, H^+ is abstracted from the nitrogen atom with Tren, while it is taken from carbon atom with Me_6tren and TMPA. As it was discussed, C* binds the Cu in the $[Cu(Me_6Tren_{-H})]^+$ case, and remains free in $[Cu(TMPA_{-H})(O_2)]^+$. From $[Cu(Me_6Tren)(X)]^+$ to $[Cu(Me_6Tren_{-H})]^+$, the loss of acid leads to a reorganization of the complex. A 2.00 Å CuC* bond is formed, to the detriment of a CuN_{eq} bond, changing the coordination sphere. The structure becomes asymmetric. The charge of Cu is very close in both structures. CuN bond lengths do not change so much, but the charge of N atoms is increased by approximately 0.3, while the charge of the deprotonated C* decreases by 0.2. The changes correspond to the one electron difference between both structures. The Mulliken spin density on Cu is the same in structures $[Cu(Tren_{-H})]^+$ and $[Cu(Me_6Tren_{-H})]^+$, but the Cu charge is higher in the Tren case, what makes it less sensible to O_2. Since the decoordination of the acid leads to the coordination of the C* carbanion on Cu, the coordination of O_2 would happen on Cu. Even if the Cu charge is not modified, one might expect that the reactivity towards O_2 is different for both complexes, since the charge of N atoms is not the same. In the TMPA case, there are no strong differences between $[Cu(TMPA)]^+$ and $[Cu(TMPA_{-H})]^+$ species: the deprotonation leads to the formation of a carbanion. The supplementary electron is totally relocalized on Cu: the charge is 0.66, like in $[Cu(TMPA)]^+$. Hence, there are two binding sites for O_2, because the complex can not be reorganized, like $[Cu(Me_6Tren_{-H})]^+$ does. Three possibilities are then possible (i) the coordination on Cu only, (ii) the coordination on C* only and (iii) coordination on both sites. The Mulliken spin density is almost concentrated on the deprotonated carbon atom, and even if Cu has a +I character, O_2 is very likely to react with radicals[42]. $[Cu(L_{-H})]^+$ complexes have been considered in the doublet spin state, due to their odd number of electrons. Indeed, quartet spin state was not considered, because the supplementary electron is relocated on Cu (as indicated by the charges), which gives it a $(4s)^0$ $(3d)^{10}$ character.

4. Gas phase O_2 coordination on Cu complexes

4.1. Gas phase O_2 coordination on $[Cu(L)]^+$ complexes

Several studies on O_2 coordination on mononuclear Cu complexes were led in the condensed phase. Between Tren, Me_6Tren and TMPA copper complexes, the most reactive towards O_2 is $[Cu(Me_6Tren)]^+$ due to the strong donor character of the amine groups ($\Delta H_{coord}°$ = -44.9 kJ·mol^{-1}[43]), followed by $[Cu(TMPA)]^+$ ($\Delta H_{coord}°$ = -29.8 kJ·mol^{-1}[43], close to the -33.5 kJ·mol^{-1} previously found[44]). $[Cu(Tren)]^+$ does not form stable complex with O_2. This trend is also observed in the gas phase, both experimentally (Figure 10) and theoretically. Actually, the coordination of O_2 was observed in the gas phase on $[Cu(Tren)]^+$, $[Cu(Me_6Tren)]^+$ and $[Cu(TMPA)]^+$ ion, after selection of the corresponding $[Cu(L)]^+$ ion followed by collisions with O_2 (with a low collision voltage). The coordination of O_2 is better according the series Me_6Tren, TMPA, Tren. Me_6Tren is then a ligand of choice for the activation of O_2, both in the condensed and in the gas phase, compared to the other two. However, $[Cu(Me_6Tren)(O_2)]^+$ and $[Cu(TMPA)(O_2)]^+$ dimerize quickly in solution[43]. Based on previous studies, we expect that B3LYP is giving reliable results of absolute BDE values, at least for non-deprotonated ligands[32]. Indeed, BDEs of LCu-O_2 have been calculated at the B3LYP/6-31+G(d,p) level of theory. Ratios of peak intensities $[Cu(L)(O_2)]^+/[Cu(L)]^+$ (Figure 10) are qualitatively in accordance with DFT results (Table 1). By comparison, $[Cu(TMG_3Tren)]^+$ (TMG_3Tren: tris(tetramethylguanidino)-Tren), known to form mononuclear adducts with O_2 in the condensed phase, exhibits a $\Delta H_{coord}°$ of only -11.52 kJ·mol^{-1}, in DMF[45]. In the gas phase, no O_2 coordination has been observed with $[Cu(TMG_3Tren)]^+$. Bulky groups of TMG_3Tren ligand, even if they prevent the $[Cu(L)(O_2)]^+$ complex to dimerization, unfavor the coordination of O_2. PES scan of the CuO_p bond length (with optimization at each step) revealed a barrierless process for O_2 coordination. The first criterion to apprehend the strength of the CuO bond is its distance. It is a little bit shorter with Me_6Tren as ligand, as a witness of the higher BDE obtained with that ligand (Table 1). To properly activate O_2, it is necessary to fill one of its semi-occupied orbitals, towards the formation of a superoxide ion, which has a radical character and a negative charge. The O_2 activation is mainly described as an electron transfer from $Cu^{(I)}$ to O_2. The coordination of O_2 on $[Cu(L)]^+$ structures leads to the contraction of the CuN_{ax} bond and to the elongation of CuN_{eq} bonds, as a consequence of (i) the electron-pumping on the d_{z^2} orbital by O_2 and

(ii) steric hindrance induced by O_2. The charge of Cu goes from roughly 0.7 e before to 1.4 e after O_2 coordination, as an obvious electron transfer from $Cu^{(I)}$ to O_2, leading to the formation of a $Cu^{(II)}$-superoxo moiety. It is consistent with the electron transfer that may take place if the ligand has efficient electron-donating character. The transferred charge (about 0.83 in both cases) is almost taken from Cu, and not from N coordinating atoms: there are no strong variations of N charges before and after coordination of O_2. Theoretical studies on $[Cu(Me_6Tren)(O_2)]^+$ and $[Cu(TMPA)(O_2)]^+$ have described them as end-on $Cu^{(II)}$-superoxos, in the triplet spin state[33,34,46]. On both $[Cu(Me_6Tren)(O_2)]^+$ (Figure 11, top) and $[Cu(TMPA)(O_2)]^+$ (Figure 11, bottom), the radical anionic nature of the O_2 moiety ion is confirmed. CuO_2 adduct possesses a charge distribution of a $Cu^{(II)}$-$O_2^{\bullet-}$ species, as indicated by the OO distances (1.27 Å), close to the expected value of a superoxide ion[47], by Bader charges and by Mulliken spin density (MSD). Global charge of O_2 are -0.82 e (Me_6Tren) and -0.85 e (TMPA) is close from the charge of free superoxo anion (-1 e). Global MSD on CuO_2 are 1.87 (Me_6Tren) and 1.93 (TMPA), out of a total of two. $[Cu(Me_6Tren)(O_2)]^+$ has a lower radical character and a more anionic O_2 moiety than $[Cu(TMPA)(O_2)]^+$. It means that $[Cu(TMPA)(O_2)]^+$, although it was not isolated in the condensed phase, is more able to abstract a hydrogen atom, while $[Cu(Me_6Tren)(O_2)]^+$ just abstract a somewhat more protonic hydrogen particle. The charge of O_2 is much lower with Tren (-0.32 e) and TMG_3Tren (-0.51 e) ligands, as a consequence of the smaller binding energy. Moreover, with TMG_3Tren as ligand, the charge is delocalized on the whole ligand. In that latter cases, CuO_2 moiety can be described as an in-between $Cu^{(I)}$-O_2 and $Cu^{(II)}$-$O_2^{\bullet-}$ characters. It is well visible that $[Cu(Tren)]^+$ has a stronger $Cu^{(I)}$-O_2 character (higher MSD and lower charges on O_2 moiety). The MSD on Cu, O_p and O_d in $[Cu(TMG_3Tren)]^+$ reaches 0.49, 0.66 and 0.71, respectively. The charges on Cu (0.91 e), on O_p (-0.29 e) and O_d (-0.22 e) indicate that the O_2 moiety has a lower anionic character. Bulky groups of TMG_3Tren ligand are responsible of the absence of coordination in the gas phase and of the poor activation of O_2 (even if the complex with O_2 is able to oxidize weak CH/OH bonds in the condensed phase[48]).

Complex	BDE /kJ·mol^{-1}
$[Cu(Tren)(O_2)]^+$	18
$[Cu(Me_6Tren)(O_2)]^+$	30
$[Cu(TMPA)(O_2)]^+$	27
$[Cu(TMG_3Tren)(O_2)]^+$	23

Table 1: O_2 coordination energies calculated at the B3LYP/6-31+G(d,p) level of theory for some tripodal Cu complexes.

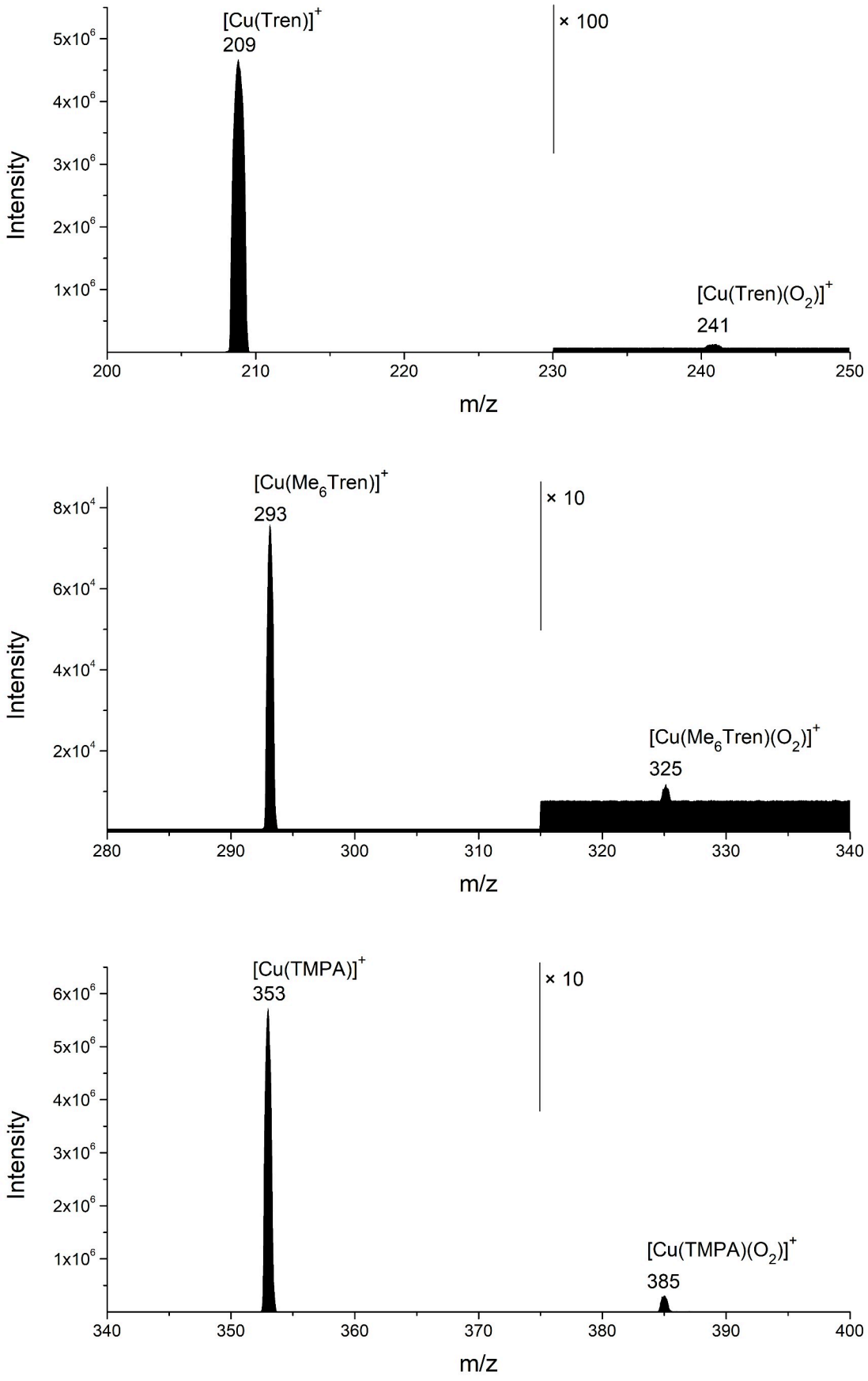

Figure 10: CAR-MSMS spectra of $[Cu(Tren)]^+$ (top), $[Cu(Me_6Tren)]^+$ (middle) and $[Cu(TMPA)]^+$ (bottom), with O_2 as collision gas ($P = 6.5 \cdot 10^{-3}$ mbar, $V_{coll} = 3$ V).

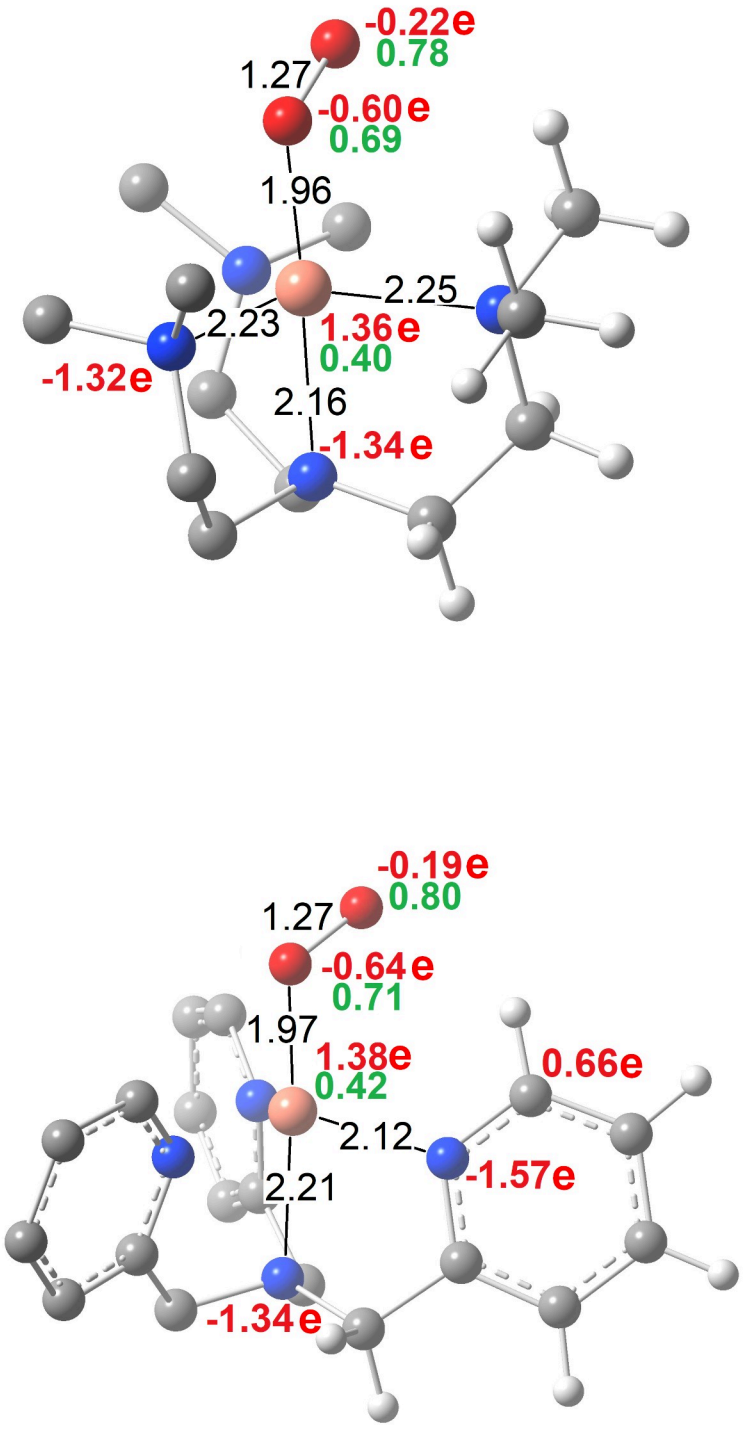

Figure 11: Structures of [Cu(Me$_6$Tren)(O$_2$)]$^+$ (top) and [Cu(TMPA)(O$_2$)]$^+$ (bottom), calculated at the B3LYP/6-31+G(d,p) level of theory. Some important distances (in Å, black), Bader charges (bold red) and Mulliken spin densities (bold green) are indicated. Some H and e *(the elementary electric charge) are removed for the sake of clarity.*

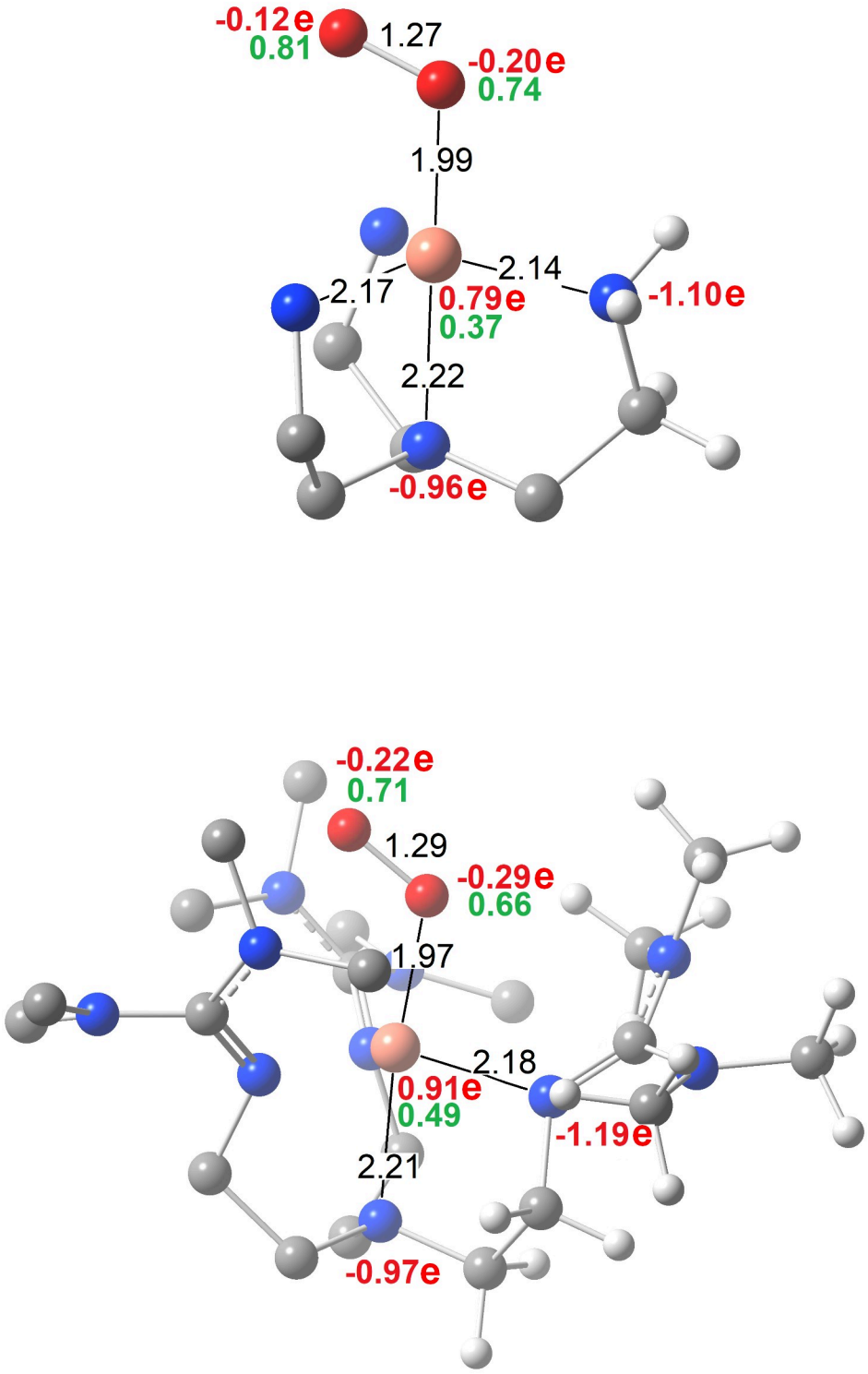

Figure 12: Structures of $[Cu(Tren)(O_2)]^+$ (top) and $[Cu(TMG_3Tren)(O_2)]^+$ (bottom), calculated at the B3LYP/6-31+G(d,p) level of theory. Some important distances (in Å, black), Bader charges (bold red) and Mulliken spin densities (bold green) are indicated. Some H and e *(the elementary electric charge) are removed for the sake of clarity.*

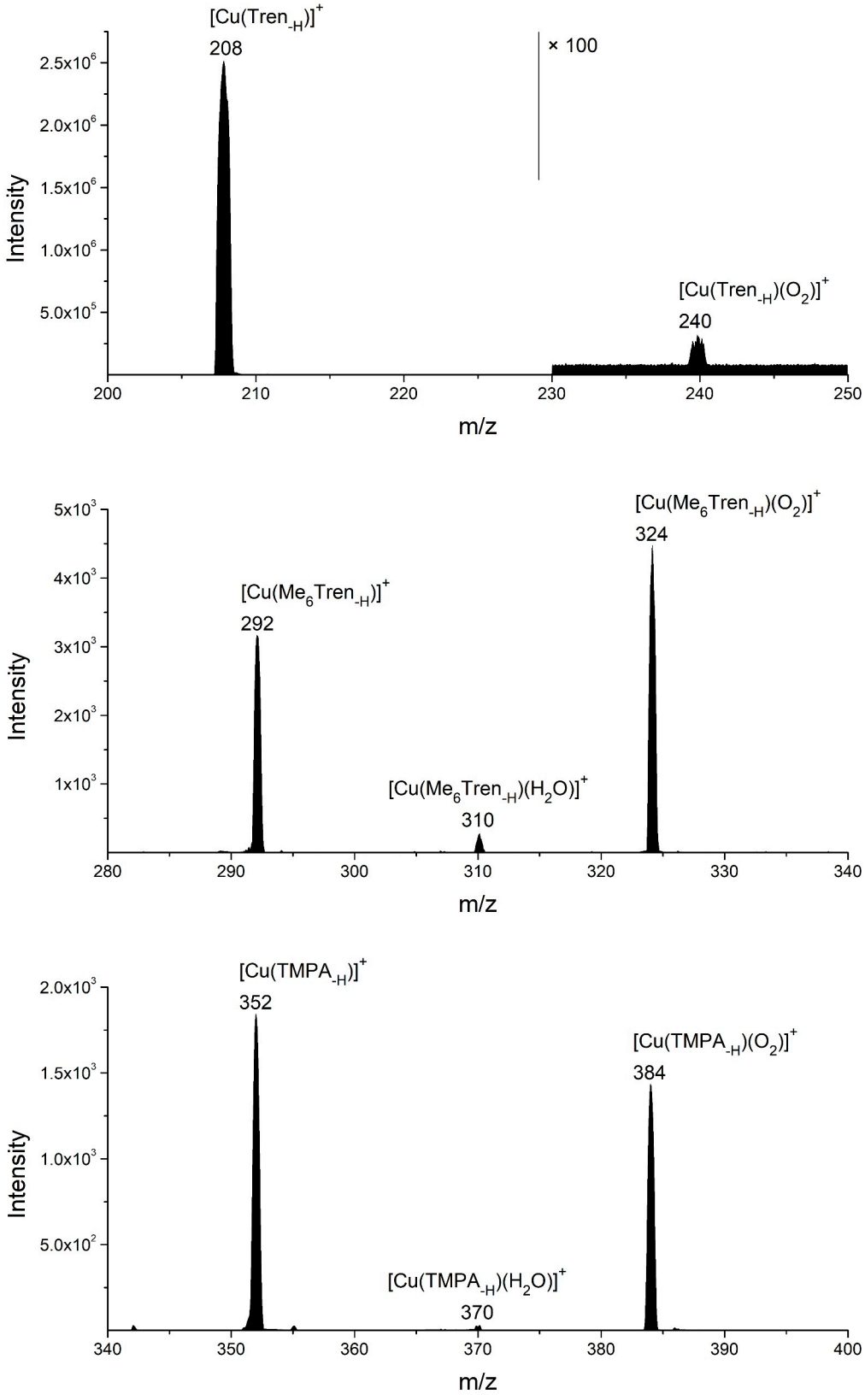

Figure 13: MSMS spectra of $[Cu(Tren_{-H})]^+$ (top), $[Cu(Me_6Tren_{-H})]^+$ (middle) and $[Cu(TMPA_{-H})]^+$ (bottom), with O_2 as collision gas ($P = 6.5 \cdot 10^{-3}$ mbar, $V_{coll} = 3$ V)

4.2. Gas phase O_2 coordination on $[Cu(L_{-H})]^+$ complexes

The coordination of O_2 on $[Cu(L)]^+$ and $[Cu(L_{-H})]^+$ was observed in the gas phase (L being Me_6Tren, TMPA). The coordination of O_2 was also tested on $[Cu(Tren_{-H})]^+$ and was found to be very low, as its non-deprotonated analogous $[Cu(Tren)]^+$. We will particularly focus on Me_6Tren and TMPA cases, since their deprotonated species exhibit an enhanced reactivity towards O_2. The coordination of O_2 on $[Cu(Me_6Tren_{-H})]^+$ is around 85 times better than on $[Cu(Me_6Tren)]^+$. Surprisingly, with TMPA as ligand, O_2 coordination is approximately 115 times better on $[Cu(TMPA_{-H})]^+$ complex (Figure 13).

4.2.1. The case of Me_6Tren

The reorganization of the molecule consecutive to H_2O departure leads to the formation of a strong CuC bond, which is a dative bond. It is even stronger than CuN_{eq} bonds. We proposed that the coordination of O_2 on $[Cu(Me_6Tren_{-H})]^+$ happens on the Cu ion. The optimized geometry of $[Cu(Me_6Tren_{-H})(O_2)]^+$ (Figure 14) clearly shows a hydrogen bonding between the distal oxygen atom and one of the hydrogen atoms of the deprotonated methyl group. The stabilization energy of a H bond is expected to be between 5 and 50 $kJ{\cdot}mol^{-1}$. So, the formation of a hydrogen bond may explain the better coordination of O_2 on $[Cu(Me_6Tren_{-H})]^+$. Bond Critical Point (BCP) analysis has used there to calculate the influence of this hydrogen bond on the O_2 coordination energy. An electronic density ρ of 0.024 electron.a_0^{-3} was found at the hydrogen bond BCP. This value, compared to the ρ value of CuO, CuN_{eq} and CuC bonds (0.091, 0.061 and 0.080 electron.a_0^{-3}, respectively), is the witness of a relatively strong hydrogen bond that stabilizes the whole structure. Hydrogen bonds also exists in $[Cu(Me_6Tren(O_2)]^+$ structure but are only 0.007 electron.a_0^{-3}. Furthermore, this strong hydrogen bond generates a five-membered cycle, which is expected to considerably stabilize the structure. It is important to note that PES scan of CuO_p bond (dissociation of CuO_2) does not exhibit a local maximum of energy. It means that the coordination of O_2 on $[Cu(Me_6Tren_{-H})]^+$ is a barrierless process. With Me_6Tren_{-H} as ligand, the CuO distance is a little bit shorter than with Me_6Tren, and the OO bond is elongated by 0.03 Å. The weakening of the OO bond is quite visible with the help of BCP analysis (Table 2). The value of ρ decreases from 0.443 to 0.421.

Species	$[Cu(Me_6Tren)(O_2)]^+$		$[Cu(Me_6Tren_{-H})(O_2)]^+$	
Bond	ρ /e.a_0^{-3}	Δρ /e.a_0^{-5}	ρ /e.a_0^{-3}	Δρ /e.a_0^{-5}
CuO	0.086	0.445	0.091	0.400
OO	0.443	-0.657	0.421	-0.573
CuN_{ax}	0.061	0.241	0.063	0.215
CuN_{eq}	0.054 0.056 (x2)	0.189 0.183 (x 2)	0.059 0.042	0.212 0.164
CuC*	--	--	0.080	0.192
O_dH (H bond)	0.007 (x3)	0.027 (x 3)	0.024	0.080
O_pH (H bond)	0.007	0.032	0.006 (x 2)	0.027 (x 2)

Table 2: Electron densities ρ / gradient of the density Δρ values at the BCP of some selected bonds. These values were calculated from B3LYP geometries.

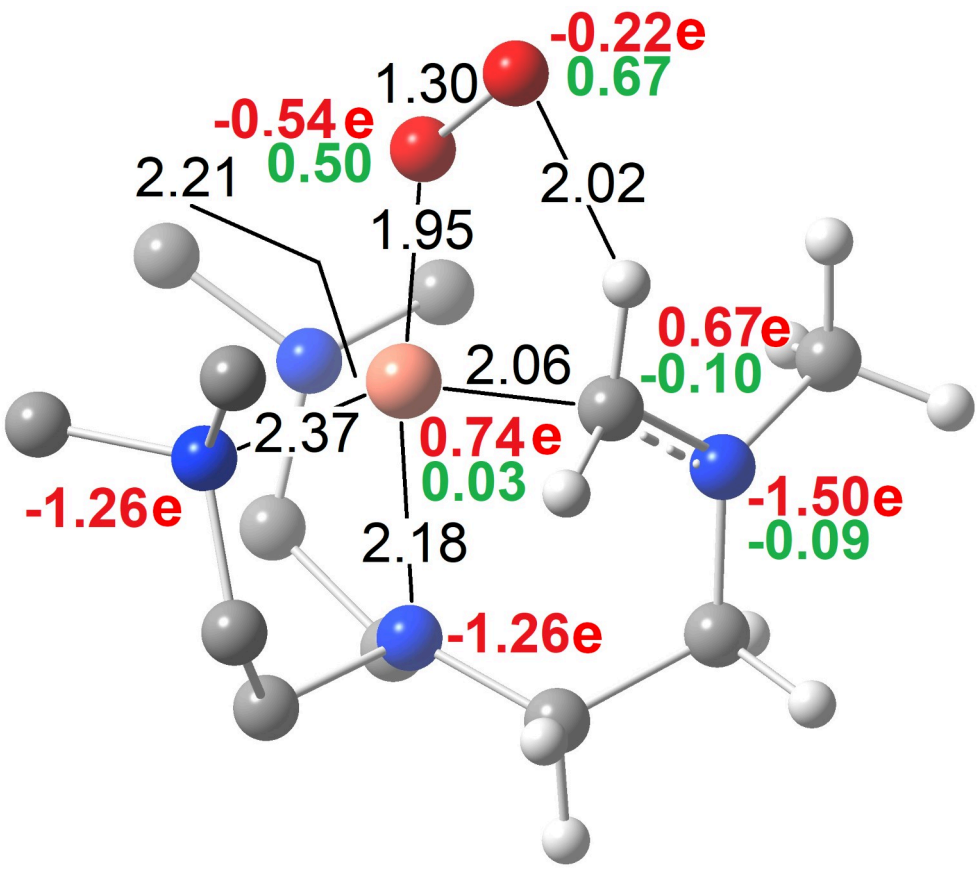

Figure 14: Structure of $[Cu(Me_6Tren_{-H})(O_2)]^+$, calculated at the B3LYP/6-31+G(d,p) level of theory. Some important distances (in Å, black), Bader charges (bold red) and Mulliken spin densities (bold green) are indicated. Some H and e *(the elementary electric charge) are removed for the sake of clarity.*

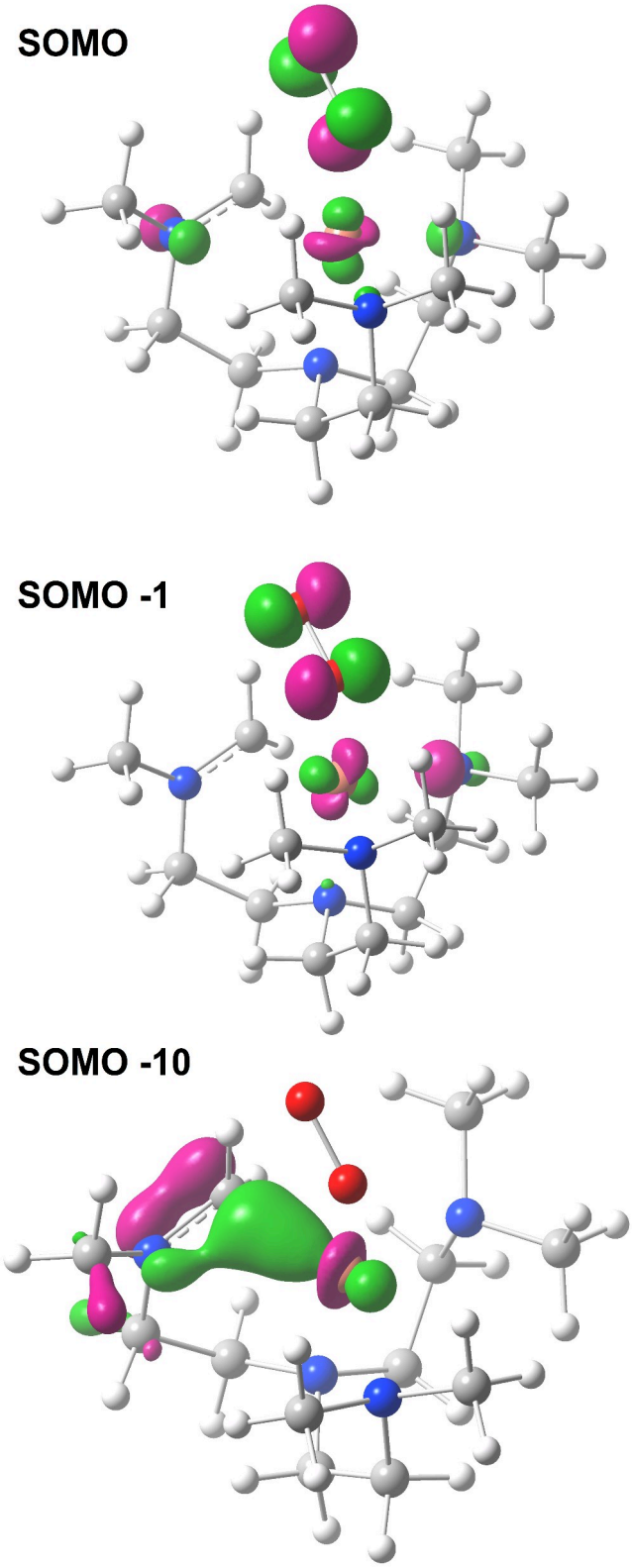

Figure 15: Selected α MOs (isovalue 0.09).

Concerning the activation of O_2, it has a lower charge (-0.76 against -0.82 in $[Cu(Me_6Tren)(O_2)]^+$) and a lower radical character (1.17 against 1.44). It might be also explained by the interaction of the distal oxygen with the H atom, which makes it less reactive. Moreover, the Cu center is closer to a +I formal charge. So, it seems like $[Cu(Me_6Tren_{-H})(O_2)]^+$ has a hybrid character between a $Cu^{(I)}$-O_2 and a $Cu^{(I)}$-$O_2^{\bullet-}$ character, stabilized by H-bonding. The former is sometimes evoked as a pre-catalytic complex in some studies[10,49] and the latter has never been proposed in the literature. Molecular orbitals analysis (Figure 15) reveal that the d_{z^2} orbital of Cu is involved in the interaction with C*. This orbital also exhibits π interaction with N*. d_{z^2} orbital is no longer implied in the bonding with the π_σ* orbital of O_2, unlike in $[Cu(Me_6Tren)(O_2)]^+$ and $d_{x^2-y^2}$ orbital is now responsible of O_2 bonding. The d orbitals of Cu are rearranged. Thus, SOMO and SOMO-1 α orbitals show $d_{x^2-y^2}$ - π_σ* (σ donation) and d_{xy} - π_v* (π back donation) interactions, explaining why the CuO bond is stronger, despite the +I character of Cu. A bond dissociation energy of 37 kJ·mol^{-1} has been calculated. Even it is lower than the BDE obtained with the non-deprotonated ligand, a difference of 7 kJ·mol^{-1} can not explain the much higher reactivity of $[Cu(Me_6Tren_{-H})]^+$ towards O_2. As we will discuss further, the use of B3LYP as functional on this unusual system is acceptable at first glance, but should be compared with other functionals.

It is possible to form $[Cu(Me_6Tren_{-H})(O_2)]^+$ in the first hexapole H0 (Figure 3), because of the strong reactivity of $[Cu(Me_6Tren_{-H})]^+$ towards O_2. Losses of 32 (O_2) and 33 ($O_2H^\bullet$) have been observed from $[Cu(Me_6Tren_{-H})(O_2)]^+$ (m/z 324, Figure 16). Only coordination of substrates (isopropanol, benzyl alcohol) have been observed when these alcohols are introduced in the collision cell. $[Cu(Me_6Tren_{-H})(O_2)]^+$ seems to be reactive towards itself. Further experiments with substrates having weaker CH/OH bonds may be performed in order to improve the understanding of what is happening.

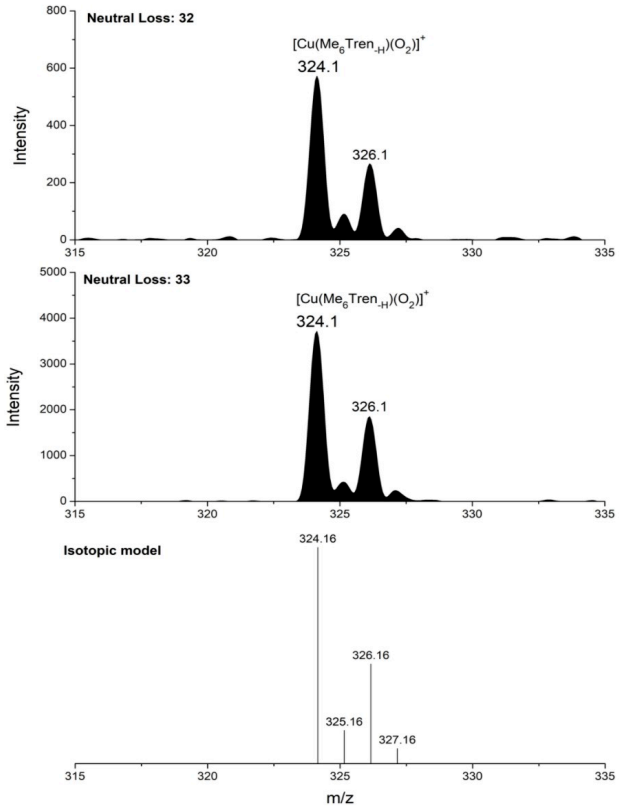

Figure 16: Neutral loss spectra with $P(O_2)$ = $5 \cdot 10^{-5}$ mbar in H0 and P(Ar) = $1.2 \cdot 10^{-3}$ mbar in collision cell (H2). Sample: $[Cu(Me_6Tren)(H_2O)](ClO_4)_2$ $5 \cdot 10^{-5}$ M in CH_3CN/H_2O 4:1.

4.2.2. The case of TMPA

Looking for stable structures of $[Cu(TMPA_{-H})(O_2)]^+$ leads to the identification of three isomers, depending on the binding mode of the dioxygen. When O_2 is only bound to Cu (Cu isomer), the bond dissociation energy (20 kJ·mol^{-1}) is lower than the one obtained with $[Cu(TMPA)]^+$ (27 kJ·mol^{-1}). This observation was also made with all the considered DFT functionals, with the gap between the two BDEs being 3 to 7 kJ·mol^{-1}, always in favor of $[Cu(TMPA)]^+$. CuO_2 possesses a $Cu^{(II)}$-superoxo character, like in $[Cu(TMPA)(O_2)]^+$. A few meaningless differences with $[Cu(TMPA)(O_2)]^+$ can be noted. Only the deprotonated carbon atom has a slightly higher charge and the negative charge is more displaced to the distal oxygen atom. Nevertheless, O_2 is well known to react with radicals. It is quite natural to consider that it can react with C*. On the one hand, when superoxo interacts with the C* only (C isomer), a strong carbon

oxygen bond is formed. The C isomer is stabilized by 165 $kJ \cdot mol^{-1}$ with respect to infinitely separed reactants (with B3LYP as functional). On the other hand, if O_2 binds both C* and Cu, the CuC isomer is stabilized by 244 $kJ \cdot mol^{-1}$ with respect to reactants. The energy of these two isomers explains the exacerbated reactivity of $[Cu(TMPA_{-H})]^+$ towards O_2.

The coordination on C* only leads to the formation of a peroxyl radical, as indicated by Mulliken spin density (almost concentrated on the OO moiety). The +I charge on Cu is confirmed by both Bader charge (0.63 e) and low MSD (0.008). In the literature, this kind of structure was proposed once as an intermediate in an oxidation mechanism[26]. With the “mono-carbon bridged bis-phenanthroline” ligand used in that publication, the distance between the metal and the radical center is more than 3 Å: O_2 is not able to coordinate both $Cu^{(I)}$ and the radical center. One can note that the nature of the metal is of prime importance to explain the observed reactivity: with $Cu^{(I)}$, a relatively electron-rich center, O_2 will prefer to attack on a close radical center, as confirmed by our DFT calculations. In our case, as proposed in the publication, one-electron relocalization happens from the lone pair of the deprotonated carbon to the $Cu^{(II)}$ center. It is necessary to have a sufficient distance between C* and Cu, to avoid the formation of a bridging O_2 (CuC isomer). The peroxyl radical is carried by a pyridine cycle that unfavors its evolution to a C=O (loss of aromaticity on the cycle).

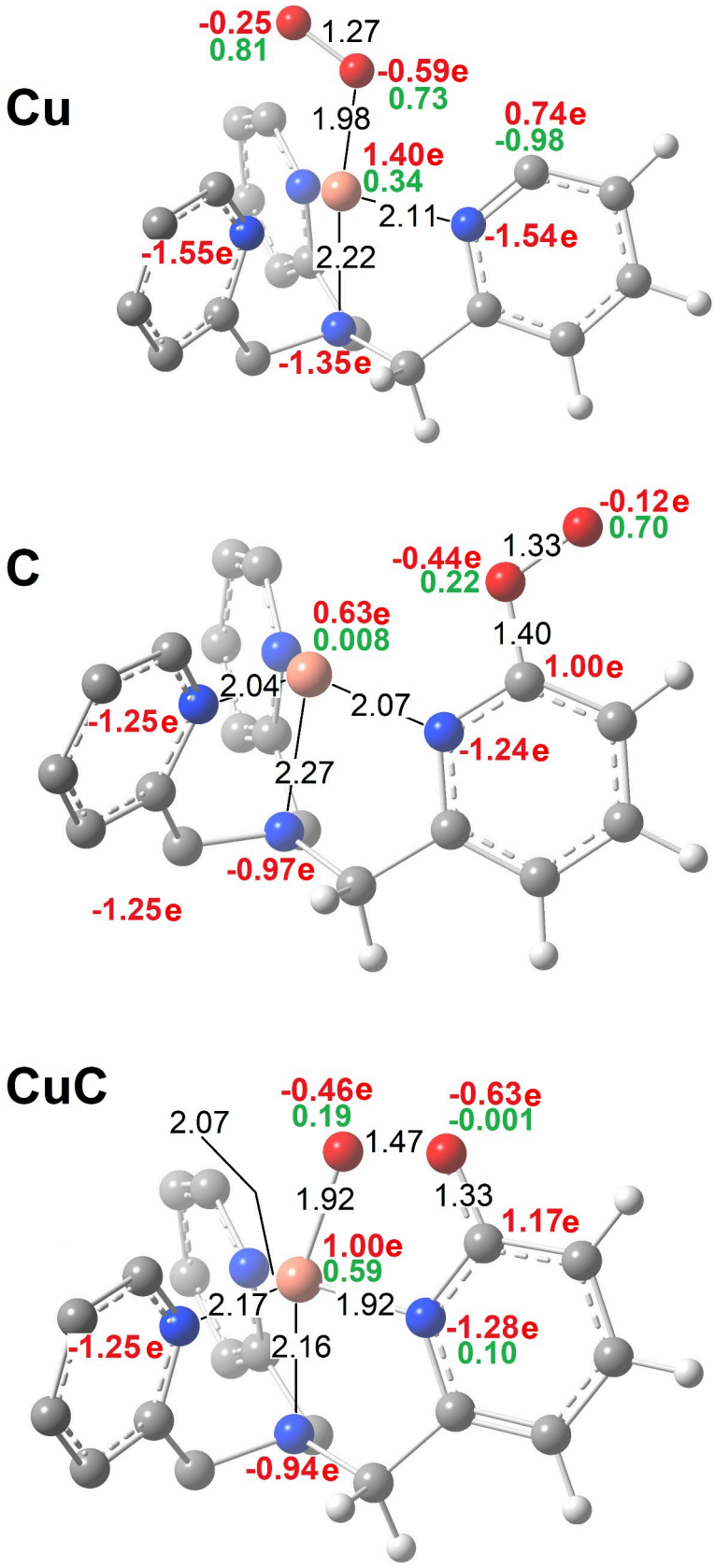

Figure 17: Structures of $[Cu(TMPA_{-H})(O_2)]^+$, calculated at the B3LYP/6-31+G(d,p) level of theory. Some important distances (in Å, black), Bader charges (bold red) and Mulliken spin densities (bold green) are indicated. Some H and e *(the elementary electric charge) are removed for the sake of clarity.*

Species	$[Cu(TMPA)(O_2)]^+$		$[Cu(TMPA_{-H})(O_2)]^+$ "Cu"	
Bond	ρ /e.a_0^{-3}	Δρ /e.a_0^{-5}	ρ /e.a_0^{-3}	Δρ /e.a_0^{-5}
CuN_{ax}	0.053	0.209	0.053	0.201
CuN_{eq}	0.072 0.069 (x2)	0.263 0.246 (x2)	0.071 0.069 (x2)	0.253 0.248 (x2)
CuO	0.075	0.429	0.082	0.407
OO	0.447	-0.689	0.455	-0.697
CuN*	0.053	0.209	0.069	0.250
C*N*	--	--	0.362	-0.326
O_dH (H bond)	0.010	0.034	0.009	0.033
O_pH (H bond)	0.007	0.032	-	-
Species	$[Cu(TMPA_{-H})(O_2)]^+$ "C"		$[Cu(TMPA_{-H})(O_2)]^+$ "CuC"	
Bond	ρ /e.a_0^{-3}	Δρ /e.a_0^{-5}	ρ /e.a_0^{-3}	Δρ /e.a_0^{-5}
CuN_{ax}	0.054	0.186	0.066	0.184
CuN_{eq}	0.082	0.281	0.078 0.063	0.247 0.207
CuO	--	--	0.100	0.390
OO	0.381	-0.242	0.263	0.039
CuN*	0.076	0.262	0.109	0.385
C*N*	0.355	-1.142	0.348	-1.088
CO	0.285	-1.042	0.321	-0.415

Table 3: Electron density ρ and gradient of the density Δρ values at the BCP of selected bonds. These values were calculated from B3LYP geometries.

If O_2 binds both Cu and C* sites (CuC isomer), the CO bond is 1.33 Å long. OO bond is well weakened by the interaction with the C atom: it is elongated by 0.20 Å, and lose its covalent character to become quite dative. Cu has a charge of 1.00 e, which corresponds to a character between $Cu^{(I)}$ and $Cu^{(II)}$, on the basis of the charges in the structures mentioned above. Along the Cu, C, CuC series, the charge of C* increases, as the witness of its growing oxidation state. For the CuC isomer, it is well visible that the C* has been oxidized: the charge of distal oxygen atom strongly decreases, while C* charge increases from 0.74 e to 1.17 e.

The coordination of O_2 on both Cu and C leads also to the reinforcement of CuN* bond, as a consequence of the formation of a stable five-membered ring. The OO bond is not totally broken,

because the loss of aromaticity on the cycle counteracts with the formation of the CO bond. The huge electronic stabilization leads to a deep change in the repartition of the charges. N atoms see their charge increased by ~ 0.4 (N_{ax}) or ~ 0.3 (N_{eq}). There is almost one negative charge that is relocated on the carbon atoms between N atoms. Charges of methylenic C atoms decrease by about 0.2 e). Here again, the development of new catalysts with a CuC* distance making it possible to bind O_2 on both sites is possible. In this perspective, the use of aliphatic and coordinating ligands with weakened CH bonds could be explored. The oxidation of an aliphatic ligand (i.e. with no energy destabilization due to loss of aromaticity) may lead to the formation of a $Cu^{(II)}$-oxyl intermediate. The experiments made with Me_6Tren (Figure 16) have been reproduced with TMPA as ligand. Only the loss of 32 (O_2) and no reactivity towards substrates have been observed.

4.3. Comparison with other functionals and basis sets

As we have seen, B3LYP functional cannot explain why $[Cu(Me_6Tren_{-H})]^+$ is so reactive towards O_2. Indeed, B3LYP is known to have weaknesses for the consideration of long-range interactions, such as H bonds. O_2 coordination energies on $[Cu(Me_6Tren)]^+$ and $[Cu(Me_6Tren_{-H})]^+$ are reported in Table 4 for some methods, chosen for their expected ability to give good predictions for the bonding of substrates on transition metals ions.

	6-31+G(d,p)		LANL2DZ (Cu) / 6-31+G(d,p) (other atoms)		6-311++G(3df,2pd)		def2-QZVP	
	$[Cu(L)]^+$	$[Cu(L_{-H})]^+$	$[Cu(L)]^+$	$[Cu(L_{-H})]^+$	$[Cu(L)]^+$	$[Cu(L_{-H})]^+$	$[Cu(L)]^+$	$[Cu(L_{-H})]^+$
B3LYP	30	37	18	26	27	31	25	30
CAM-B3LYP	22	24	-	-	18	20	16	17
mPWPW	60	77	47	63	58	74	54	70
BP86	59	79	-	-	56	75	53	72
B97-1	35	39	26	29	-	-	-	-
M06	47	56	-	-	40	47	29	35
MN15	32	52	17	44	27	48	22	42
TPSSKCIS	65	82	52	69	-	-	-	-
τ-HCTHhyb	37	45	27	34	-	-	-	-

Table 4: BDEs (in kJ·mol^{-1}) for O_2 coordination on $[Cu(Me_6Tren)]^+$ and $[Cu(Me_6Tren_{-H})]^+$ complexes calculated at different levels of theory. For high basis sets (6-311++G(3df,2pd) and def2-QZVP) calculations, geometries have been computed at the 6-31+G(d,p) basis set. ZPEs are from the 6-31+G(d,p) level of theory.

The add of a pseudo-potential on the metallic center was sometimes used in the literature to model the core electrons of transition metal ions. However, it does not strongly affect the BDE difference. It even tends to reduce the stabilization energy of O_2 bonding, by about 10 $kJ \cdot mol^{-1}$, for the investigated functionals. One can naturally ask about the size of the basis set we have used. No improvements were obtained with bigger basis sets (6-311++G(3df,2pd) and def2-QZVP were tested). BDEs are reduced by a few $kJ \cdot mol^{-1}$ when functionals are used in combination with these extended basis sets. The use of diffuse functions with 6-311(3df,2pd) is on purpose to model better hydrogen bonds[50]. On a qualitative point of view, all the methods are in accordance to designate $[Cu(Me_6Tren_{-H})]^+$ as a better coordinating species than $[Cu(Me_6Tren)]^+$, excepted CAM-B3LYP, for which very close BDE values were obtained. However, only MN15, mPWPW, BP86 and TPSSKCIS seem to take into account the hydrogen bonding. Even if the use of B3LYP is recommended for the coordination of O_2 on Cu complexes, the unusual nature of the adducts formed here may require the use of functionals more able to describe the system.

Conclusions

In this chapter, we have presented the reactivity of Cu complexes towards O_2 in the gas phase, with the help of the CAR-MSMS method. Cu complexes of tripodal ligands, such as Tren, Me_6Tren and TMPA have shown low affinity with O_2. However, the electrospray source allows the formation of deprotonated Cu complexes, which has already been described in the literature. The position of the proton to be abstracted has been discussed with the help of partially deuterated ligands. On the basis of DFT calculations, we have shown that the flexible $[Cu(Me_6Tren_{-H})]^+$ complex is reorganized (formation of a CuC bond), while the loss of proton from the more rigid $[Cu(Tren_{-H})]^+$ and especially $[Cu(TMPA_{-H})]^+$ do not strongly modify the geometry around Cu. Bader charges and Mulliken spin densities have shown that the supplementary electron is relocated on the Cu, giving it a $(4s)^0$ $(3d)^{10}$ character. The deprotonated complexes $[Cu(Me_6Tren_{-H})]^+$ and $[Cu(TMPA_{-H})]^+$ have shown remarkable properties to bind O_2 in the gas phase, for different reasons. In the case of flexible ligand (Me_6Tren), the better reactivity has been explained by the presence of a strong H bond that stabilize the superoxo moiety. On the other hand, the coordination of O_2 is favored by the presence of a distinct radical center on rigid ligand (TMPA). Two very stable isomers were found and explain the exacerbated reactivity of $[Cu(TMPA_{-H})]^+$ towards O_2.

These results may lead to the emergence of new metal-radical complexes for activation of substrates. Two interesting possibilities can be proposed. On the one hand, the presence of a carboradical close to the metal center M might allow the formation of a bridging M-OO-C species, that can evolve into a CuO^+ species which is an oxidative species. This reactivity is on condition that the OO can be broken, in other terms, that the ligand can be oxidized. On the other hand, if metal center and the carboradical are separated enough to avoid the formation of M-OO-C, the resulting peroxyl radical has a strong abstracting power of H atom and a free coordination site is still accessible to substrates on the metallic center, following the example of Neumann and coworkers[26].

References

1. Chen, P.; Root, D.E.; Campochiaro, C.; Fujisawa, K.; Solomon, E.I. Spectroscopic and Electronic Structure Studies of the Diamagnetic Side-On CuII-Superoxo Complex Cu(O2)[HB(3-R-5-IPrpz)3]: Antiferromagnetic Coupling versus Covalent Delocalization. *J. Am. Chem. Soc.* **2003**, *125*, 466–474, doi:10.1021/ja020969i.

2. Thomas, F. Ten Years of a Biomimetic Approach to the Copper(II) Radical Site of Galactose Oxidase. *Eur. J. Inorg. Chem.* **2007**, *2007*, 2379–2404, doi:10.1002/ejic.200601091.

3. Ciano, L.; Davies, G.J.; Tolman, W.B.; Walton, P.H. Bracing Copper for the Catalytic Oxidation of C–H Bonds. *Nat. Catal.* **2018**, *1*, 571–577, doi:10.1038/s41929-018-0110-9.

4. Abe, T.; Morimoto, Y.; Tano, T.; Mieda, K.; Sugimoto, H.; Fujieda, N.; Ogura, T.; Itoh, S. Geometric Control of Nuclearity in Copper(I)/Dioxygen Chemistry. *Inorg. Chem.* **2014**, *53*, 8786–8794, doi:10.1021/ic501461n.

5. Fukatsu, A.; Morimoto, Y.; Sugimoto, H.; Itoh, S. Modelling a ‘Histidine Brace’ Motif in Mononuclear Copper Monooxygenases. *Chem. Commun.* **2020**, *56*, 5123–5126, doi:10.1039/D0CC01392G.

6. Kim, S.; Lee, J.Y.; Cowley, R.E.; Ginsbach, J.W.; Siegler, M.A.; Solomon, E.I.; Karlin, K.D. A N3S(Thioether)-Ligated CuII-Superoxo with Enhanced Reactivity. *J. Am. Chem. Soc.* **2015**, *137*, 2796–2799, doi:10.1021/ja511504n.

7. Bhadra, M.; Transue, W.J.; Lim, H.; Cowley, R.E.; Lee, J.Y.C.; Siegler, M.A.; Josephs, P.; Henkel, G.; Lerch, M.; Schindler, S.; et al. A Thioether-Ligated Cupric Superoxide Model with Hydrogen Atom Abstraction Reactivity. *J. Am. Chem. Soc.* **2021**, *143*, 3707–3713, doi:10.1021/jacs.1c00260.

8. Schindler, S. Reactivity of Copper(I) Complexes Towards Dioxygen. *Eur. J. Inorg. Chem.* **2000**, *2000*, 2311–2326, doi:10.1002/1099-0682(200011)2000:11<2311::AID-EJIC2311>3.0.CO;2-7.

9. Schatz, M.; Becker, M.; Thaler, F.; Hampel, F.; Schindler, S.; Jacobson, R.R.; Tyeklár, Z.; Murthy, N.N.; Ghosh, P.; Chen, Q.; et al. Copper(I) Complexes, Copper(I)/O2 Reactivity, and Copper(II) Complex Adducts, with a Series of Tetradentate Tripyridylalkylamine Tripodal Ligands. *Inorg. Chem.* **2001**, *40*, 2312–2322, doi:10.1021/ic000924n.

10. Prigge, S.T.; Eipper, B.A.; Mains, R.E.; Amzel, L.M. Dioxygen Binds End-On to Mononuclear Copper in a Precatalytic Enzyme Complex. *Science* **2004**, *304*, 864–867, doi:10.1126/science.1094583.

11. Will, J.; Würtele, C.; Becker, J.; Walter, O.; Schindler, S. Synthesis, Crystal Structures and Reactivity towards Dioxygen of Copper(I) Complexes with Tripodal Aliphatic Amine Ligands. *Polyhedron* **2019**, *171*, 448–454, doi:10.1016/j.poly.2019.07.007.

12. Würtele, C.; Gaoutchenova, E.; Harms, K.; Holthausen, M.C.; Sundermeyer, J.; Schindler, S. Crystallographic Characterization of a Synthetic 1:1 End-On Copper Dioxygen Adduct Complex. *Angew. Chem. Int. Ed.* **2006**, *45*, 3867–3869, doi:10.1002/anie.200600351.

13. Diaz, D.E.; Quist, D.A.; Herzog, A.E.; Schaefer, A.W.; Kipouros, I.; Bhadra, M.; Solomon, E.I.; Karlin, K.D. Impact of Intramolecular Hydrogen Bonding on the Reactivity of Cupric Superoxide Complexes with O−H and C−H Substrates. *Angew. Chem. Int. Ed.* **2019**, *58*, 17572–17576, doi:https://doi.org/10.1002/anie.201908471.

14. Maiti, D.; Fry, H.C.; Woertink, J.S.; Vance, M.A.; Solomon, E.I.; Karlin, K.D. A 1:1 Copper−Dioxygen Adduct Is an End-on Bound Superoxo Copper(II) Complex Which Undergoes Oxygenation Reactions with Phenols. *J. Am. Chem. Soc.* **2007**, *129*, 264–265, doi:10.1021/ja067411l.

15. Kobayashi, Y.; Ohkubo, K.; Nomura, T.; Kubo, M.; Fujieda, N.; Sugimoto, H.; Fukuzumi, S.; Goto, K.; Ogura, T.; Itoh, S. Copper(I)-Dioxygen Reactivity in a Sterically Demanding Tripodal Tetradentate Tren Ligand: Formation and Reactivity of a Mononuclear Copper(II) End-On Superoxo Complex. *Eur. J. Inorg. Chem.* **2012**, *2012*, 4574–4578, doi:10.1002/ejic.201200177.

16. Koyanagi, G.K.; Caraiman, D.; Blagojevic, V.; Bohme, D.K. Gas-Phase Reactions of Transition-Metal Ions with Molecular Oxygen: Room-Temperature Kinetics and Periodicities in Reactivity. *J. Phys. Chem. A* **2002**, *106*, 4581–4590, doi:10.1021/jp014145j.

17. Caraiman, D.; Bohme, D.K. Periodic Trends in Reactions of Benzene Clusters of Transition Metal Cations, M(C6H6)1,2+ with O2. *J. Phys. Chem. A* **2002**, *106*, 9705–9717, doi:10.1021/jp0208900.

18. Donnelly, J.M.; Lermyte, F.; Wolny, J.A.; Walker, M.; Breeze, B.G.; Needham, R.J.; Müller, C.S.; O'Connor, P.B.; Schünemann, V.; Collingwood, J.F.; et al. Cu(III)–Bis-Thiolato Complex Forms an Unusual Mono-Thiolato Cu(III)–Peroxido Adduct. *Chem. Commun.* **2021**, *57*, 69–72, doi:10.1039/D0CC06921C.

19. Molina-Svendsen, H.; Bojesen, G.; McKenzie, C.J. Gas-Phase Reactivity of Coordinatively Unsaturated Transition Metal Complex Ions toward Molecular Oxygen. *Inorg. Chem.* **1998**, *37*, 1981–1983, doi:10.1021/ic970345r.

20. Lavanant, H.; Virelizier, H.; Hoppilliard, Y. Reduction of Copper(II) Complexes by Electron Capture in an Electrospray Ionization Source. *J. Am. Soc. Mass Spectrom.* **1998**, *9*, 1217–1221, doi:10.1016/S1044-0305(98)00100-7.

21. Lavanant, H.; Hecquet, E.; Hoppilliard, Y. Complexes of L-Histidine with Fe2+, Co2+, Ni2+, Cu2+, Zn2+ Studied by Electrospray Ionization Mass Spectrometry. *Int. J. Mass Spectrom.* **1999**, *185–187*, 11–23, doi:10.1016/S1387-3806(98)14044-7.

22. Gianelli, L.; Amendola, V.; Fabbrizzi, L.; Pallavicini, P.; Mellerio, G.G. Investigation of Reduction of Cu(II) Complexes in Positive-Ion Mode Electrospray Mass Spectrometry. *Rapid Commun. Mass Spectrom.* **2001**, *15*, 2347–2353, doi:10.1002/rcm.510.

23. Tisato, F.; Peruzzo, V.; Zanchetta, G.; Tamburini, S.; Traldi, P.; Porchia, M. Electrospray Ionization in the Study of the Interactions between Cytotoxic Phosphino Cu(I) Complexes and Selected Amino Acids and GlyGlyHis Peptide Model. *Eur. J. Mass Spectrom.* **2016**, *22*, 275–287, doi:10.1255/ejms.1441.

24. Böhme, D.K. Charge State Chemistry: What a Difference a Charge Makes in Gas-Phase Chemistry! *Int. J. Mass Spectrom.* **2021**, 116674, doi:10.1016/j.ijms.2021.116674.

25. Whittaker, J.W. Galactose Oxidase. In *Advances in Protein Chemistry*; Copper-Containing Proteins; Academic Press, 2002; Vol. 60, pp. 1–49 ISBN 10.1016/S0065-3233(02)60050-6.

26. Shen, K.; Diskin-Posner, Y.; Shimon, L.J.W.; Leitus, G.; Carmieli, R.; Neumann, R. Aerobic Oxygenation Catalyzed by First Row Transition Metal Complexes Coordinated by Tetradentate Mono-Carbon Bridged Bis-Phenanthroline Ligands: Intra- versus Intermolecular Carbon–Hydrogen Bond Activation. *Dalton Trans.* **2019**, *48*, 6396–6407, doi:10.1039/C9DT00828D.

27. Zhong, K.; Shan, C.; Zhu, L.; Liu, S.; Zhang, T.; Liu, F.; Shen, B.; Lan, Y.; Bai, R. Theoretical Study of the Addition of Cu–Carbenes to Acetylenes to Form Chiral Allenes. *J. Am. Chem. Soc.* **2019**, *141*, 5772–5780, doi:10.1021/jacs.8b13055.

28. Iacobucci, C.; Lebon, A.; De Angelis, F.; Memboeuf, A. CuAAC Click Reactions in the Gas Phase: Unveiling the Reactivity of Bis-Copper Intermediates. *Chem. - Eur. J.* **2016**, *22*, 18690–18694, doi:10.1002/chem.201603518.

29. Choi, Y.J.; Cho, K.-B.; Kubo, M.; Ogura, T.; Karlin, K.D.; Cho, J.; Nam, W. Spectroscopic and Computational Characterization of CuII–OOR (R = H or Cumyl) Complexes Bearing a Me6-Tren Ligand. *Dalton Trans.* **2011**, *40*, 2234, doi:10.1039/c0dt01036g.

30. Davydov, R.; Herzog, A.E.; Jodts, R.J.; Karlin, K.D.; Hoffman, B.M. End-On Copper(I) Superoxo and Cu(II) Peroxo and Hydroperoxo Complexes Generated by Cryoreduction/Annealing and Characterized by EPR/ENDOR Spectroscopy. *J. Am. Chem. Soc.* **2022**, *144*, 377–389, doi:10.1021/jacs.1c10252.

31. Karlin, K.D.; Hayes, J.C.; Juen, S.; Hutchinson, J.P.; Zubieta, J. Tetragonal vs. Trigonal Coordination in Copper(II) Complexes with Tripod Ligands: Structures and Properties of [Cu(C21H24N4)Cl]PF6 and [Cu(C18H18N4)Cl]PF6. *Inorg. Chem.* **1982**, *21*, 4106–4108, doi:10.1021/ic00141a049.

32. Ducéré, J.-M.; Goursot, A.; Berthomieu, D. Comparative Density Functional Theory Study of the Binding of Ligands to Cu+ and Cu2+: Influence of the Coordination and Oxidation State. *J. Phys. Chem. A* **2005**, *109*, 400–408, doi:10.1021/jp047971b.

33. de la Lande, A.; Gérard, H.; Moliner, V.; Izzet, G.; Reinaud, O.; Parisel, O. Theoretical Modelling of Tripodal CuN3 and CuN4 Cuprous Complexes Interacting with O2, CO or CH3CN. *JBIC J. Biol. Inorg. Chem.* **2006**, *11*, 593–608, doi:10.1007/s00775-006-0107-8.

34. de la Lande, A.; Salahub, D.; Moliner, V.; Gérard, H.; Piquemal, J.-P.; Parisel, O. Dioxygen Activation by Mononuclear Copper Enzymes: Insights from a Tripodal Ligand Mimicking Their CuM Coordination Sphere. *Inorg. Chem.* **2009**, *48*, 7003–7005, doi:10.1021/ic900567z.

35. Hratchian, H.P.; Schlegel, H.B. Finding Minima, Transition States, and Following Reaction Pathways on Ab Initio Potential Energy Surfaces. In *Theory and applications of computational chemistry: the first forty years*; Dykstra, C.E., Frenking, G., Kim, K., Scuseria, G.E., Eds.; Elsevier: Amsterdam ; Boston, 2005 ISBN 978-0-444-51719-7.

36. Matta, C.F. Hydrogen–Hydrogen Bonding: The Non-Electrostatic Limit of Closed-Shell Interaction Between Two Hydro. In *Hydrogen Bonding—New Insights*; Grabowski, S.J., Ed.; Springer Netherlands: Dordrecht, 2006; pp. 337–375 ISBN 978-1-4020-4853-1.

37. Jacobson, R.R.; Tyeklar, Zoltan.; Farooq, Amjad.; Karlin, K.D.; Liu, Shuncheng.; Zubieta, Jon. A Copper-Oxygen (Cu2-O2) Complex. Crystal Structure and Characterization of a Reversible Dioxygen Binding System. *J. Am. Chem. Soc.* **1988**, *110*, 3690–3692, doi:10.1021/ja00219a071.

38. Jacobson, R.R.; Tyeklar, Z.; Karlin, K.D.; Zubieta, J. Fluoride as a Terminal and Bridging Ligand for Copper: Isolation and x-Ray Crystallographic Characterization of Copper Monomeric and Dimeric Complexes [CuII(TMPA)F]Nn+ (n = 1 or 2; TMPA = Tris[(2-Pyridyl)Methyl]Amine). *Inorg. Chem.* **1991**, *30*, 2035–2040, doi:10.1021/ic00009a017.

39. Prigge, S.T.; Kolhekar, A.S.; Eipper, B.A.; Mains, R.E.; Amzel, L.M. Substrate-Mediated Electron Transfer in Peptidylglycine Alpha-Hydroxylating Monooxygenase. *Nat. Struct. Biol.* **1999**, *6*, 976–983, doi:10.1038/13351.

40. Aboelella, N.W.; Gherman, B.F.; Hill, L.M.R.; York, J.T.; Holm, N.; Young, V.G.; Cramer, C.J.; Tolman, W.B. Effects of Thioether Substituents on the O2 Reactivity of β-Diketiminate−Cu(I) Complexes: Probing the Role of the Methionine Ligand in Copper Monooxygenases. *J. Am. Chem. Soc.* **2006**, *128*, 3445–3458, doi:10.1021/ja057745v.

41. de la Lande, A.; Parisel, O.; Gérard, H.; Moliner, V.; Reinaud, O. Theoretical Exploration of the Oxidative Properties of a [(TrenMe1)CuO2]+ Adduct Relevant to Copper Monooxygenase Enzymes: Insights into Competitive Dehydrogenation versus Hydroxylation Reaction Pathways. *Chem. - Eur. J.* **2008**, *14*, 6465–6473, doi:10.1002/chem.200701595.

42. Eskola, A.J.; Pekkanen, T.T.; Joshi, S.P.; Timonen, R.S.; Klippenstein, S.J. Kinetics of 1-Butyl and 2-Butyl Radical Reactions with Molecular Oxygen: Experiment and Theory. *Proc. Combust. Inst.* **2019**, *37*, 291–298, doi:10.1016/j.proci.2018.05.069.

43. Weitzer, M.; Schindler, S.; Brehm, G.; Schneider, S.; Hörmann, E.; Jung, B.; Kaderli, S.; Zuberbühler, A.D. Reversible Binding of Dioxygen by the Copper(I) Complex with Tris(2-Dimethylaminoethyl)Amine (Me6tren) Ligand. *Inorg. Chem.* **2003**, *42*, 1800–1806, doi:10.1021/ic025941m.

44. Karlin, K.D.; Wei, N.; Jung, B.; Kaderli, S.; Zuberbuehler, A.D. Kinetic, Thermodynamic, and Spectral Characterization of the Primary Copper-Oxygen (Cu-O2) Adduct in a Reversibly Formed and Structurally Characterized Peroxo-Dicopper(II) Complex. *J. Am. Chem. Soc.* **1991**, *113*, 5868–5870, doi:10.1021/ja00015a054.

45. Lanci, M.P.; Smirnov, V.V.; Cramer, C.J.; Gauchenova, E.V.; Sundermeyer, J.; Roth, J.P. Isotopic Probing of Molecular Oxygen Activation at Copper(I) Sites. *J. Am. Chem. Soc.* **2007**, *129*, 14697–14709, doi:10.1021/ja074620c.

46. Solomon, E.I.; Heppner, D.E.; Johnston, E.M.; Ginsbach, J.W.; Cirera, J.; Qayyum, M.; Kieber-Emmons, M.T.; Kjaergaard, C.H.; Hadt, R.G.; Tian, L. Copper Active Sites in Biology. *Chem. Rev.* **2014**, *114*, 3659–3853, doi:10.1021/cr400327t.

47. Abrahams, S.C.; Kalnajs, J. The Crystal Structure of α-Potassium Superoxide. *Acta Crystallogr.* **1955**, *8*, 503–506, doi:10.1107/S0365110X55001540.

48. Maiti, D.; Lee, D.-H.; Gaoutchenova, K.; Würtele, C.; Holthausen, M.C.; Narducci Sarjeant, A.A.; Sundermeyer, J.; Schindler, S.; Karlin, K.D. Reactions of a Copper(II) Superoxo Complex Lead to C-H and O-H Substrate Oxygenation: Modeling Copper-Monooxygenase C-H Hydroxylation. *Angew. Chem.* **2008**, *120*, 88–91, doi:10.1002/ange.200704389.

49. Evans, J.P.; Ahn, K.; Klinman, J.P. Evidence That Dioxygen and Substrate Activation Are Tightly Coupled in Dopamine β-Monooxygenase: Implications for the Reactive Oxygen Species. *J. Biol. Chem.* **2003**, *278*, 49691–49698, doi:10.1074/jbc.M300797200.

50. Boese, A.D. Density Functional Theory and Hydrogen Bonds: Are We There Yet? *ChemPhysChem* **2015**, *16*, 978–985, doi:10.1002/cphc.201402786.

Conclusions

Global warming and energy-related issues have led the scientific community to imagine sustainable solutions. To face the end of oil era, nature is a source of inspiration. Indeed, enzymes are pretty nice examples of how nature uses abundant resources to add value to a lot of molecules. They are catalysts of choice operating with high selectivity, reducing drastically energy barriers leading to high reaction rates. The use of cheap, abundant transition metals, such as iron and copper, and of the freely available dioxygen as oxidant respects the principles of green chemistry. The first chapter of this thesis was an opportunity to recall why mononuclear cuproenzymes have retained our attention, because of their efficiency to oxidize a large variety of substrates, and of the wide range of models that have been already designed to reproduce their activity. Many studies have been led on these enzymes and their relative models to try to understand the way they work. Mechanisms still have gray areas, but the main intermediates have been unveiled. The mechanisms of the enzymes considered here (galactose oxidase, amine oxidase, lytic polysaccharide monooxygenase, dopamine beta-monooxygenase) reveal similarities. A main reaction pattern has been presented in this thesis. For a decade, structural biomimetism was the approach used by the scientific community to mimic the active sites of the enzymes. The first approach is based on geometric considerations. On the basis of crystallographic studies, the structures of the active sites have been determined, and the first coordination sphere is reproduced by molecular models, i.e. a transition metal ion surrounded by ligands. The number and the nature of coordinating atoms and the geometry around the metallic center have been taken into account for the elaboration of such models. A lot of efficient models were proposed to reproduce the structure of the active sites.

In the second chapter, we have shown what is the influence of the ligand and of a $Cu^{(I)}$ ion on the oxidation of toluene by O_2. The role of the ligand has been systematically studied in the literature, either by varying the number and the nature of coordinating groups or by ligand screening (variation of one functional group on the carbon backbone,…). However, its seems that the presence of the ligand itself has not been deepened. Although it is necessary to have ligand(s) to perform catalysis, its role was evaluated on the basis of relative comparisons, and generally not from an absolute reference. This is why we have proposed an approach based on the study of a model mechanism without ligand. The main advantages of this ligand/solvent-free approach are the following:

— It allows to find out reaction intermediates and that may be put in parallel with mechanisms of enzymes and their relative models.

— It may favor the elaboration of new catalysts by targeting of an intermediate/a TS (efforts to obtain a given species/to reduce a given energy barrier that may favor the obtaining of a given product in higher yields/selectivity).

— It might be applied to different catalytic systems that are less described in the literature, in order to get deeper insights on the way they work.

Some drawbacks can be also identified. In the one hand, the considered reactions could remain at the stage of computational studies, since the ligands are primordial for the activation of little molecules. Nevertheless, time scale of the reactions might be adapted, since the transition states are expected to be high in energy. Taking into account the environment (ligand, solvent) is then necessary to have deeper insights on the role of spin state. We have chosen to study the oxidation of toluene by O_2, using Cu^+ as catalyst, towards the formation of benzaldehyde and water (four-electron oxidation). The coordination of O_2 (and its activation) was considered as a pre-catalytic step. The first step of our mechanism is the abstraction of a hydrogen atom on the methyl group of the toluene. On the triplet spin state surface, it leads to the formation of a Cu-hydroperoxo species. However, it exists a similar TS on the singlet spin surface. It corresponds to the insertion of the distal oxygen atom in the CH bond of the methyl group. It can be seen as a H abstraction/OH rebound mechanism. Then, the H atom is transferred from the distal oxygen atom to the proximal oxygen atom. A benzylperoxide is formed at this step. In other words, this second step is the insertion of the oxygen atom into the O_dH bond. Finally, the benzylperoxide species evolves into benzaldehyde and water, via a concerted TS (break of the OO bond, H transfer from CH_2O moiety to OH). Bare Cu^+ is not able to properly activate O_2 and was found to have a limited influence on the overall pathway. However, similarities have been found with the enzymatic mechanisms, especially with the first step of our mechanism. In the literature, H abstraction by $Cu^{(II)}$-superoxo, followed by OH migration has also been proposed as reliable mechanism in mononuclear cuproenzymes. A two-electron oxidation is performed in one step in our model mechanism, provided that there is a crossing point between the triplet spin state (favored for reactant) and the singlet spin state (favored after OH rebound). The following steps of our model mechanism (formation of benzylperoxide, followed by its degradation towards benzaldehyde and water) are not proposed to happen in the mechanisms of enzymes or of their relative models. Bond Critical Points analysis and Bader charge calculations have been used to validate the hybrid nature of the first intermediate and the peroxide-like structure of the second intermediate. They have been also useful to explain the evolution of the mechanism. Different functionals from different DFT families have

been tested in order to evaluate the barrier heights of our model mechanism. Geometries of intermediates were found to be in relatively good accordance with most of the functionals used, excepted non-local functionals. Once the influence of the ligand has been elucidated, the role of Cu was also investigated by comparison with free-Cu mechanism. However, Cu^{+} was found to have mainly a role of platform that bring together the reactants.

In the third chapter, we focused our experimental effort on the coordination of O_2 on Cu complexes. Characterization of highly reactive Cu-oxygen species ($Cu^{(II)}$-superoxo, $Cu^{(II)}$-hydroperoxo, $Cu^{(II)}$-oxyl) is challenging. Low-temperature experiments, or stopped-flow techniques, are most often put in place to observe the signature of mononuclear superoxo and hydroperoxo species. Mass spectrometry may offer the opportunity to isolate reactive species. The coordination of O_2 has been observed with the help of CAR-MSMS technique. With bidentate bipyridyl ligands, the coordination sphere of Cu is completed by one solvent molecule. A ligand-exchange strategy has been set up to generate CuO_2 species. CH_3CN is then replaced by O_2 via a two-step mechanism. The influence of functionals groups has been investigated, on both the coordination of O_2 and on the characterization of CuO_2 moiety. It was found that electron-donating groups favor the coordination of O_2 on Cu, while they smoothly reinforce the $Cu^{(II)}$-superoxide character of CuO_2 moiety. A linear relationship has been observed between experimental and DFT studies, demonstrating that a simple correlation can be made between gas-phase experimental measurements of O_2 affinity and calculated BDEs. Cooling of ions was also proposed to happen in the collision cell. Calculated BDEs were plotted against Hammett parameters. Values can be separated in two linear relationships (electron-donating and electron-withdrawing R groups). The groups most likely to form hydrogen bonds with the solvent (R = -OH, $-CO_2Me$) have shown significant deviations from the linear models. DFT calculations have shown that $[Cu(R_2bpy)(O_2)]^{+}$ adducts are well described as Cu-superoxo species in a side-on fashion, in the triplet spin state. No reactivity was observed between Cu-superoxo and substrates in the gas phase.

In the fourth chapter, we have studied the coordination of O_2 on Cu coordinated by tetradentate tripodal ligands. On these complexes, the coordination of O_2 has been made by direct coordination. Here also, the donor character of the ligand has an influence on the coordination of O_2. End-on coordination, in the triplet spin state, is enforced by the bulk of the ligand. As in the literature, we have shown that these species can be electronically described as $Cu^{(II)}$-superoxo species. The electrospray ionization source (ESI) has provided the opportunity to generate deprotonated Cu complexes with tripodal ligands. It was shown that these deprotonated complexes

have a much greater affinity for O_2, but for different reasons, depending on the structure of the ligand. Thus, we have experimentally obtained structural information on these deprotonated complexes. Deuterated ligands have been used in order to determine where the proton is abstracted on the Tren, Me_6Tren and TMPA ligands. We propose that the arms of the tripodal ligands are not decoordinated from the Cu. DFT calculations have explained at first sight why $Cu^{(I)}$-radical systems improve the coordination of O_2, and open the way to the design of new efficient catalysts for O_2 activation. Experimental and computational studies are yet to be performed to evaluate the reactivity of these new adducts.

These experimental studies have broaden the pool of complexes that are able to bind O_2 in the gas phase. Nevertheless, one can legitimately ask whether it is possible to make reactions between the $Cu^{(II)}$-superoxos that we have formed and gaseous substrates. In that perspective, it is necessary to underline two main issues that have been revealed by our studies. Firstly, both sufficient amounts of catalyst and relatively high substrate pressure have to be obtained in the reaction cell. Secondly, the reaction time might be increased with the help of ion traps or flow tubes. The internal energy of the ions (i.e. their temperature) might also be modulated to favor reactive collisions, and advanced kinetics studies might be proposed to overcome these energetic issues. This thesis opens up some perspectives that should be highlighted. On the one hand, the similarities observed between the model mechanism of toluene oxidation and the oxidation mechanisms postulated in the literature justify the extension of this original approach to other less detailed mechanisms. The addition of small ligands could make it possible to study their mechanistic and energetic contribution on the model mechanism. On the other hand, the gas phase characterization of $LCuO_2^+$ compounds highlights the contribution of mass spectrometry for the isolation of adducts that are unstable or very reactive in solution. The influence of the ligand having repercussions in the gas phase, the development of catalytic systems could possibly go through studies in mass spectrometry. Finally, the generation of O_2-sensitive $Cu^{(I)}$-radical intermediates, although currently restricted to a few systems, is encouraging for the development of new efficient catalysts.

Appendix

Instrumentation and

Molecular Modeling

Annexes

Instrumentation et

Modélisation Moléculaire

This chapter (written in French) aims to present the various instrumentations and tools used during this thesis. The first part concerns mass spectrometry, recalling its principle, general information on the various components of the devices used (ion source – in particular electrospray – and mass analyzers) as well as on the types of measurement at the disposal of the experimenter. The second part deals with quantum chemistry. It includes a description of the calculation methods. English speakers can learn about these aspects in the following books :

In this chapter, many models are mentioned. It should be remembered here that a model is a simplification of reality which, while it explains experimental data and correctly predicts certain experimental results, does not take into account all the complexity of reality and poses hypotheses allowing solve the problem.

1. Spectrométrie de masse

La spectrométrie de masse est apparue au début du XX^{ème} siècle, sous l'impulsion des travaux de Wilhelm Wien (1864-1928) qui observa la déviation d'un flux de particules chargées soumis à un champ magnétique (1898) et de Sir Joseph J. Thomson (1856-1940, prix Nobel de Physique 1906) qui découvrit l'électron et en mesura le rapport m/e (1897) ainsi que les isotopes non radioactifs du Néon (1913). Thomson est par ailleurs considéré comme l'inventeur du premier spectromètre de masse (1912). Francis W. Aston, un de ses étudiants, améliora par la suite le système de Thomson. Il découvrit et étudia de nombreux isotopes d'éléments non radioactifs (Prix Nobel de Chimie 1922 pour ces travaux[1]).

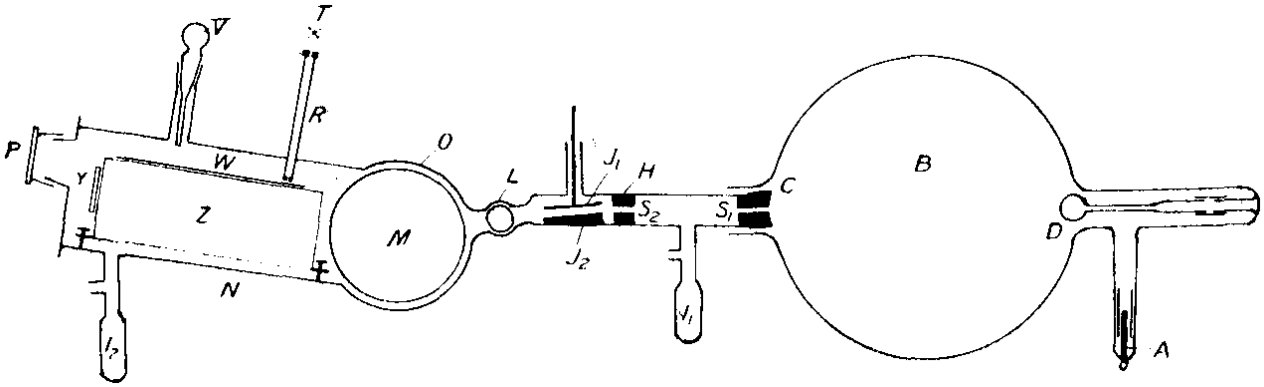

***Figure 1**: Spectrographe de masse d'Aston[2], avec la permission de Taylor & Francis.*

Le spectrographe de masse d'Aston[2] (Figure 1) est placé dans une enceinte sous vide, afin d'éviter toute collision des ions formés avec les molécules de gaz. Les ions sont générés à la cathode (C) d'un tube à décharge (B) puis guidés au travers de fentes (S1/S2) avant d'être déviés par un champ électrique (J1/J2) puis magnétique (M) et détectés selon leur rapport masse/charge (m/z) sur une plaque photographique (W). Ces éléments seront par la suite transformés, améliorés et déclinés mais le principe de la spectrométrie de masse était posé.

1.1. Applications et principe de la spectrométrie de masse

La spectrométrie de masse est une technique analytique qui porte sur la séparation des ions en phase gazeuse selon leur rapport masse/charge à l'aide de champs électriques/magnétiques constants ou dépendants du temps (Figure 2). C'est une technique d'une grande sensibilité (faibles limites de détection et de quantification), applicable à une large gamme de composés (protéines[3], oligosaccharides[4], lipides[5], complexes de métaux de transition[6,7], polymères[8], clusters[9]), dotée aujourd'hui d'une haute résolution. La spectrométrie de masse peut être considérée comme une méthode lourde à mettre en œuvre (besoin d'une alimentation électrique puissante, d'un système de refroidissement adapté et d'un système de pompage sous vide efficace). Elle permet d'obtenir des informations structurales, énergétiques et quantitatives.

La spectrométrie s'applique comme technique analytique dans de nombreux domaines, tels que le contrôle qualité alimentaire, la lutte contre le dopage, les analyses médicales ou environnementales, la détection de substances illicites, la protéomique, l'archéologie et la géologie, l'astrochimie …

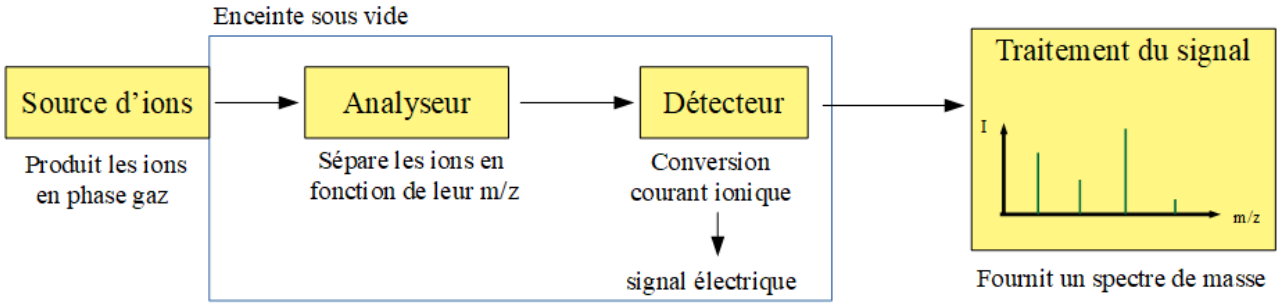

***Figure 2**: Schéma général d'un spectromètre de masse*

La source est l'élément primordial pour l'obtention d'ions en phase gaz, c'est-à-dire l'ionisation. L'échantillon est introduit dans la source sous forme solide, liquide ou gazeuse. Il est

possible d'étudier les composés neutres, aussi bien que les composés ioniques. Là où un composé ionique peut être transféré directement en phase gaz, un composé neutre doit cependant subir une ionisation.

Suivant le type de source utilisé, les mécanismes d'ionisation diffèrent (M étant l'analyte) :

- Par perte d'électron e^- : $M + e^- \rightarrow [M]^{\cdot +} + 2e^-$ (Electron Impact, EI) ;
- Par collision avec un gaz G dans un état excité : $G^* + M \rightarrow G + M^{\cdot +} + e^-$ (Atmospheric-pressure chemical ionization, APCI) ;
- Par ionisation avec une lampe UV : $M + h\nu \rightarrow M^* \rightarrow M^{\cdot +} + e^-$ (Atmospheric Pressure PhotoIonization, APPI) ;
- Par transfert de charge entre une matrice liquide excitée avec un faisceau d'atomes (Fast Atom Bombardment, FAB), ou une matrice solide excitée avec un laser (Matrix-Assisted Laser Desorption/Ionization MALDI) ;
- Par désolvatation (électro-nébulisation) d'ions déjà existants, une charge positive provenant d'un proton, d'un cation alcalin, alcalino-terreux, d'un métal de transition ou encore d'un ion moléculaire (NH_4^+, …) ; une charge négative provenant d'un anion halogénure ou d'un anion moléculaire ($HCOO^-$, …) ou suite à une déprotonation préalable (ElectroSpray Ionization, ESI).

En tant que particules chargées, les ions sont soumis aux champs électriques. Cette propriété permet de les guider les anions ou les cations, grâce à des potentiels électriques croissants ou décroissants, respectivement, appliqués de la source jusqu'au détecteur. Les ions sont focalisés tout au long de leur parcours grâce à des guides d'ions ou des lentilles optiques. L'intérêt d'une mesure en spectrométrie de masse repose sur la séparation des ions en fonction de leurs rapport masse/charge (m/z). Différents types d'analyseurs, placés en amont d'un détecteur, vont permettre de séparer les ions selon ce rapport.

Si des plaques photographiques recouvertes de bromure d'argent étaient utilisées initialement, permettant de lire une intensité en fonction de la noirceur d'une tache, les multiplicateurs d'électrons et les MCP (MicroChannel Plates) sont aujourd'hui utilisés comme détecteurs.

1.2. La source d'ionisation par électronébulisation ("électrospray")

1.2.1. Génération des ions en phase gaz

Les expériences réalisées au laboratoire ont nécessité uniquement une source de type « électrospray » (ou ESI, *ElectroSpray Ionisation*), utilisée pour la première fois en 1968 pour la spectrométrie de masse par M. Dole[10], puis popularisée dans les années 70-80 par J.V. Iribarne, B.A. Thomson et J.B. Fenn (entre autres), ce dernier recevant le Prix Nobel de Chimie en 2002 pour ses travaux sur ce type de source[11].

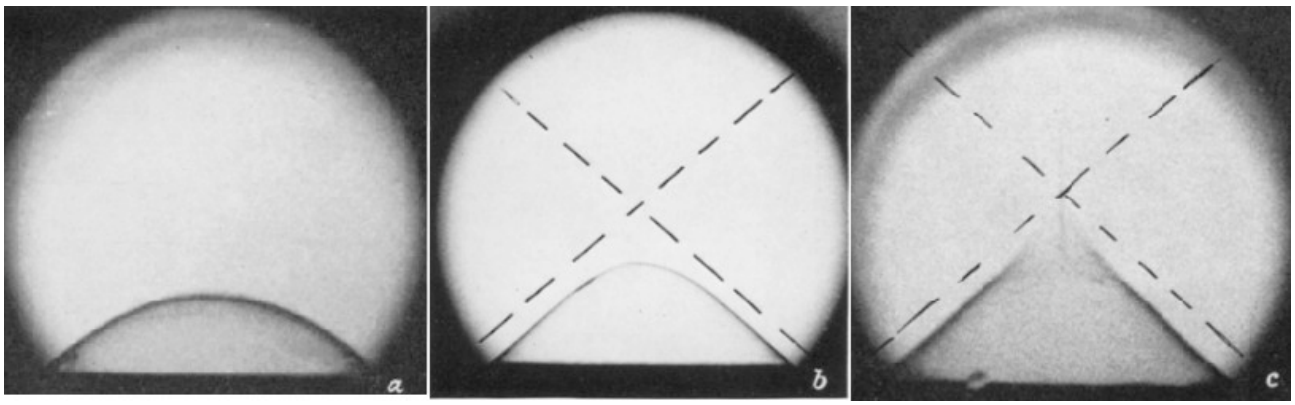

Figure 3*: Goutte d'eau savonneuse à l'extrémité d'un capillaire. a) Avant l'application d'un champ électrique. b) Avec un champ électrique < E_0, la surface est bombée sous l'effet de l'accumulation de charges. c) Avec champ électrique > E_0, formation du spray. Photographies tirées de [12], avec la permission de Proceedings of the Royal Society A, obtenue par CCC, Inc.*

Un pousse-seringue est généralement utilisé pour une injection régulière continue (débits entre 1 et 100 µL.min^{-1}). La solution contenant la ou les analytes d'intérêt (dont la concentration dépend du solvant et du type d'analyseur à disposition) est injectée via un capillaire métallique ($Ø_{int}$ ~ 0,1 mm) dans la source *electrospray*. Une forte différence de potentiel (entre 2 et 5 kV) est appliquée entre ce capillaire métallique et une électrode auxiliaire (tension positive en mode positif – détection de cations –, négative en mode négatif – détection d'anions –). Cette contre-électrode peut être le cône (*sampling cone*) ou un capillaire monté sur une plaque et est située entre 1 et 3 cm du capillaire. Pour les explications suivantes, nous considérerons l'application d'une tension positive (mode positif). L'application d'un fort champ électrique entraîne la migration des ions positifs vers la contre-électrode, tandis qu'une partie des ions négatifs sont retenus dans le capillaire. Les ions positifs se concentrent à la surface du ménisque, déformant la surface de ce

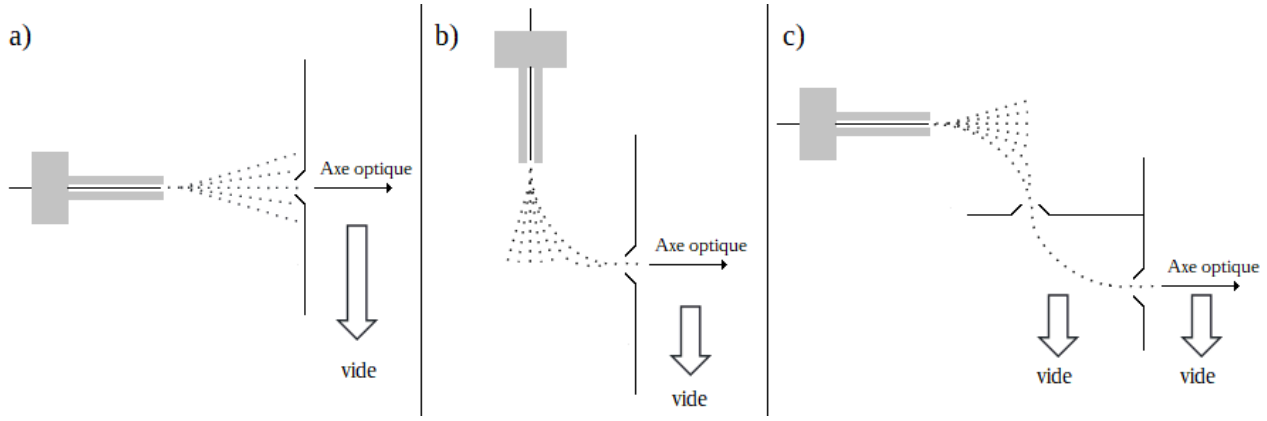

***Figure 4**: Géométries de la source électrospray. a) En ligne, b) orthogonale, c) en Z-spray.*

dernier et lui donnant une forme bombée. Si le champ électrique appliqué dépasse la condition de champ limite E_0, calculée comme suit (Équation 1.2), le ménisque se déforme encore jusqu'à former un cône de Taylor[12] (dynamique) prolongé d'un jet (Figure 3). Le champ électrique est relié à la tension appliquée (l'Équation 1.2 est valable pour une contre-électrode plane de surface bien supérieure à celle du capillaire).

$$E_0 = \frac{\sqrt{2\,\gamma\,\cos 49{,}3°}}{\varepsilon_0\, r_c} \qquad \text{Équation 1.1}$$

$$E_0 = \frac{2\,V_0}{r_c \ln(4\,d/r_c)} \qquad \text{Équation 1.2}$$

Ce jet, sous l'influence de la forte densité de charges, se pulvérise en une plume de gouttelettes chargées. Le rayon des gouttelettes émises dépend de la tension de surface du solvant, du débit et de la conductivité de l'échantillon[13]. Le déplacement des gouttelettes chargées vers le cône entraîne la perte de molécules neutres de solvant. Un flux de gaz chaud (généralement N_2), coaxial au capillaire métallique, permet d'améliorer cette désolvatation. De la perte de solvant résulte une forte densité de charge à la surface des gouttelettes. Une explosion (ou fission) coulombienne, a lieu lorsque la répulsion électrostatique devient plus forte que la tension de surface. Le critère de stabilité a été défini par Lord Rayleigh[14] (Équation 2).

$$q_{Ry} = 8\,\pi\left(\varepsilon_0\,\gamma\,R_{Ry}^3\right)^{1/2} \qquad \text{Équation 1.3}$$

La répartition des charges n'étant pas homogène à la surface de la goutte, celle-ci s'allonge et libère des gouttelettes d'un rayon environ dix fois inférieur[15] (Figure 5). Le ratio charge sur masse s'en trouve augmenté, mais la répulsion électrostatique est plus faible[13]. Ces étapes

(évaporation/fission coulombienne) se répètent plusieurs fois jusqu'à obtenir de très petites gouttelettes.

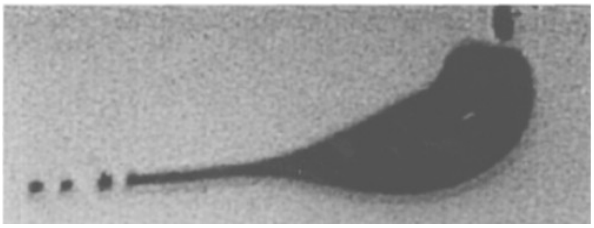

***Figure 5**: Fission coulombienne d'une gouttelette (image obtenue par ombroscopie, le flux d'azote provient du haut). Photographie tirée de [15], avec la permission d'AIP Publishing.*

Quelques modèles ont été proposés pour expliquer la génération d'ions à partir de ces très petites gouttelettes chargées. M. Dole proposa le modèle CRM (*Charge Residue Model*) en 1968[10]. Ce modèle suggère l'évaporation du solvant d'une nano-gouttelette contenant quelques charges (protons ou cations alcalins/alcalino-terreux). La ou les charges résiduelles sont retenues par le composé d'intérêt, qui peut alors être analysé. L'IEM (*Ion Evaporation Model*) proposé par J.V. Iribarne et B.A.Thomson en 1976[16] consiste en l'exclusion d'un ion solvaté de la gouttelette, en passant par un état de transition. La barrière énergétique dépend de la tension de surface et du rayon des gouttelettes[17]. Les dernières molécules de solvant sont éliminées par évaporation, et les ions peuvent alors être analysés. D'autres propositions ont également été formulées dans la littérature, notamment basées sur des mesures de mobilité ionique, et montrent que les petits ions sont plutôt générés par IEM, et les ions plus imposants par CRM. Récemment, une publication a tout de même montré que l'ubiquitine (8 566 Da) pouvait être générée en phase gaz par IEM[18]. Un troisième modèle, nommé CEM (*Chain Ejection Model*), pourrait s'appliquer aux polymères désordonnés ou aux protéines dénaturées. La chaîne de monomères ou d'acides aminés est progressivement extrudée de la gouttelette, tout en récupérant une partie des charges présentes à la surface de celle-ci. Ces différents modèles sont illustrés par la Figure 6.

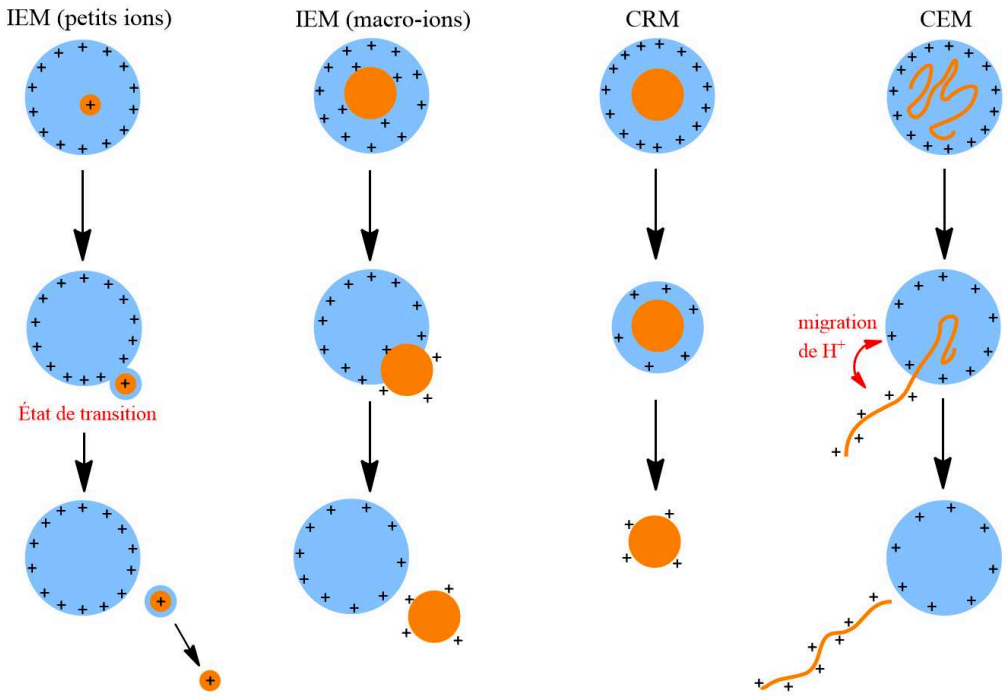

***Figure 6**: Génération des ions en phase gaz, selon différents mécanismes de désolvatation*

La géométrie de la source « électrospray » a évolué au cours du temps. Le capillaire métallique et l'axe optique du spectromètre étaient initialement alignés. Puis, afin d'éviter un encrassement trop rapide de la zone située après le cône et pour obtenir le signal le plus intense possible, les géométries orthogonale et Z-spray ont été proposées (Figure 4). Ainsi les ions totalement désolvatés, qui se trouvent plutôt sur la bordure extérieure de l'aérosol, sont transférés dans l'appareil[19]. Avec ces types de géométrie, la sensibilité augmente car la quantité d'espèces entrant dans la machine est exonérée en grande partie des molécules neutres. Les ions générés par la source électrospray à pression atmosphérique sont dirigés vers le *sample cone*, derrière lequel la pression chute drastiquement, sous l'effet de turbopompes, assistées généralement par des pompes à palettes. Une tension est appliquée sur le cône pour envoyer les ions sur l'axe optique du spectromètre de masse.

1.2.2. La source electrospray *: une cellule électrochimique*

Nous considérons encore ici qu'une tension positive est appliquée entre le capillaire et la contre-électrode. Pour assurer la formation de gouttelettes chargées positivement, il est nécessaire qu'une oxydation ait lieu à l'interface liquide-métal du capillaire. En effet, l'accumulation de charges négatives dans le capillaire métallique doit être contrebalancée, par la formation soit d'espèces neutres, soit d'espèces chargées positivement (Figure 7, adaptée de [20]). Cette électrolyse a été mise en évidence par l'observation d'espèces oxydées. Celles-ci peuvent être des molécules de solvant[21], des anions, des analytes neutres[22,23] ou encore le métal du capillaire. Il est en effet possible d'observer la formation de cations métalliques[24]. À la contre-électrode, une partie des ions positifs entre dans le spectromètre de masse, tandis que le reste subit une réaction de réduction. À l'inverse, lorsqu'une tension négative est appliquée, des réactions de réduction ont lieu à l'interface liquide-métal, tandis que les ions négatifs sont oxydés à la contre-électrode. La source électrospray se comporte comme une cellule électrolytique à courant contrôlé spéciale, du fait du transport de charge dans une phase non-continue (Figure 2).

La quantité de courant est donnée par la loi de Faraday, avec i_{ES} la quantité de courant, n le nombre d'électrons impliqués dans les processus redox, C la concentration des espèces, F la constante de Faraday et ν_f le débit de l'injection (Équation 1.4).

$$i_{ES} = \sum_j n_j C_j F \nu_f \qquad \text{Équation 1.4}$$

La quantité de courant est également dépendante de plusieurs paramètres expérimentaux, liés par la relation empirique suivante[13,17], découlant de l'équation de Hendricks[25] (Équation 1.5).

$$i_{ES} = H \nu_f^a \sigma_S^b E_{ES}^c \qquad \text{Équation 1.5}$$

H est le coefficient de Hendricks, dépendant de la tension de surface et de la permittivité du solvant. Différentes études ont tenté de définir la valeur des exposants *a*, *b* et *c[22]*. Celles-ci sont interdépendantes et assujetties aux valeurs de débit ν_f, de conductivité de la solution σ_S et du champ électrique appliqué E_{ES}. Ainsi, les conditions de l'expérience vont définir le courant mesuré et les espèces susceptibles de s'oxyder (en mode positif) ou de se réduire (en mode négatif) dans le capillaire.

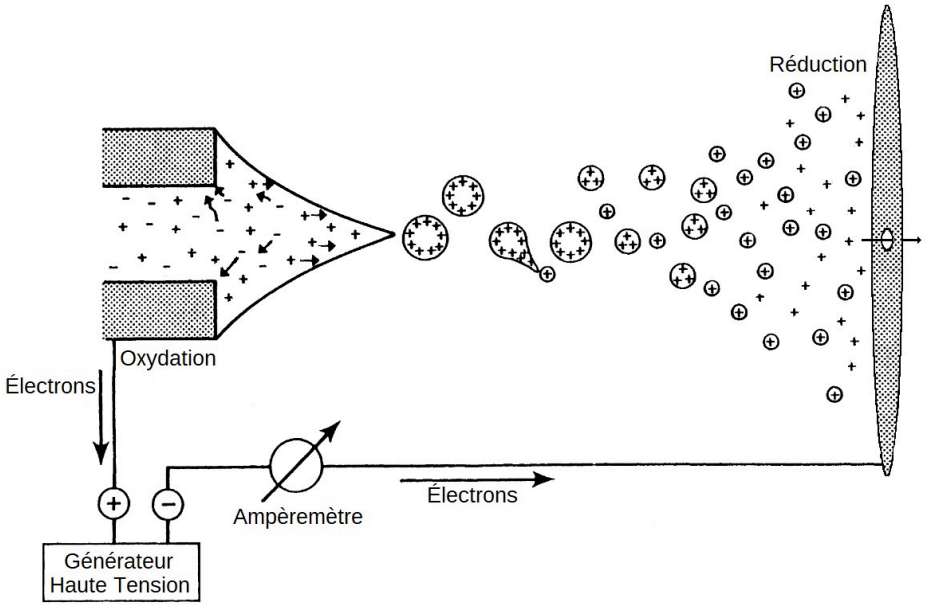

***Figure** 7: Schéma de la source électrospray en mode posittif, montrant la formation des gouttelettes et la génération d'un courant par la séparation des ions en phase liquide (Figure adaptée avec permission de [20], Copyright 2021 American Chemical Society).*

Cependant, même en mode positif, il est possible d'observer des espèces ayant subi une réduction. Cette réduction peut prendre place en amont (réduction chimique en solution[26], réduction électrochimique dans une cellule à flux[27]) ou en aval de la source électrospray. Il est possible de distinguer deux types de réduction en aval de la source :

— Les dispositifs ECD (transfert d'électron entre deux espèces), ETD (ajout d'électron sur une espèce) ou de photodissociation (activation photonique), placés après la source, permettent de réduire les espèces *a posteriori*.

— La réduction d'espèces a également été observée sans dispositif prévu à cet effet. Cette réduction est essentiellement chimique : un cation d'un métal de transition ou d'un alcalino-terreux multi-chargé perd un ligand acide (transfert de proton ligand → ligand[28]) ou oxydé (transfert de charge métal → ligand[29]), ce qui permet la génération d'au moins une espèce mono-chargée (cation métallique ou ligand oxydé[30]). La réduction par capture d'un électron dans la source électrospray a également été avancée[31,32]. L'hypothèse repose sur la formation d'un plasma, due à une décharge électrique (arc) entre les deux électrodes, les électrons libérés pouvant alors réduire les ions, peut-être par l'intermédiaire d'une molécule de solvant[33].

Différents phénomènes de transfert[28] (Équation 1.6), de gain[34] (Équation 1.7) et de perte[35] (Équation 1.8, avec M : Ni, Cu ; L1 un ligand cyclam fonctionnalisé et X : Cl, Br) de charges positives (protons) peuvent également avoir lieu dans la source ESI. Ces échanges acido-basiques sont dus d'une part à un échelonnage différent des pKa en phase gaz et d'autre part, à la minimisation globale des charges (positives et négatives) lors du processus d'électronébulisation.

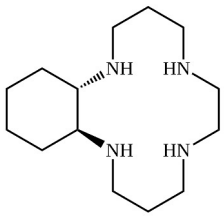

Figure 8: L1

$$[Ca(H_2O)_2]^{2+} \rightarrow [Ca(OH)]^{+} + H_3O^{+} \qquad \text{Équation 1.6}$$

$$\text{Myoglobine} + n\ NH_4^{+} \rightarrow [\text{Myoglobine} + nH^{+}] + n\ NH_3 \qquad \text{Équation 1.7}$$

$$[M(L1)X]^{+} \rightarrow [M(L1) - H]^{+} + HX \qquad \text{Équation 1.8}$$

1.2.3. *Avantages et inconvénients de la source* electrospray

La source ESI présente de nombreux avantages. Tout d'abord, elle est considérée comme une source d'ionisation douce, car elle permet de transférer en phase gaz des espèces fragiles sous la forme d'ions moléculaires ou d'adduits (dans le cas de molécules neutres). Cette source est placée en règle générale à la pression atmosphérique, permettant un entretien facile. Il est également possible de travailler avec les deux modes positif et négatif, sur des ions mono- et multi-chargés. Le fait d'observer des ions multi-chargés est un avantage pour l'analyse de grosses molécules, car certains analyseurs ont une gamme de fonctionnement m/z limitée. La source électrospray nécessite un analyte en solution, ce qui en fait une méthode de choix pour le couplage instrumental avec une colonne de chromatographie liquide (- *High Performance - Liquid Chromatography*, (HP)-LC)[36], une cellule électrochimique[37] ou une électrophorèse capillaire[38]. L'ionisation par électronébulisation s'utilise avec un grand nombre de composés, de tailles et de natures diverses[3–9,39].

Le manque de répétabilité est un des principaux inconvénients de l'ionisation *electrospray*. Les paramètres expérimentaux doivent être soigneusement définis. Certains composés et solvants ne sont pas adaptés à l'ESI (ex : DMSO,...). Il convient aussi de souligner que la source électrospray n'est pas indiquée pour l'étude de molécules peu polaires. Si tant est que l'on puisse obtenir un signal de plusieurs composés, leur analyse quantitative reste difficile. En injection directe, il est possible de faire un étalonnage externe pour des échantillons « purs ». Dans le cas de mélanges,

l'étalonnage externe n'est pas recommandé car il y a des interactions entre les analytes et compétition lors de l'ionisation. Il est également envisageable de faire un étalonnage interne (marquage isotopique, substitution ou dilution isotopique). Dans le cas d'échantillons complexes, on se ramène au cas d'analytes "quasi-purs" par couplage HPLC. En effet, la réponse de la source pour ces différents composés peut varier de manière importante. La présence de sels - tels que NaCl ou KCl - complexifie les spectres de masse (ionisation croisée) et diminue la quantité d'ions d'intérêt lors du processus d'ionisation (compétition de charge)[40]. Dans certains cas (et ce n'est pas forcément un inconvénient de l'ESI), la formation de microgouttelettes chargées concentre les réactifs et peut modifier un suivi cinétique[41,42]. Enfin, la fluctuation du signal est quasiment inévitable, et l'acquisition devra se faire sur des temps suffisamment longs afin de moyenner correctement le signal et réduire les écarts-type de mesure.

1.3. L'analyseur en masse

L'analyseur est l'élément crucial du spectromètre de masse, qui permet de mesurer le ratio m/z d'un ion ou d'une particule chargée. L'un des premiers analyseurs fut conçu par A.J. Dempster[43] (1917). Les ions produits (à partir de sels) dans la source passent par une fente dans l'analyseur semi-circulaire. Le champ magnétique étant uniforme et statique, c'est la différence de potentiel appliquée dans la source qui permet de diriger les ions produits vers le détecteur (Figure 9). La séparation des ions se fait donc sur un critère énergétique (comme l'analyseur magnétique à double focalisation). Par la suite, la séparation des ions s'est basée sur la séparation dans le temps (analyseur Time-Of-Flight TOF, 1946), la transmission (quadripôle, 1953) ou la périodicité d'un mouvement (trappe à ions, 1953 ; Fourier-Transform Ion Cyclotron Resonance FTICR, 1974 ; Orbitrap, 2000) dans un champ électrodynamique. Parmi les différents types d'analyseurs disponibles, deux sont utilisés dans notre laboratoire : le quadripôle et le piège à ions. Nous les détaillerons en détail avant d'évoquer rapidement l'analyseur temps de vol, qu'il paraît judicieux de mentionner, pour sa grande sensibilité et sa précision. Les capacités d'un analyseur peuvent être définies sur la base des caractéristiques suivantes :

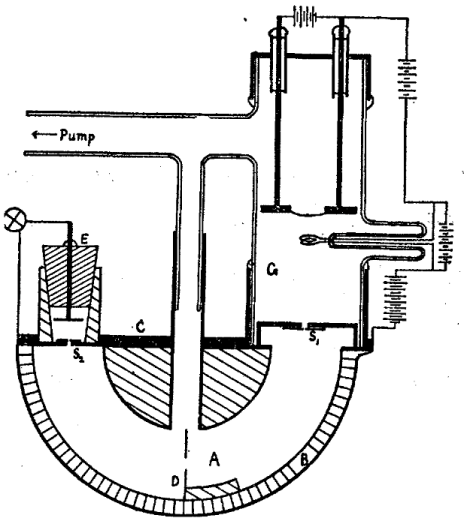

***Figure 9**: Spectromètre de masse de Dempster. Illustration tirée de [43], Copyright 2021, American Physical Society.*

- la gamme de masses mesurable ;
- la vitesse de balayage ;
- le taux de transmission (pourcentage d'ions détectés après avoir traversé l'analyseur) ;
- la précision sur la mesure du ratio m/z ;
- la résolution m/Δm (Δm étant la largeur à mi-hauteur du pic considéré).

1.3.1. L'analyseur quadripôlaire

W. Paul (Prix Nobel de Physique 1989[44]) et H. Steinwedel décrivirent le principe de l'analyseur quadripolaire en 1953. Cet analyseur est composé de quatre barres cylindriques parallèles, opposées deux à deux d'une distance de $2r_0$ (Figure 10). Sur chaque paire d'électrodes est appliquée une tension $\pm \Phi_0$ (Équation 1.7), avec U, un potentiel continu et ω, la fréquence d'un potential alternatif V. Ainsi les polarités sont inversées au cours du temps, par l'application de V.

$$\Phi_0 = U - V_0 . \cos(\omega t)$$ Équation 1.7

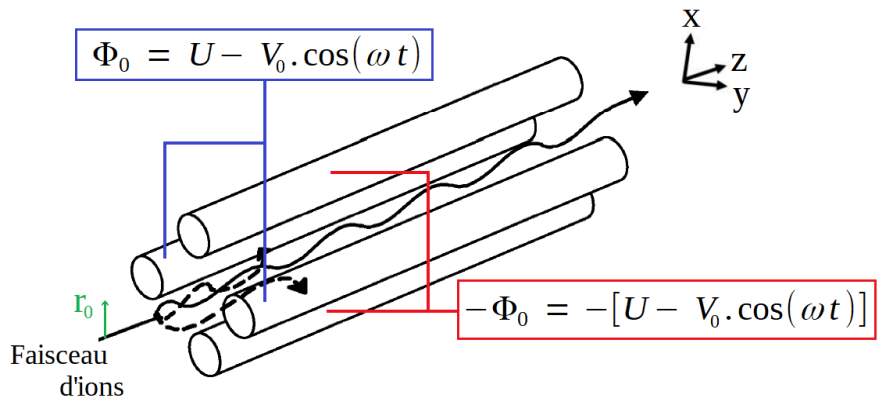

***Figure 10**: Schéma de l'analyseur quadripolaire (les flèches en pointillés représentent des trajectoires instables)*

Lorsque les ions, focalisés (par un hexapôle, par exemple) et accélérés par quelques lentilles, arrivent dans l'analyseur, ils sont soumis à un champ quadripolaire.

Les ions sont attirés par les électrodes de polarité opposée, et décrivent une trajectoire hélicoïdale qui peut être définie par les équations 1.8, 1.9 et 1.10.

$$\frac{d^2x}{dt^2} + \left[\frac{e}{mr_0^2}\left[U + V . \cos(\omega t)\right]\right]x = 0$$ Équation 1.8

$$\frac{d^2y}{dt^2} + \left[\frac{e}{mr_0^2}\left[-U - V . \cos(\omega t)\right]\right]y = 0$$ Équation 1.9

$$\frac{d^2z}{dt^2} = 0$$ Équation 1.10

Il est possible d'y reconnaître la forme d'une équation de Mathieu (Équation 1.11), grâce à un changement de variable (Équation 1.12).

$$\frac{d^2u}{d\xi^2} + [a - 2q.\cos(2\xi)]u = 0 \qquad \text{Équation 1.11}$$

$$\text{avec} \quad \xi = \frac{\omega t}{2} = \pi f_{RF} t \qquad \text{Équation 1.12}$$

Par identification des équations 1.7 et 1.8 avec l'équation 1.11, nous retrouvons *a* et *q*, les paramètres de stabilité, selon les axes x et y (Équations 1.13 et 1.14).

$$a_x = -a_y = \frac{8ezU}{mr_0^2\omega^2} \qquad \text{Équation 1.13}$$

$$q_x = -q_y = -\frac{4ezV_0}{mr_0^2\omega^2} \qquad \text{Équation 1.14}$$

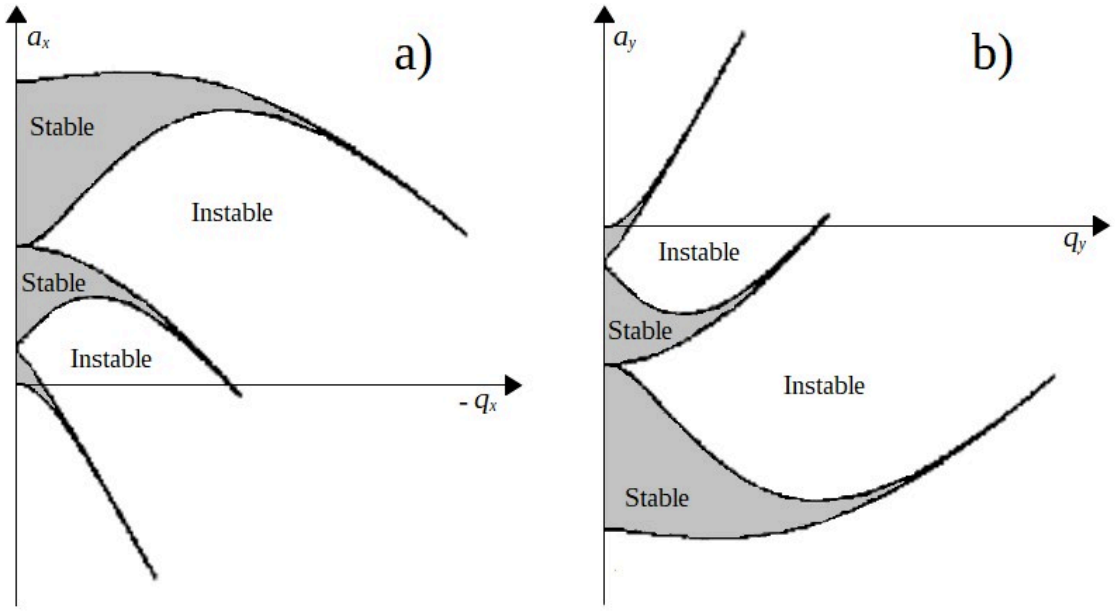

***Figure 11**: Régions de stabilité de Mathieu, a) selon x (a_x ; $-q_x$) et b) selon y (a_y ; q_y). Les parties grisées représentent les trajectoires stables.*

Ces équations sont données en fonction des tensions de courant continu (U) et de courant alternatif (V_0). Ainsi, en fixant précisément ces valeurs de tension, il est possible de guider les ions, d'une valeur m/z donnée, de manière à ce qu'ils ne se déchargent pas sur les parois ou les électrodes. Ce sont les ions qui ont une trajectoire stable, c'est-à-dire une trajectoire qui ne diverge

pas avec le temps et leur permet de traverser l'analyseur. Les autres ions, aux trajectoires instables, sont chassés de l'analyseur ou rencontrent les électrodes. Les trajectoires stables et instables, selon x et selon y, sont représentées sur la Figure 11. La superposition des deux diagrammes donne les quatre zones de stabilité dans l'analyseur (indiquées sur la Figure 12).

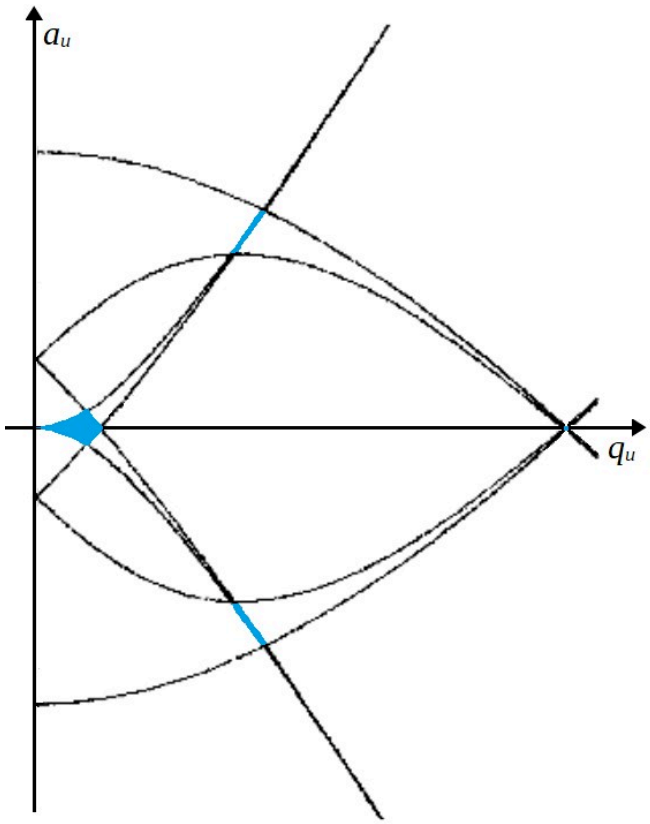

***Figure 12**: Diagramme de stabilité (a_y ;q_y) des ions dans l'analyseur quadripolaire (superposition des deux parties de la Figure 11). Les quatre régions en bleu définissent les zones de stabilité suivant les directions x et y.*

La zone la plus étendue est celle qui est habituellement retenue (car les tensions à appliquer sont plus faibles et le contrôle des conditions de stabilité plus fin). La symétrie de l'analyseur permet de garder uniquement la partie supérieure. La ligne de scan, ou ligne opératoire, correspond au ratio U/V_0. En balayant ce ratio de manière appropriée, les ions associés à une condition donnée passent les uns après les autres à travers l'analyseur et peuvent être détectés (Figure 13.a). Plus la ligne de scan est proche de la condition limite de stabilité pour une masse donnée, plus la résolution sera élevée. En revanche, l'intensité du signal en sera affectée (Figure 13.b).

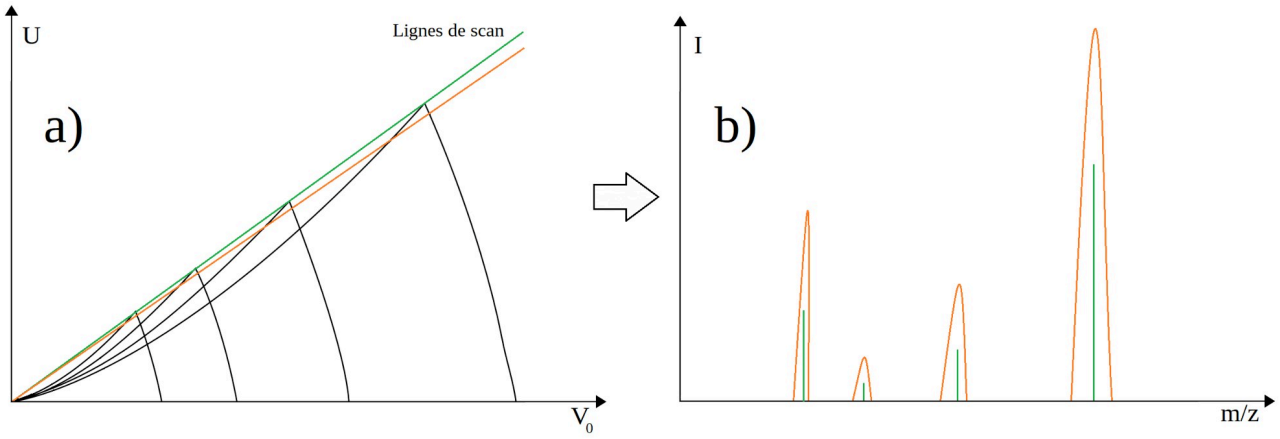

***Figure 13**: a) Lignes de scan sur un diagramme de stabilité (U;V), pour quatre ions de m/z croissants selon V_0 . b) Spectre de masse associé à chaque ligne de scan.*

Un analyseur quadripolaire permet d'étudier la gamme de masse comprise entre 10 à 4 000 Da, tout en perdant de la sensibilité au-dessus de 2 kDa. La résolution obtenue avec de tels analyseurs n'est pas très élevée (≈ 1000 - 5000), mais permet tout de même de séparer correctement les isotopologues (« résolution unitaire »).

1.3.2. Le piège à ions

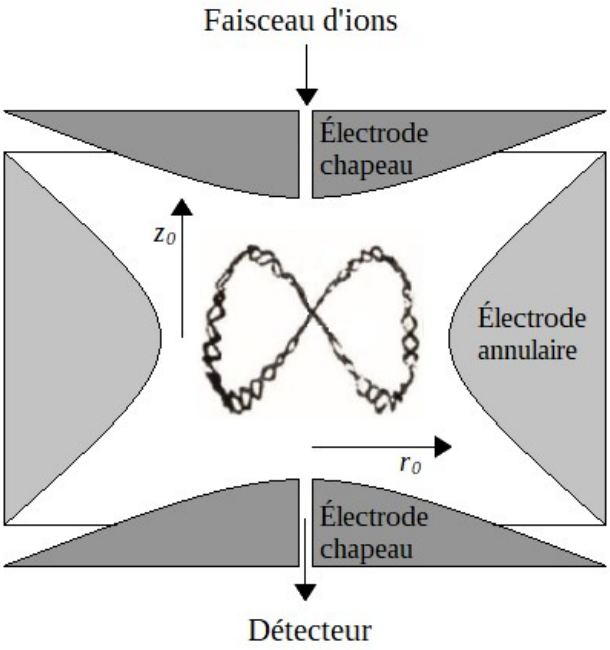

***Figure 14**: Schéma en coupe transversale d'un piège à ions. Au centre, une trajectoire d'ion (en trois dimensions) est représentée.*

Le piège à ions (ou trappe à ions) est un système proche de l'analyseur quadripolaire, et fut développé lui aussi par W. Paul, qui s'inspira des travaux de John R. Pierce et de Frans M. Penning. Ici, il convient de considérer trois dimensions (accélération selon z non nulle). Le piège à ions se compose d'une électrode annulaire et de deux électrodes « chapeaux ». Ces *cap electrodes* sont percées afin de laisser entrer ou sortir les ions (Figure 14). À l'intérieur du piège, les ions sont ralentis et refroidis par une faible pression d'hélium (≈ 10^{-4} - 10^{-5} mbar). Grâce à la symétrie axiale autour de l'axe z, il est possible de transformer les coordonnées cartésiennes en coordonnées cylindriques (Équations 1.14, 1.15, 1.16).

$$x = r.\cos\theta$$ Équation 1.15

$$y = r.\sin\theta$$ Équation 1.16

$$r^2 = x^2 + y^2$$ Équation 1.17

Les équations 1.12 et 1.13 peuvent être réécrites dans ce nouveau système de coordonnées (Équations 1.17 et 1.18).

$$a_r = -\frac{a_z}{2} = \frac{8ezU}{m(r_0^2+2z_0^2)\omega^2}$$ Équation 1.18

$$q_r = -\frac{q_z}{2} = -\frac{4ezV_0}{m(r_0^2+2z_0^2)\omega^2}$$ Équation 1.19

avec r_0 et z_0 les distances entre le centre du piège et l'électrode annulaire ou l'électrode chapeau, respectivement. Le diagramme de stabilité est alors dissymétrique[45] (Figure 15).

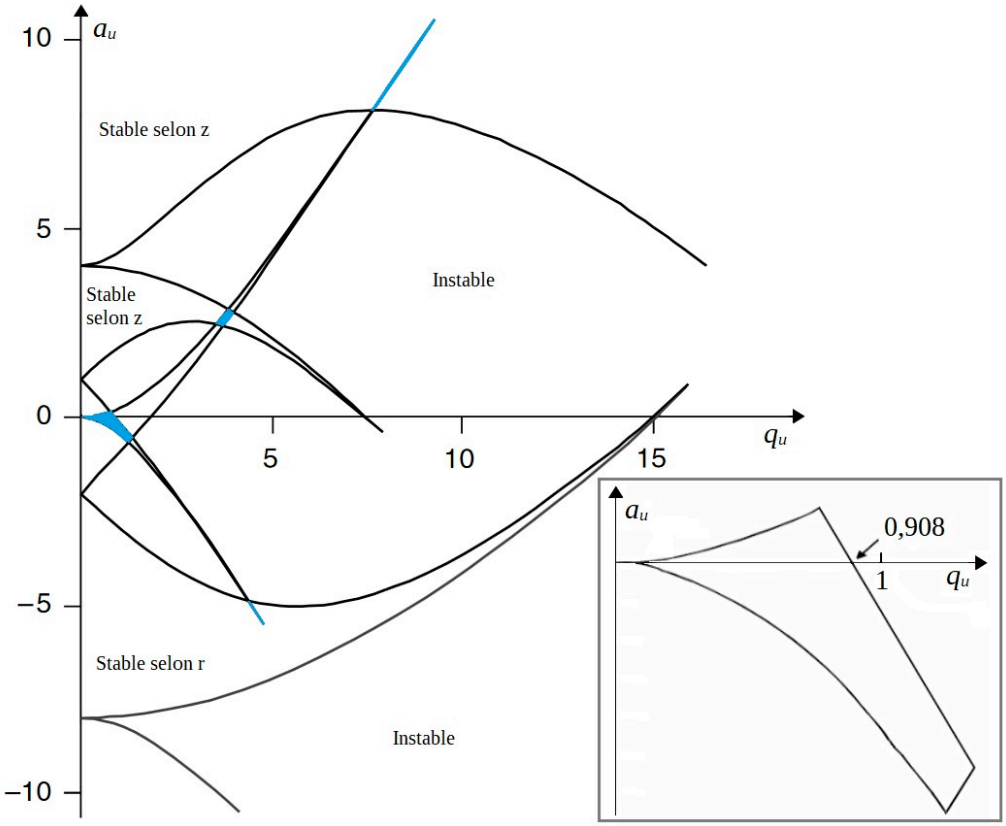

***Figure 15**: Diagramme de stabilité (a_z, q_z) des ions dans l'analyseur piège à ions. Les quatre régions en bleu définissent les zones de stabilité selon r et z. Dans l'encadré, agrandissement de la première zone de stabilité. Diagramme issu de [45].*

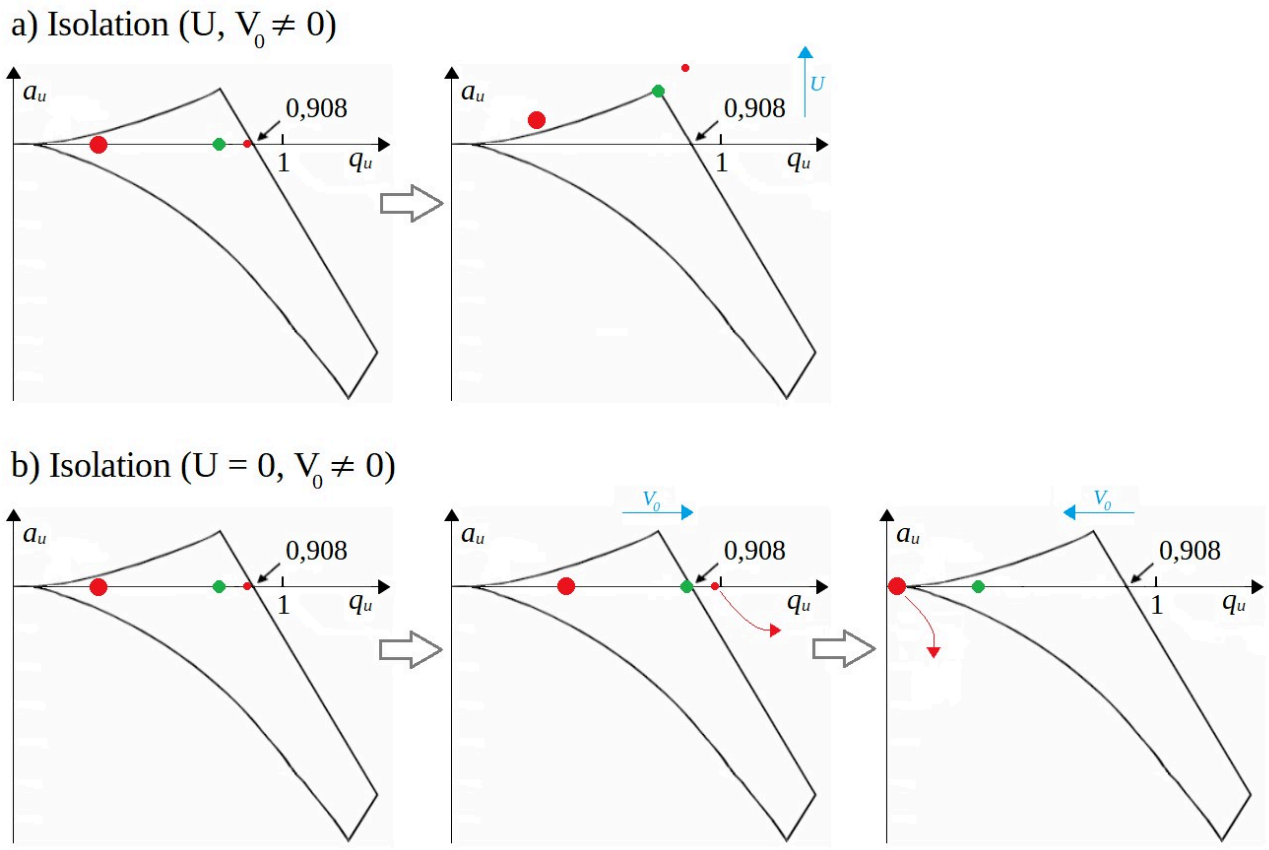

***Figure 16**: Opérations possibles pour isoler un ion d'intérêt*

Les ions peuvent être emprisonnés dans le piège si, et seulement si, leurs trajectoires sont stables selon r et selon z. La trajectoire empruntée par les ions est une sinusoïde tridimensionnelle bouclée. Une fois piégés, les ions peuvent être conservés ou éjectés. Il est possible de sélectionner une valeur de m/z et de garder les ions correspondants à l'intérieur du piège (en vue d'une fragmentation, par exemple) par deux approches :

1. U est augmenté progressivement jusqu'à ne conserver que les ions d'intérêt (Figure 16.a).
2. Un balayage selon V_0 (à $U = 0$) éjectera les ions piégés vers le détecteur (selon l'axe z, c'est-à-dire l'axe entre l'entrée et la sortie du piège) dès que le paramètre de stabilité q_z dépasse 0,908. Une isolation est également envisageable en faisant varier V_0 de 0 à 0.908 (Figure 16.b).

La gamme de masse accessible avec un QIT s'étend jusqu'à 20 000. La résolution peut atteindre 10000.

1.3.3. L'analyseur temps de vol (TOF)

Il est ordinairement considéré que W. E. Stephens développa le premier un analyseur temps de vol, en 1946. L'analyseur TOF fonctionne selon le principe de séparation des ions par leurs temps de parcours jusqu'au détecteur. Chaque ion sortant de la source ou d'une série de lentilles possède la même énergie cinétique. En entrant dans la cellule à temps de vol (TOF), ils ne sont plus soumis à aucun champ électrique ou magnétique : c'est la vitesse qu'ils mettront à parcourir la distance jusqu'au détecteur qui permettra leur séparation en masse (Équation 1.19, Figure 17.a).

$$t = \frac{L}{\sqrt{\frac{2zeV}{m}}}$$ Équation 1.20

Pour mieux séparer encore les ions, des réflectrons (en V ou même en W) ont été ajoutés dans ces analyseurs, pour allonger le parcours des ions (Figure 17.b). De plus, le réflectron compense la dispersion en énergie cinétique : les ions de même énergie cinétique pénètrent à la même profondeur dans le réflectron, tandis que les ions ayant une énergie cinétique légèrement supérieure ou inférieure vont plus ou moins loin, respectivement. Pour que les ions entrent en même temps dans l'analyseur, ils y sont envoyés de manière pulsée. Puisqu'aucun champ n'est utilisé, la masse des ions n'est pas une contrainte (théoriquement). La résolution d'un TOF peut atteindre 75 000 (en mode W). En comparaison, la résolution atteignable avec un Orbitrap est de 350 000 (pour de faibles masses ~100 Da, mais chute très vite avec la masse ~100 000 à 1000 Da), celle d'un FT-ICR dépasse 2 000 000[46].

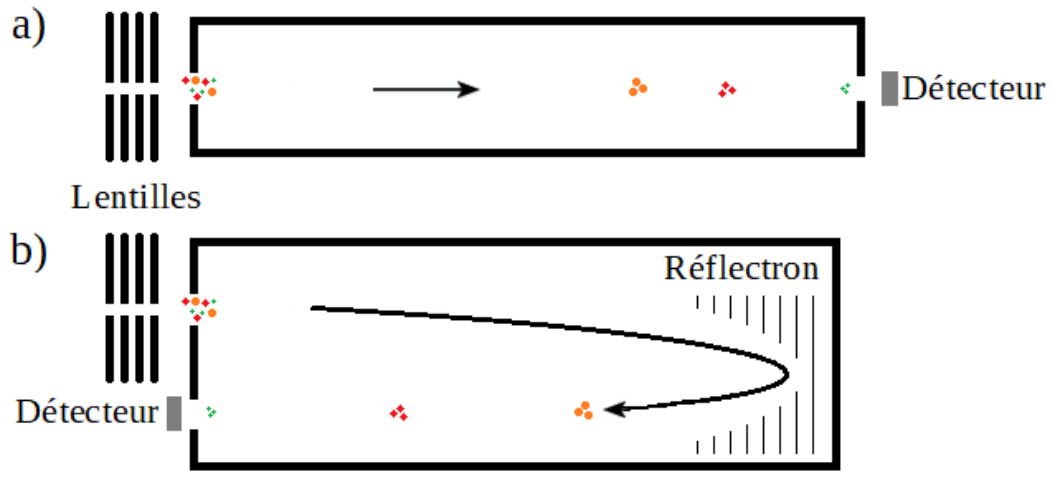

Figure 17: Schéma d'un analyseur TOF a) linéaire, b) avec un système réflectron

1.4. Spectrométrie de masse en tandem

Il est également possible de réaliser le couplage de plusieurs analyseurs en masse, identiques ou différents, afin d'obtenir un instrument qu'on appelle « spectromètre de masse hybride ». Ce type d'instrument permet de bénéficier des avantages des différents analyseurs lors d'expériences dite de spectrométrie de masse en tandem ou MS/MS (Figure 18), qui sont devenues essentielles lors des analyses structurales et quantitatives. Ces expériences consistent à introduire l'échantillon dans le spectromètre de masse (en générant des ions), suivi d'une première analyse en masse permettant d'isoler les ions d'intérêt pour une valeur m/z préalablement choisie. Les ions sélectionnés subissent une activation, dans une cellule prévue à cet effet. Il peut s'agir d'une dissociation induite par collisions (Collision Induced Dissociation, CID), d'une dissociation induite par collision avec une surface (Surface Induced Dissociation, SID), d'une photodissociation (InfraRed MultiPhoton Dissociation, IRMPD ; Blackbody Infrared Radiative Dissociation, BIRD), de fragmentations induites par transfert ou capture d'électrons (Electron Transfer Dissociation, ETD ; Electron Capture Dissociation, ECD) ou encore d'y réaliser des réactions chimiques (Collision Activated Reaction, CAR, cf. Chapitre III de cette thèse). Les ions fragments produits et les ions précurseurs non fragmentés sont ensuite analysés en masse. Cette technique est très utilisée pour l'identification de composés, la détection et la quantification d'analytes, la résolution de structures ou de mécanismes réactionnels ...

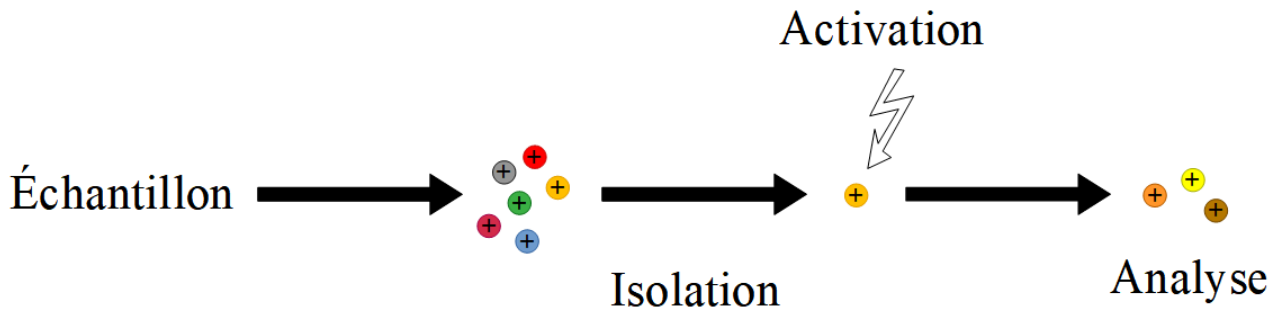

***Figure 18**: Principe de la spectrométrie de masse MSMS*

1.4.1. MS/MS dans l'espace

Dans le cas d'un triple quadripôle, les deux analyseurs sont des quadripôles. Deux modes peuvent être appliqués à un analyseur. En premier lieu, un mode statique, pour lequel une seule

fréquence ω est utilisée. Ensuite, un mode *scan*, qui balaie les fréquences, permet d'obtenir un spectre de masse complet. Il est possible d'introduire du gaz dans la cellule de collisions, où se fait l'activation des ions sélectionnés. Un gaz de collision chimiquement inerte (Ar en général) permet d'augmenter l'énergie interne des ions par collisions successives. L'ion, dans un état d'excitation vibrationnelle, se décompose ensuite pour donner des ions fragments et des molécules neutres, comme le montre l'Équation 1.21.

$$m_p^+ + Ar \rightarrow m_p^{+\neq} \rightarrow m_f^+ + N \qquad \text{Équation 1.21}$$

Dans notre cas, la fragmentation des ions sélectionnés ne sera pas toujours l'objectif des expériences MS/MS. En effet, la coordination ou l'échange de ligand peut également avoir lieu. Différents types de mesure (avec cellule de collision active) sont envisageables :

- le *product ion scan* : après sélection et fragmentation d'un ion précurseur (premier quadripôle en mode statique), le deuxième quadripôle fonctionne en mode scan et détecte tous les ions fragments (fragmentations directes et successives) ;
- le *precursor ion scan* : le deuxième quadripôle fonctionne en mode statique, le premier en mode scan, pour détecter tous les ions précurseurs d'un ion fragment donné ;
- le *neutral gain scan* ou *neutral loss scan* : les deux quadripôles fonctionnent en mode scan, avec une différence en fréquence correspondant à une masse de molécule neutre donnée ;
- le *SIR scan* ou *MRM scan* : les deux quadripôles fonctionnent en mode statique, et permettent de suivre la fragmentation d'un ion fragment donné (SIR) ou de plusieurs ions fragments (MRM) par rapport à un ion précurseur donné.

1.4.2. MS/MS dans le temps

Dans le cas d'une trappe d'ions, le piège est le siège de toutes les étapes de la MS/MS. Les ions non désirés sont chassés du piège. L'activation des ions précurseurs piégés se fait par l'application d'une tension auxiliaire sur les *cap electrodes*, ce qui a pour effet d'augmenter l'énergie interne des ions par collisions successives avec l'hélium présent dans le piège. Les ions fragments sont ensuite piégés et refocalisés au centre du piège pour être finalement analysés en masse. Il est possible de faire des expériences MS^n en répétant la séquence précédente, tant que le signal est suffisant.

1.5. Équipements utilisés

Pendant cette thèse, différents appareils ont été utilisés :

— Un triple quadripôle Quattro II Micromass/Waters, équipé d'une source ESI *Z-spray* (Waters), piloté par MassLynx V4.0. Les cellules de transfert (connectant la source et le premier analyseur) et de collision (située entre les analyseurs), consistent en des systèmes de focalisation hexapolaires.

— un triple quadripôle Ultima Micromass/Waters, équipé d'une source ESI *Z-spray* (Waters), piloté par MassLynx V4.1. Les cellules de transfert et de collision consistent en des systèmes de guide d'ions T-wave (les ions sont piégés dans les creux d'une onde électrique sinusoidale se propageant suivant la ligne optique du dispositif).

— un piège à ions HCT+ Bruker, équipé d'une source ESI orthogonale (Agilent), piloté par DataAnalysis V3.4.

À noter que l'expression « triple quadripôle » constitue un abus de langage : les quadripôles intermédiaires (cellules de collision) sont remplacés par des hexapôles/octopôles, ou des guides d'ions, plus à même de focaliser les ions. Il est ainsi préférable d'utiliser la notation QhQ, plutôt que QqQ (ou tQ). Le QhQ Quattro II a été modifié de telle façon qu'il soit possible d'injecter différents réactifs gazeux en différents endroits de la machine (hexapôle de transfert et cellule de collision,Figure 19). Les différents réactifs peuvent être gazeux (une bouteille sous pression directement connectée à la machine) ou liquides (ils sont alors placés purs ou en mélange dans un petit ballon sous vide). La pression de ces réactifs est fixée grâce à des vannes de précision. Il devient ainsi possible de réaliser des réactions activées par collision (CAR).

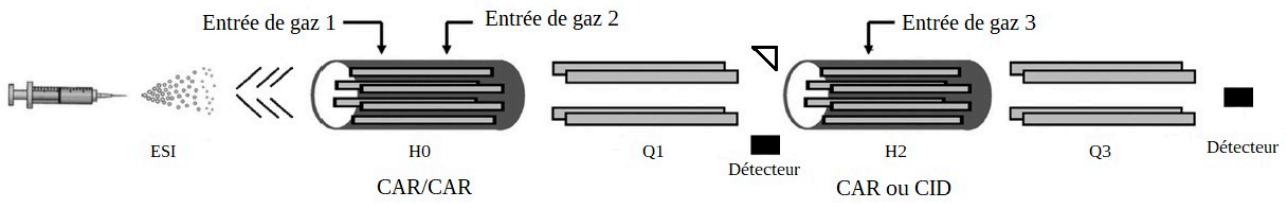

***Figure 19**: Schéma du QhQ Quattro II modifié, équipé d'une source ESI Z-Spray.*

2. Modélisation moléculaire et chimie quantique

2.1. Bref historique concernant la théorie quantique

Lord Kevin (William Thomson, 1824 – 1907) considérait, en 1901, que tous les phénomènes observables pouvaient s'expliquer par la physique et que celle-ci était en quelque sorte complète. Il soulignait trois points (*clouds*) à éclaircir: les anomalies dans les orbites de Vénus, la nature de l'éther et le rayonnement des corps condensés ou « catastrophe ultraviolette » (la loi du rayonnement de Wien n'est plus vérifiée pour les faibles longueurs d'onde). Les deux premiers points furent à l'origine des théories de la relativité restreinte et générale d'Einstein (1905 et 1915), tandis que le troisième signe l'avènement de la théorie quantique. Au début du XX^{ème} siècle, les deux thèses majeures des travaux de Max Planck (Prix Nobel de Physique 1918[47]) sur la quantification du rayonnement d'un corps noir et d'Albert Einstein (Prix Nobel de Physique 1921[48]) sur l'effet photoélectrique décrivent la nature quantique de l'énergie et la nature duale onde/corpuscule du photon. En 1924, ce concept de dualité a ensuite été étendu de manière très originale par Louis de Broglie (Prix Nobel de Physique 1929[49]) à l'ensemble des particules matérielles. En 1926, Max Born postule qu'il est possible d'associer une fonction d'onde $\Psi(\vec{r},\vec{t})$ à toute particule élémentaire (Ψ peut être complexe), dont le produit avec son conjugué conduit à une probabilité réelle de trouver la particule dans un élément de volume dV, autour du point repéré par le vecteur $\vec{r}$ [50]. L'intégrale, sur un volume V, de la fonction d'onde associée à la particule multipliée par son conjugué, fournit la densité de probabilité de présence de la particule dans V (Équation 2.1). Le calcul de cette intégrale sur tout l'Univers doit ainsi, par extrapolation, prendre la valeur 1 (puisqu'il est absolument certain de trouver la particule dans l'Univers).

$$P = \int_{v} dP = \int_{v} \Psi \Psi^{*} dV \quad \text{avec} \int_{Univers} dP = \int_{Univers} \Psi \Psi^{*} dV = 1 \qquad \text{Équation 2.1}$$

Il est remarquable, par ailleurs, que cette fonction d'onde Ψ associée au système contient à elle seule toute l'information sur ce système. C'est par l'action d'opérateurs mathématiques linéaires sur Ψ que ces informations en seront extraites (en particulier, les résultats des mesures pourront être calculés à partir de cette fonction d'onde, pour autant qu'elle soit connue). Le cas emblématique de cette procédure est celui de l'opérateur Hamiltonien $\hat{H}$ agissant sur Ψ, qui donne l'énergie du système par l'intermédiaire de l'équation de Schrödinger.

2.2. L'équation de Schrödinger

En mécanique classique, on postule que tout système physique peut être décrit à l'aide d'une fonction permettant de calculer en tout point (représenté par le vecteur position $\vec{r}$, à chaque instant t et avec un mouvement caractérisé par $\vec{p}$) la valeur d'une grandeur comme l'énergie E. Cette fonction, dite de Hamilton, conduit à l'égalité : $H(\vec{r},\vec{p},t) = E$. En mécanique quantique, par analogie, l'opérateur hamiltonien $\hat{H}$ agissant sur une fonction d'onde Ψ (Équation 2.2) est défini de la façon suivante :

$$\hat{H}(\vec{r},\vec{p},t)\Psi(\vec{r},t) = i\hbar\frac{\partial\Psi(\vec{r},t)}{\partial t} \qquad \text{Équation 2.2}$$

avec $\Psi(\vec{r},t)$ la fonction d'onde associée au système, i le nombre imaginaire pur, $\hbar = \frac{h}{2\pi}$ la constante de Planck réduite. La forme générale des solutions stationnaires associées au système physique étudié, c'est-à-dire les solutions d'amplitudes constantes dans le temps est :

$$\Psi_n(\vec{r},t) = \psi_n(\vec{r})e^{-i\omega_n t} \qquad \text{Équation 2.3}$$

où les contributions spatiale et temporelle de la fonction d'onde solution ont été séparées, avec $\omega_n = 2.\pi.\nu_n$ la pulsation associée à la solution stationnaire périodique. L'hamiltonien $\hat{H}$ étant un opérateur linéaire, la solution générale de l'équation de Schrödinger (Équation 2.2) peut ainsi s'écrire comme la somme des solutions particulières (incluant donc toutes les les solutions stationnaires précédentes), soit :

$$\Psi(\vec{r},t) = \sum_n \Psi_n(\vec{r},t) = \sum_n \psi_n(\vec{r})e^{-i\omega_n t} \qquad \text{Équation 2.4}$$

Ces solutions sont intéressantes pour le chimiste car elles sont caractéristiques du système moléculaire et permettent d'accéder aux propriétés mesurables des substances étudiées (énergie, distribution spatiale des charges, spectres optiques,…) et d'en déduire notamment les valeurs des grandeurs thermochimiques.

Ainsi, en recherchant les solutions stationnaires de l'Équation 2.2, l'*équation de Schrödinger* indépendante du temps est obtenue en y injectant l'expression précédente, soit :

$$\hat{H}(\vec{r},\vec{p})\psi_n(\vec{r}) = \hbar\omega_n\psi_n(\vec{r}) \qquad \text{Équation 2.5}$$

$$\hat{H}(\vec{r},\vec{p})\psi(\vec{r}) = E\psi(\vec{r}) \qquad \text{Équation 2.6}$$

Cette *équation de Schrödinger* indépendante du temps est une équation aux valeurs propres, qu'il faudra résoudre afin d'obtenir les informations moléculaires recherchées sur nos systèmes.

2.3. L'approximation de Born-Oppenheimer

L'opérateur hamiltonien s'écrit de manière générale comme la somme des opérateurs énergie cinétique $\hat{T}$ et énergie potentielle $\hat{V}$ associées au système, soit :

$$\hat{H} = \hat{T} + \hat{V} \qquad \text{Équation 2.7}$$

Pour un système composé d'électrons chargés négativement en interaction avec des noyaux chargés positivement, le hamiltonien devient alors :

$$\hat{H} = \hat{T}_e + \hat{T}_N + \hat{V}_{Ne} + \hat{V}_{ee} + \hat{V}_{NN} + \hat{V}_{ext} \qquad \text{Équation 2.8}$$

avec e désignant les électrons, N les noyaux et V_{ext} le potentiel d'interaction avec l'environnement (solvant, champs extérieurs …). Dans le cas de la phase gaz (qui nous intéressera plus particulièrement dans cette thèse), V_{ext} = 0 et le hamiltonien complet s'écrira, dans le cas de N électrons en interaction avec M noyaux, en cooordonnées sphériques :

$$\hat{H} = -\sum_{i=1}^{N}\frac{\hbar^2}{2m_i}\nabla_i^2 - \sum_{A=1}^{M}\frac{\hbar^2}{2M_A}\nabla_A^2 - \sum_{i=1}^{N}\sum_{A=1}^{M}\frac{Z_A e^2}{r_{iA}} + \sum_{i=1}^{N}\sum_{j>1}^{N}\frac{e^2}{r_{ij}} + \sum_{A=1}^{M}\sum_{B>A}^{M}\frac{Z_A Z_B e^2}{R_{AB}}$$

Équation 2.9

Les unités atomiques sont en général utilisées, car elles sont plus adaptées aux systèmes microscopiques qui nous intéressent et qu'elles permettent d'avoir des équations sans dimensions (qui fournissent des lois de comportement plus facilement généralisables). La conversion des unités atomiques vers les unités du système international est présentée dans le Tableau 1. C'est dans ce

système que seront données les équations dans les développements à suivre et qui seront utilisées dans cette thèse (sauf mention contraire).

Constantes physiques	Symbole	S.I.	Unités atomiques
Masse de l'électron au repos	m_e	$9{,}10938.10^{-31}$ kg	1
Constante de Planck	h	$6{,}62607.10^{-34}$ J.s	2π
Constante de Planck réduite	$\hbar$ ($= h/2\pi$)	$1{,}0546.10^{-34}$ J.s	1
Charge	e	$1{,}6022.10^{-19}$ C	1
Constante de structure fine	α ($= e^2/4\pi\varepsilon_0\hbar c$)	$7{,}29735.10^{-3}$	$7{,}29735.10^{-3}$
Longueur (Rayon de Bohr)	a_0 ($= \hbar/m_e c\alpha$)	$5{,}29167.10^{-11}$ m	1
Énergie	E ($= m_e c^2\alpha^2$)	$4{,}3598.10^{-18}$ J	1 (Hartree)
Vitesse de la lumière	c ($= a_0 E/\hbar\alpha$)	$2{,}99792.10^{8}$ m.s^{-1}	137,037

Tableau 1: Conversion des unités du Système International en unités atomiques

L'expression suivante du hamiltonien est alors obtenue :

$$\hat{H} = -\sum_{i=1}^{N} \frac{1}{2}\nabla_i^2 - \sum_{A=1}^{M} \frac{1}{2\,M_A/m_e}\nabla_A^2 - \sum_{i=1}^{N}\sum_{A=1}^{M} \frac{Z_A}{r_{iA}} + \sum_{i=1}^{N}\sum_{j>1}^{N} \frac{1}{r_{ij}} + \sum_{A=1}^{M}\sum_{B>A}^{M} \frac{Z_A Z_B}{R_{AB}}$$

Équation 2.10

L'Équation 2.10 peut être simplifiée grâce à l'approximation de Born-Oppenheimer (proposée en 1927). Cette approximation consiste à considérer que, la masse des nucléons étant très supérieure à la masse des électrons ($m_{proton} \approx 1840.m_{e^-}$), le centre de masse atomique est confondu avec le centre de masse du noyau. Ainsi, la vitesse des noyaux est très faible par rapport à la vitesse des électrons et les électrons se meuvent dans le champ électrique des noyaux fixes. L'énergie cinétique des noyaux $\hat{T}_N$ est alors nulle et l'énergie potentielle d'interaction entre les noyaux $\hat{V}_{NN}$ est constante. L'approximation de Born-Oppenheimer consiste alors à découpler le mouvement des électrons de celui des noyaux, ce qui nous permet alors de séparer le hamiltonien du système moléculaire en un hamiltonien électronique et un hamiltonien nucléaire.

Le hamiltonien électronique peut donc s'écrire :

$$\hat{H}_{él} = -\sum_{i=1}^{N} \frac{1}{2}\nabla_i^2 - \sum_{i=1}^{N}\sum_{A=1}^{M} \frac{Z_A}{r_{iA}} + \sum_{i=1}^{N}\sum_{j>i}^{N} \frac{1}{r_{ij}} + \hat{V}_{NN} \qquad \text{Équation 2.11}$$

et l'équation de Schrödinger devient alors :

$$\hat{H}_{él}(\vec{r}_i, \{\vec{R}_A\})\psi_{él}(\vec{r}_i, \{\vec{R}_A\}) = E_{él}(\{\vec{R}_A\})\psi_{él}(\vec{r}_i, \{\vec{R}_A\}) \qquad \text{Équation 2.12}$$

où les positions des noyaux R_A sont présentées comme des paramètres de l'équation de Schrödinger. plutôt que comme des variables indépendantes.

Le hamiltonien nucléaire décrivant le mouvement des noyaux dans le champ électrique moyen créé par les électrons (signifié par $\langle ... \rangle$) est alors :

$$\hat{H}_{nuc} = -\sum_{A=1}^{M} \frac{1}{M_A/m_e}\nabla_A^2 + \sum_{A=1}^{M}\sum_{B>A}^{M} \frac{Z_A Z_B}{R_{AB}} + \langle -\sum_{i=1}^{N} \frac{1}{2}\nabla_i^2 - \sum_{i=1}^{N}\sum_{A=1}^{M} \frac{Z_A}{r_{iA}} + \sum_{i=1}^{N}\sum_{j>i}^{N} \frac{1}{r_{ij}} \rangle$$

Équation 2.13

ou $$\hat{H}_{nuc} = -\sum_{A=1}^{M} \frac{1}{M_A/m_e}\nabla_A^2 + \sum_{A=1}^{M}\sum_{B>A}^{M} \frac{Z_A Z_B}{R_{AB}} + \hat{V}_{él} \qquad \text{Équation 2.14}$$

où $V_{él}$ est l'énergie électronique qui peut alors être vue comme un potentiel électrique auquel sont soumis les noyaux en mouvement.

et l'équation de Schrödinger correspondante :

$$\hat{H}_{nuc}(\vec{R}_A)\psi(\vec{r}_i, \vec{R}_A) = E_{totale}\psi(\vec{r}_i, \vec{R}_A) \quad \text{avec} \quad \psi(\vec{r}_i, \vec{R}_A) = \psi_{él}(\vec{r}_i, \{\vec{R}_A\}).\psi_{nuc}(\vec{R}_A)$$

Équation 2.15

Cette approximation est essentielle lors de la modélisation moléculaire car elle nous permet de résoudre l'équation de Schrödinger en deux étapes principales après avoir « construit » le système étudié (dans ce travail de thèse, à l'aide du logiciel GaussView5[51], ou la version d'essai de ChemCraft[52]) :

1) La fonction d'onde électronique est calculée dans une configuration nucléaire donnée, en résolvant le problème électronique (cf. Équations 2.11 et 2.12) : c'est la procédure du champ auto-cohérent (*Self-Confident Field*, SCF, cf. Section 2.5.1.) puis,

2) La configuration nucléaire qui va minimiser l'énergie totale est déterminée en résolvant le problème nucléaire (cf. Équations 2.13, 2.14 et 2.15), ce qui nous permet d'obtenir la géométrie optimale pour notre système moléculaire (cf. Section 2.5.2.).

2.4. La fonction d'onde moléculaire

Afin de décrire le comportement des électrons dans des édifices multi-électroniques, il a été proposé d'écrire la fonction d'onde multi-électronique comme un produit de Hartree (ce qui est appellé *« l'approximation orbitalaire »*, qui consiste à associer une orbitale à un électron), soit, pour un système à *n* électrons (Équation 2.16) :

$$\Psi(\vec{r}_1, \vec{r}_2 \ldots \vec{r}_n) = \psi(\vec{r}_1)\psi(\vec{r}_2)\ldots\psi(\vec{r}_n) \qquad \text{Équation 2.16}$$

Or, il est apparu nécessaire de considérer explicitement un nouveau nombre quantique dès lors que plusieurs électrons sont en interaction[53] : le nombre quantique de spin (s = 1/2 dans le cas des électrons). Chaque électron peut ainsi être décrit par une fonction d'onde ne dépendant que de ses coordonnées spatiales $\vec{r}$ mais doit inclure également une fonction de spin *ω(s)*, il s'agit alors d'une spin-orbitale χ_i, avec : $\vec{x}_i = \psi_i(\vec{r}_i)\omega(s)$. Le principe d'exclusion de Pauli (1925) interdit à deux particules, telles que des électrons, de se trouver dans le même état quantique (ou d'être décrits par la même spin-orbitale). Le nombre quantique magnétique de spin ne pouvant prendre que 2 valeurs ($m_s = \pm s = \pm 1/2$), seuls deux électrons peuvent être décrits par la même orbitale spatiale (ils seront alors de spin opposé). Ce principe de Pauli nécessite que la fonction d'onde multi-électronique soit antisymétrique, c'est-à-dire qu'elle change de signe par simple échange des électrons (Équation 2.17) :

$$\Psi(\vec{r}_1, \vec{r}_2) = -\Psi(\vec{r}_2, \vec{r}_1) \qquad \text{Équation 2.17}$$

Ainsi, la fonction d'onde multi-électronique écrite comme un produit de Hartree doit respecter le principe d'exclusion de Pauli, ce qui est réalisable en l'écrivant sous la forme d'une combinaison linéaire de produits de Hartree. C'est ce qu'on appelle le déterminant de Slater (Equation 2.18).

$$\Psi(\vec{r}_1,\vec{r}_2\ldots\vec{r}_n) = (n!)^{-1/2}\begin{vmatrix} \chi_1(\vec{r}_1) & \chi_2(\vec{r}_1) & \ldots & \chi_n(\vec{r}_1) \\ \chi_1(\vec{r}_2) & \chi_2(\vec{r}_2) & \ldots & \chi_n(\vec{r}_2) \\ \ldots & \ldots & \ldots & \ldots \\ \chi_1(\vec{r}_n) & \chi_2(\vec{r}_n) & \ldots & \chi_n(\vec{r}_n) \end{vmatrix} \qquad \text{Équation 2.18}$$

où le coefficient $(n!)^{-1/2}$ est un facteur de normalisation. Ici, le déterminant est écrit pour un système de *n* électrons (identifiés par les lignes) occupant *n* spins-orbitales (identifiées par les colonnes) ou *n/2* orbitales spatiales. À noter que ψ peut être une orbitale atomique ou une orbitale moléculaire (c'est-à-dire une combinaison d'orbitales atomiques). Ce déterminant possède les propriétés d'antisymétrie (le déterminant devient nul si deux colonnes sont égales) et d'interchangeabilité des électrons (l'échange de deux lignes change le signe du déterminant). Ce déterminant fait donc apparaître des effets d'échange ($|\Psi|^2$ est invariant si deux électrons sont échangés) ainsi que des effets d'échange-corrélation (le mouvement des électrons de spins parallèles est corrélé).

2.5. L'équation de Hartree-Fock

Entre 1927 et 1935, Hartree et Fock mettent au point une méthode incrémentielle permettant de résoudre, de manière approximative, l'équation de Schrödinger[54,55]. Partant de l'approximation de Born-Oppenheimer, elle consiste à utiliser l'approximation orbitalaire (un électron dans une seule spin-orbitale) et à écrire la fonction d'onde moléculaire comme un produit de Hartree antisymétrisé (un déterminant de Slater[56], cf. ci-dessus). L'hamiltonien multi-électronique est écrit comme la somme d'hamiltoniens mono-électroniques Pour un système complexe à couches pleines (*closed-shell)* à *N* électrons (les *N* électrons sont appariés), un jeu d'équations mono-électroniques a ainsi été posé (Équation 2.19) :

$$\hat{f}(i)\chi(x_i) = \epsilon_i^{HF}.\chi(x_i) \qquad \text{Équation 2.19}$$

où ε_i est l'énergie de la spin-orbitale *i* considérée. *f* est appelé opérateur de Fock et se définit à l'aide de l'Équation 2.20. La somme des opérateurs de Fock mono-électroniques donne le hamiltonien d'Hartree-Fock.

$$\hat{f}(i) = -\frac{1}{2}\nabla_i^2 - \sum_{A=1}^{M}\frac{Z_A}{r_{iA}} + v^{HF}(i) \qquad \text{Équation 2.20}$$

où v^{HF} est le potentiel d'interaction moyen subi par l'électron *i* de la part de tous les autres électrons. v^{HF} est constitué d'un opérateur de Coulomb $\hat{J}$ (qui représente la répulsion moyenne des autres électrons) et d'un opérateur d'échange $\hat{K}$ (qui n'a pas de signification physique mais se rattache à la propriété d'antisymétrie du déterminant de Slater ; il apparaît lorsqu'il y a des électrons de spin parallèles). L'idée de Hartree était donc de réduire le problème multi-électronique à un problème mono-électronique, en considérant la répulsion électron-électron de manière moyennée. La résolution de l'ensemble des équations mono-électroniques se fait de manière itérative (et selon le principe variationnel, c'est-à-dire qu'il est possible de trouver une solution minimale).

2.5.1. Procédure de champ auto-cohérent appliquée à la structure électronique

Afin de trouver la structure électronique optimale, une procédure dite de « champ auto-cohérent » (*Self-Consistent Field*, SCF) est mise en place (Figure 20). Cette méthode est basée sur le principe variationnel, qui affirme que l'énergie de l'état fondamendal (ψ optimale) est la plus basse, et que toute fonction d'essai (appelée *trial* ou *guess*) mène à une énergie supérieure ou égale. La procédure SCF nécessite de construire le déterminant de Slater à partir de fonctions de base φ_μ, ou *basis functions*, à partir desquelles les spin-orbitales sont construites (Équation 2.21).

$$\chi_i(x) = \psi_i(r).\omega = \omega.\sum_{\mu=1}^{K} c_{\mu i}\phi_\mu(r) \qquad \text{Équation 2.21}$$

Puis, l'opérateur de Fock est formé. Il dépend de la fonction de départ estimée (*guess*), afin de satisfaire l'écriture de l'équation aux valeurs propres (EVP, Équation 2.6). Le système d'équations mono-électroniques est résolu. L'énergie E^{HF} est donnée par l'Équation 2.22 : c'est la somme des énergies ϵ_i^{HF} de tous les niveaux d'énergie occupés.

$$E^{HF} = \sum_{i=1}^{N}\epsilon_i^{HF} \qquad \text{Équation 2.22}$$

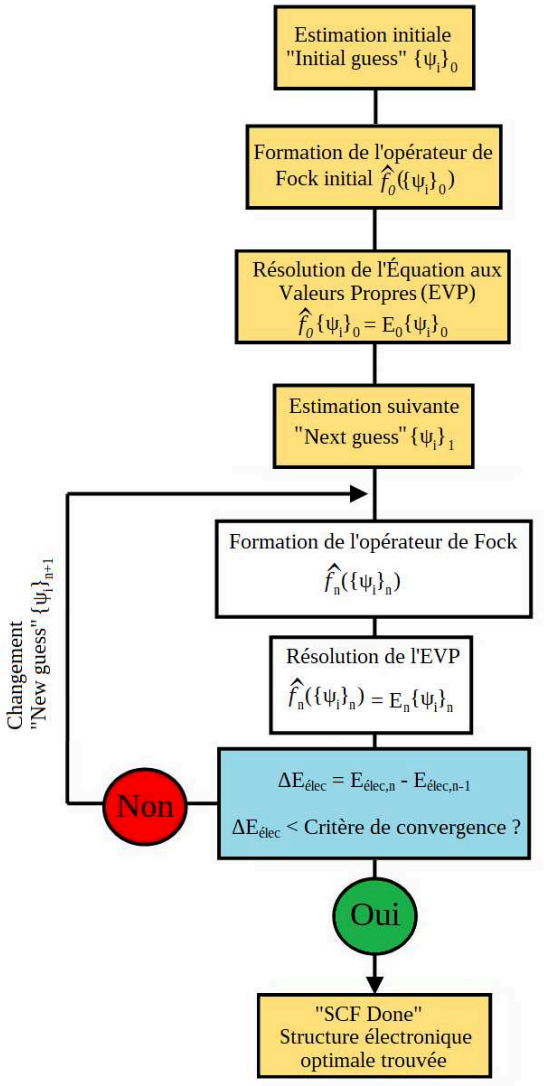

Figure 20: Algorithme de résolution Self Consistent Field *(SCF) de la structure électronique optimale.*

À partir du système de spin-orbitales précédent, un nouveau jeu de fonctions est proposé, avant de reprendre la procédure. Lorsque le gain en énergie δE^{HF} devient marginal, la procédure SCF est stoppée. Aussi, la définition des spin-orbitales est primordiale. Plus les *basis functions* vont être larges, plus les spin-orbitales vont être flexibles et vont permettre de réduire l'énergie. Ces fonctions de base sont en général des fonctions gaussiennes - plus faciles à manipuler que les fonctions de Slater - dont la forme est donnée par l'Équation 2.23. Augmenter la taille des bases a un coût en temps de calcul.

$$G(x) = \frac{1}{\sigma\sqrt{2\pi}} e^{\frac{-(x-\mu)^2}{2\sigma^2}}$$ Équation 2.23

2.5.2. Procédure SCF appliquée à l'optimisation d'une structure moléculaire

À partir de la procédure SCF appliquée à la structure électronique d'une molécule donnée, il est également possible d'optimiser la structure nucléaire, à l'aide de la même procédure SCF, cette-fois-ci appliquée à la résolution de l'hamiltonien nucléaire (Équations 2.14 et 2.15). En intercalant une procédure d'optimisation électronique entre chaque pas d'optimisation de la structure nucléaire (Figure 21), il est possible d'obtenir une structure moléculaire optimale. Une fois la convergence électronique acquise, une nouvelle structure nucléaire est proposée. Lorsque la différence d'énergie totale (somme des énergies électronique et nucléaire) est inférieure au critère de convergence, alors la procédure SCF est stoppée. La structure moléculaire et la répartition des électrons (orbitales moléculaires) sont précisées dans des fichiers de sortie, exploitables en tant que tels, mais également consultables par le biais des logiciels de visualisation.

La méthode Hartree-Fock est dite *ab initio* (c'est-à-dire sans faire appel à des données expérimentales), mais elle n'a été que peu utilisée avant les années 1950 et l'arrivée des calculateurs (auparavant, des méthodes semi-empiriques étaient utilisées). La méthode HF ne prend pas en compte l'énergie de corrélation (l'interaction entre deux électrons de spin opposé), ce qui entraîne des déviations importantes sur l'énergie finale. L'énergie de corrélation E_{correl} est l'écart entre l'énergie exacte du système E et l'énergie de Hartree-Fock E^{HF} (Équation 2.24).

$$E_{correl} = E - E^{HF} \qquad \text{Équation 2.24}$$

Ce problème peut être contourné avec l'aide de certaines théories, dites *post Hartree-Fock*, telles que la théorie de la perturbation de Møller-Plesset, les méthodes *Coupled Cluster* et *Complete Active Space Self-Consistent Field* (CASSCF) ou la méthode de *Configuration Interaction* (CI). Ces dernières méthodes ne sont applicables qu'à des systèmes restreints, car elles sont extrêmement lourdes à mettre en place (étapes de préparation, puissance de calcul).

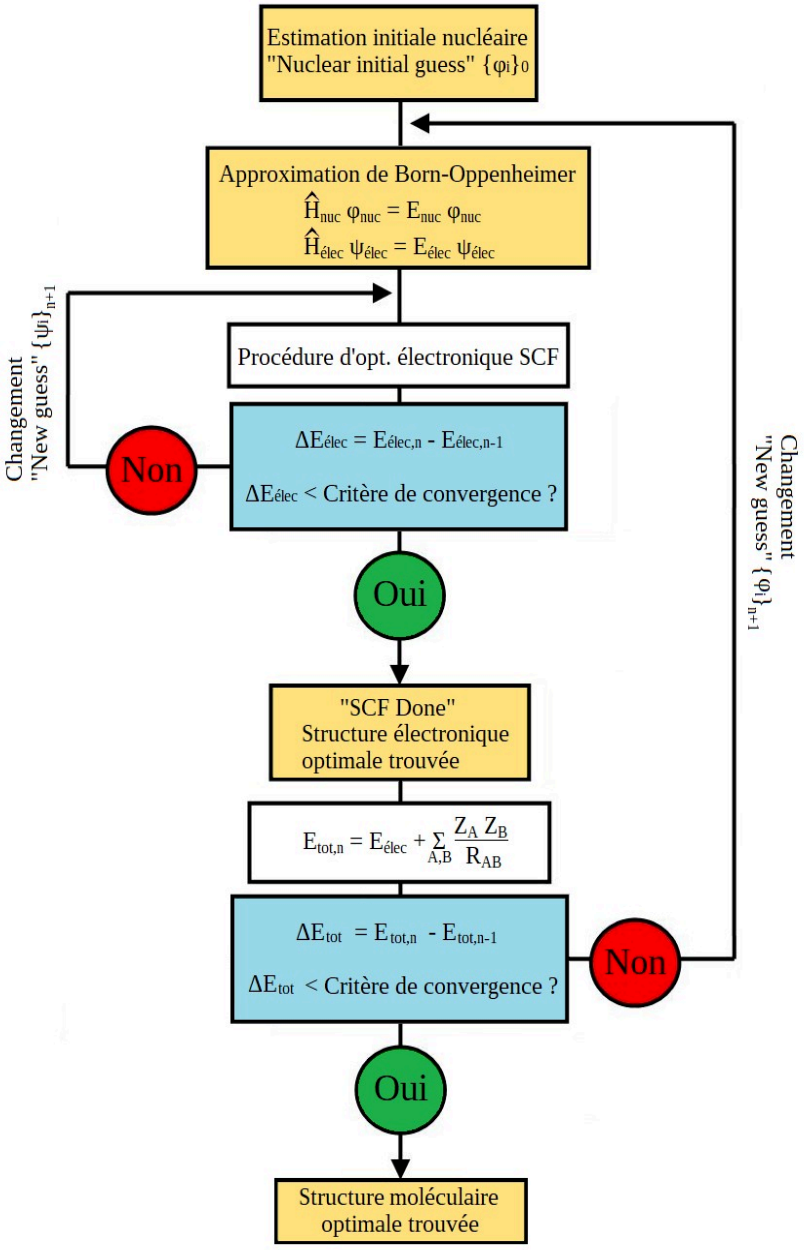

Figure 21: Algorithme de résolution Self Consistent Field (SCF) de la structure moléculaire optimale.

2.6. La théorie de la fonctionnelle de la densité (DFT)

Une nouvelle quantité, la densité électronique (définie par l'Équation 2.25, avec $\phi(r)$, une fonction d'onde mono-électronique), faisait en parallèle l'objet d'études afin de résoudre, au moins approximativement, l'équation de Schrödinger. La densité électronique est une observable, qui peut être mesurée par diffraction des rayons X. Elle s'annule à l'infini et, intégrée sur tout l'espace, donne N, le nombre d'électrons du système. Elle permet de réduire drastiquement le nombre de variables à considérer (3 contre 4N auparavant).

$$\rho(r) = N \int |\Psi(r, r_2, \ldots, r_n)|^2 \, dr_2 \ldots dr_n = \sum_{i=1}^{N} \phi_i(r)^* \, \phi_i(r)$$

Équation 2.25

En 1927, Llewellyn Thomas (1903-1992) et Enrico Fermi (1901-1954, Prix Nobel de Physique en 1938[57]) calculent l'énergie d'un atome donné comme la somme des énergies cinétiques des électrons, des énergies potentielles d'interaction noyau-électrons et d'interaction électron-électron[58,59]. Ces énergies dépendent de la densité électronique ρ(r). Malgré l'aide de Paul Dirac (1902-1984, Prix Nobel de Physique 1933[60]) qui y ajouta un terme décrivant l'interaction d'échange dépendant aussi de la densité, ce modèle n'était acceptable que pour des systèmes mono-atomiques[61]. Le modèle Thomas-Fermi-Dirac, bien que proposant une nouvelle façon de considérer le problème électronique, ne prenait pas en compte la corrélation électronique et décrivait l'énergie cinétique de manière peu précise. Pour contourner les manques de la théorie HF, et considérer la corrélation des électrons de spin opposés, les modèles basés sur la densité électronique sont toutefois dignes d'intérêt. Pierre Hohenberg (1934-2017) et Walter Kohn (1923-2016, Prix Nobel de Chimie en 1998[62]) émirent deux théorèmes fondamentaux en 1964[63] :

— Pour tout système moléculaire, le potentiel extérieur $V_{ext}(r)$ est déterminé par la densité à une constante additive près. L'énergie E du système est liée au potentiel externe.

— Pour chaque potentiel V_{ext}, il existe une valeur E minimale qui correspond à la densité électronique exacte (principe variationnel).

Ces deux théorèmes, bien qu'exacts, ne sont pas applicables tels quels à la détermination de l'énergie et des propriétés d'un système. En pratique, ce sont les équations de W. Kohn et Lu J. Sham (né en 1938) qui vont permettre de calculer l'énergie minimale[64].

Il est possible d'écrire un nouvel hamiltonien, semblable à celui donné par l'Équation 2.12, mais dépendant à présent de la densité électronique *ρ(r)* (Équation 2.26).

$$\hat{H} = \hat{T}_e(\rho(r)) + \hat{V}_{ee}(\rho(r)) + \hat{V}_{ext}(\rho(r)) \qquad \text{Équation 2.26}$$

Cet hamiltonien se traduit sous la forme d'une fonctionnelle (Équations 2.27 et 2.28) :

$$E[\rho(r)] = F[\rho(r)] + \int V_{ext}(r)\rho(r)dr \qquad \text{Équation 2.27}$$

$$F[\rho(r)] = T_e[\rho(r)] + V_{ee}[\rho(r)] \qquad \text{Équation 2.28}$$

$F[\rho(r)]$ peut être défini comme la somme des fonctionnelles liées à l'énergie cinétique des électrons et à l'énergie potentielle. Ces fonctionnelles ne sont pas exprimables pour un système de particules en interaction. W. Kohn et L. J. Sham proposèrent de réécrire la fonctionnelle $F[\rho(r)]$ pour un système d'électrons indépendants, et de la corriger ensuite à l'aide de nouveaux termes (Équation 2.29).

$$F[\rho(r)] = T_s[\rho(r)] + E_H[\rho(r)] + E_{xc}[\rho(r)] \qquad \text{Équation 2.29}$$

Où $T_s[\rho(r)]$ est l'énergie cinétique des électrons indépendants, $E_H[\rho(r)]$ est l'énergie d'interaction électron-électron (aussi appelée énergie de Hartree) et $E_{xc}[\rho(r)]$ est l'énergie d'échange-corrélation contient la différence entre l'énergie cinétique des électrons en interaction et l'énergie cinétique des électrons indépendants, ainsi que l'énergie d'échange. Enfin, pour minimiser la fonctionnelle $E[\rho(r)]$, sa dérivée doit être égale à zéro, ce qui conduit à l'hamiltonien de Kohn-Sham (Équation 2.30).

$$\hat{H}^{KS} = \frac{\delta E[\rho(r)]}{\rho(r)} = -\frac{1}{2}\nabla_i^2 + V_{ext}(r) + V_H(r) + V_{xc}(r) \qquad \text{Équation 2.30}$$

À l'instar de ce qui a été exposé pour la méthode HF, une procédure SCF peut être mise en place avec un jeu de fonctions mono-électroniques, mais cette fois, avec l'opérateur de Kohn-Sham, qui prend en compte la corrélation des électrons.

$$\hat{H}^{KS}(i)\psi_i(r) = \epsilon^{KS}.\psi_i(r) \qquad \text{Équation 2.31}$$

L'expression de l'énergie d'échange-corrélation reste toutefois à définir. Comme dans le rêve de Jacob (Genèse 28,12), John P. Perdew (né en 1943) imagine une échelle, partant de la théorie de Hartree (la terre), tendant vers l'exactitude de la prédiction calculatoire (le paradis)[65]. J. Perdew distingue cinq barreaux :

— LDA (Local Density Approximation) : Cette approximation consiste à séparer l'énergie d'échange-corrélation en deux composantes (Équations 2.32 et 2.33), l'une d'échange (Équation 2.34 : proposée par Paul Dirac pour compléter le modèle de Thomas-Fermi), l'autre de corrélation (paramétrisée). L'approximation LDA peut être complétée par la prise en compte du spin dans l'énergie d'échange (LSDA ; Équation 2.35).

$$E_{xc}^{LDA}(\rho(r)) = \int \rho(r)\ \epsilon_{xc}^{LDA}(\rho(r))\ dr \qquad \text{Équation 2.32}$$

$$\epsilon_{xc}^{LDA}(\rho(r)) = \epsilon_{x}^{LDA}(\rho(r)) + \epsilon_{c}^{LDA}(\rho(r)) \qquad \text{Équation 2.33}$$

$$\epsilon_{x}^{LDA}(\rho(r)) = -\frac{3}{4}\left(\frac{3}{\pi}\right)^{1/3} \int \rho(r)^{4/3}\ d^3r \qquad \text{Équation 2.34}$$

$$\epsilon_{x}^{LSDA}(\rho(r)) = -2^{1/3}.-\frac{3}{4}\left(\frac{3}{\pi}\right)^{1/3} \int \rho_\alpha(r)^{4/3}\ \rho_\beta(r)^{4/3}\ d^3r \qquad \text{Équation 2.35}$$

— GGA (Generalized Gradient Approximation) : Ici, la fonctionnelle d'échange-corrélation est découpée en deux composantes et dépend à la fois de la densité électronique $\rho(r)$ et de son gradient $\nabla\rho(r)$ (Équation 2.36).

$$E_{xc}^{GGA}(\rho(r)) = \int \rho(r)\ \epsilon_{xc}^{GGA}(\rho_\alpha(r),\rho_\beta(r),\nabla\rho_\alpha(r),\nabla\rho_\beta(r))\ d^3r \qquad \text{Équation 2.36}$$

— méta-GGA : La fonctionnelle d'échange-corrélation dépend de la densité électronique $\rho(r)$, de son gradient $\nabla\rho(r)$ et de sa dérivée seconde $\nabla^2\rho(r)$.

— Les fonctionnelles hybrides, qui contiennent une part de la fonctionnelle d'échange HF (Équation 2.37), une part d'échange GGA et une fonctionnelle de corrélation GGA. Les paramètres sont fixés empiriquement, à l'aide de bases de données expérimentales. Différentes formes de fonctionnelles hybrides existent, et notamment la fameuse B3LYP[66] utilisée lors de cette thèse (qui tient son nom de Becke, Lee, Yang et Parr et des trois paramètres a_0, a_x et a_c ; Équations 2.38, 2.39, 2.40, le terme $\rho(r)$ étant simplifié en ρ, les fonctionnelles B88 (échange) et PW91

(corrélation) sont des GGA). Des fonctionnelles hybrides utilisant des fonctionnelles méta-GGA ont également vu le jour.

$$E_x^{HF} = \frac{1}{2} \sum_{i,j} \iint \psi_i^*(r_1)\psi_j^*(r_1) \frac{1}{r_{12}} \psi_i(r_2)\psi_j(r_2)\, dr_1\, dr_2 \qquad \text{Équation 2.37}$$

$$E_{xc}(\rho) = E_x^{LDA}(\rho) + a_0(E_x^{HF} - E_x^{LDA}(\rho)) + a_x \Delta E_x^{B88}(\rho) + a_c \Delta E_c^{PW91}(\rho) \qquad \text{Équation 2.38}$$

$$\Delta E_x^{B88}(\rho) = E_x^{B88}(\rho) - E_x^{LSDA}(\rho) \qquad \text{Équation 2.39}$$

$$\Delta E_c^{PW91}(\rho) = E_c^{PW91}(\rho) - E_c^{VWN,LSDA}(\rho) \qquad \text{Équation 2.40}$$

— Le dernier barreau est constitué par les fonctionnelles non-locales, prenant en compte les orbitales non-occupées.

La méthode DFT ne peut être considérée comme une méthode *ab initio* à part entière. Même si les travaux de P. Hohenberg, W. Kohn et L. J. Sham sont établis théoriquement, la fonctionnelle d'échange-corrélation prend toujours appui sur des bases de données expérimentales, afin de fixer les paramètres.

2.7. Résultats attendus

2.7.1. Types de calculs

Grâce à l'apport de la chimie quantique, de nombreux résultats théoriques (présentés dans le Tableau 2) peuvent être obtenus. Ici, le logiciel considéré pour les calculs est Gaussian16[67].

Calcul effectué	Information obtenue	Procédure
Calcul *Single-Point*	Énergie du système	Les noyaux atomiques sont fixés, et l'énergie du système est calculée grâce à une procédure SCF électronique.
Optimisation de géométrie	Structure stable optimisée en énergie	La position des noyaux atomiques est optimisée par une procédure SCF, dans laquelle s'intercalent des procédures SCF électroniques. Il est possible d'optimiser le système vers un minimum local (la surface d'énergie potentielle PES peut avoir plusieurs minima locaux).
	Structure d'un TS optimisée en énergie	La géométrie d'un état de transition (ou *Transition State*, un maximum d'énergie sur la surface d'énergie potentielle, pour une coordonnée de réaction donnée) peut également être trouvée, à l'aide d'une procédure SCF.
Calcul de fréquences	Fréquences de vibration du système (Spectre IR)	Le spectre IR est déterminé sur la base de l'hypothèse d'un potentiel harmonique.
Calcul de données thermodynamiques	Fonctions de partition, corrections sur l'énergie, H (enthalpie), G (enthalpie libre), ZPE	Le calcul de données thermodynamiques est consécutif au calcul de fréquences, à partir desquelles les fonctions de partition puis les autres données thermodynamiques sont calculées.
Scan	Variations de l'énergie suivant une coordonnée	Il est possible de scanner une coordonnée donnée sur la PES et d'obtenir le profil de la PES suivant cette coordonnée.
IRC	Variations de l'énergie de la PES suivant la coordonnée de réaction	Autour du TS, la variation d'énergie de la surface d'énergie potentielle peut être déterminée en modifiant petit à petit la coordonnée de réaction et en calculant la géométrie et l'énergie associée à chaque pas. Le calcul de l'IRC permet de valider un chemin réactionnel.
Divers	Charges, Spectres UV, Raman, RMN	---

Tableau 2: Résultats pouvant être obtenus grâce au logiciel Gaussian16.

2.7.2. Densité électronique totale

Après convergence de la procédure SCF, une vue globale de la répartition électronique peut être obtenue (*Total SCF Density*). Les cartes de localisation électronique obtenues par diffraction des rayons X peuvent être rapprochées des surfaces de densité électronique totale. Les logiciels de visualisation permettent de choisir une isovaleur, comprise entre 0 et 1, qui a trait au pourcentage d'électrons inclus sous la surface représentée. En général, une isovaleur forte (qui correspond à un faible pourcentage d'électrons représentés) permet de mettre en évidence la répartition électronique sur les différents atomes, tandis qu'une isovaleur faible (pourcentage élevé d'électrons représentés) donne des informations sur les liaisons chimiques (Figure 22). Cette vue d'ensemble de la répartition de la densité électronique permet par exemple de localiser les groupements électrodonneurs ou électroattracteurs. La soustraction de la densité électronique d'un spin donné par la densité de l'autre spin permet d'accéder à une isosurface de densité de spin. Cette densité de spin permet de repérer les atomes où les électrons célibataires sont concentrés (lors d'un calcul *open-shell*). Expérimentalement, la densité de spin peut être obtenue grâce à la spectroscopie par résonance paramagnétique électronique (*Electron Paramagnetic Resonance*, EPR, ou *Electron Spin Resonance*, ESR)

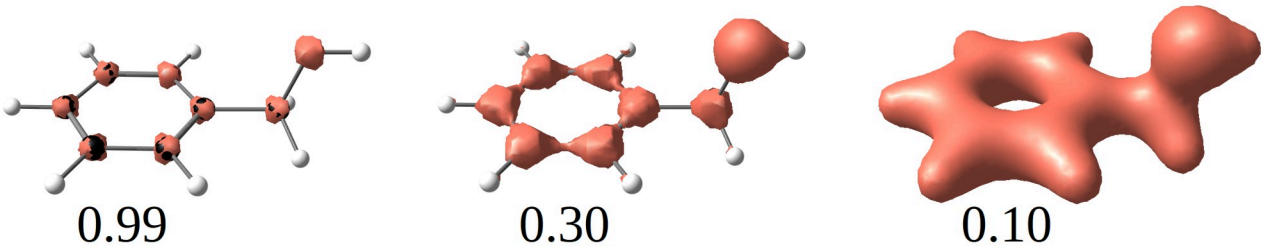

Figure 22: Densité électronique totale pour la molécule d'alcool benzylique, avec trois isovaleurs différentes (0.99, 0.30 et 0.10).

2.7.3. Orbitales moléculaires

Le concept des orbitales moléculaires[68–70] fut introduit entre 1926 et 1928 par Friedrich Hund (1896-1997) et Robert Mulliken (1896-1986, Prix Nobel de Chimie 1966[71]). Elles sont construites par combinaison linéaire d'orbitales atomiques (*Linear Combination of Atomic Orbitals*, LCAO, théorie proposée par John Lennard-Jones (1894-1954) en 1929[72]) et servent à la résolution des procédures SCF. Pour une bonne description des orbitales moléculaires, il faut se donner un nombre suffisant de fonctions de base localisées sur les différents atomes de la molécule.

Les fonctions de base de type gaussienne sont souvent des fonctions de choix. La visualisation des orbitales moléculaires permet d'avoir une vue d'ensemble sur les interactions entre atomes et sur la réactivité de la molécule. En particulier, les orbitales moléculaires de valence de plus haute énergie (*Highest Occupied Molecular Orbitals*, HOMO ou *Singly Occupied Molecular Orbitals*, SOMO, dans le cas d'un calcul *open-shell*) et les orbitales moléculaires vacantes de plus basse énergie (*Lowest Unoccupied Molecular Orbitals*, LUMO) contiennent des informations sur les atomes ou groupes d'atomes les plus à même de capter ou libérer des électrons, des protons, des atomes. Les orbitales de cœur n'interviennent pas dans la réactivité. La nomenclature des orbitales moléculaires repose sur leur symétrie : l'interaction de deux orbitales de symétrie sphérique mène à une interaction de type σ ; l'interaction de deux orbitales de symétrie planaire mène à une interaction de type π ; l'interaction de deux orbitales de symétrie supérieure mène à des interactions de type δ voire φ. Des orbitales en phase formeront des liaisons liantes, tandis que des orbitales en opposition de phase formeront des liaisons anti-liantes. Un dernier type d'orbitales, qualifiées de non-liantes, correspondent aux orbitales qui n'interagissent pas. Il s'agit en général de doublets non-liants.

2.7.4. Analyse des points critiques

Richard Bader, avec sa théorie *Atoms In Molecules* (AIM)[73], définit les atomes comme des attracteurs de la densité électronique et délimite des bassins, en fonction du gradient de la densité. Cette théorie se base sur le fait que la densité électronique est un champ scalaire. En tout point de ce champ (excepté les noyaux atomiques), la dérivation de ce champ scalaire permet d'obtenir le gradient de la densité (champ vectoriel). Une surface de flux nul est appelée séparatrice et sépare les bassins entre eux (Figure 23). Le volume d'un atome est défini par l'intégration de l'élément de volume dτ dans le bassin (Ω) (Équation 2.41).

$$V(\Omega) = \int_{\Omega} d\tau$$ Équation 2.41

L'intégration se fait sur un certain volume, jusqu'à atteindre une valeur faible de la densité. La population moyenne $\bar{N}_{\Omega}$ d'un bassin (c'est à dire de l'atome considéré) s'obtient en intégrant la densité électronique sur le volume du bassin (Équation 2.42).

$$\bar{N}_{\Omega} = \int_{\Omega} \rho(r) d(r)$$ Équation 2.42

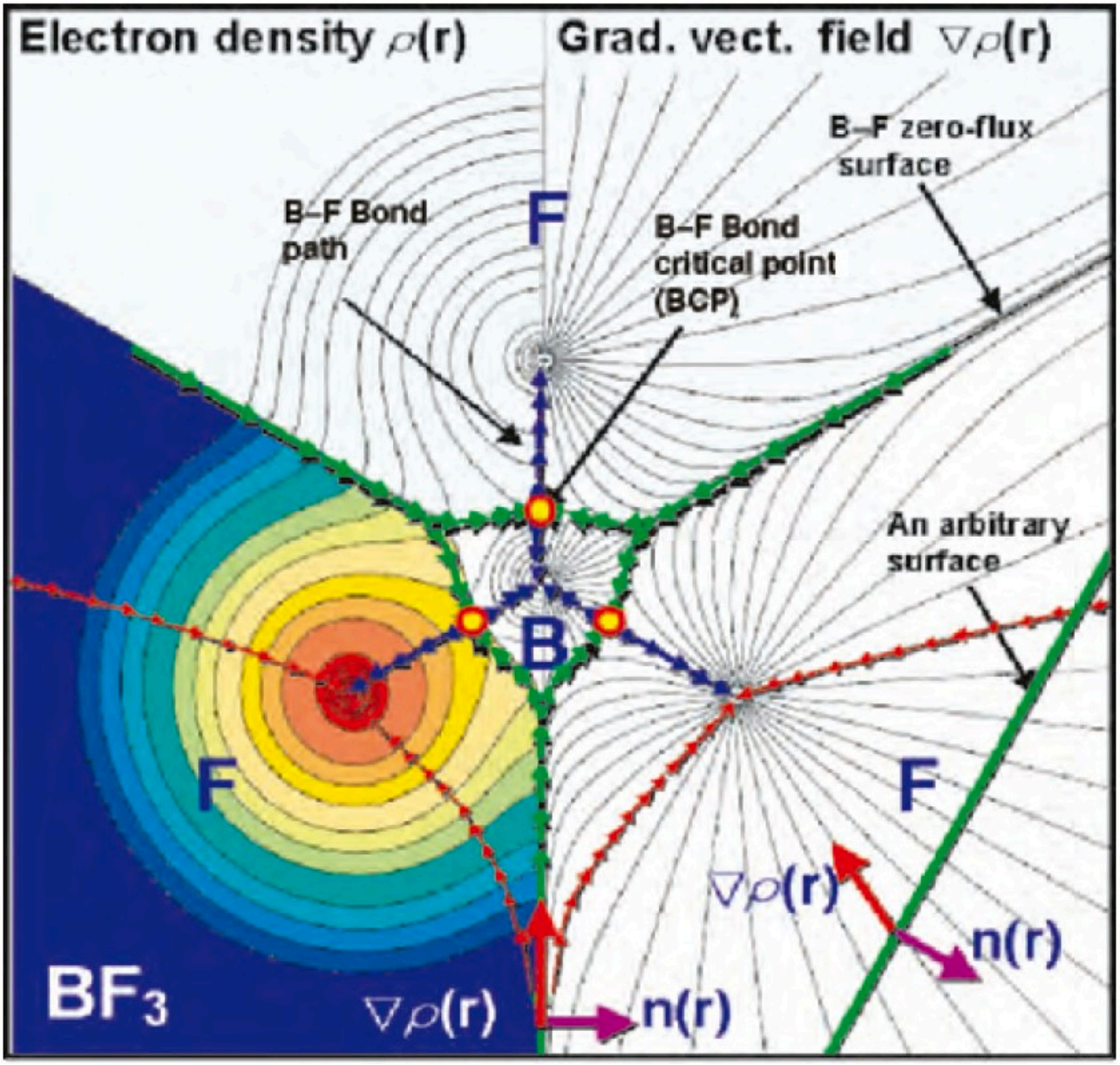

Figure 23: Représentation de la molécule BF_3 dans la théorie Quantum Topology Atoms In Molecules *(QTAIM). Sur la gauche, la densité électronique ρ(r) (champ scalaire) autour des atomes est représentée. Son gradient∇ρ(r) est présentée sur la droite. Les lignes de flux sont représentées par des flèches rouges (vers un maximum local de ρ(r), correspondant à un atome), bleues (chemin de liaison, passant par un minimum local appelé* Bond Critical Point *(BCP) et vertes (ligne de flux nul, correspondant à une séparatrice de bassins).*

Ainsi, entre deux atomes, s'établit un minimum local de la densité électronique appelé *Bond Critical Point* (BCP). Les BCP correspondent toujours à un minimum de ρ(r) suivant l'axe de la liaison et à deux maxima dans le plan perpendiculaire (ils sont représentés par des points jaunes cerclés de rouge sur la Figure 23). Des *Ring Critical Points* (RCP) sont également courants dans les molécules présentant des cycles : ils correspondent à un minimum local de ρ(r) dans le plan du

cycle et à un maximum local sur la droite perpendiculaire au cycle. L'utilisation de méthodes topologiques permet d'avoir un regard spécifique sur la liaison chimique. Le calcul de certains indicateurs au point critique ($\rho(r)$, $\Delta\rho(r)$, énergies cinétique, potentielle et totale) permettent de déterminer la nature d'une liaison[74]. Il est aussi possible de calculer le moment dipolaire, l'ordre de liaison, l'électrophilicité ou la nucléophilicité. Le logiciel DGrid5.1[75] (charges atomiques et indicateurs) et le code d'Henkelman[76] (charges atomiques) ont été utilisés au cours de cette thèse.

Il est important de rappeler que l'apport de la chimie quantique est souvent un complément à l'expérimentation, et que des résultats théoriques doivent être soigneusement examinés, avec le recul nécessaire. Le choix d'une méthode de calcul (HF, DFT,…), d'une fonctionnelle (dans le cadre de la DFT) et d'une base de fonctions adaptées est primordial afin d'obtenir des résultats fiables. Chaque fonctionnelle a été testée sur une base de données expérimentales, qu'il convient de croiser avec d'éventuelles publications scientifiques pour évaluer sa capacité à donner des résultats fiables pour les systèmes d'intérêt. D'autre part, la chimie quantique tend à briser l'aspect formel de la chimie générale. La chimie quantique et les méthodes d'analyse de population révèlent souvent des valeurs de charges portées par les atomes ou des ordres de liaisons non entiers , ou encore des interaction trinucléaires. Ces méthodes d'analyse obligent donc à nuancer des prédictions comme celles relatives aux états d'oxydation où une charge formelle est supposée.

Références

1. The Nobel Prize in Chemistry 1922 Available online: https://www.nobelprize.org/prizes/chemistry/1922/aston/biographical/ (accessed on 10 December 2021).

2. Aston, F.W. The Mass-Spectra of Chemical Elements. *Lond. Edinb. Dublin Philos. Mag. J. Sci.* **1920**, *39*, 611–625, doi:10.1080/14786440508636074.

3. Domon, B.; Aebersold, R. Mass Spectrometry and Protein Analysis. *Science* **2006**, *312*, 212–217, doi:10.1126/science.1124619.

4. Kailemia, M.J.; Ruhaak, L.R.; Lebrilla, C.B.; Amster, I.J. Oligosaccharide Analysis by Mass Spectrometry: A Review of Recent Developments. *Anal. Chem.* **2014**, *86*, 196–212, doi:10.1021/ac403969n.

5. Gode, D.; Volmer, D.A. Lipid Imaging by Mass Spectrometry – a Review. *The Analyst* **2013**, *138*, 1289, doi:10.1039/c2an36337b.

6. Colton, R.; D'Agostino, A.; Traeger, J.C. Electrospray Mass Spectrometry Applied to Inorganic and Organometallic Chemistry. *Mass Spectrom. Rev.* **1995**, *14*, 79–106, doi:10.1002/mas.1280140203.

7. Baron, D.; Hering, J.G. Analysis of Metal-EDTA Complexes by Electrospray Mass Spectrometry. *J. Environ. Qual.* **1998**, *27*, 844–850, doi:10.2134/jeq1998.00472425002700040019x.

8. Memboeuf, A.; Jullien, L.; Lartia, R.; Brasme, B.; Gimbert, Y. Tandem Mass Spectrometric Analysis of a Mixture of Isobars Using the Survival Yield Technique. *J. Am. Soc. Mass Spectrom.* **2011**, *22*, 1744–1752, doi:10.1007/s13361-011-0195-8.

9. Martin, T.P.; Schaber, H. Mass Spectra of Si, Ge, and Sn Clusters. *J. Chem. Phys.* **1985**, *83*, 855–858, doi:10.1063/1.449501.

10. Dole, M.; Mack, L.L.; Hines, R.L.; Mobley, R.C.; Ferguson, L.D.; Alice, M.B. Molecular Beams of Macroions. *J. Chem. Phys.* **1968**, *49*, 2240–2249, doi:10.1063/1.1670391.

11. The Nobel Prize in Chemistry 2002 Available online: https://www.nobelprize.org/prizes/chemistry/2002/fenn/biographical/ (accessed on 14 December 2021).

12. Taylor, G. Disintegration of Water Drops in an Electric Field. *Proc. R. Soc. Lond. Ser. Math. Phys. Sci.* **1964**, *280*, 383–397.

13. Cole, R.B. Some Tenets Pertaining to Electrospray Ionization Mass Spectrometry. *J Mass Spectrom* **2000**, 10.

14. Lord Rayleigh, J.W.S., F.R.S. XX. On the Equilibrium of Liquid Conducting Masses Charged with Electricity. *Lond. Edinb. Dublin Philos. Mag. J. Sci.* **1882**, *14*, 184–186, doi:10.1080/14786448208628425.

15. Gomez, A.; Tang, K. Charge and Fission of Droplets in Electrostatic Sprays. *Phys. Fluids* **1994**, *6*, 404–414, doi:10.1063/1.868037.

16. Iribarne, J.V.; Thomson, B.A. On the Evaporation of Small Ions from Charged Droplets. *J. Chem. Phys.* **1976**, *64*, 2287–2294, doi:10.1063/1.432536.

17. Ikonomou, M.G.; Blades, A.T.; Kebarle, Paul. Electrospray-Ion Spray: A Comparison of Mechanisms and Performance. *Anal. Chem.* **1991**, *63*, 1989–1998, doi:10.1021/ac00018a017.

18. Aliyari, E.; Konermann, L. Formation of Gaseous Proteins via the Ion Evaporation Model (IEM) in Electrospray Mass Spectrometry. *Anal. Chem.* **2020**, *92*, 10807–10814, doi:10.1021/acs.analchem.0c02290.

19. Wilm, M. Principles of Electrospray Ionization. *Mol. Cell. Proteomics* **2011**, *10*, M111.009407, doi:10.1074/mcp.M111.009407.

20. Kebarle, P.; Tang, L. From Ions in Solution to Ions in the Gas Phase - the Mechanism of Electrospray Mass Spectrometry. *Anal. Chem.* **1993**, *65*, 972A-986A, doi:10.1021/ac00070a001.

21. Van Berkel, G.J.; Zhou, F.; Aronson, J.T. Changes in Bulk Solution PH Caused by the Inherent Controlled-Current Electrolytic Process of an Electrospray Ion Source. *Int. J. Mass Spectrom. Ion Process.* **1997**, *162*, 55–67, doi:10.1016/S0168-1176(96)04476-X.

22. Van Berkel, G.J.; Zhou, Feimeng. Characterization of an Electrospray Ion Source as a Controlled-Current Electrolytic Cell. *Anal. Chem.* **1995**, *67*, 2916–2923, doi:10.1021/ac00113a028.

23. Van Berkel, G.J.; Zhou, Feimeng. Electrospray as a Controlled-Current Electrolytic Cell: Electrochemical Ionization of Neutral Analytes for Detection by Electrospray Mass Spectrometry. *Anal. Chem.* **1995**, *67*, 3958–3964, doi:10.1021/ac00117a022.

24. Blades, A.T.; Ikonomou, M.G.; Kebarle, Paul. Mechanism of Electrospray Mass Spectrometry. Electrospray as an Electrolysis Cell. *Anal. Chem.* **1991**, *63*, 2109–2114, doi:10.1021/ac00019a009.

25. Pfeifer, R.J.; Hendricks, C.D. Parametric Studies of Electrohydrodynamic Spraying. *AIAA J.* **1968**, *6*, 496–502, doi:10.2514/3.4525.

26. Liu, H.; Lei, Q.P.; Washabaugh, M. Characterization of IgG2 Disulfide Bonds with LC/MS/MS and Postcolumn Online Reduction. *Anal. Chem.* **2016**, *88*, 5080–5087, doi:10.1021/acs.analchem.5b04368.

27. Cramer, C.N.; Haselmann, K.F.; Olsen, J.V.; Nielsen, P.K. Disulfide Linkage Characterization of Disulfide Bond-Containing Proteins and Peptides by Reducing Electrochemistry and Mass Spectrometry. *Anal. Chem.* **2016**, *88*, 1585–1592, doi:10.1021/acs.analchem.5b03148.

28. Blades, A.T.; Jayaweera, P.; Ikonomou, M.G.; Kebarle, P. Studies of Alkaline Earth and Transition Metal M++ Gas Phase Ion Chemistry. *J. Chem. Phys.* **1990**, *92*, 5900–5906, doi:10.1063/1.458360.

29. Xu, Y.; Xin, Z.; Yergey, A.L. Electrospray Ionization of Copper—Glycine Solutions. *J. Am. Soc. Mass Spectrom.* **1996**, *7*, 25–29, doi:10.1016/1044-0305(95)00625-7.

30. Barlow, C.K.; McFadyen, W.D.; O'Hair, R.A.J. Formation of Cationic Peptide Radicals by Gas-Phase Redox Reactions with Trivalent Chromium, Manganese, Iron, and Cobalt Complexes. *J. Am. Chem. Soc.* **2005**, *127*, 6109–6115, doi:10.1021/ja043088f.

31. Lavanant, H.; Virelizier, H.; Hoppilliard, Y. Reduction of Copper(II) Complexes by Electron Capture in an Electrospray Ionization Source. *J. Am. Soc. Mass Spectrom.* **1998**, *9*, 1217–1221, doi:10.1016/S1044-0305(98)00100-7.

32. Cramer, C.N.; Kelstrup, C.D.; Olsen, J.V.; Haselmann, K.F.; Nielsen, P.K. Complete Mapping of Complex Disulfide Patterns with Closely-Spaced Cysteines by In-Source Reduction and Data-Dependent Mass Spectrometry. *Anal. Chem.* **2017**, *89*, 5949–5957, doi:10.1021/acs.analchem.7b00424.

33. Gianelli, L.; Amendola, V.; Fabbrizzi, L.; Pallavicini, P.; Mellerio, G.G. Investigation of Reduction of Cu(II) Complexes in Positive-Ion Mode Electrospray Mass Spectrometry. *Rapid Commun. Mass Spectrom.* **2001**, *15*, 2347–2353, doi:10.1002/rcm.510.

34. Kelly, M.A.; Vestling, M.M.; Fenselau, C.C.; Smith, P.B. Electrospray Analysis of Proteins: A Comparison of Positive-Ion and Negative-Ion Mass Spectra at High and Low PH. *Org. Mass Spectrom.* **1992**, *27*, 1143–1147, doi:10.1002/oms.1210271028.

35. Alfonso, I.; Astorga, C.; Gotor, V. Electrospray Ionization Mass Spectrometry (ESI-MS) as a Useful Tool for Fast Evaluation of Anion and Cation Complexation Abilities of a Cyclam Derivative. *J. Incl. Phenom. Macrocycl. Chem.* **2005**, *53*, 131–137, doi:10.1007/s10847-005-1827-z.

36. Lee, M.S.; Kerns, E.H. LC/MS Applications in Drug Development. 93.

37. Gun, J.; Bharathi, S.; Gutkin, V.; Rizkov, D.; Voloshenko, A.; Shelkov, R.; Sladkevich, S.; Kyi, N.; Rona, M.; Wolanov, Y.; et al. Highlights in Coupled Electrochemical Flow Cell-Mass Spectrometry, EC/MS. *Isr. J. Chem.* **2010**, *50*, 360–373, doi:10.1002/ijch.201000035.

38. Ramautar, R.; Somsen, G.W.; de Jong, G.J. CE-MS in Metabolomics. *ELECTROPHORESIS* **2009**, *30*, 276–291, doi:10.1002/elps.200800512.

39. Fenn, J.B.; Mann, M.; Meng, C.K.; Wong, S.F.; Whitehouse, C.M. Electrospray Ionization for Mass Spectrometry of Large Biomolecules. *Science* **1989**, *246*, 64–71, doi:10.1126/science.2675315.

40. Tang, K.; Page, J.S.; Smith, R.D. Charge Competition and the Linear Dynamic Range of Detection in Electrospray Ionization Mass Spectrometry. *J. Am. Soc. Mass Spectrom.* **2004**, *15*, 1416–1423, doi:10.1016/j.jasms.2004.04.034.

41. Lai, Y.-H.; Sathyamoorthi, S.; Bain, R.M.; Zare, R.N. Microdroplets Accelerate Ring Opening of Epoxides. *J. Am. Soc. Mass Spectrom.* **2018**, *29*, 1036–1043, doi:10.1007/s13361-018-1908-z.

42. Sahota, N.; I. AbuSalim, D.; L. Wang, M.; J. Brown, C.; Zhang, Z.; J. El-Baba, T.; P. Cook, S.; E. Clemmer, D. A Microdroplet-Accelerated Biginelli Reaction: Mechanisms and Separation of Isomers Using IMS-MS. *Chem. Sci.* **2019**, *10*, 4822–4827, doi:10.1039/C9SC00704K.

43. Dempster, A.J. A New Method of Positive Ray Analysis. *Phys. Rev.* **1918**, *11*, 316–325, doi:10.1103/PhysRev.11.316.

44. The Nobel Prize in Physics 1989 Available online: https://www.nobelprize.org/prizes/physics/1989/paul/biographical/ (accessed on 14 December 2021).

45. March, R.E.; Todd, J.F.J. *Quadrupole Ion Trap Mass Spectrometry*; Chemical analysis; 2. ed.; Wiley-Interscience: Hoboken, NJ, 2005; ISBN 978-0-471-48888-0.

46. Fiehn Lab - Mass Resolution and Resolving Power Available online: https://fiehnlab.ucdavis.edu/projects/seven-golden-rules/mass-resolution (accessed on 10 December 2021).

47. The Nobel Prize in Physics 1918 Available online: https://www.nobelprize.org/prizes/physics/1918/planck/biographical/ (accessed on 14 December 2021).

48. The Nobel Prize in Physics 1921 Available online: https://www.nobelprize.org/prizes/physics/1921/einstein/biographical/ (accessed on 14 December 2021).

49. The Nobel Prize in Physics 1929 Available online: https://www.nobelprize.org/prizes/physics/1929/broglie/biographical/?_pjax=%23pjax-well (accessed on 14 December 2021).

50. Born, M. Zur Quantenmechanik der Stoßvorgänge. *Z. Für Phys.* **1926**, *37*, 863–867, doi:10.1007/BF01397477.

51. Dennington, R.; Keith, T.A.; Millam, J.M. *GaussView*; Semichem Inc.: Shawnee Mission, KS, 2003;

52. Andreienko, G. Chemcraft - Graphical Program for Visualization of Quantum Chemistry Computations Available online: https://www.chemcraftprog.com/ (accessed on 29 April 2020).

53. *Chemcraft - Graphical Software for Visualization of Quantum Chemistry Computations*;

54. Gerlach, W.; Stern, O. Das magnetische Moment des Silberatoms. *Z. Für Phys.* **1922**, *9*, 353–355, doi:10.1007/BF01326984.

55. Hartree, D.R. The Wave Mechanics of an Atom with a Non-Coulomb Central Field. Part II. Some Results and Discussion. *Math. Proc. Camb. Philos. Soc.* **1928**, *24*, 111–132, doi:10.1017/S0305004100011920.

56. Fock, V. Näherungsmethode zur Lösung des quantenmechanischen Mehrkörperproblems. *Z. Für Phys.* **1930**, *61*, 126–148, doi:10.1007/BF01340294.

57. Slater, J.C. The Theory of Complex Spectra. *Phys. Rev.* **1929**, *34*, 1293–1322, doi:10.1103/PhysRev.34.1293.

58. The Nobel Prize in Physics 1938 Available online: https://www.nobelprize.org/prizes/physics/1938/fermi/biographical/ (accessed on 14 December 2021).

59. Thomas, L.H. The Calculation of Atomic Fields. *Math. Proc. Camb. Philos. Soc.* **1927**, *23*, 542–548, doi:10.1017/S0305004100011683.

60. Fermi, E. Statistical Method to Determine Some Properties of Atoms. *Rendiconti Accad. Naz. Lincei* **1927**, *6*, 602–607.

61. The Nobel Prize in Physics 1933 Available online: https://www.nobelprize.org/prizes/physics/1933/dirac/biographical/ (accessed on 14 December 2021).

62. Dirac, P. a. M. Note on Exchange Phenomena in the Thomas Atom. *Math. Proc. Camb. Philos. Soc.* **1930**, *26*, 376–385, doi:10.1017/S0305004100016108.

63. The Nobel Prize in Chemistry 1998 Available online: https://www.nobelprize.org/prizes/chemistry/1998/Kohn/biographical/ (accessed on 14 December 2021).

64. Hohenberg, P.; Kohn, W. Inhomogeneous Electron Gas. *Phys. Rev.* **1964**, *136*, B864–B871, doi:10.1103/PhysRev.136.B864.

65. Kohn, W.; Sham, L.J. Self-Consistent Equations Including Exchange and Correlation Effects. *Phys. Rev.* **1965**, *140*, A1133–A1138, doi:10.1103/PhysRev.140.A1133.

66. Perdew, J.P.; Schmidt, K. Jacob's Ladder of Density Functional Approximations for the Exchange-Correlation Energy. *AIP Conf. Proc.* **2001**, *577*, 1–20, doi:10.1063/1.1390175.

67. Becke, A.D. Density-functional Thermochemistry. III. The Role of Exact Exchange. *J. Chem. Phys.* **1993**, *98*, 5648–5652, doi:10.1063/1.464913.

68. M. J. Frisch; G. W. Trucks; H. B. Schlegel; G. E. Scuseria; M. A. Robb; J. R. Cheeseman; G. Scalmani; V. Barone; G. A. Petersson; H. Nakatsuji; et al. *Gaussian16*; Gaussian, Inc.: Wallingford CT, 2016;

69. Hund, F. Zur Deutung einiger Erscheinungen in den Molekelspektren. *Z. Für Phys.* **1926**, *36*, 657–674, doi:10.1007/BF01400155.

70. Mulliken, R.S. Electronic States and Band Spectrum Structure in Diatomic Molecules. IV. Hund's Theory; Second Positive Nitrogen and Swan Bands; Alternating Intensities. *Phys. Rev.* **1927**, *29*, 637–649, doi:10.1103/PhysRev.29.637.

71. Mulliken, R.S. The Assignment of Quantum Numbers for Electrons in Molecules. I. *Phys. Rev.* **1928**, *32*, 186–222, doi:10.1103/PhysRev.32.186.

72. The Nobel Prize in Chemistry 1966 Available online: https://www.nobelprize.org/prizes/chemistry/1966/mulliken/biographical/ (accessed on 14 December 2021).

73. Lennard-Jones, J.E. The Electronic Structure of Some Diatomic Molecules. *Trans. Faraday Soc.* **1929**, *25*, 668–686, doi:10.1039/TF9292500668.

74. Bader, R.F.W. *Atoms in Molecules: A Quantum Theory*; Reprint édition.; Clarendon Press: Oxford

Résumé en français

Principaux Résultats
des Travaux de Thèse

État de l'art

Situation du problème

La compréhension des mécanismes enzymatiques est au cœur des problématiques environnementales et énergétiques actuelles. En effet, la nature est efficace pour oxyder même les liaisons les plus fortes, en diminuant fortement la demande énergétique de ces réactions d'oxydation. Il apparaît que certaines enzymes à cuivre sont efficaces pour transférer des électrons sur des distances variables, coordiner, activer et transporter le dioxygène et les espèces nitrogénées (N_2O, NO_2^-) ou encore faciliter les réactions d'oxydation de divers substrats[1]. Parmi elles, les cuproenzymes mononucléaires (galactose oxydase, dopamine-β-hydroxylase, monooxygénase polysaccharidique lytique, amine oxydase) ont retenu l'attention de la communauté scientifique, puisqu'elles sont capables d'activer le dioxygène et oxyder des liaisons CH et OH grâce à un seul site Cu, ce qui les rend plus faciles à copier. La structure des sites actifs a été déterminée grâce à la cristallographie aux rayons X. Elles possèdent un ion cuivrique ou cuivreux, entouré par des acides aminés possédant des atomes donneurs sur leur chaîne latérale (histidine, tyrosine, méthionine, cystéine). Durant les deux dernières décennies, le biomimétisme structurel a été l'approche utilisée par la communauté scientifique pour imiter les sites actifs des enzymes. La première approche est basée sur des considérations géométriques. La première sphère de coordination est reproduite par des modèles moléculaires, c'est-à-dire un ion d'un métal de transition entouré de ligands. Le nombre et la nature des atomes de coordination ainsi que la géométrie autour du centre métallique ont été pris en compte pour l'élaboration de tels modèles. Le rôle du ligand a été systématiquement étudié dans la littérature, soit en faisant varier le nombre et la nature des groupes de coordination, soit par criblage de ligands (variation d'un groupe fonctionnel sur le squelette carboné,…). Grâce à des études (spectroscopiques, cristallographiques, cinétiques, électrochimiques, magnétiques et calculatoires (DFT)), certains intermédiaires réactionnels ($Cu^{(II)}$-superoxo, $Cu^{(II)}$-hydroperoxo, $Cu^{(II)}$-oxyl) ont été proposés. Dans le cas des enzymes mononucléaires et de leurs modèles, un schéma global de réactivité a été identifié. La première étape du mécanisme est la coordination d'O_2 sur l'ion $Cu^{(I)}$. Un transfert d'électron a lieu, ce qui mène à la formation d'un adduit $Cu^{(II)}$-$O_2^{\bullet -}$ (superoxo). Cet adduit a la capacité d'arracher un atome

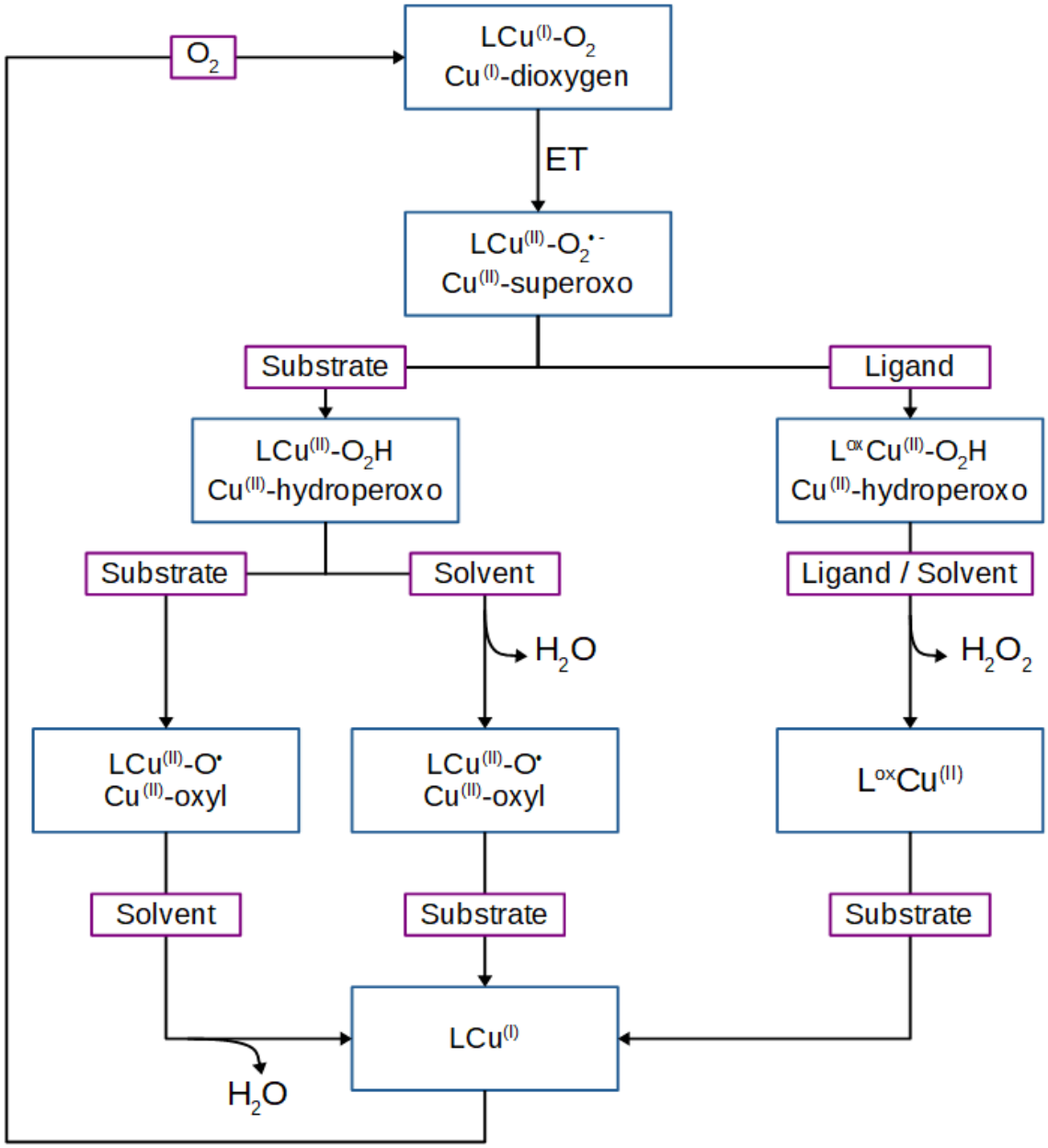

Figure 1: Schéma général de la réactivité attendue des sites actifs enzymes à cuivre mononucléaires, ou de leurs modèles biomimétiques respectifs. TE signifie Transfert d'Électron.

d'hydrogène dans son environnement, par HAT (transfert d'atome d'hydrogène) ou PCET (transfert couplé d'un électron et d'un proton, le transfert de l'un entraînant le transfert concerté de l'autre). L'espèce $Cu^{(II)}$-hydroperoxo résultante est parfois proposée étant comme l'espèce oxydante. Cependant,

la possibilité qu'elle évolue soit vers une espèce $Cu^{(II)}$-$O^{\bullet}$ (oxyl) oxydante, soit vers une espèce $Cu^{(II)}$-radical (départ de H_2O_2) a aussi été proposée. Après l'étape d'oxydation du substrat, l'espèce finale peut réagir avec le solvant pour régénérer le catalyseur (Figure 1). Même si la réactivité de ces systèmes enzymatiques et biomimétiques est relativement bien connue, il reste toutefois des zones d'ombre sur la plupart des mécanismes. Les espèces réactives ont des durées de vie très courtes, et leur observation reste difficile, sans appareillage spécialisé. À ce jour, aucune espèce $Cu^{(II)}$-oxyl n'a d'ailleurs été observée en phase condensée. D'autre part, la compréhension des mécanismes des enzymes/modèles mononucléaires peut permettre de mieux appréhender les mécanismes des enzymes/modèles polynucléaires, qui font toujours l'objet d'intenses débats.

Objectifs

En partant d'une réactivité CuO_2 abondamment décrite dans la littérature, le premier objectif de cette thèse était l'élaboration d'un modèle de mécanisme d'oxydation, sans solvant et sans ligand. Cette approche novatrice a pour objectif d'approfondir les connaissances sur l'influence du ligand sur une réaction d'oxydation. Bien qu'il soit nécessaire de disposer de ligand(s) pour réaliser la réaction de catalyse, le rôle du ligand a surtout été évalué sur la base de comparaisons relatives, parfois systématique (*screening* de ligands) et non à partir d'une référence absolue. L'étude d'une réaction avec le seul ion métallique comme centre catalytique peut permettre de distinguer les étapes intrinsèques de la réaction d'oxydation, tout en évaluant le rôle que le ligand joue. La première étape des mécanismes, c'est-à-dire la coordination et l'activation du dioxygène par Cu a été étudiée expérimentalement. L'objectif était de former et détecter des adduits CuO_2 en phase gaz grâce à deux classes de ligands, les ligands bipyridine (et phénanthroline) et les ligands tripodaux N_3N. Différentes stratégies ont été mises en place en fonction des ions présents sur le spectre MS. Les adduits observés ont été caractérisés grâce à l'aide de la DFT.

Méthodes

Lors de cette thèse, les techniques de spectrométrie de masse et de modélisation moléculaire ont été utilisées. La spectrométrie de masse est un outil de choix pour isoler des adduits peu stables, puisqu'elle permet de supprimer les interactions avec l'environnement (le solvant) et de les préserver de la dégradation. Ainsi, des complexes de cuivre ioniques ont pu être introduits dans la cellule de collision du triple quadripôle, principalement utilisé lors de cette thèse (Figure 2). L'utilisation O_2 comme gaz de collision a permis de former des adduits CuO_2. La modélisation moléculaire, en s'appuyant sur des données de la littérature, a permis de caractériser ces adduits. L'analyse de population (charges de Bader[2] et Bond Critical Points[3,4]) a été utilisée pour étayer le raisonnement et justifier de la caractérisation des espèces.

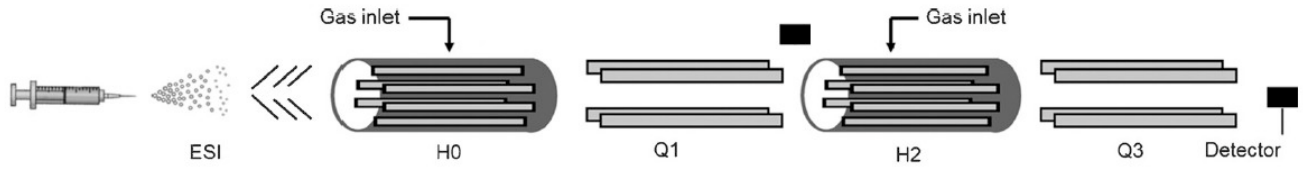

Figure 2: Schéma de l'appareil ESI-triple quadripôle (Quattro II) utilisé.

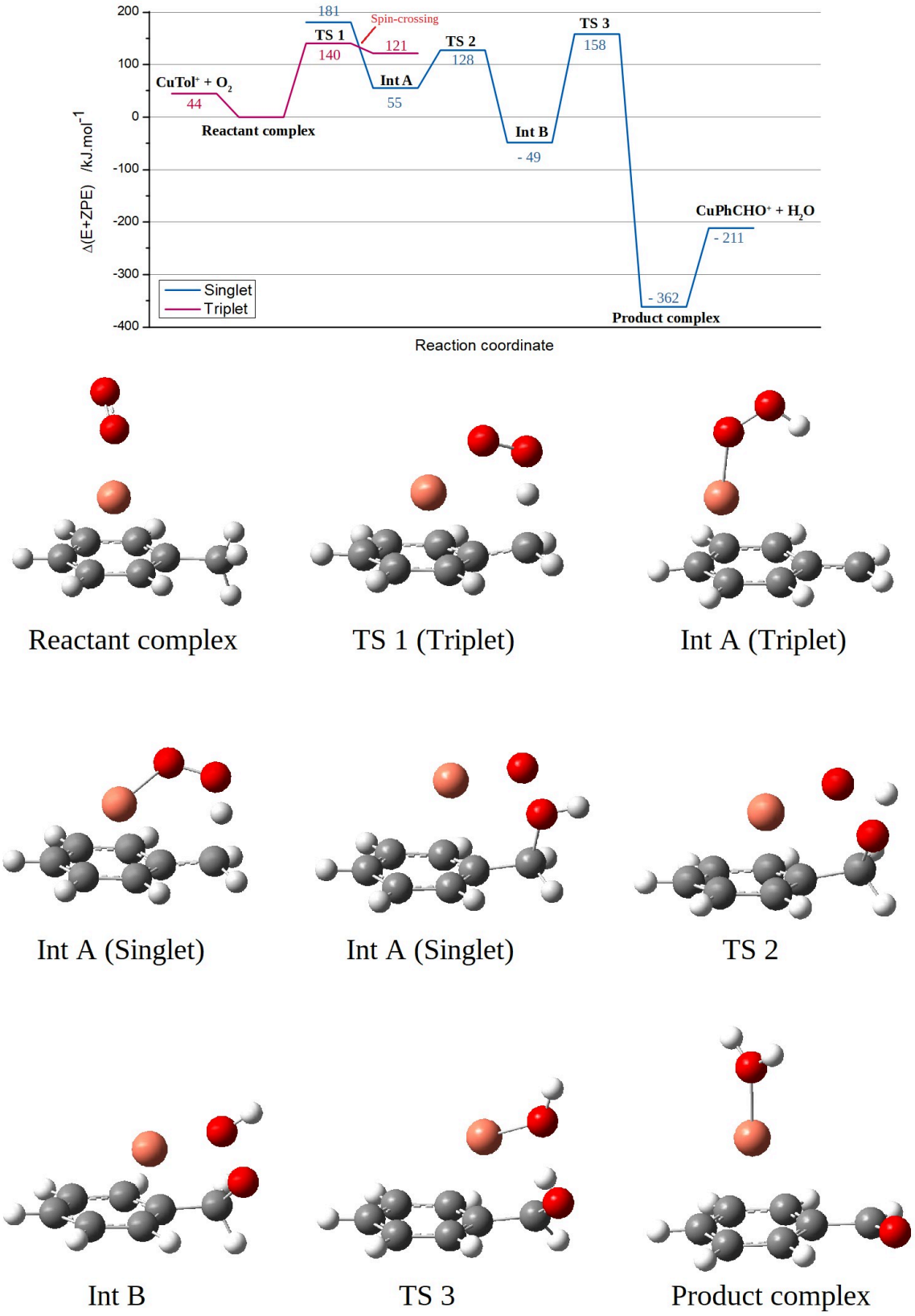

Figure 3: Mécanisme modèle de l'oxydation du toluène par O_2, avec Cu^+ comme catalyseur.

Étude d'un mécanisme modèle pour la compréhension de mécanismes enzymatiques

Nous avons choisi d'étudier la réaction d'oxydation du toluène par O_2, en utilisant le seul $Cu^{(I)}$ comme catalyseur (Figure 3). La première étape du mécanisme est la coordination d'O_2 sur l'ion $Cu^{(I)}$, selon un mode *end-on* (un seul atome d'oxygène est lié au Cu). L'atome d'oxygène qui coordine O_2 est appelé proximal, tandis que l'autre est qualifié de distal. Cette première étape est favorable énergétiquement, mais les études de population (charges de Bader, densité de spin de Mulliken) ont montré que le dioxygène est faiblement activé par Cu^{+}. En effet, la charge du Cu varie peu (ce qui montre que le transfert d'électron du cuivre vers O_2 est limité), tandis que la majorité de la densité de spin reste concentrée sur les atomes d'oxygène. Un mécanisme en trois étapes a ensuite été dégagé. La présence d'un ligand donneur permet la formation d'un adduit $Cu^{(II)}$-$O_2^{\bullet-}$ activé, car il favorise le transfert d'électron depuis le Cu vers O_2. Un tel adduit peut attaquer un substrat pour former un adduit Cu-OOH (hydroperoxo). Dans notre cas CuO_2 révèle majoritairement un caractère $Cu^{(I)}$-O_2, aussi la barrière d'énergie pour un éventuel transfert d'atome d'hydrogène en sera d'autant plus élevée. Un état de transition correspondant au transfert d'un atome d'hydrogène entre le groupement méthyl du toluène et CuO_2 a été trouvé, à la fois dans l'état de spin triplet, plus stable en énergie, et dans l'état singulet. La procédure IRC (Intrinsic Reaction Coordinate) qui permet de suivre le chemin de plus basse énergie autour de l'état de transition a révélé deux comportements différents, selon l'état de spin. Dans le cas triplet, l'IRC mène à la formation d'une espèce hydroperoxo tandis que dans l'état de spin singulet, elle montre le transfert de l'atome d'hydrogène suivi par la rotation de la liaison OO sur elle-même. Cette rotation mène à la formation d'une liaison entre l'atome de carbone du toluène et l'atome d'oxygène distal (qui porte l'atome d'hydrogène). Finalement, un intermédiaire stable possédant un caractère hybride est obtenu. Cette étape peut être vue comme l'insertion d'un atome d'hydrogène dans la liaison CH du toluène. La liaison CO obtenue, bien que légèrement plus longue que la liaison CO d'un alcool, a un caractère presque covalent. D'autre part, il est également possible de reconnaître dans la structure de cet intermédiaire un hydroperoxo en interaction avec Ph-CH_2. Dans ce cas, l'état singulet impose la formation de la liaison CO. Cependant, cette étape fait penser à un chemin réactionnel proposé dans la littérature (abstraction de H suivie de la recoordination d'un radical $OH^{\bullet}$ sur le substrat). Cet intermédiaire singulet est plus stable en énergie que l'intermédiaire Cu-hydroperoxo de l'état triplet. Il

est donc nécessaire d'avoir un point de croisement des surfaces de spin pour parvenir à l'intermédiaire stable de l'état singulet. En dépit des calculs effectués à l'aide de méthodes multi-déterminantales (qui permettent de mélanger des fonctions d'onde de différents états de spin), aucun point de croisement de surfaces de spin n'a été trouvé avec certitude. Des considérations sur la géométrie des états de transition et sur les chemins IRC ont cependant été proposées, jusqu'à l'obtention d'une structure possédant des énergies très proches dans les deux états de spin considérés.

Étant donné que l'intermédiaire A ne peut réagir avec l'environnement pour mener à la formation de l'alcool benzylique, une deuxième oxydation a donc été envisagée. Ainsi, l'atome d'hydrogène porté par l'atome d'oxygène distal est transféré à l'atome d'oxygène proximal. En d'autres termes, l'atome d'oxygène distal est inséré dans la liaison $O_{proximal}$ – H. Ce deuxième intermédiaire peut être vu comme un benzylperoxide, qui n'a jamais été proposé comme intermédiaire dans les mécanismes des cuproenzymes mononucléaires. Comme peroxide, cette espèce peut se dégrader pour mener à la formation du benzaldéhyde et d'eau, via un troisième état de transition.

Le calcul des charges de Bader et l'analyse des points critiques (BCP) a permis de consolider l'analyse sur la nature des intermédiaires. Différentes méthodes DFT de plusieurs familles de fonctionnelles ont été testées. Il a été démontré qu'il est nécessaire d'inclure une part d'échange HF dans la fonctionnelle, les méthodes locales menant à des incohérences majeures, tant au niveau énergétique (sous-estimation de l'énergie des états de transition) qu'au niveau mécanistique (la procédure IRC ne permet pas de retrouver les intermédiaires A et B autour du deuxième état de transition). Cette étude théorique a confirmé que le ligand jouait un rôle primordial dans la coordination d'O_2, son activation, et l'oxydation de substrats. La présence d'un ou plusieurs ligands est nécessaire pour améliorer le transfert d'électron de $Cu^{(I)}$ vers O_2. Le ligand permet en outre de fragiliser la liaison OO, soit pour la formation de H_2O_2, soit pour être cassée et oxyder un substrat. Troisième point d'importance, l'écart entre les surfaces d'énergie potentielles (en général singulet et triplet) est réduit par la présence du ou des ligands[5]. Le mécanisme de la première étape montre des similitudes avec la réactivité proposée au sein des enzymes. Pour déterminer aussi le rôle du cuivre dans la réaction modèle, la comparaison avec un mécanisme sans cuivre a été faite. Les barrières énergétiques d'abstraction d'atome d'hydrogène (premier état de transition) et de dégradation du peroxide (troisième état de transition) ne sont que faiblement diminuées en présence de Cu^{+}.

Coordination d'O_2 sur des complexes Cu-bipyridine en phase gaz

La première étape des mécanismes d'oxydation au sein des enzymes et de leurs modèles respectifs est donc la coordination d'O_2 sur le Cu. La formation d'adduits O_2 a été observée quelques fois en phase gaz[6–8]. L'étude de la coordination d'O_2 sur des centres ioniques métalliques est utile, car son activation est au cœur de nombreuses réactions d'oxydation dans les systèmes biologiques ou biomimétiques. Les mécanismes d'activation et de conversion de l'oxygène en oxyde et apparentés (H_2O, OH^-) sont toujours très discutés. La caractérisation d'adduits CuO_2 est donc fondamentale en chimie inorganique, d'autant plus qu'ils ont en général une durée de vie très courte et nécessitent des appareillages spécialisés pour être mis en évidence. La mise en place d'expériences résolues en temps, ou à des basses températures a été plébiscitée. La spectrométrie de masse est un outil de choix pour l'isolation d'adduits réactifs, car la phase gaz permet de retirer toutes les interactions d'un ion avec son environnement (solvant). Il n'a pas été possible d'observer la coordination d'O_2 directement sur les ions Cu^+ nus ou complexés par des petits ligands monodentates (eau, triéthylamine, acétonitrile, N-méthylimidazole). Les ligands R_2bpy (ligands bipyridine fonctionnalisés en positions 4 et 4' par deux groupements R identiques – OMe, tBu, Me, H, CO2Me et NO2 –) et phen (phénantroline) ont été utilisés pour préparer des complexes de Cu à même de réagir avec O_2, comme proposé dans la littérature[9–11]. Des solutions contenant 5.10^{-5} M de $Cu(OTf)_2$ et un équivalent de R_2bpy (ou phen) ont été injectées dans la source d'ionisation par électronébulisation d'un triple quadripôle. La réduction des complexes de $Cu^{(II)}$ a été observée[12,13]. Ainsi, il a été possible d'observer les pics correspondants aux complexes $[Cu(R_2bpy)(CH_3CN)]^+$. En revanche, les conditions d'ionisation douces n'ont pas permis de générer les ions $[Cu(R_2bpy)]^+$. La stratégie mise en place a donc consisté à faire un échange de ligands entre CH_3CN et O_2, en isolant les adduits $[Cu(R_2bpy)(CH_3CN)]^+$ (ions précurseurs) et en utilisant O_2 comme gaz de collision. Deux mécanismes ont été proposés pour cet échange de ligands. D'une part, un mécanisme dissociatif : la première étape est la décoordination de l'acétonitrile, qui mène à la formation des ions $[Cu(R_2bpy)]^+$, suivie de la coordination d'O_2. D'autre part, un mécanisme associatif, où la coordination d'O_2 se fait en premier lieu, suivie de la décoordination de l'acétonitrile. Bien que ces deux mécanismes apparaissent comme étant compétitifs, le mécanisme dissociatif est préférentiel, puisque l'intensité du pic correspondant à $[Cu(R_2bpy)]^+$ est bien plus élevée que celle du

pic correspondant à $[Cu(R_2bpy)(CH_3CN)(O_2)]^+$, pour tous les ligands utilisés. Des conditions optimales pour l'échange de ligands ont été déterminées en se basant sur la maximisation du signal total (TIC) mais aussi du ratio de l'intensité du pic correspondant à $[Cu(R_2bpy)(O_2)]^+$ sur celle du pic correspondant à $[Cu(R_2bpy)]^+$. La pression d'O_2 a été fixée à 8.10^{-3} mbar, et la tension de collision à 5 V. Ce ratio (appelé bpy^R) a été calculé à partir des spectres MS/MS de chaque ligand R_2bpy, dans les mêmes conditions expérimentales. Le logarithme du ratio bpy^R/bpy^H (où H correspond à H_2bpy) a été tracé point par point par rapport à la valeur du paramètre de Hammett pour chaque groupement fonctionnel R[14] (Figure 4, graphique de gauche). Une relation linéaire a été obtenue pour les groupements électro-donneurs. Les groupements fonctionnels R ont une influence sur la coordination d'O_2 en phase gaz. Plus un groupement R est électro-donneur, et plus le complexe $[Cu(R_2bpy)]^+$ sera susceptible de coordiner O_2.

La DFT, au niveau de théorie B3LYP/6-31+G(d,p), permet d'évaluer la géométrie des adduits CuO_2 et $BDE(CuO_2)$, l'énergie de dissociation de la liaison CuO_2, calculée comme suit :

$$BDE(CuO_2) = E_{LCu^+} + ZPE_{LCu^+} + E_{O2} + ZPE_{O2} - E_{LCuO2^+} - ZPE_{LCuO2^+}$$

où E est l'énergie électronique, ZPE, l'énergie du point zéro et L le ligand R_2bpy impliqué.

L'énergie (E+ZPE) de l'adduit $Cu(R_2bpy)(O_2)]^+$ dépend de la façon dont O_2 est coordiné sur le centre métallique. Deux modes de coordination possibles ont été envisagés, *end-on* et *side-on*, selon l'hapticité d'O_2 (η^1 et η^2, respectivement). La coordination *side-on*, dans l'état de spin triplet, a été calculée comme étant la plus stable pour chacun des complexes étudiés (Figure 5). Ce résultat rejoint une étude précédente, dans laquelle un ligand biquinolyl a été utilisé[15]. Cette coordination *side-on* s'explique par le faible encombrement du ligand bipyridine, ainsi que par l'orientation préférentielle des orbitales $d_{x^2-y^2}$ (dans le plan du ligand) et d_{xy} (perpendiculaire au plan du ligand) pour la coordination d'O_2. Un modèle mathématique simplifié a montré une bonne corrélation entre calculs de chimie quantique et expérience (Figure 4, graphique de droite). Il est basé sur l'hypothèse d'un régime thermique, c'est-à-dire que l'échelle de temps de l'expérience suffit à établir un équilibre thermodynamique. Ainsi, le ratio de l'intensité du pic correspondant à $[Cu(R_2bpy)(O_2)]^+$ sur celle du pic correspondant à $[Cu(R_2bpy)]^+$ est lié à l'énergie de dissociation de la liaison CuO_2. Ce modèle a été établi par rapport à la référence H_2bpy. Les BDE calculées ont été tracés en fonction des paramètres de

Hammett. Les valeurs peuvent être séparées en deux relations linéaires (selon que les groupements R sont donneurs ou accepteurs d'électrons). Les groupes les plus susceptibles de former des liaisons hydrogène avec le solvant (R = -OH, -CO_2Me) ont montré des écarts significatifs par rapport aux modèles linéaires. Ainsi, nos calculs permettraient d'obtenir des paramètres de Hammett corrigés de l'influence du solvant.

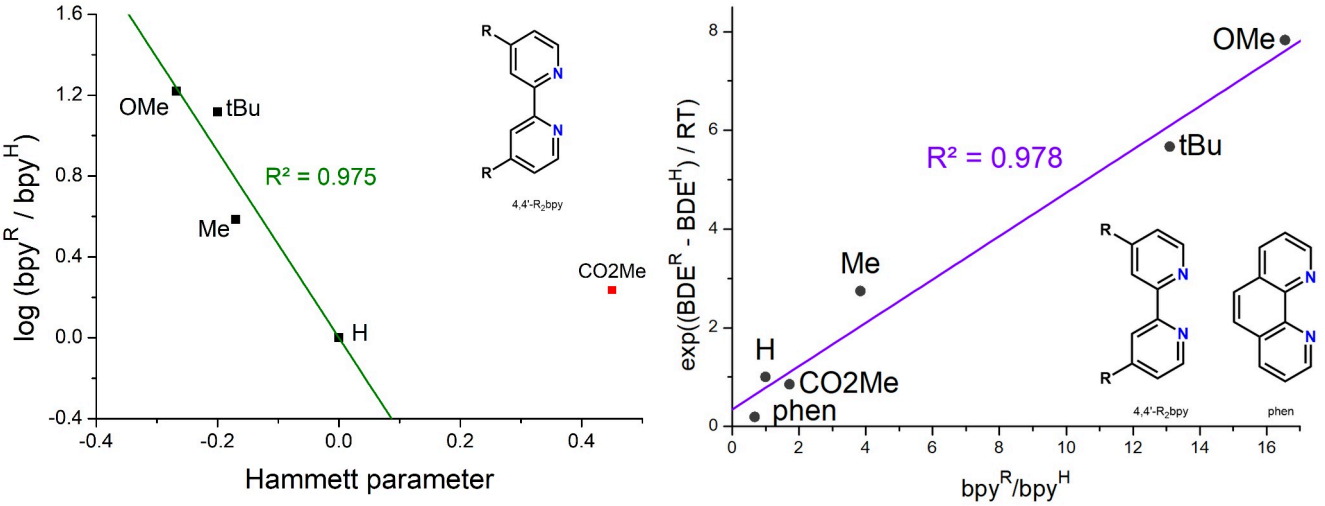

Figure 4: À gauche, graphique de Hammett des ratios des intensités $I(LCuO_2^+)/I(LCu^+)$ expérimentales obtenues par spectrométrie de masse, L étant un ligand R_2bpy. À droite, relation entre énergies de dissociation calculées par DFT et expérience (ratio bpy^R/bpy^H).

Les indicateurs calculés (énergies de dissociation, distances entre les atomes d'oxygène, charges de Bader, densité de spin de Mulliken) ont montré une faible variation au long de la série des groupements fonctionnels. Cependant, il est possible de distinguer leurs effets grâce à la spectrométrie de masse.

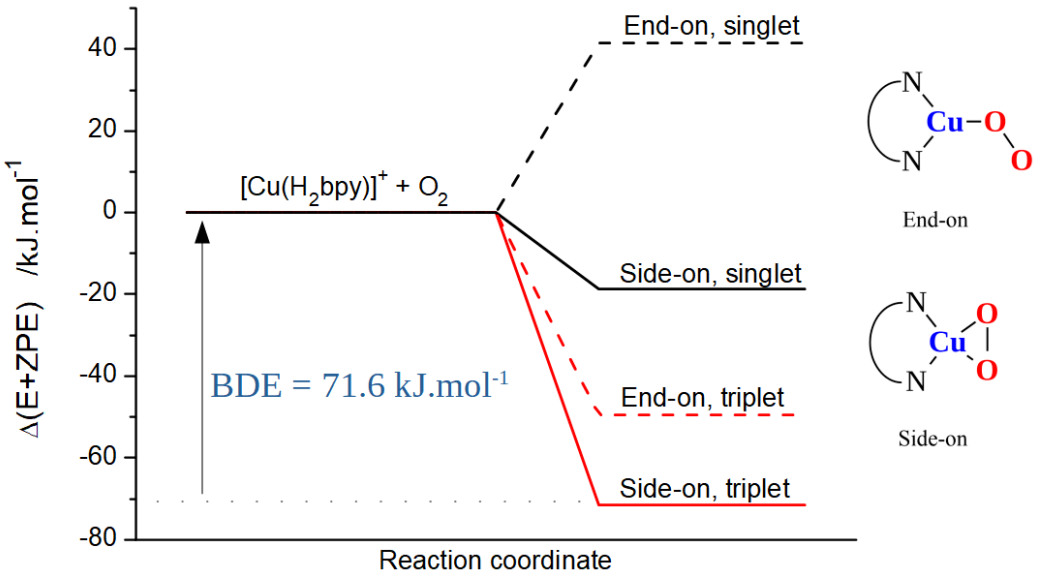

Figure 5: Diagramme de stabilité des différents adduits $[Cu(H_2bpy)(O_2)]^+$ en fonction de leur mode de coordination et de leur état de spin.

Coordination d'O_2 sur des complexes de Cu avec des ligands tripodaux en phase gaz

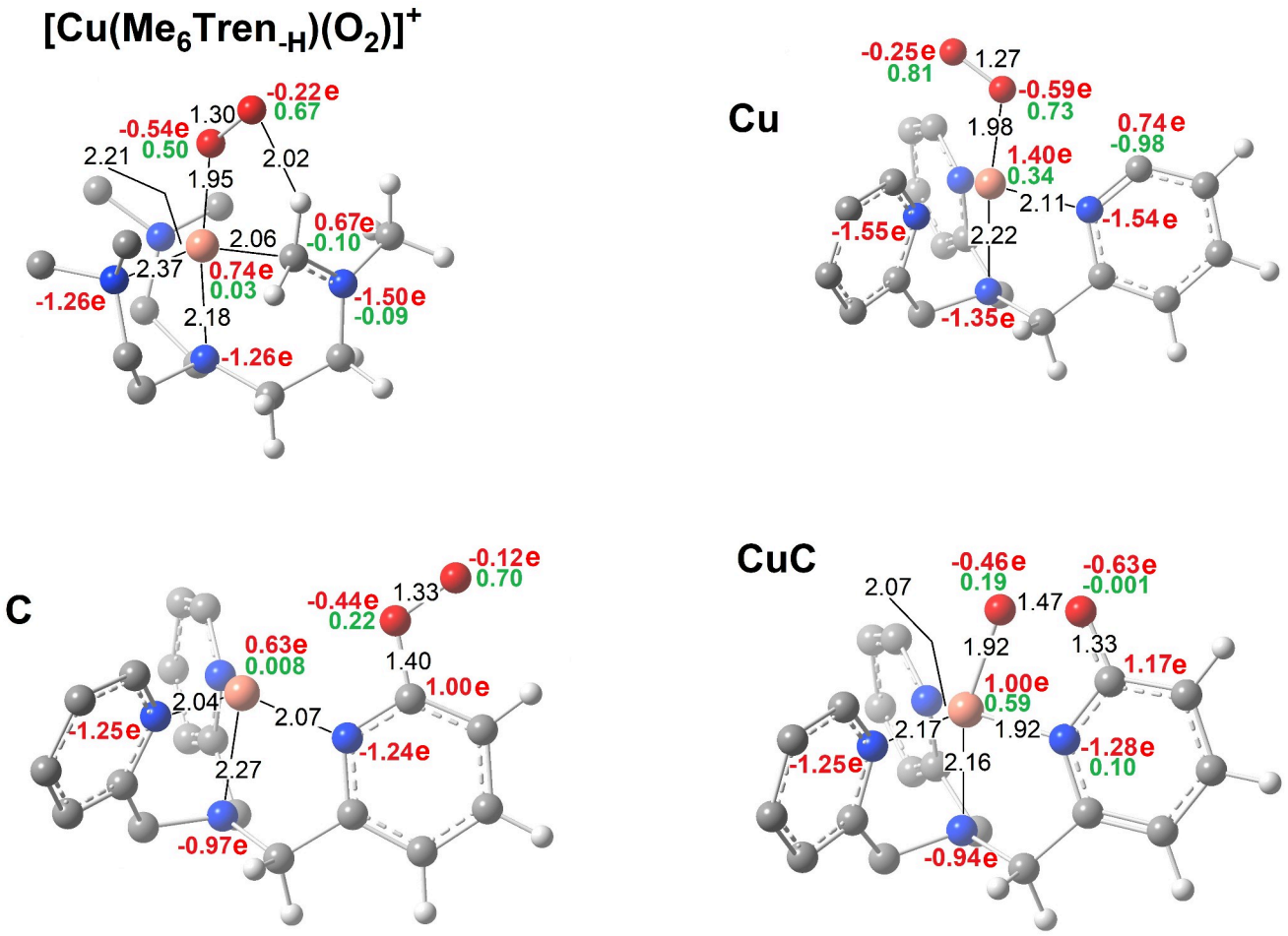

Figure 6: Structures de [Cu(Me$_6$Tren$_{-H}$)(O$_2$)]$^+$ et de [Cu(TMPA$_{-H}$)(O$_2$)]$^+$ (isomères Cu, C et CuC), calculées au niveau de théorie B3LYP/6-31+G(d,p). Quelques distances importantes (en Å, noir), les charges de Bader (rouge) et les densités de spin de Mulliken (vert) de quelques atomes sont indiquées. Une partie des atomes d'hydrogène a été retirée par souci de clarté.

Afin de complexifier encore le système autour du Cu, des ligands tripodaux bien connus pour former des complexes stables avec Cu$^{(I)}$[16] ont été utilisés pour tenter de coordiner et d'activer O_2 en phase gaz. Les ligands Me_6Tren (tris[2-(dimethylamino)éthyl]amine) et TMPA (tris(2-pyridylméthyl)-amine) sont connus pour leur capacité à former des adduits avec le dioxygène en phase condensée, qui réagissent très rapidement pour former des adduits {LCu}$_2$(μ-O_2)[17,18]. Les adduits CuO_2 ont été

modélisés comme étant des espèces $Cu^{(II)}$-superoxo, avec une coordination *end-on*, dans l'état de spin triplet[19]. Les spectres MS des complexes de $Cu^{(II)}$ avec des ligands tripodaux (Tren (tris-2-aminoéthylamine), Me_6Tren, TMPA) montrent les pics correspondant à $[Cu(L)(X)]^+$ et $[Cu(L)]^+$ (L étant le ligand tripodal, X un contre-ion). L'utilisation d'eau comme solvant induit la coordination d'ions OH^- sur le centre $Cu^{(II)}$. L'ion $[Cu(L)(OH)]^+$ résultant peut être fragmenté en source (Figure 8, bas), ou dans la cellule de collision (Figure 7). La perte d'une molécule d'eau (- 18 Da) a été observée, ce qui mène à la formation d'ions $[Cu(L_{-H})]^+$, où l'indice "$_{-H}$" représente une perte de proton sur le ligand. Des ligands Tren et TMPA partiellement deutérés ont été utilisés pour déterminer sur quelle position le proton est arraché. Les spectres MS/MS ont montré que les bras des ligands ne se décoordinent pas de l'atome de Cu et que l'abstraction d'un proton se fait sur le site le plus proche du contre-ion. Les groupements NMe_2 du ligand Me_6Tren étant plus donneurs que NH_2 (Tren) et pyridyl (TMPA), nous avons émis l'hypothèse que les bras du Me_6Tren n'étaient pas non plus décoordinés, et que l'abstraction du proton se fait sur un des groupements CH_3. Dans le cas du ligand TMPA, la structure de l'ion $[Cu(L_{-H})]^+$ est proche de celle de l'ion $[Cu(L)]^+$. De même, la La répartition de la densité de spin de Mulliken montre la présence d'un radical sur le carbone déprotonné. Un électron excédentaire est délocalisé sur le Cu, comme le prouve la répartition des charges sur l'ion Cu: le même nombre de charges est obtenu pour les deux structures (0.66 e). Un intermédiaire tel que celui-ci a déjà été proposé dans la littérature[20]. Dans le cas de Me_6Tren, l'abstraction d'un atome d'hydrogène mène à la coordination de l'atome de carbone du groupement CH_3 déprotonné sur le Cu. Ici encore, la formation d'un carbanion mène à la formation d'un $Cu^{(I)}$ en interaction avec un carboradical. Ce type de complexe n'a jamais été proposé comme intermédiaire réactionnel.

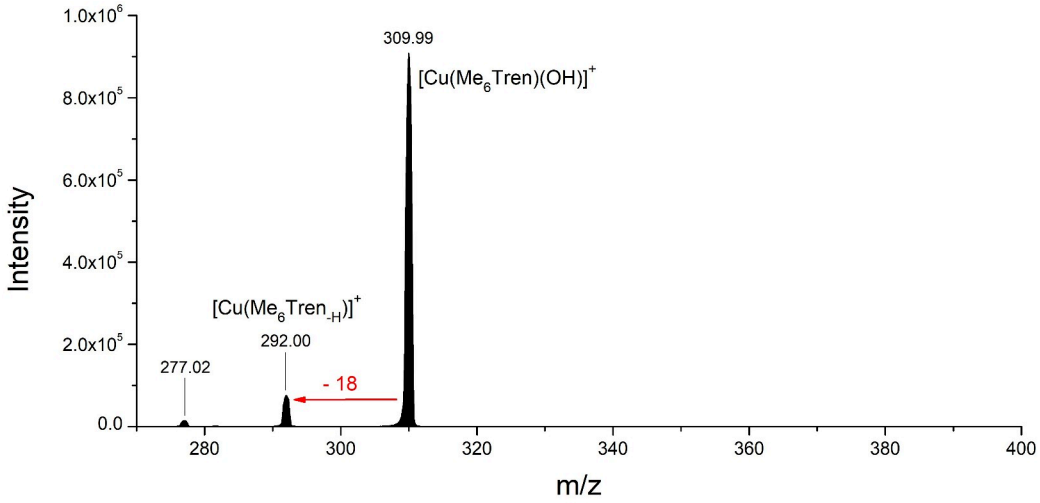

Figure 7: Spectre MSMS du pic m/z 310, correspondant à l'ion [Cu(Me₆Tren)(OH)]⁺.

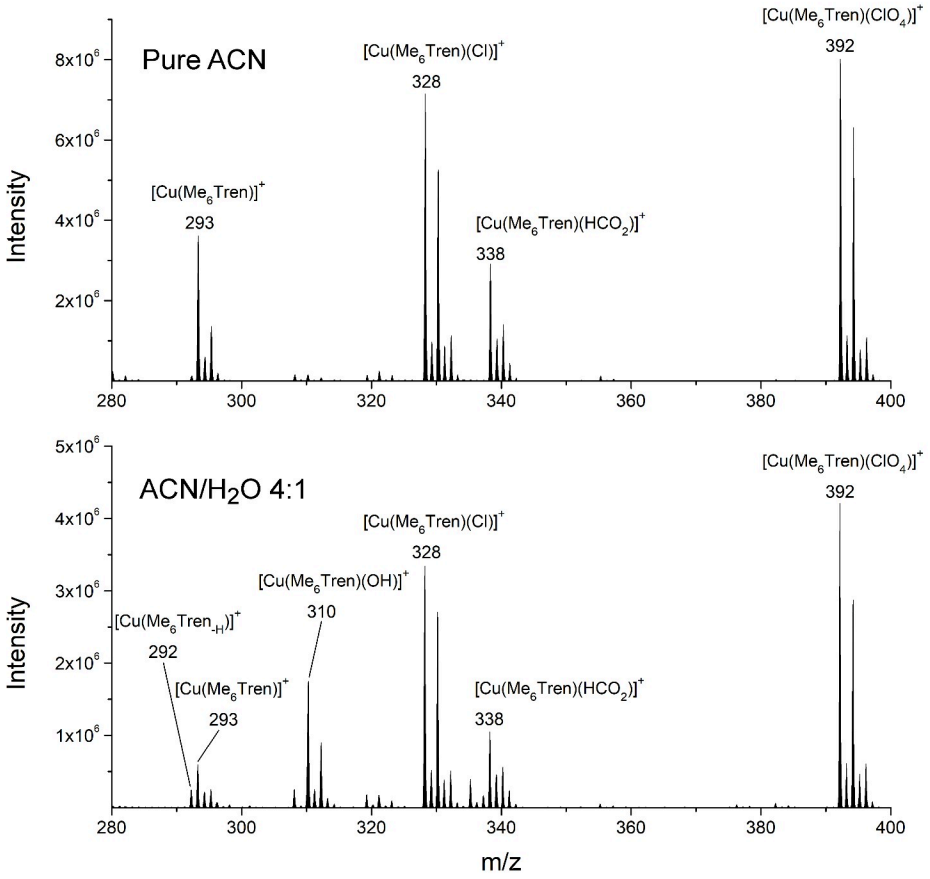

Figure 8: Effet du solvant sur le spectre ESI-MS de [Cu(Me₆Tren)(H₂O)](ClO₄)₂ à 5.10⁻⁵ M.

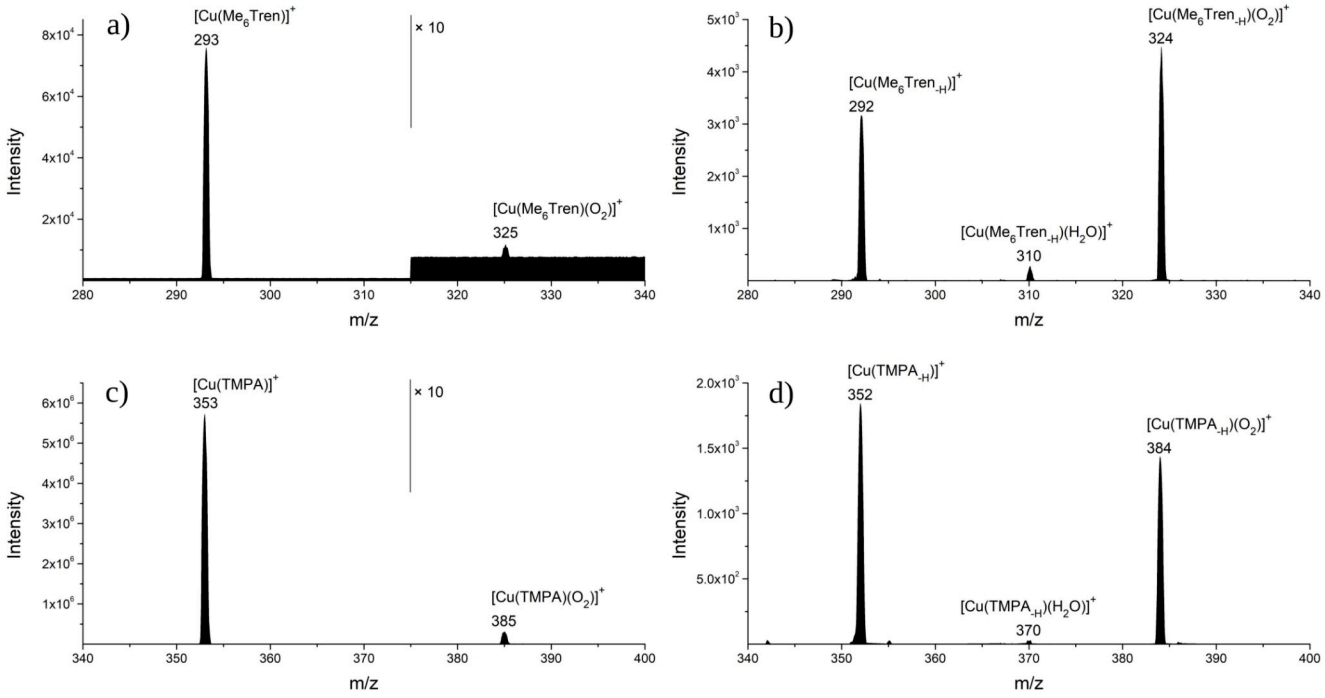

Figure 9: Spectres MSMS de a) $[Cu(Me_6Tren)]^+$, b) $[Cu(Me_6Tren_{-H})]^+$, c) $[Cu(TMPA)]^+$ et d) $[Cu(TMPA_{-H})]^+$, avec O_2 comme gaz de collision ($P(O_2)= 6{,}5.10^{-3}$ mbar, $V_{coll} = 3$ V).

Nos expériences CAR-MS/MS ont permis de générer des adduits CuO_2, par coordination directe. Les complexes de cuivre déprotonnés $[Cu(Me_6Tren_{-H})]^+$ et $[Cu(TMPA_{-H})]^+$ ont montré une réactivité exacerbée vis-à-vis du dioxygène par rapport à leurs équivalents $[Cu(Me_6Tren)]^+$ et $[Cu(TMPA)]^+$, respectivement (Figure 9). Dans le cas du complexe $[Cu(TMPA_{-H})(O_2)]^+$, trois isomères possibles ont été calculés (Cu, C et CuC sur la Figure 6). O_2 est connu pour réagir avec les radicaux[21]. La présence d'un radical sur le cycle pyridine permet d'expliquer la forte réactivité du dioxygène, au vu de la forte énergie de stabilization des isomères C et CuC (Tableau 1). La formation d'une liaison hydrogène forte entre l'atome d'oxygène distal et un atome d'hydrogène du CH_2 lié au Cu rend la coordination d'O2 plus favorable sur $[Cu(Me_6Tren_{-H})]^+$ que sur $[Cu(Me_6Tren)]^+$ (Tableau 1). Si B3LYP est parfois recommandée pour les espèces CuO_2[19,22], elle semble ne pas bien prendre en compte l'énergie de stabilisation due à la formation de cette liaison hydrogène. Une caractérisation $Cu^{(I)}$-superoxo a été proposée pour l'adduit $[Cu(Me_6Tren_{-H})(O_2)]^+$. Cet intermédiaire est capable d'arracher un atome d'hydrogène sur le ligand, comme en témoigne la perte d'un radical O_2H (-33 Da) lorsque $[Cu(Me_6Tren_{-H})(O_2)]^+$ est formé dans l'hexapole de transfert précédant le premier quadripôle.

Espèce	Énergie de dissociation d'O_2 / kJ.mol^{-1}
$[Cu(Me_6Tren)(O_2)]^+$	30
$[Cu(Me_6Tren_{-H})(O_2)]^+$	37
$[Cu(TMPA)(O_2)]^+$	27
$[Cu(TMPA_{-H})(O_2)]^+$ isomère Cu	20
$[Cu(TMPA_{-H})(O_2)]^+$ isomère C	165
$[Cu(TMPA_{-H})(O_2)]^+$ isomère CuC	240

Tableau 1: Énergie de dissociation des complexes CuO_2 avec les ligands Me_6Tren, Me_6Tren-H, TMPA et $TMPA_{-H}$ (trois isomères: Cu, C et CuC), en kJ.mol^{-1}. Ces énergies ont été calculées avec B3LYP/6-31+G(d,p).

Conclusions

L'élaboration d'un mécanisme modèle d'oxydation d'un substrat (le toluène) par O_2 a permis de compléter les connaissances quant au rôle du ligand sur les réactions d'oxydation. La présence du ligand apparaît comme nécessaire pour activer le dioxygène et réduire les barrières énergétiques des mécanismes d'oxydation.

La coordination du dioxygène sur des complexes de $Cu^{(I)}$ avec des ligands bidentates (4,4'-R_2bpy et phen) et des ligands tétradentates tripodaux (Tren, Me_6Tren, TMPA) a été observée pour la première fois en phase gaz avec ces classes de ligands. Différentes stratégies de coordination ont été mises en place, selon les ions présents sur le spectre de masse. Ainsi, l'échange de ligands (principalement selon un mécanisme dissociatif) a été favorisé pour les ligands bidentates, quand la coordination directe a été employée pour les ligands tripodaux. L'influence du ligand (nature des groupements coordinants, fonctionnalisation) se répercute sur les spectres MS/MS : plus un ligand est donneur, plus le ratio des intensités de $LCuO_2^+$ sur LCu^+ est élevé, selon les séries de ligands considérées. La DFT a permis de calculer les énergies de dissociation des complexes $LCu(O_2)$ ainsi que le mode de coordination préférentiel de chaque complexe. Enfin, des complexes de Cu avec des ligands tripodaux déprotonnés (Me_6Tren_{-H}, $TMPA_{-H}$) ont montré une réactivité exacerbée vis-à-vis d'O_2, ce qui a été expliqué par la formation d'un cycle à cinq chaînons (par le biais d'une liaison hydrogène) dans le cas du Me_6Tren, et par la réaction du dioxygène avec un radical carbone dans le cas du TMPA.

Cette thèse ouvre quelques perspectives qu'il convient de souligner. D'une part, les similarités observées entre le mécanisme modèle de l'oxydation du toluène et des mécanismes d'oxydation postulés dans la littérature légitiment l'extension de cette approche originale à d'autres mécanismes moins détaillés. L'ajout de petits ligands pourrait permettre d'étudier leur apport mécanistique et énergétique. D'autre part, la caractérisation en phase gaz de composés $LCuO_2^+$ permet de souligner l'apport de la spectrométrie de masse pour l'isolation d'adduits peu stables ou très réactifs en solution. L'influence du ligand se répercutant en phase gaz, la mise au point de systèmes catalytiques pourrait éventuellement passer par des études en spectrométrie de masse. Enfin, la génération d'intermédiaires $Cu^{(I)}$-radical sensibles à O_2, quoique restreinte pour l'instant à quelques systèmes, est encourageante pour le développement de nouveaux catalyseurs efficaces.

Références

1. Kaim, W.; Rall, J. Copper—A “Modern” Bioelement. *Angew. Chem. Int. Ed. Engl.* **1996**, *35*, 43–60, doi:10.1002/anie.199600431.

2. Bader, R.F.W. *Atoms in Molecules: A Quantum Theory*; Reprint édition.; Clarendon Press: Oxford England : New York, 1994; ISBN 978-0-19-855865-1.

3. Henkelman, G.; Arnaldsson, A.; Jónsson, H. A Fast and Robust Algorithm for Bader Decomposition of Charge Density. *Comput. Mater. Sci.* **2006**, *36*, 354–360, doi:10.1016/j.commatsci.2005.04.010.

4. Popelier, P.L.A. *Atoms in Molecules: An Introduction*; Prentice Hall: Harlow, 2000; ISBN 978-0-582-36798-2.

5. Cramer, C.J.; Gour, J.R.; Kinal, A.; Włoch, M.; Piecuch, P.; Moughal Shahi, A.R.; Gagliardi, L. Stereoelectronic Effects on Molecular Geometries and State-Energy Splittings of Ligated Monocopper Dioxygen Complexes. *J. Phys. Chem. A* **2008**, *112*, 3754–3767, doi:10.1021/jp800627e.

6. Molina-Svendsen, H.; Bojesen, G.; McKenzie, C.J. Gas-Phase Reactivity of Coordinatively Unsaturated Transition Metal Complex Ions toward Molecular Oxygen. *Inorg. Chem.* **1998**, *37*, 1981–1983, doi:10.1021/ic970345r.

7. Koyanagi, G.K.; Caraiman, D.; Blagojevic, V.; Bohme, D.K. Gas-Phase Reactions of Transition-Metal Ions with Molecular Oxygen: Room-Temperature Kinetics and Periodicities in Reactivity. *J. Phys. Chem. A* **2002**, *106*, 4581–4590, doi:10.1021/jp014145j.

8. Donnelly, J.M.; Lermyte, F.; Wolny, J.A.; Walker, M.; Breeze, B.G.; Needham, R.J.; Müller, C.S.; O’Connor, P.B.; Schünemann, V.; Collingwood, J.F.; et al. Cu(III)–Bis-Thiolato Complex Forms an Unusual Mono-Thiolato Cu(III)–Peroxido Adduct. *Chem. Commun.* **2021**, *57*, 69–72, doi:10.1039/D0CC06921C.

9. McCrory, C.C.L.; Ottenwaelder, X.; Stack, T.D.P.; Chidsey, C.E.D. Kinetic and Mechanistic Studies of the Electrocatalytic Reduction of O2 to H2O with Mononuclear Cu Complexes of Substituted 1,10-Phenanthrolines. *J. Phys. Chem. A* **2007**, *111*, 12641–12650, doi:10.1021/jp076106z.

10. McCrory, C.C.L.; Devadoss, A.; Ottenwaelder, X.; Lowe, R.D.; Stack, T.D.P.; Chidsey, C.E.D. Electrocatalytic O2 Reduction by Covalently Immobilized Mononuclear Copper(I) Complexes: Evidence for a Binuclear Cu2O2 Intermediate. *J. Am. Chem. Soc.* **2011**, *133*, 3696–3699, doi:10.1021/ja106338h.

11. Hoover, J.M.; Ryland, B.L.; Stahl, S.S. Mechanism of Copper(I)/TEMPO-Catalyzed Aerobic Alcohol Oxidation. *J. Am. Chem. Soc.* **2013**, *135*, 2357–2367, doi:10.1021/ja3117203.

12. Lavanant, H.; Virelizier, H.; Hoppilliard, Y. Reduction of Copper(II) Complexes by Electron Capture in an Electrospray Ionization Source. *J. Am. Soc. Mass Spectrom.* **1998**, *9*, 1217–1221, doi:10.1016/S1044-0305(98)00100-7.

13. Gianelli, L.; Amendola, V.; Fabbrizzi, L.; Pallavicini, P.; Mellerio, G.G. Investigation of Reduction of Cu(II) Complexes in Positive-Ion Mode Electrospray Mass Spectrometry. *Rapid Commun. Mass Spectrom.* **2001**, *15*, 2347–2353, doi:10.1002/rcm.510.

14. Hansch, Corwin.; Leo, A.; Taft, R.W. A Survey of Hammett Substituent Constants and Resonance and Field Parameters. *Chem. Rev.* **1991**, *91*, 165–195, doi:10.1021/cr00002a004.

15. Polestshuk, P.M.; Magdesieva, T.V. Computational Exploration of the Mechanism of Alcohol Oxidation by Dioxygen Activated with Biquinolyl-Containing Cu Complexes. *Inorg. Chem.* **2010**, *49*, 3370–3386, doi:10.1021/ic9024537.

16. Blackman, A.G. The Coordination Chemistry of Tripodal Tetraamine Ligands. *Polyhedron* **2005**, *24*, 1–39, doi:10.1016/j.poly.2004.10.012.

17. Schatz, M.; Becker, M.; Thaler, F.; Hampel, F.; Schindler, S.; Jacobson, R.R.; Tyeklár, Z.; Murthy, N.N.; Ghosh, P.; Chen, Q.; et al. Copper(I) Complexes, Copper(I)/O2 Reactivity, and Copper(II) Complex Adducts, with a Series of Tetradentate Tripyridylalkylamine Tripodal Ligands. *Inorg. Chem.* **2001**, *40*, 2312–2322, doi:10.1021/ic000924n.

18. Becker, M.; Heinemann, F.W.; Schindler, S. Reversible Binding of Dioxygen by a Copper(I) Complex with Tris(2-Dimethylaminoethyl)Amine (Me6tren) as a Ligand. *Chem. - Eur. J.* **1999**, *5*, 3124–31296, doi:10.1002/(SICI)1521-3765(19991105)5:11<3124::AID-CHEM3124>3.0.CO;2-D.

19. de la Lande, A.; Gérard, H.; Moliner, V.; Izzet, G.; Reinaud, O.; Parisel, O. Theoretical Modelling of Tripodal CuN3 and CuN4 Cuprous Complexes Interacting with O2, CO or CH3CN. *JBIC J. Biol. Inorg. Chem.* **2006**, *11*, 593–608, doi:10.1007/s00775-006-0107-8.

20. Shen, K.; Diskin-Posner, Y.; Shimon, L.J.W.; Leitus, G.; Carmieli, R.; Neumann, R. Aerobic Oxygenation Catalyzed by First Row Transition Metal Complexes Coordinated by Tetradentate Mono-Carbon Bridged Bis-Phenanthroline Ligands: Intra- versus Intermolecular Carbon–Hydrogen Bond Activation. *Dalton Trans.* **2019**, *48*, 6396–6407, doi:10.1039/C9DT00828D.

21. Eskola, A.J.; Pekkanen, T.T.; Joshi, S.P.; Timonen, R.S.; Klippenstein, S.J. Kinetics of 1-Butyl and 2-Butyl Radical Reactions with Molecular Oxygen: Experiment and Theory. *Proc. Combust. Inst.* **2019**, *37*, 291–298, doi:10.1016/j.proci.2018.05.069.

22. Ducéré, J.-M.; Goursot, A.; Berthomieu, D. Comparative Density Functional Theory Study of the Binding of Ligands to Cu+ and Cu2+: Influence of the Coordination and Oxidation State. *J. Phys. Chem. A* **2005**, *109*, 400–408, doi:10.1021/jp047971b.

UNIVERSITE MATIERE BRETAGNE MOLECULES LOIRE ET MATERIAUX

UBO Université de Bretagne Occidentale

Titre : Complexification d'un système $LCu^{(I)}$ pour la coordination et l'activation du dioxygène : étude par spectrométrie de masse et DFT

Mots clés : Mécanisme modèle, Réactions ion-molécule, Spectrométrie de masse tandem, Calculs DFT

Résumé : Les problématiques environnementales et les besoins en énergie actuels ont amené la communauté scientifique à copier les sites actifs des enzymes pour produire de l'énergie ou des carburants de manière plus respectueuse de l'environnement. Les enzymes à cuivre ont démontré leurs capacités à activer le dioxygène, abondant dans l'air, pour oxyder des petites molécules. Les mécanismes de fonctionnement de ces enzymes ou de leurs modèles respectifs possèdent toujours des zones d'ombre, notamment sur le rôle du ligand au cours des réactions d'oxydation. Le premier objectif de ce travail a été de déterminer par DFT le mécanisme d'une réaction modèle, l'oxydation du toluène par O_2, en utilisant le seul Cu^+ comme catalyseur. Par comparaison, cette approche a permis de clarifier le rôle du ligand sur les réactions d'oxydation et pourrait être appliquée à des systèmes moins connus. La coordination et l'activation d'O_2 sur le centre métallique a été étudiée expérimentalement par spectrométrie de masse, celle-ci permettant de former et d'isoler des composés supposés très réactifs en phase liquide. Différentes stratégies de coordination ont été mises en place (échange de ligand, coordination directe) en fonction des ligands utilisés. L'influence du ligand sur la coordination d'O_2 en phase gaz ainsi que le caractère $Cu^{(II)}$-superoxo des adduits formés (DFT) ont été mis en évidence. La réactivité exacerbée de complexes de Cu déprotonés (formés dans la source d'ionisation par électronébulisation) vis-à-vis d'O_2 a été expliquée par des interactions intramoléculaires et ouvre la voie au développement de nouveaux catalyseurs.

Title: Growing complexity of $LCu^{(I)}$ to elucidate O_2 coordination and activation: a mass spectrometric and DFT study

Keywords: Model mechanism, ion-molecule reactions, Tandem mass spectrometry, DFT calculations

Abstract: Environmental issues and current energy needs have led the scientific community to copy the active sites of enzymes to produce energy or fuels in a "greener" way. Copper enzymes have demonstrated their ability to activate dioxygen, abundant in air, to oxidize small molecules. The operating mechanisms of these enzymes or their respective models still have gray areas, in particular on the role of the ligand during oxidation reactions. The first objective of this work was to determine by DFT the mechanism of a model reaction, the oxidation of toluene by O_2, using only Cu^+ as a catalyst. By comparison, this approach has made possible to clarify the role of the ligand on oxidation reactions and might be extended to less detailed systems. The first step of these mechanisms, which is the coordination and the activation of O_2 on the metal center, has been experimentally studied by mass spectrometry, which allows the formation and isolation of reactive intermediates. Different coordination strategies have been used (ligand exchange, direct coordination) depending on the ligands used. The influence of the ligand on the coordination of O_2 in the gas phase has been demonstrated as well as the $Cu^{(II)}$-superoxo character of the adducts formed (DFT). The exacerbated reactivity of Cu deprotonated complexes (formed in the electrospray source) has been explained by intramolecular interactions and opens the way to the development of new efficient catalysts.